

INAUGURAL-DISSERTATION

zur Erlangung der Doktorwürde der

GESAMTFAKULTÄT FÜR MATHEMATIK, INGENIEUR- UND
NATURWISSENSCHAFTEN

der

RUPRECHT-KARLS-UNIVERSITÄT
HEIDELBERG

vorgelegt von

Verena Fürnkranz

geb. in Wien, Österreich

Tag der mündlichen Prüfung: 21.10.2024

The Small-Scale Structure of the Milky Way's Orbit Distribution

Gutachter: Prof. Dr. Hans-Walter Rix
Prof. Dr. Eva Grebel

ZUSAMMENFASSUNG

Die Milchstraße bietet die einzigartige Möglichkeit die Bahnen von Sternen in der galaktischen Scheibe von ihrer anfänglichen „klumpigen Verteilung“ bis hin zu ihrer späteren „glatten Verteilung“ zu untersuchen. Sterne entstehen in Haufen, die verschieden ausgeprägt sein können: manche dieser Objekte sind kompakt und gebunden, andere wiederum sind nur flüchtige lose Assoziationen von Sternen. Über die Zeit lösen sich die meisten Sternhaufen auf, verstreuen sich im Bahn- und Phasenraum und erschaffen so die galaktische Feldpopulation. Hat man eine Alters- und Bahnverteilung solcher Gruppen, kann man näher untersuchen, auf welchen Bahnen Sterne geboren werden, wie schnell sich diese Systeme auflösen und inwieweit die Verteilung der Bahnen die ausgedehnten molekularen Gasfilamente widerspiegelt, aus denen die Sterne entstanden sein könnten. Diese Arbeit zeigt, dass wir mit dem außergewöhnlichen Datenset des Gaia Satelliten solche Sterngruppen als kleinskalige, überdichte Strukturen im Bahn- und Phasenraum detektieren können. Beim Betrachten der Bahnverteilung dieser Gruppen zeigt sich, dass sich Sternhaufen bevorzugt auf ähnlichen Bahnen, in unterschiedlichen Bahnphasen befinden. Daran anknüpfend entwickeln und präsentieren wir eine Methode, um mit Isochronen die Alter von stellaren Ensembles abzuschätzen, welche ursprünglich nur eine kleine Zahl von Sternen haben. Dabei finden wir heraus, dass es Mehrdeutigkeiten bei der Altersbestimmung von Sterngruppen gibt, bei denen weder die untere Hauptreihe noch die Abzweigung der Hauptreihe Altershinweise liefern. Abschließend zeigen wir in einem kurzen Ausblick wie man Alters- und Bahnkorrelationen von stellaren Gruppen untersuchen kann, um deren Zerstreuung in der Scheibe der Milchstraße künftig zu erforschen.

ABSTRACT

The Milky Way offers a unique opportunity to study the ‘clumpy-to-smooth’ orbit transition of stars in the Galactic disk: newly born stars are clustered across a wide range of scales, from compact bound objects to ephemeral birth clusterings and loose associations. Subsequently, most groups of stars disperse over time, spreading out in orbit and orbital-phase space and building up the Galactic field population. The age and orbit distribution of such co-natal groups offers the possibility to study on which orbits stars are born, how rapidly these systems disperse, and to what extent the orbit distribution reflects a possible birth from extended molecular gas filaments. Specifically, this thesis shows that with the advent of the powerful Gaia dataset, we can identify stellar groups as small-scale overdensities in orbit and orbital phase space. We explore their distribution and discover that stellar groups are frequently located on similar orbits, aligned at distinct orbital phases. We then develop and apply an isochrone fitting method to derive age estimates of stellar populations, for which we only have a small set of stars initially. We find age-dating ambiguities that exist for groups where neither the lower main-sequence nor the main-sequence turn-off offer age information. Finally, we lay out avenues for exploring age and orbit correlations as a basis to map the dispersal of stellar ensembles in the Milky Way disk.

CONTENTS

ZUSAMMENFASSUNG	v
ABSTRACT	vii
1 INTRODUCTION	1
1.1 Galaxies: an Overview	1
1.1.1 History and Classification	1
1.1.2 Galaxy Formation in the Λ CDM Cosmological Context	2
1.2 The Milky Way as a Model Disk Galaxy	5
1.2.1 Basic Properties of Disk Galaxies	5
1.2.2 Components of the Milky Way	7
1.3 Stellar Orbits in Disks	10
1.3.1 How to describe Orbits	10
1.3.2 Orbit Evolution in the Galactic Disk	11
1.4 The Gaia Galactic Survey	12
1.5 Clusters in the Galactic Disk	16
1.5.1 Young Stellar Clusters	16
1.5.2 Formation and Dispersal	17
1.5.3 How to find Clusters	19
1.5.4 Up-to-Date Census of Clusters in the Galactic Disk	21
1.6 Age Dating of Clusters	25
1.6.1 CMD Isochrone Fitting	26
1.7 Goals and Outline of the Thesis	30
2 PEARLS ON A STRING: NUMEROUS STELLAR CLUSTERS STRUNG ALONG THE SAME ORBIT	33
2.1 Details of Publication and Authorship	33
2.2 Abstract	34
2.3 Introduction	34
2.4 Data	37
2.4.1 The Gaia EDR3-RVS Sample	37
2.4.2 A Mock Catalog with a Smooth and Phase-Mixed Orbit Distribution	37

2.5	Quantifying clumping in action-angle space: Pearls	38
2.5.1	Action-angle computation	38
2.5.2	Finding action-angle groups in GEDR3	38
2.5.3	Defining orbit patches around an action-angle overdensity	41
2.5.4	The angle distribution of stars within an orbit patch	43
2.6	Population Properties of Pearls	48
2.6.1	Pearls on a string: three case studies	48
2.6.2	Algorithmically identifying pearls	51
2.6.3	On-sky distribution of pearls on the same string	52
2.6.4	The statistics of pearls	55
2.7	Summary and Discussion	57
2.8	Appendix	59
2.8.1	3D Action ellipsoid continued	59
2.8.2	Case study: Coma Berenices as Pearl of Pisces Eridanus	59
2.8.3	Offset orbit patch continued	62
2.8.4	Isolated groups	62
2.8.5	Properties and Membership of the initial 55 groups	62
3	THE AGE DISTRIBUTION OF STELLAR ORBIT SPACE CLUMPS	67
3.1	Details of Publication and Authorship	67
3.2	Abstract	67
3.3	Introduction	68
3.4	Data	70
3.4.1	Excerpts of the Gaia DR3 catalog	70
3.4.2	Gaia EDR3 mock catalog	71
3.4.3	PARSEC isochrones	71
3.5	Stellar Groups in Action-Angle Space	72
3.5.1	Action-angle computation	72
3.5.2	Identifying Stellar Overdensities in 6D Action-Angle Space	72
3.5.3	Associating additional member stars in the 5D space of positions and proper motions	75
3.6	Age determination	77
3.6.1	Reddening correction	78
3.6.2	Basic Fitting Methodology	79
3.6.3	Accounting for Binaries and Outliers	81
3.6.4	Incorporating Age dispersion	81
3.7	Results	82
3.7.1	Illustrating the Age Constraints from Isochrone Fits	82

3.7.2	Ages, Age Dispersions, [M/H] and Spatial Structure of the Action-Angle Groups	84
3.8	Summary and Discussion	89
4	AGES FOR LARGE SETS OF STELLAR AGGREGATES	93
4.1	Pre-abstract	93
4.2	Large sets of stellar clusters	93
4.2.1	Identifying groups with action-angle space clustering	94
4.2.2	State-of-the-art cluster catalog by Hunt et al. 2023	94
4.3	Associating additional member stars in 5D position-proper motion space	96
4.4	Spectroscopic metallicities by Andrae et al. 2023	98
4.5	Results and Discussion	98
4.5.1	Age distributions	99
4.5.2	Comparison with literature ages	102
4.5.3	Final remarks	103
5	SUMMARY AND OUTLOOK	107
5.1	Exploration of the orbit-age space	108
5.2	Future prospects	110
	LIST OF FIGURES	113
	LIST OF TABLES	114
	ACKNOWLEDGEMENTS	117
	PERSONAL BIBLIOGRAPHY	119
	BIBLIOGRAPHY	121

1 INTRODUCTION

1.1 GALAXIES: AN OVERVIEW

Galaxies are vast collections of stars, gas, dust and dark matter that populate our universe. They have been recognized as *island universes* of millions or billions of stars for about one hundred years (E. P. Hubble, 1926). For much of the late 20th century, galaxy research has focused on understanding their individual and population properties, with the emphasis shifting over the last decades to understanding their formation and structure as a consequence of structure formation in a hierarchical dark matter and dark energy dominated Universe. Throughout this research history, our own Milky Way has played an exceptional role as an exemplary galaxy that we can observe in unmatched detail.

1.1.1 HISTORY AND CLASSIFICATION

The first galaxies were discovered by the French astronomer Charles Messier in the 17th century, which he described as *fuzzy nebulae objects*. Although he primarily devoted his work to the search for comets, he compiled and published a catalog known as the ‘Messier catalog’ consisting of star clusters and spiral nebulae (galaxies) - without knowing at that time what these fuzzy spiral nebulae were (Messier, 1781). In 1920, the astronomers Harlow Shapley and Heber Curtis argued in the National Academy of Sciences whether these spiral nebulae were relatively small, nearby objects in the Milky Way or whether they were more distant, rotating systems of stars like our Milky Way. This debate is known as the ‘Shapley-Curtis Debate’ or the ‘Great Debate’. The argument continued throughout the 1920s until the American astronomer Edwin Hubble finally determined the distance to one of these spiral nebulae, today known as the Andromeda galaxy, by measuring the period of a Cepheid variable star. Using the known luminosity-period relationship of the Cepheids, Hubble proved that the object was located outside the Milky Way (E. Hubble, 1929). This ended the debate of the nature of the spiral nebulae (galaxies), and ushered in a new era of extragalactic astronomy.

Galaxies have a wide variety of morphologies, and Hubble was the first astronomer to classify galaxies on the basis of their appearance. Today, this classification is known as the ‘Hubble sequence’ or the ‘Hubble tuning fork’ (E. P. Hubble, 1926), which separates the objects mainly into the following categories (see for

reference [Weigert and Wendker, 1989](#)): *Spiral Galaxies* (Type S) are comprised of a bulge, a disk with spiral arms, and a dark halo, and are further divided by the dominance of their spiral arms in contrast to the bulge. About 50%-70% of spiral galaxies are so-called *Barred Spiral Galaxies* (Type SB), which form a parallel sequence to the spiral galaxies. Overall, both types of galaxy are similarly defined, but the latter comprises a bar as an additional nonaxisymmetric feature, as does the Milky Way galaxy. Bars in galaxies can be variously pronounced and can show a range of different sizes and forms. *Elliptical Galaxies* (Type E) do not have a disk and resemble mostly the bulges of spiral galaxies. They are further categorized by the amount of ellipticity of their appearance. *Lenticular Galaxies* (Type S0) are object types between spiral and elliptical galaxies. They have a weakly pronounced disk and a strong ellipsoidal component. Finally, *irregular galaxies* (Type Irr) lack any clear structures or symmetries.

In 1959, the astronomer Gérard Henri de Vaucouleurs published an extended Hubble classification scheme in the book 'Handbuch der Physik' by adding a number of additional features ([de Vaucouleurs, 1959](#)). He subdivided spiral galaxies into three categories: spirals (Type SA), intermediate spirals (Type SAB), and barred spirals (Type SB). He furthermore subdivided S0 galaxies, indicating a progression from more elliptical-like to more spiral-like structures. He also introduced a notation to indicate the presence of a ring structure (r) around a galaxy, or the presence of a spiral structure (s).

Together, elliptical and lenticular galaxies are often referred to as *early-type galaxies*, while spiral and irregular galaxies make up the class of *late-type galaxies* ([Maoz, 2016](#)). Early-type galaxies are characterized by low amounts of gas and dust. Their stellar component consists of old red stars that move on random orbits with a wide range of inclinations and eccentricities, rather than in a well-defined rotational pattern. They show a smooth ellipsoidal morphology, with little or no ongoing star formation. In contrast, late-type galaxies have more complex morphologies, often with disk and spiral arm features. They have large amounts of gas and dust, particularly in the spiral arms, with ongoing star formation. Therefore, their stellar component contains young, hot, and blue stars in the spiral arms and older stars in the bulge. The stars in the disk follow nearly circular orbits in a well-defined plane around the Galactic center.

This work examines a special late-type barred spiral galaxy, our home galaxy, the Milky Way. In fact, the focus lies on the Galactic disk component, where this thesis studies the distribution of orbits and ages of young stars. Before the Milky Way as a *benchmark galaxy* will be introduced in more detail, the following Section 1.1.2 briefly discusses the basic concepts and ideas of how galaxies form in the Λ CDM cosmological context.

1.1.2 GALAXY FORMATION IN THE Λ CDM COSMOLOGICAL CONTEXT

The Universe started in a dense, hot, and expanding state, with small random density fluctuations in place ([Lemaître, 1927](#)). The explosive event where all matter in the universe formed, known as the *Big Bang*, occurred approximately 13.8 billion years ago and is evidenced by two major discoveries. The first

evidence is the expansion of the universe, which was discovered by the astronomer Edwin Hubble in the 1920s (E. Hubble, 1929; and has been proposed by Lemaître, 1927). Hubble found that the redshift of galaxies increases systematically with their distance, indicating that the more distant a galaxy is, the faster it moves away from us. This relation is known as the ‘Hubble law’ or ‘Hubble-Lemaître law’:

$$v_r = H_0 \cdot d,$$

where the radial velocity v_r in $[km\ s^{-1}]$ is the velocity along the line of sight, and is proportional to the distance d in $[Mpc]$, with the constant of proportionality H_0 , which is known as the ‘Hubble parameter’. The current value of the Hubble parameter is $H_0 \simeq 70\ km\ s^{-1}\ Mpc^{-1}$, which represents the current rate of expansion of the Universe. Observations reveal that the expansion of the universe is accelerating, therefore the Hubble parameter is time-dependent: $H(t)$. This discovery was awarded the Nobel Prize for Physics in 2011 (Perlmutter et al., 1999; Riess et al., 1998).

The second piece of observational evidence for the Big Bang is the discovery of the cosmic microwave background (CMB) by Penzias and Wilson, 1965, who detected a constant radio signal across the whole sky in the 1960s. This radio background is leftover thermal radiation from the Big Bang, e.g. the cool remnant of the first light in the universe, which was emitted after the Big Bang at a redshift of ~ 1100 . The CMB radiation is very uniform and cold, with an estimated temperature of $T = 2.728\ K$ as measured by the COBE satellite (Mather et al., 1990; Smoot et al., 1992). However, it does exhibit small temperature fluctuations (faint anisotropies). These are only at the level of $\Delta T = 10^{-5}\ K$ in all directions, but these tiny fluctuations caused by small density perturbations give rise to the pattern of galaxies and larger cosmic structures we see today.

Since the late 1990s, the ‘Lambda Cold Dark Matter’ model (Λ CDM) has been established as the standard model for explaining the evolution of the universe from the Big Bang to the present day. The key components of the Λ CDM model are the cosmological constant (Λ) which is associated with dark energy and accounts for about 68% of the total energy density of the universe, non-baryonic cold dark matter (CDM) which comprises approximately 27%, and baryonic matter which makes up the remaining 5% (Planck Collaboration et al., 2020). The Λ CDM model is based on the ‘cosmological principle’, which states that the universe is homogeneous and isotropic on large scales (these large-scale structures are known under the term ‘cosmic web’, e.g. the filamentary pattern of galaxies and matter on scales much larger than individual galaxies or galaxy groups), meaning that it looks the same at every location in every direction. The smooth average evolution of the universe is mathematically described by the Robertson-Walker metric (H. P. Robertson, 1935; Walker, 1937) and the Friedmann equations (Friedmann, 1922; 1924; Lemaître, 1927).

In the context of the Λ CDM paradigm, the work of White and Rees, 1978 presents the groundwork for understanding galaxy formation in the presence of dark matter as a hierarchical process, where small structures form first, and larger structures form later through merging of smaller ones. In the early universe small density fluctuations in the dark-matter distribution collapse under their own gravity and form

1 Introduction

dark-matter halos. These halos grow hierarchically as they merge and accrete over time. The baryonic gas falls into the gravitational potential wells created by the dark-matter halos, where it compresses and heats up adiabatically. The heated gas radiates away over time, leading the gas cloud to condense and cool, which is called radiative cooling. When the gas cools, it collapses to high densities, fragments, and forms stars (see Section 1.5.2 on star formation).

Over the last decade, this galaxy formation scenario has been ever-better fleshed out by simulations that incorporate the complex interplay of e.g. dark matter collapse, merging, gas cooling, and baryonic feedback, leading to realistic galaxy properties starting from initial fluctuations. Among the most established cosmological simulations are, e.g., IllustrisTNG (Pillepich et al., 2018), SIMBA (Davé et al., 2019), EAGLE (Schaye et al., 2015), and ASTRID (Bird et al., 2022). Figure 1.1 shows a cosmological simulation, modeling a cubic volume of about 500 million lightyears (B. E. Robertson et al., 2019). It illustrates how dark-matter structures - the seeds of galaxy formation - connect to galaxies. In the left panel, dark matter structures are colored scaling with the dark matter velocity dispersion, e.g. lighter colors represent regions with large random motions, reflecting deep gravitational potential wells (dark matter halos). In these regions with densities so high that they undergo gravitational collapse, galaxies form, and their locations are illustrated in the right panel of Figure 1.1. The color of galaxies reflects the mass surface density of their host dark-matter halo, which correlates with stellar mass through the stellar mass–halo mass relation (B. E. Robertson et al., 2019).

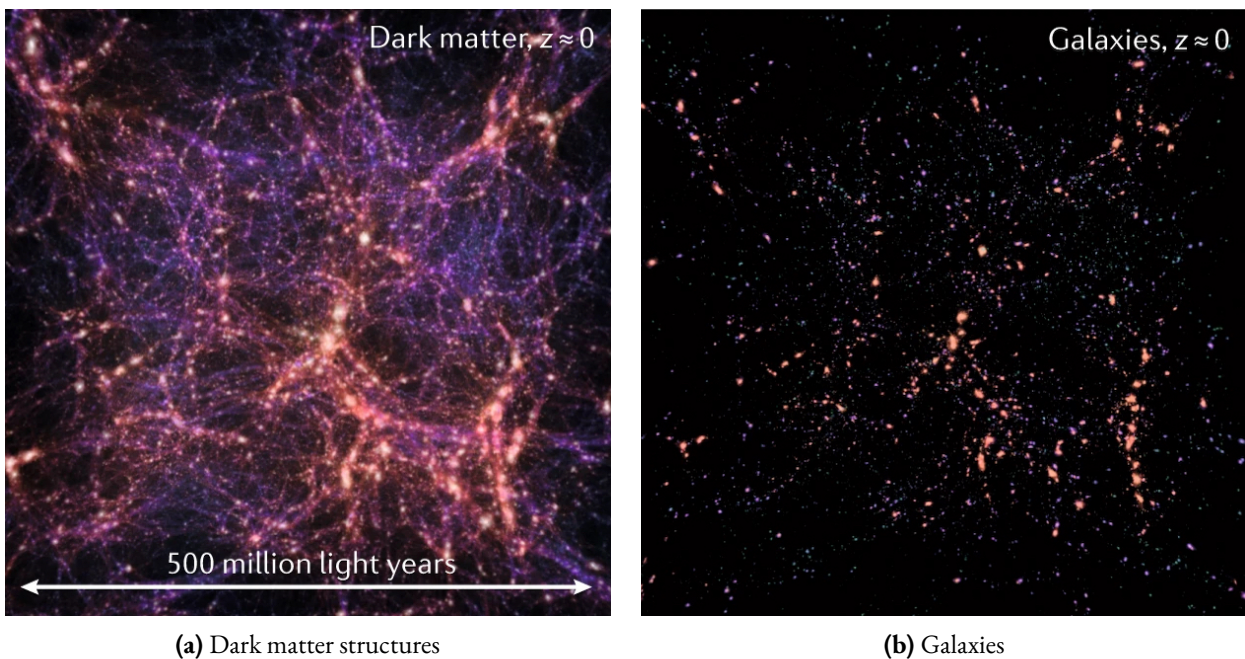


Figure 1.1. A cosmological simulation showing the connection between dark matter structures in panel (a) and galaxies in panel (b) at the present day ($z=0$). The colors in panel (a) scale with the dark matter velocity dispersion, and the colors in panel (b) reflect the mass surface density of the host dark matter halo, which correlates with the stellar mass of the galaxies. **Figure credit:** B. E. Robertson et al., 2019

Fall and Efstathiou, 1980 proposed a theoretical model to explain the formation of rotationally supported gas disks in galaxies through gas cooling under angular momentum conservation: as the gas cools it loses pressure support and begins to flow in towards the center of the potential well of the dark matter halo (‘cooling flow’). The cooling gas settles into a rotationally supported disk because it conserves angular momentum. Stellar disks are thought to assemble in an ‘inside-out’-mechanism as a natural consequence of the way the gas accretes and cools in the rotationally supported disk, with the low angular momentum gas cooling, settling and forming stars on shorter timescales than the high angular momentum gas (Larson, 1976). These processes are the reason why disk galaxies are expected and observed to be the dominant form of galaxies in the universe. One of these disk galaxies, the Milky Way, forms the focus of this thesis. In particular, empirical studies of the configurations and orbits of young stars will be pursued in the following scientific chapters of this thesis. Empirical studies of these processes on a star-by-star basis are crucial, as despite some high resolution simulations, such as e.g. STARFORGE (Grudić et al., 2021), LYRA (Gutcke et al., 2021), VINTERGATAN (Agertz et al., 2021), GRIFFIN (Lahén et al., 2020), SILCC (Walch et al., 2015), the actual star-formation processes in galaxies remain often poorly resolved, or treated in a very approximate way. Before the target topic - the orbits of stars in the Galactic disk - will be introduced, the following Section 1.2 provides the basic properties and components of disk galaxies, with an emphasis on the Milky Way.

1.2 THE MILKY WAY AS A MODEL DISK GALAXY

1.2.1 BASIC PROPERTIES OF DISK GALAXIES

Disk galaxies have complex morphologies and are typically characterized by having a thin, rotationally supported disk with spiral arms and often a bar, a central bulge component, and a spheroidal stellar halo (Mo et al., 2010). The spiral structure of disk galaxies is best seen in a face-on view, as illustrated in Figure 1.2a for the galaxy NGC 3982. Its spiral structure is dominated by young blue stars, HII regions (regions of ionized atomic hydrogen, leading to intense star formation), molecular gas, and dust absorption (Mo et al., 2010). Looking at a galaxy edge-on, as shown in Figure 1.2b for the galaxy NGC 4565 (Needle galaxy), reveals the typical flattened vertical structure of disk galaxies, combined with a bright bulge in the inner part, which is covered by lanes of gas and dust.

The surface brightness profiles of disk galaxies can be described with an exponential profile for the stellar disk:

$$I(R) = I_0 \cdot \exp(-R/R_d),$$



(a) Face-on spiral galaxy NGC 3982

(b) Edge-on spiral galaxy NGC 4565

Figure 1.2. Two spiral galaxies as seen from different angles. Panel (a) shows a face-on view on NGC 3982 with concise spiral arm structures, dominated by blue young stars. Panel (b) shows NGC 4565, also called the Needle Galaxy. The edge-on view reveals the galaxy’s small vertical extent and displays a bright yellowish bulge in its center. On top, dust lanes cover the stellar disk. **Figure credit:** ESA/Hubble & NASA, ESO

where I_0 is the central luminosity surface density, R is the Galactocentric radius, and R_d represents the scalelength of the disk, and a Sérsic profile for the bulge (Mo et al., 2010). The vertical extent of disk galaxies is not infinitesimally thin, with a disk luminosity density in the vertical (z -)direction of

$$L(z) = L_0 \cdot \text{sech}^2(z/z_d),$$

where L_0 is the surface luminosity in the Galactic plane, z describes the vertical height from the midplane, and z_d is the scaleheight of the disk. This corresponds to a self-gravitating isothermal sheet (Spitzer, 1942). The surface brightness distribution in the vertical direction is largely independent of the distance from the disk center (Mo et al., 2010).

Unlike elliptical galaxies that predominantly contain gas in a hot and highly ionized state, the gas component in spiral galaxies is mainly neutral hydrogen (HI) and molecular hydrogen (H_2) (Mo et al., 2010).

The stars and cold gas in the galaxy disks move in the disk plane on roughly circular orbits (Mo et al., 2010). Therefore, the kinematics of a galaxy disk can be described by its rotation curve $v_{circ}(R)$, which expresses the circular rotational velocity of stars as a function of the distance to the Galactic center:

$$v_{circ}(R) = \sqrt{\frac{GM(R)}{R}} \sim \text{const.}$$

Here, v_{circ} is the circular velocity of stars or gas in the galaxy at radius R from the Galactic center. $M(R)$ is the mass enclosed within the radius, and G is the gravitational constant. Disk galaxies have flat rotation

curves, which stay constant over a large radial range. Initially, this was an unexpected result, as the rotation velocity should decrease as a function of distance to the Galactic center because the stellar mass does not scale with the radius as it would need to to support constant rotation. The observation of flat rotation curves was later explained by the presence of dark matter, e.g. by the presence of more mass than just the mass observed from the stellar component of the galaxies (Rubin et al., 1980; Rubin & Ford, 1970).

Disk galaxies obey a well-defined empirical scaling relation between luminosity and rotation velocity of galaxies, known as the ‘Tully-Fisher relation’ (Tully & Fisher, 1977). This relation, which can be derived from the virial theorem, relates the rotation speed of the galaxy to its luminosity and is often used to determine distances in the universe.

As we sit inside a disk galaxy ourselves, the Milky Way, we have a unique opportunity to study its structure on a star-by-star resolution. This is why the Milky Way is the subject of study in this thesis. The following Section 1.2.2 introduces the Milky Way by outlining its different structural components.

1.2.2 COMPONENTS OF THE MILKY WAY

The Milky Way is a fairly typical disk galaxy, and follows the Tully-Fisher relation to within 1σ uncertainty, when considering measurement uncertainties and natural scatter of galaxies about the relation (Bland-Hawthorn & Gerhard, 2016). It is one of two dominant member galaxies of the Local Group galaxy cluster, located in a low-density filament in the far outer reaches of the Virgo supercluster of galaxies (Tully et al., 2014). The other dominant member of the Local group is the Andromeda (M31) galaxy. Both galaxies lie in the co-called ‘green valley’ of the galaxy color-magnitude diagram, meaning that their star formation is slowing down because they are both running out of gas (Mutch et al., 2011). The recent evolution of the Milky Way was quiet, as it has not experienced a merger with major effects on its structure and evolution over the past 8 Gyr (Stewart et al., 2008). However, in about 4-6 Gyr the Milky Way and the Andromeda galaxy will reach the pericenter passage and merge, which is known from measurements of Andromeda’s motion by the Hubble space mission (Sohn et al., 2012).

Figure 1.3 illustrates the main components of the Milky Way. As in many other spiral galaxies it consists of a bright bulge/bar in its innermost parts, with an extended flat-disk component split into a thin disk and a thick disk part. It is surrounded by a Galactic halo, comprised of a stellar halo and a dark matter halo. The stellar halo is a low mass spheroid that reaches beyond 40 kpc from the Galactic center. The estimated total stellar halo mass is $1 - 1.4 \cdot 10^9 M_{\odot}$, which is only about 1% of the Milky Way’s total stellar mass. Stars in the halo are either formed in situ or were accreted from satellite galaxies (e.g. globular clusters, stellar halo streams). The dominant mass component of the Milky Way is the dark halo. Although dark matter cannot be observed directly, its presence is inferred from the Milky Way rotation curve, and its mass is estimated to be $1 - 1.7 \cdot 10^{12} M_{\odot}$, about 90% of the Galaxy’s total mass (Deason et al., 2019).

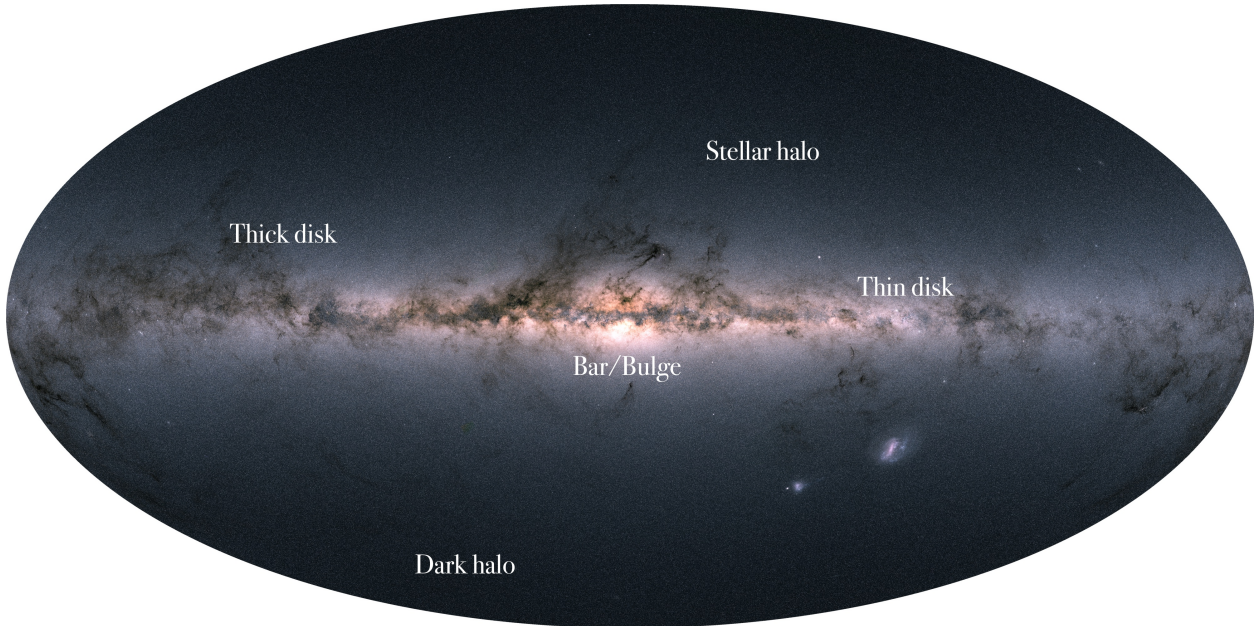


Figure 1.3. An all-sky view of the Milky Way as observed by the Gaia mission. Labelled are the main components of the Galaxy: a bulge/bar, a thin disk, a thick disk, and a stellar halo, and a dark matter halo. Most stars in the Milky Way are located in the bright stellar disk, which - in visible light - is covered by dark lanes of interstellar gas and dust. **Figure credit:** ESA/Gaia/DPAC, with manually added labels of the Milky Way components as inspired by a Figure in [Helmi, 2020](#)

The inner part of the Milky Way is the Galactic bulge, with a rotating triaxial structure known as the Galactic bar. The total stellar mass of the bulge is estimated to be $1.4 - 1.7 \cdot 10^{10} M_{\odot}$ ([Portail et al., 2015](#)). The bulge is a pseudo-bulge, which is formed by the internal slow secular evolution of the disk (rather than galaxy mergers) through the inflow of gas driven by the bar or spiral arms, and has a boxy-peanut shape. The bar is ~ 5 kpc long and rotates as a solid body with a pattern speed of $\sim 41 \text{ km s}^{-1} \text{ kpc}^{-1}$ ([Bovy et al., 2019](#); [Sanders et al., 2019](#); [Wegg et al., 2015](#)). Resonances with the Galactic bar cause stars in the solar vicinity to form large-scale substructures, known as ‘moving groups’¹. In the center of the Galactic bulge is Sagittarius A*, a supermassive black hole, with an estimated mass of $4.3 \cdot 10^6 M_{\odot}$ ([Gillessen et al., 2009](#)). It is surrounded by a nuclear star cluster, embedded in a nuclear stellar disk.

The Galactic disk is the main stellar mass component of the Milky Way, with an estimated stellar mass of $5 \cdot 10^{10} M_{\odot}$ ([Bland-Hawthorn & Gerhard, 2016](#)). The Sun is located close to the disk’s midplane, with a distance of ~ 8 kpc from the Galactic Center, ~ 25 pc above the midplane, and rotating with a circular velocity of $\sim 240 \text{ km s}^{-1}$ ([Bovy et al., 2012](#)). The Galactic disk can be decomposed into two components based on stellar abundances. The *thin low- α disk*² has a radial scale length of ~ 3 kpc, a vertical scale height of ~ 0.3 kpc, and an overall diameter of ~ 30 kpc ([López-Corredoira et al., 2002](#); [McMillan, 2011](#)). Its

¹To avoid confusion: The terminology ‘moving group’ here is used for large-scale arch-like velocity structures in the Galactic disk, caused by resonances of the Galactic bar and spiral arms, and not co-moving birth stellar associations.

²The terms ‘low- α ’ and ‘high- α ’ refer to the abundance of α -elements (e.g. O, Mg, Si, S, and Ca) in the stars within the Galactic disk. These elements - formed in the α -process - are predominantly produced by Type II supernovae of massive, short-lived stars.

stars are poor in α -elements, indicating that its stars formed later when the interstellar medium had more time to be enriched by Type Ia supernovae, which produce more iron relative to α -elements. Its stars move in near-circular orbits around the Galactic center. The current star formation rate in the low- α disk is $\dot{M} = \sim 1.65 M_{\odot} \text{ yr}^{-1}$ (Licquia & Newman, 2015). Thin disk stars have higher metallicities ($[\text{Fe}/\text{H}]$), reflecting that they formed later in the galaxy’s history. The *thick high- α disk* is older and kinematically hotter, meaning that its stars have a higher velocity dispersion and move on more eccentric, random orbits than the stars in the thin disk. The metallicity distribution of thick disk stars peaks at lower metallicities, indicating that they formed when the interstellar medium was less enriched with metals. The radial scale length of the high- α disk is similar to that of the low- α disk, but its vertical scale length is ~ 1 kpc. Stars in the high- α disk rotate slower around the center of the galaxy as compared to stars in the low- α disk, with a rotation velocity at a solar radius of $\sim 175 \text{ km s}^{-1}$ (Mo et al., 2010).

Within the Milky Way disc, the main sites for star formation and young stars are the spiral arms. Although it is challenging to picture the spiral structure of the Milky Way from the Sun’s point of view, it is believed that our Solar System is located in the local Orion arm, between the Sagittarius arm and the Perseus arm. In disk galaxies, most spiral arms are trailing, winding in the same direction as the galactic rotation. Historically, the formation of spiral arms was explained with the ‘density wave theory’ (Lin & Shu, 1964; Shu, 2016), where spiral arms (in contrast to the differential rotation of the stars and interstellar medium) rotate like a rigid solid body at a constant pattern speed, causing spiral arms to be long-lived structures (Castro-Ginard et al., 2021). However, nowadays many observations favor a transient short-lived spiral arm theory as proposed by Toomre, 1964. In this theory, spiral arm structures are composed of individual arms acting as waves at a constant pattern speed and overlapping, causing transient spirals without a global pattern speed (Castro-Ginard et al., 2021; Quillen et al., 2011; Sellwood & Carlberg, 2014).

The study of the structure, formation, and history of the Milky Way is called ‘Galactic Archaeology’, and performed by observing its stellar populations. These populations can be classified into thin and thick disk stars, halo stars, bulge stars, and stellar streams and substructures (Bland-Hawthorn & Gerhard, 2016). The basic idea is that stars retain the memory of their origin, which is imprinted in their chemical compositions, ages, and kinematics. Measuring these stellar properties for large populations of stars can provide a diverse array of insights, such as the Galaxy’s star formation history, the origin of abundances, and the Milky Way’s secular evolution that shaped the orbit distribution we observe today. In this regard, Section 1.3 describes how we can estimate orbits of stars in the Galactic disk, and will briefly outline the secular orbit evolution of stars in the Milky Way disk.

1.3 STELLAR ORBITS IN DISKS

1.3.1 HOW TO DESCRIBE ORBITS

The kinematics of a star can be described by 6D phase space coordinates, e.g. 3D positions and 3D velocities (x, v) . Given a gravitational potential Φ , we can find conserved quantities along an orbit, which are integrals of motions or *actions* (J), and time-independent. This reduces the description of orbits to 3 dimensions, e.g. the radial action J_R , the azimuthal action J_ϕ and the vertical action J_Z , with the assumption that the other three coordinates are just orbital phases or *angles* (Θ), e.g. the radial angle Θ_R , the azimuthal angle Θ_ϕ and the vertical angle Θ_Z . This is true under the assumption that the gravitational potential is axisymmetric and time-independent. The Milky Way comprises nonaxisymmetric features such as spiral arms and a rotating bar, and its gravitational field is not time-independent. However, the secular evolution of the Galaxy happens on long timescales and can therefore be assumed to be in steady state, where the mass distribution does not change over time. Also, we can consider the mass distribution in the disk to be symmetric with respect to rotations around a central axis, and neglect perturbations caused by the bar, as most stars are located outside it. Then, the transformation of $(x, v) + \Phi \rightarrow (J, \Theta)$ proves useful and convenient.

The Hamiltonian formalism provides a framework to derive action angle coordinates³. A system with n degrees of freedom can be described by the Hamiltonian $H(q_i, p_i)$, where q_i are the generalized coordinates (related to the positions) and p_i are their canonical momenta (related to the velocities). The Hamiltonian equations of motion are the following:

$$\dot{p}_i = -\frac{\partial H}{\partial q_i} \quad \dot{q}_i = \frac{\partial H}{\partial p_i} \quad i = 1, \dots, n.$$

In this framework, actions J_i are specified as:

$$J_i = \frac{1}{2\pi} \oint_{orbit} p_i dq_i,$$

where the ring integral represents the closed path around an orbital tours, and (p_i, q_i) are canonically conjugate phase-space coordinates. The actions are integrals of motions and conserved along the orbit. Therefore, the Hamiltonian equations of motion in these coordinates become:

$$\dot{J} = -\frac{\partial H}{\partial \Theta} = 0 \quad \dot{\Theta} = \frac{\partial H}{\partial J} = \Omega(J) = const,$$

³A comprehensive introduction to action angle coordinates is provided in [J. Binney and Tremaine, 2008](#).

where $\Omega(J)$ is the fundamental frequency associated with each action variable. The actions J are constant and so are the fundamental frequencies Ω . Angles Θ are the canonical conjugates of actions and increase linearly with time t , with the fundamental frequency Ω .

$$\Theta_i(t) = \Theta_i(0) + \Omega_i \cdot t.$$

Angles determine the position or orbital phase on the orbit through the radial angle Θ_R , the azimuthal angle Θ_ϕ and the vertical angle Θ_Z ; within the interval $[0, 2\pi]$. The orbit coordinates are comprised of the radial action J_R which quantifies the orbit's radial oscillation, the azimuthal action J_ϕ which is the angular momentum (L_Z) and the vertical action J_Z which is the up-and-down motion. An overview of the three action coordinates is provided in Table 1.1. A radial action of $J_R = 0$ indicates that a star is on a circular orbit, and a vertical action of $J_Z = 0$ means that a star is located in the Galactic midplane. If we divide the azimuthal action J_ϕ by $(8 \text{ kpc} \times 220 \text{ km s}^{-1})$, the Sun is at $J_\phi = 1$.

Table 1.1: Overview of action coordinates.

Action	Abbr.	Interval	Description
radial action	J_R	$[0, \infty]$	measure of orbit eccentricity
azimuthal action = angular momentum	$J_\phi = L_Z$	$[-\infty, \infty]$	amount of rotation around the Galactic center
vertical action	J_Z	$[0, \infty]$	extent of vertical excursion around the mid-plane

For general potentials, actions can only be estimated and not analytically solved, and this is typically very computationally expensive. Efficient methods for conversion between (x, v) and (J, Θ) have been developed, and the state-of-the-art is the Stäckel fudge algorithm (J. Binney, 2012), which approximates the potential of the Milky Way with a Stäckel potential. In practice, this is an efficient way to calculate approximate actions and is incorporated in the Bovy, 2015 package.

1.3.2 ORBIT EVOLUTION IN THE GALACTIC DISK

The Milky Way's recent orbit history can be described as relatively 'quiet'. The reason for this is that the last major merger of the Milky Way, e.g. a collision with a galaxy of comparable size, occurred ~ 8 Gyr ago, with a galaxy referred to as Gaia-Sausage-Enceladus (Helmi et al., 2018). This merger had a massive impact on the kinematics of the stars in the Galaxy and probably influenced the conditions under which the division of the stars in the Galactic disk into the thin and thick disk components occurred. If we study the orbit evolution of stars as we observe today, we can therefore focus on the internally driven evolution

of the Milky Way, which is governed by processes with a timescale much longer than τ_{dyn} ⁴, and is called the Milky Way’s ‘secular evolution’.

We know that the birth orbit of the Sun is not the same orbit we observe today. Almost 20 years ago, [Wielen et al., 1996](#) postulated that since the Sun is observed to be more metal-rich than the stars in the solar vicinity, it may have formed in a region in the Galactic disk that is closer to the Galactic center. This idea is supported by recent work by [Frankel et al., 2018](#), who show that stars migrate by about a half-mass radius of 5.9 kpc, which is the radius where the mass profile is half of its maximum value, over the age of the Galactic disk. [Frankel et al., 2019](#) find that the birth orbit of the Sun is located at ~ 5.2 kpc from the Galactic center, and claim that the evolution of the Sun’s birth orbit to its present-day orbit was caused by an internal process of the Milky Way’s secular evolution, known as ‘radial migration’.

Radial migration is a process in which stars change the angular momentum (L_Z) of their orbit (which is the mean radius) and move inward or outward the Galactic disk, without increasing the orbital random energy ([Rix & Bovy, 2013](#)). In [Sellwood and Binney, 2002](#) this process is called ‘churning’. It is triggered by the resonances of the bar and the spiral arm features and significantly impacts the orbit distribution and redistribution of stars in the Galactic disk. Stars can move inward or outward within the Galactic disk without significant changes in their orbital eccentricities. This leads to a mixing of stellar populations of different ages and different metallicities across the Galactic disk.

Another internal secular orbit evolution mechanism that shapes the orbit distribution of stars in the Galaxy is called ‘blurring’, which refers to changes in the orbital eccentricity or inclination of a star while keeping the guiding radius constant ([Sellwood & Binney, 2002](#)). ‘Blurring’ leads to higher eccentricity orbits, which is also known as ‘disk heating’ ([Frankel et al., 2018](#)). Together, radial migration and disk heating lead stars to orbits and radii that are different from those on which they were born and shape the present-day orbit structure of stars in the Milky Way disk. In the following Section 1.4 we present the data set that we use in this thesis to study the orbit distribution of the stars in the Milky Way disk.

1.4 THE GAIA GALACTIC SURVEY

The ideal data set for galactic archaeologists is provided by the Gaia Galactic Survey. This mission charts a three-dimensional map of the Milky Way by collecting astrometric, photometric, and spectroscopic measurements of roughly 1% of all stars in our home galaxy. Its data cover the whole sky, are open to the entire community (accessible via the *Gaia Archive*: <https://gea.esac.esa.int/archive/>), and are unprecedented in both quantity and precision.

Gaia was launched by the European Space Agency in 2013. Its launch vehicle was a Soyuz-Fregat rocket, which brought the satellite into a Lissajous-type orbit around the second Lagrange point. It is the follow-

⁴The dynamical timescale τ_{dyn} is one orbital period at Solar radius, for which we adopt the value $\log \tau = 8.33$.

up mission of the first astrometric space mission Hipparcos, which operated between 1989 and 1993 and produced a catalog of about 2.5 million stars, 118 000 of them with high precision. The Gaia mission immensely improved this database, by providing measurements for more than 1 billion stars, about 200 times more accurately than its predecessor mission.

In order to map stars in the Galaxy, Gaia measures stars in two fields of view, separated by a constant angle of 106.5° . In order to observe a cycle (one full 360° rotation), the spacecraft spins at a rate of 1° per minute around the satellite spin axis, which is perpendicular to the fields of view. Therefore, stars pass the second field of view 106.5 minutes after they are observed in the first. One full circle takes six hours to scan, making four complete rotations per day. Furthermore, the satellite spin axis rotates at a 45° angle and with a period of 63 days around the Sun. The 45° angle ensures that the payload is shaded from the Sun while the solar panels can generate sufficient power. The 63-day period allows for different parts of the sky to be scanned.

The data collected by the Gaia mission so far have been made public between 2016 and 2022, divided into four data releases: DR1, DR2, early DR3, and DR3. Its main data products comprise precise positions on the sky in right ascension and declination (α, δ), proper motions (μ_α, μ_δ), parallaxes (ϖ), and photometry in three passbands (G, G_{BP}, G_{RP}), covering a total wavelength range of $\lambda \sim 330 \text{ nm} - 1050 \text{ nm}$. In addition, Gaia measures the radial velocities/line-of-sight velocities (v_{los}) and low-resolution spectra of brighter subsamples of sources. The next data release (DR4) is not expected before the end of 2025. An overview of current available data is listed here.

- Full astrometric solution ($\alpha, \delta, \mu_\alpha, \mu_\delta, \varpi$) for ~ 1.46 billion sources, with a limiting magnitude of $G \approx 21$ and a bright limit of $G \approx 3$.
- Two-parameter solutions (α, δ) for additional ≈ 344 million sources.
- G magnitudes for around ≈ 1.8 billion sources.
- G_{BP} and G_{RP} magnitudes for ≈ 1.54 billion and ≈ 1.55 billion sources, respectively.
- Mean radial velocities (v_{los}) for ≈ 33 million sources.
- Mean BP/RP spectra for ≈ 219 million, most of them with $G < 17.6$ mag.
- Mean RVS spectra for ≈ 1 million sources.

This set of measurements provided by the Gaia satellite enables us to calculate additional stellar parameters. Firstly, measuring the parallax (ϖ) of a star has become an established tool to estimate its distance (d). The parallax is defined as the angle between two lines of sight that observe the same object from two different locations. As the Earth rotates around the Sun, the parallax can be described as an apparent shift of the stars, where the movements of the closer stars seem to be larger. The connection between parallax and distance of a star is given by:

$$d[\text{pc}] \approx \frac{1000}{\varpi[\text{mas}]}.$$

1 Introduction

However, this relation is only valid in the absence of measurement uncertainties. Despite the precision of Gaia parallaxes, for distant and fainter sources their fractional parallax uncertainties are large, and the conversion between distance and parallax becomes non-linear. This issue was tackled by, e.g. [Bailer-Jones et al., 2018](#) and [Bailer-Jones et al., 2021](#), who infer distances from Gaia parallaxes with a probabilistic method. Although a method like this should in principle be applied to obtain reliable distance estimates, for studies of nearby stars (< 1 kpc) the simple conversion between parallax distance represents a fairly good estimate.

The Gaia photometric system includes measurements in three passbands, which cover the following wavelength (λ) ranges:

- Broad G passband: $\lambda \sim 330$ nm - 1050 nm
- Blue G_{BP} passband: $\lambda \sim 330$ nm - 680 nm
- Red G_{RP} passband: $\lambda \sim 630$ nm - 1050 nm

From an observed magnitude (m_G), combined with a distance estimate d , we can determine the absolute magnitude (M_G) of a star via the distance modulus as follows:

$$M_G[\text{mag}] = m_G[\text{mag}] + 5 - 5 \cdot \log_{10}(d[\text{pc}]).$$

The absolute magnitude of a star, combined with its color/spectral type, can be used to produce a ‘color magnitude diagram’ (CMD), a very powerful diagnostic tool in astronomy and widely used for studying stellar evolution. The analysis of color-magnitude diagrams will be described in more depth in [Section 1.6](#).

Gaia’s full 5D astrometric solution ($\alpha, \delta, \mu_\alpha, \mu_\delta, \varpi$) can be extended to a 6D astrometric solution when combined with the radial velocity v_{los} . This data set is limited by the radial velocity measurement, which is available for stars only in the temperature interval $T_{eff} \in [3100, 14500]$ K for bright sources ($G \leq 12$ mag) and $[3100, 6750]$ K for fainter sources. The median formal precision of the measurement of radial velocity is 1.3 km s^{-1} at $G_{RVS} = 12$ mag and 6.4 km s^{-1} at $G_{RVS} = 14$ mag ([Katz et al., 2023](#)).

As described in [Section 1.3](#), this 6D astrometric dataset - combined with an assumed gravitational potential - can be used to compute stellar actions (J) and angles (Θ). However, this calculation is strongly affected by the measurement uncertainties of radial velocities. This is illustrated in [Figure 1.4](#) in the action plane J_ϕ - J_R on the left and for the Θ_Z - Θ_R angle plane on the right. The gray background represents all stars with radial velocity measurements within 500 pc of the Sun. The red data points represent 50 randomly sampled stars from this dataset. For each of these stars, 50 additional data points are sampled from its radial velocity error distribution, which is assumed to be Gaussian. Their location in the action and angle planes is illustrated in orange in [Figure 1.4](#).

The effects of the radial velocity uncertainty on the action-angle computation is striking and non-negligible, as they transform the action and angle coordinates of each star into elongated, banana-shaped structures with complex orientations. In comparison, the same test applied to the $(\alpha, \delta, \mu_\alpha, \mu_\delta, \varpi)$ coordinates does

not reveal a significant impact on the action-angle computation. Despite these challenges, in this thesis, we work with the coordinates of the action angle and describe our motivation therefore in Section 1.5.3.

In addition, Gaia BP/RP spectra (also referred to as XP spectra) can be used to obtain information about the chemical composition of stars, which is reflected in their metallicities $[M/H]$. Metallicity estimates for 175 million stars were derived by Andrae et al., 2023. These estimates suffer some strong biases; however, for solar-type stars with $0.5 \text{ mag} \leq \text{BP-RP} \leq 1.5 \text{ mag}$ they are very robust.

In summary, Gaia measurements enable us to derive a vast number of additional stellar parameters across a large portion of the Galaxy. Understanding the uncertainties of the measurements as well as their limitations is crucial; nevertheless, Gaia provides a unique, unprecedented dataset to study the stellar component of the Milky Way. In particular, its precise position and velocity measurements combined with magnitude measurements in three passbands have revolutionized the community's knowledge of stellar clusters in our home galaxy in various ways: e.g. detecting previously unknown clusters; increasing the number of cluster member stars; studying internal cluster structure and kinematics; detecting cluster evaporation processes; or studying their impact on Galactic disk properties. The next Section 1.3 provides an introduction to stellar clusters and reviews the up-to-date census of stellar clusters in the Galactic disk.

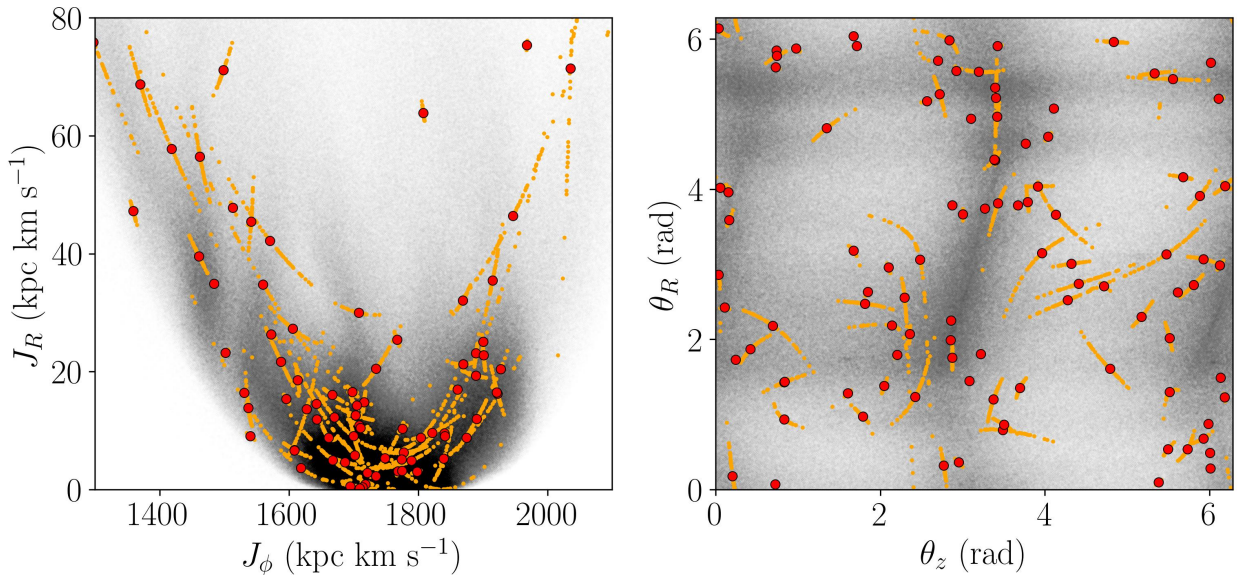


Figure 1.4. Radial velocity measurement uncertainties shape action-angle coordinates into elongated, banana-like structures, represented for the J_ϕ - J_R plane (left) and the Θ_Z - Θ_R plane (right). *Gray*: all Gaia stars with radial velocity measurements within 500 pc of the Sun. *Red*: 50 randomly sampled stars from this dataset. *Orange*: 50 datapoints sampled from the (Gaussian) radial velocity error distribution of each red star.

1.5 CLUSTERS IN THE GALACTIC DISK

1.5.1 YOUNG STELLAR CLUSTERS

A star cluster is an ensemble of stars that are held together by gravitational forces. Stars of a star cluster are born in the same molecular cloud and hence share the same composition and age. They are located at approximately the same distance to the Sun and orbit the Galactic center on the same orbit and at the same orbital phase. There are different types of star cluster in a galaxy, and their definitions differ within the astronomy community. However, star clusters are typically divided into three main categories: globular clusters, open clusters, and stellar associations.

Globular clusters are the most massive star clusters, with masses typically $\geq 10^5 M_{\odot}$, and contain about 10^4 - 10^5 member stars. Their stars are tightly bound by gravity and are spherically distributed, with an extent typically around 20 pc. They reside in the Galactic halo or in the Galactic bulge. Their stars are metal-poor and among the oldest objects associated with the Galaxy, with ages ≥ 10 Gyr.

Open clusters are younger and less massive, with ages typically ≤ 1 Gyr and masses $\leq 10^4 M_{\odot}$. They are made up of about 10 - 10^3 member stars, which are loosely gravitationally bound. They are concentrated close to the Galactic disk, and their morphology can be spherical or irregular, with a typical extent of 3-10 pc. Their stars are more metal-rich compared to globular clusters. Open clusters are only found in spiral and irregular galaxies where star formation is still ongoing, whereas globular clusters are also present in elliptical galaxies.

Stellar associations are loose groups of stars that were born together and are still moving together in space, but are not gravitationally bound. Due to this, they disperse quickly and are not easy to detect, because they hardly stand out against background stars. They have masses and member stars similar to open clusters. They are located in the Galactic disk, close to their birth sites. Their stars are typically very young with ages ≤ 50 Myr. They are often referred to as OB associations due to their large number of young and massive O and B stars, or as moving groups⁵.

In recent years, a variety of complex spatial arrangements of comoving stars were discovered and published in the literature, blurring this traditional distinction made between open clusters and stellar associations (Cantat-Gaudin, 2022a), and new vocabulary was introduced to distinguish between different stellar aggregates, e.g. stellar streams or stellar strings (Kounkel & Covey, 2019; Meingast et al., 2019). Additionally, the dissolution processes of open clusters have been studied extensively in the past few years, tracing member stars out to several tidal radii, extending the typical sizes, masses, and number of member stars of open clusters. These features are named, for example, tidal tails, or stellar coronae (Fürnkranz et al., 2019; Mein-

⁵To avoid confusion: The terminology ‘moving group’ is commonly in use for both large-scale arch-like velocity structures in the Galactic disk, caused by resonances of the Galactic bar and spiral arms, and the comoving stellar associations in the solar neighborhood.

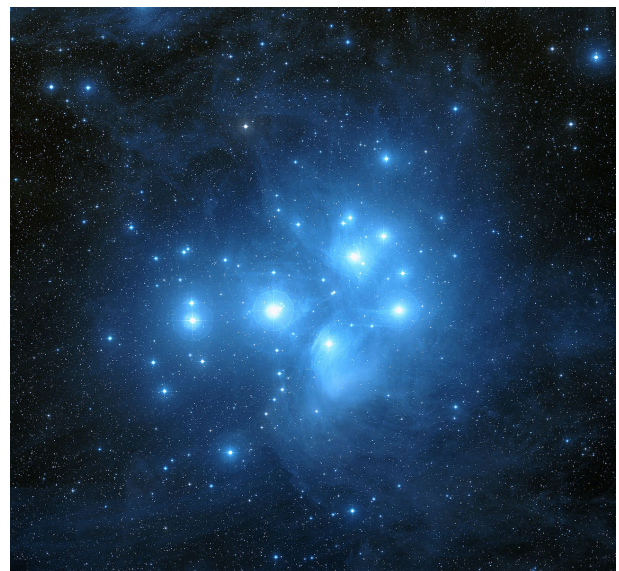
gast & Alves, 2019; Meingast et al., 2021; Röser & Schilbach, 2019; Röser et al., 2019; Tang et al., 2019), and will be reviewed in more detail in Section 1.5.4.

Today, thousands of star clusters are known in the Milky Way, but the minority of all stars in our home galaxy are clustered. We know that stars are born clustered in special places in the Galaxy. What makes these birth orbits special is not clear, as well as how quickly star clusters disperse and leave their birth orbits, over time building up the Galactic field population. The following Section 1.5.2 will serve an introduction to the formation and dissolution processes of star clusters in the Milky Way disk.

1.5.2 FORMATION AND DISPERSAL



(a) Stellar birth site: Pillars of Creation



(b) Open cluster: Pleiades

Figure 1.5. *Left:* An image by the James Webb Space Telescope of Pillars of Creation, a star forming region within the vast Eagle Nebula. The gas and dust clouds visible in the image are ideal birth sites for young star clusters. *Right:* The Pleiades or M45 open cluster. It is a young (~ 100 Myr) open star cluster, located at a distance of about 130 pc from the Sun. **Figure credit:** NASA, ESA, CSA, STScI; J. DePasquale, A. Koekemoer, A. Pagan (STScI) / Davide De Martin & the ESA/ESO/NASA Photoshop FITS Liberator

Lada and Lada, 2003 postulate that most stars are born in clusters⁶. Cold (10 K) and dense H_2 molecular clouds are ideal birth sites for stars. These clouds are in equilibrium, as the gas pressure stabilizes them against gravitational forces. Small perturbations (e.g. cloud-cloud collisions, nearby supernova explosions, galaxy interactions, shockwaves from spiral arms) can trigger a gravitational contraction of the

⁶Recent work shows that stars form in ‘hierarchical clusters’, meaning they can already in-situ be formed as extended low-density structures (Ward et al., 2020; Wright & Mamajek, 2018).

1 Introduction

cloud. The Jeans mass M_J is the critical mass, above which the cloud becomes gravitationally unstable (Jeans, 1902):

$$M_J = \pi^{\frac{3}{2}} \frac{1}{\sqrt{\rho}} \left(\frac{RT}{\mu G} \right)^{\frac{2}{3}}.$$

The Jeans-mass M_J is primarily dependent on the density ($\propto \rho^{-1/2}$), the temperature ($\propto T^{2/3}$), and the radius ($\propto R^{2/3}$). The molecular gas mass is denoted as μ and G is the gravitational constant.

Cooling processes in the cloud initially keep the temperature constant, whereas the density increases (isothermal collapse). This leads to fragmentation of the cloud, as the mass limit of the Jeans criterion decreases, and subsequently small initial density inhomogeneities become unstable as well and collapse independently. The cores of these fragments increase in density and temperature until nuclear fusion begins, which stabilizes the system against gravitational forces. The typical timescale for star formation is short, around ~ 1 Myr.

In the first 2-5 Myr, new born star clusters remain embedded in their natal molecular cloud. About 90% of these young clusters disperse at this early stage. This process is called ‘infant mortality’, which is mainly driven by gas expulsion: stellar feedback (e.g. massive stellar winds, radiation pressure, supernovae) drives out the gas which was not used for star formation, and disrupts the young star clusters (Lada & Lada, 2003). For the surviving clusters, it takes approximately 10 Myr to be free of their natal gas.

Figure 1.5a shows a James Webb Space Telescope NIRCам image of the ‘Pillars of Creation’, a star-forming region within the Eagle Nebula, located at about 2 kpc from the Sun. The dense cloud formations, made of cool gas and dust, provide ideal conditions for star formation. They appear semitransparent in near-infrared light, revealing a lot of newly born stars that are estimated to be only a few hundred thousand years old. Figure 1.5b shows the famous Pleiades or M45 open cluster, with a distance of about 130 pc among the closest open clusters to the Sun. It is dominated by hot blue stars that formed about 100 Myr ago. On a dark night, it is one of only a few star clusters that can be seen from Earth with the naked eye.

Even though there are star clusters that survive their violent formation phase, there is a lack of old open clusters in the Galactic disk. Open clusters suffer continuous mass loss due to further disruption processes, which influence and shorten their lifetimes. This mass loss results in their dissolution and evaporation of stars into the field, building up the galactic field population. This dynamical evolution of a star cluster can be divided into two evolutionary stages: the expansion-dominated phase and the evaporation-dominated phase (Martínez-Barbosa et al., 2016).

The expansion dominated phase lasts for about 40% of a cluster’s lifetime and is primarily driven by internal effects: stellar evolution, evolution-induced mass loss, and two-body relaxation (Lamers et al., 2010). Evolution-induced mass loss is caused by the expansion of the cluster radius and the decrease of the tidal radius during ongoing stellar evolution and results in an escape of stars with velocities above the

escape velocity. Two-body relaxation can be caused by one or more encounters of a star with another star, producing a velocity change that can result in a velocity above the escape velocity (J. Binney & Tremaine, 2008). In addition to these effects, equipartition - the tendency of kinetic energy to equalize during an encounter - can result in mass segregation: then, the orbits of less massive stars possibly expand until a star escapes the cluster.

The evaporation-dominated phase is shaped by external effects, with the tidal forces of the Galaxy such as tidal stripping or interactions with spiral arms or giant molecular clouds becoming important. Tidal stripping stretches clusters into ellipsoids oriented toward the Galactic center, producing cluster tails that pour out from their endpoints, known as tidal tail features (Kharchenko et al., 2009). Furthermore, interactions with the galaxy's high-density regions disrupt open clusters, such as tidal shocks through the Galactic disk (disk shocks) or the Galactic bulge (bulge shocks), as well as passages through spiral arms and encounters with giant molecular clouds.

The Gaia mission (described in Section 1.4) provides an ideal data set to detect and study young stellar clusters in the solar neighborhood. They can be used as excellent tracers of the structure of the Milky Way, as their distribution $P(\textit{orbit}, \textit{age})$ encodes much about the formation history of our home galaxy. In this regard, Section 1.5.3 provides an overview of how stellar clusters can be detected in the Gaia dataset. Section 1.5.4 summarizes the recently published literature on stellar clusters, with a focus on studies of their dissolution processes. Finally, Section 1.6 will show how Gaia photometry and distances can be used to obtain ages for young stellar clusters.

1.5.3 HOW TO FIND CLUSTERS

Within the wealth of Gaia data, small-scale structures such as clusters and associations are not easy to detect, as they need to stand out against the Galactic field population. This is especially true for loose associations or other sparse groups that have a low contrast within the Galactic field.

A key characteristic of young stellar clusters is their small velocity dispersion of 1.5-5 km s⁻¹ (Kuhn et al., 2019; Preibisch & Mamajek, 2008; Riedel et al., 2017), significantly smaller than measured for the Galactic field population. Therefore, they appear as small-scale velocity structures in the Milky Way disk, and are typically detected as small-scale overdensity peaks in velocity space, for example, in 2D proper motions (μ_α, μ_δ), combined with the parallax ϖ in 2D tangential velocities (v_α, v_δ), or in 3D Galactic cartesian velocities (U, V, W) and Galactocentric cylindrical velocities (v_R, v_Φ, v_Z) for the radial velocity subset (e.g. Fűrnkranz et al., 2019; Meingast and Alves, 2019; Röser et al., 2019). In addition, very compact clusters or the prominent cores of more extended groups can appear also as overdensities in position space, e.g. in 2D right ascension and declination (α, δ), Galactic longitude and latitude (l, b) or - combined with the parallax ϖ - in the 3D Galactic Cartesian coordinate frame (X, Y, Z).

1 Introduction

Ideally, clusters are detected in the combined full 6D position-velocity parameter space. However, this information is only available for the subset of sources that have radial velocity measurements, and much more data are available for the 5D position-proper motion solution. [Kounkel and Covey, 2019](#) make use of this information and cluster stars in 3D position and 2D velocities. However, identifying comoving groups in proper motion or tangential velocity space is challenging, as projection effects influence the appearance of extended structures on the sky ([Meingast et al., 2021](#)).

Another way to detect stellar clusters within the radial velocity subset is the 6D action-angle space (J, Θ) as shown in e.g. [Coronado et al., 2020](#), under the assumption of a gravitational potential. This is especially advantageous in identifying groups on large scales ($\gtrsim 100$ pc): young groups can have a significant extent on the sky, as well as in vertical height above and below the plane. Looking at the vertical oscillation of the stars shows that they get accelerated ($\sim 5 \text{ km s}^{-1}$) as they move through the Galactic midplane. Therefore, clustering stars in velocity space would only be correct under the assumption that all stars always move on straight lines at constant velocity. This can be improved by using the velocity set ($v_{\text{tangential}}, v_{\text{radial}}, v_{\text{vertical}}$); however, this would only be correct if all orbits were exact circular orbits. In practice, searching in velocity space is sufficient to find groups on small scales; however, if the extent of the groups is so large that the acceleration of the stars is larger than the internal velocity dispersion of the group, action-angle coordinates have proven to be the better choice when searching for stars on the same or similar orbit, which can be widely dispersed on the sky. It can be seen from Figure 2 of [Price-Whelan et al., 2021](#) that, assuming an internal velocity dispersion of 1 km s^{-1} for stellar clusters, the acceleration of stars already exceeds the internal velocity dispersion if groups are more extended than ~ 25 pc. This is the motivation why we investigate stellar groups in action-angle phase space, rather than in the more commonly used position-velocity space.

Also, since stars in a cluster are formed from the same molecular cloud, they share the same chemical composition, with a small dispersion in elemental abundances ([Zucker et al., 2022](#)). Therefore, another approach to identify stellar clusters is chemical tagging, as suggested in the work by [Freeman and Bland-Hawthorn, 2002](#). With the advent of spectroscopic surveys like Gaia-ESO, GALAH and APOGEE there are several studies clustering sources in elemental abundance space (e.g. [Buder et al., 2021](#); [Jönsson et al., 2020](#); [Kos et al., 2021](#); [Price-Jones et al., 2020](#); [Spina et al., 2022](#)).

Stars of a stellar cluster are born at the same time; therefore stellar clusters are often validated by their clean color-magnitude-diagrams, requiring to form a narrow sequence, compatible with a single stellar population. Figure 1.6 - adapted from [Castro-Ginard et al., 2022](#) - illustrates the properties of two example stellar clusters: LP 589 in cyan and NGC 2509 in yellow. The top left plot shows the groups as overdensities in position space, with the vectors illustrating the common proper motions of each star in a cluster. Both clusters are also seen as clear overdensity blobs in proper motion space, as is shown in the top-right panel. The panel on the bottom left validates their coeval state, as all stars in each cluster form a narrow sequence in the color-magnitude-diagram, with NGC 2509 revealing to be a significantly older

population than LP 589. The bottom right panel shows the parallax or distance distribution for each star, showing larger measurement uncertainties for fainter sources.

Typically, star clusters in the Gaia data set are detected with existing clustering algorithms. Three well-established density-based clustering algorithms that have been commonly used in existing open cluster studies are DBSCAN (Castro-Ginard et al., 2018; Hao et al., 2022; Z. He et al., 2022; Liu & Pang, 2019), Gaussian mixture models (GMM), and HDBSCAN (Hunt & Reffert, 2023). Their feasibility was discussed in detail in Hunt and Reffert, 2021. Additionally, stars have been linked via friends-of-friends algorithms (Coronado et al., 2020; Liu & Pang, 2019; Tian, 2020) and via nearest-neighbor approaches (Z.-H. He et al., 2021), or extracted with a density cut from kernel density distributions or wavelets (Meingast et al., 2019).

Even with these attributes in mind the detection of cluster member stars is still challenging: first, different clustering methods introduce different biases that must be kept in mind (Hunt & Reffert, 2021). Additionally, field stars can by chance share the same position and velocity of stellar cluster members. Therefore, contamination of field stars in the resulting membership catalogs should be estimated, and the number of contaminating background sources should be reduced to a minimum. Moreover, with the discovery of stellar cluster dissolution it became unclear and remains somewhat arbitrary to define the boundary of star clusters, e.g. to define up to what extent sources can and should be associated with a cluster.

1.5.4 UP-TO-DATE CENSUS OF CLUSTERS IN THE GALACTIC DISK

The number of scientific works and publications on stellar clusters in the Milky Way disk has increased drastically since the Gaia data releases, making it difficult - if not impossible - to keep up with the current literature. Although there have been numerous studies on individual open clusters and associations (e.g. studying their properties, morphologies, dynamics, and dispersal), a couple of studies published large all-sky catalogs, aiming to extend and complete the scope of young stellar clusters in the solar neighborhood.

Before Gaia, the largest and most cited catalogs were ~ 1500 open clusters published by Dias et al., 2002 and ~ 3000 objects published by Kharchenko et al., 2013, including mainly open clusters, but also stellar associations and globular clusters. Since the second Gaia data release was published in 2018, several papers have revised the open cluster census in the solar neighborhood: Cantat-Gaudin and Anders, 2020; Cantat-Gaudin et al., 2018; 2020; Castro-Ginard et al., 2018; 2019; 2020; 2022. The largest open cluster catalog to date was published by Hunt and Reffert, 2023 and contains ~ 7000 objects, with more than 2000 objects yet unreported in the literature. Applying a more stringent cut on their catalog leaves ~ 4000 objects, with more than 700 candidate new objects.

In addition to this, several studies focused on the structure, kinematics, and subpopulations of young, extended OB associations in the solar vicinity: the Orion star formation complex was studied by e.g. Großschedl

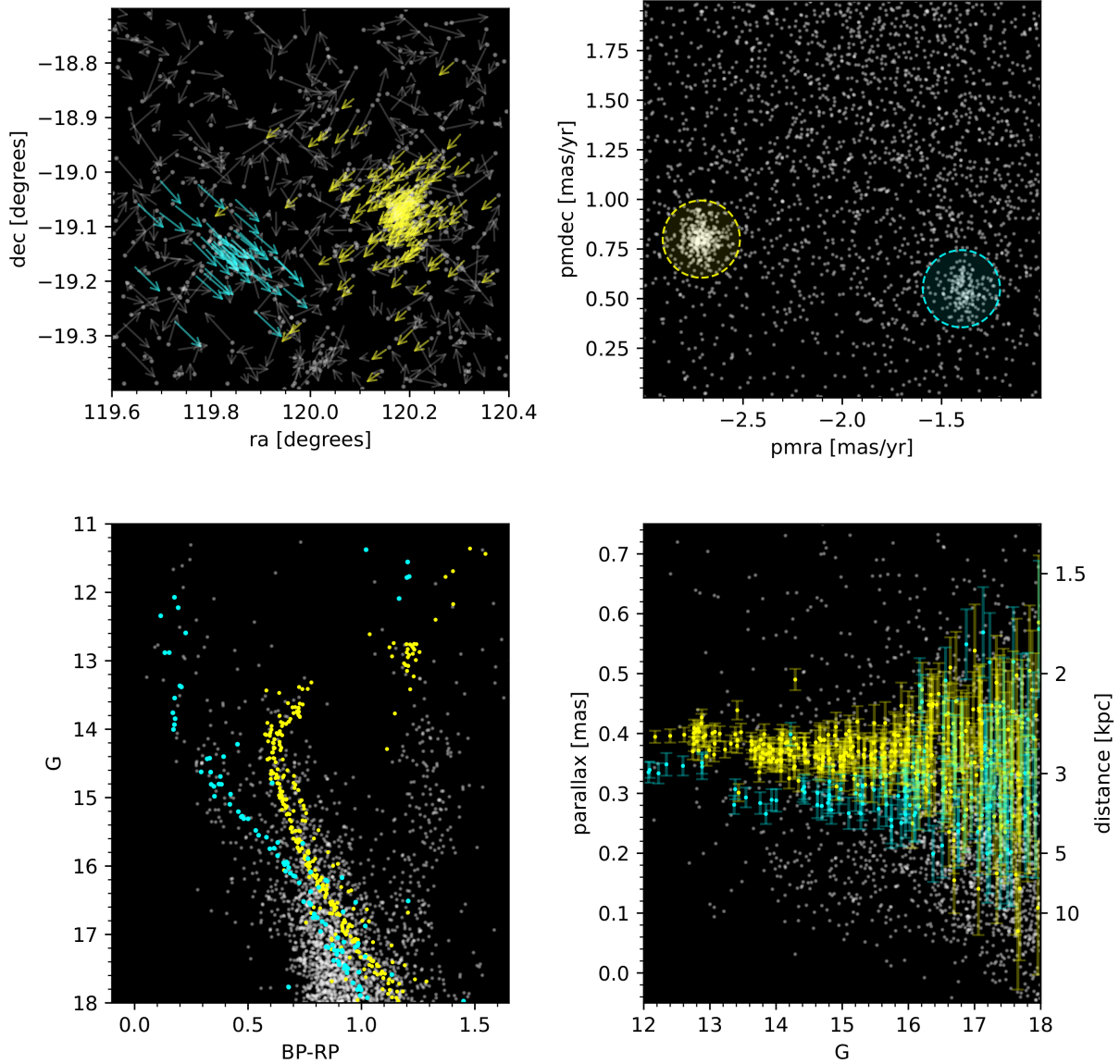


Figure 1.6. Two example clusters: LP 589 in cyan and NGC 2509 in yellow. Top left: both clusters in position space with vectors indicating their proper motions. Top right: both clusters as overdensity blobs in proper motion space. Bottom left: both clusters as narrow coeval sequences in a color-magnitude diagram. Bottom right: parallaxes and distances of both clusters, with increasing uncertainties for fainter sources. **Figure credit:** [Cantat-Gaudin, 2022a](#)

[et al., 2018; 2021; Jerabkova, Beccari, et al., 2019; Jerabkova, Boffin, et al., 2019; Kos et al., 2019; Swiggum et al., 2021; Zari et al., 2019](#); the Scorpius–Centaurus region was investigated by e.g. [Luhman and Esplin, 2020; Wright and Mamajek, 2018; Žerjal et al., 2023](#); and the Vela-Puppis complex was examined by e.g. [Cantat-Gaudin, Jordi, et al., 2019; Cantat-Gaudin, Mapelli, et al., 2019; Wang et al., 2022](#); as were many other young stellar associations (e.g. Taurus, Canis Major, Lupus).

However, the distinction between open clusters and stellar associations (see Section 1.5.1) became blurred by recent publications, revealing more complex morphological varieties of young and potentially primordial stellar groups, and leading to new vocabulary to describe stellar groups in recent literature. [Meingast](#)

et al., 2019 discovered a coeval *stellar stream* - known as Pisces-Eridanus or Meingast 1 - at a distance of ~ 100 pc from the Sun. Its stars form an elongated structure that extends over 400 pc, with a 3D velocity dispersion of only 1.3 km s^{-1} . Its age of 120 Myr was determined using gyrochronology (Curtis et al., 2019), and its mass is estimated to be $2000 M_{\odot}$ (Ratzenböck et al., 2020). In addition, the identification of *stellar strings* within 3 kpc from the Sun was proposed by Kounkel and Covey, 2019; Kounkel et al., 2020. These strings are described as filamentary structures oriented in parallel to the Galactic plane, extending hundreds of parsecs in length. They are discussed as potentially primordial, preserving the shape of filamentary giant molecular clouds from which stars have formed (Kounkel et al., 2020). Among the new classes of stellar structures with more extended and complex spatial distributions are also, e.g. *snakes* (Tian, 2020; Wang et al., 2022), *rings* (Cantat-Gaudin, Mapelli, et al., 2019), *relic filaments* (Beccari et al., 2020; Jerabkova, Boffin, et al., 2019). Furthermore, the new terminology *pearls* will be introduced as part of this thesis (Coronado et al., 2022). A re-examination and comparison of some of these novel stellar classes is provided by Zucker et al., 2022.

The pace at which cluster discoveries have been published in recent years makes it difficult to keep catalogs updated (Cantat-Gaudin, 2022b), and leads to a set of difficulties with the up-to-date cluster census: many stellar groups lack independent verification, and cross-identification between catalogs is challenging, because clusters frequently have differing numbers of member stars depending on the methods and definitions used in the individual studies. Additionally, this could cause clusters presented in papers as newly might already have been reported by papers. In addition, papers published almost simultaneously can lead to cluster duplicates. Further, some studies might split clusters into subgroups, while others - depending on their clustering algorithm and cluster definitions - do not.

It is also not clear how complete the census of open clusters in the solar neighborhood is. Kharchenko et al., 2013 claimed that their sample of open clusters is almost complete up to 1.8 kpc from the Sun, which has been proven wrong by recent publications. Anders et al., 2021 made an attempt to estimate the cluster completeness in terms of age and distance. However, it is reasonable to believe that more open clusters will be detected with the next Gaia data release, for example, or with a potential future near-infrared astrometry mission (GaiaNIR, see Section 1.7).

Another puzzle for the open-cluster census is that a large number of reported open clusters could not be re-detected by recent Gaia studies (e.g. Cantat-Gaudin and Anders, 2020; Cantat-Gaudin et al., 2018; Hunt and Reffert, 2023; Kos et al., 2018). Although some studies investigated the existence of selected individual clusters, the existence of most clusters in questions is still not solved, but could be explained by a number of reasons proposed in Hunt and Reffert, 2023: First of all, the nonexistence of some clusters could be caused by limitations of the clustering algorithms, different definitions of open clusters (e.g. different minimum number of member stars), or different data quality cuts between different works. Secondly, it could be caused by limitations of the Gaia dataset, as e.g. heavily reddened objects are not possible to

1 Introduction

detect. Third, it is possible that some reported clusters simply do not exist, and despite their member stars sharing the same location on the sky, Gaia shows that they do not share the same motion.

In addition to the amount of (re)discovered clusters in the Gaia dataset, numerous studies on science done with open clusters have been published in the past few years. One highlight of the precise position and velocity data is the possibility of observing the dissolution effects of open clusters. For the first time, tidal tails of known open clusters could be detected, increasing the clusters historical spatial extent and their number of member stars, e.g. Hyades (Meingast & Alves, 2019; Röser et al., 2019), Coma Berenices (Fürnkranz et al., 2019; Tang et al., 2019), and Praesepe (Röser & Schilbach, 2019). In addition, Tarricq et al., 2022 detected tidal tails for a set of 71 open clusters. These tidal tails are an effect of cluster dissolution due to the tidal forces of the Milky Way and have been predicted by simulations (e.g. Kharchenko et al., 2009). In addition to this, Meingast et al., 2021 report the discovery of *stellar coronae* around the cores of young (<300 Myr) known open clusters. Stars in these coronae are comoving with the cluster cores, appear coeval in the observational CMDs, and extend the original open clusters sizes ≥ 100 pc. Possible explanations for the formation of these coronae involve the morphology and kinematics of the molecular clouds in which they are born, the ability of young stars to maintain their birth motion, the consequences of gas expulsion and relaxation, and the differential rotation of the Galactic disk (Meingast et al., 2021). Figure 1.7 shows a top-down view of ten open cluster cores surrounded by massive stellar coronae, which encompasses up to several hundred parsecs.

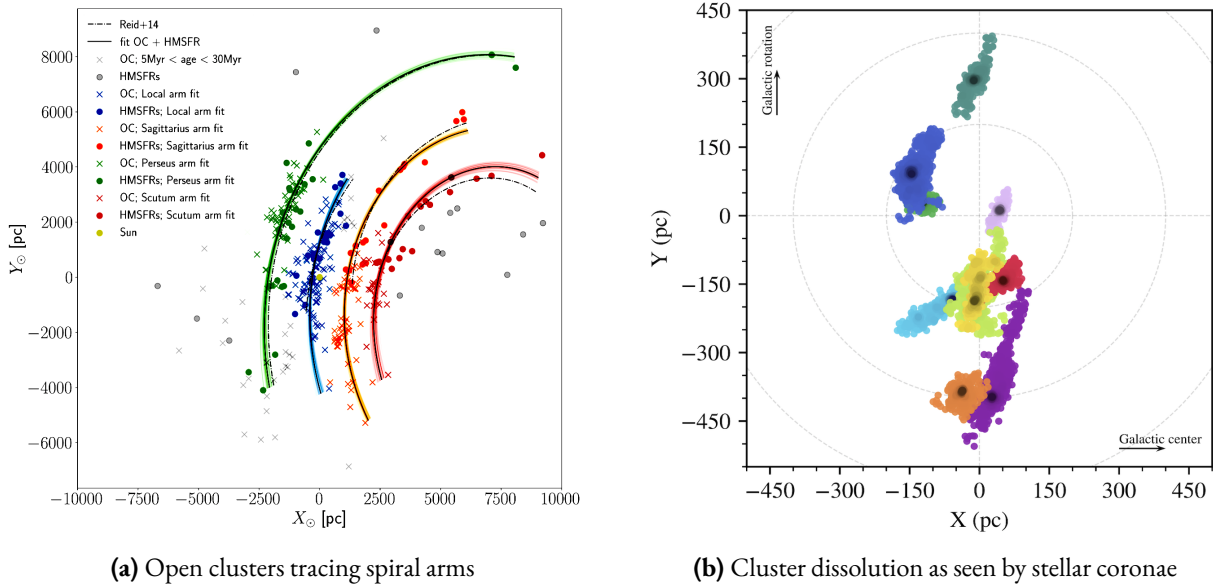


Figure 1.7. The impact of Gaia on the structure of the Milky Way, and on cluster dissolution. Panel (a) shows young star clusters that trace the spiral arms of the Milky Way. Panel (b) illustrates that most clusters do not only consist of a dense cluster core, but are surrounded by ‘stellar coronae’ due to cluster dissolution processes. **Figure credit: (a) Castro-Ginard et al., 2021, (b) Meingast et al., 2021**

Moreover, open clusters are excellent tracers of the structure of the Milky Way disk. Young open clusters can be used to trace the spiral arm structure, as shown, e.g. Castro-Ginard et al., 2021. Figure 1.7 shows

the distribution of open clusters with ages < 30 Myr (crosses), and regions of high-mass stars forming from Reid et al., 2014 (dots), with different colors representing different spiral arms. They found that the pattern speeds between different spiral arms differ, favoring their short-lived and transient behavior instead of the classical density wave theory (Castro-Ginard et al., 2021). Some studies (e.g. Cantat-Gaudin et al., 2020) investigate the vertical extent with respect to the Galactic midplane of open clusters as a function of age and Galactocentric radius. They show that young clusters are preferentially found at low altitudes, while older clusters reach higher vertical extents. Also, they find a lack of old open clusters in the inner disk. Explanations for this could be more frequent interactions of open clusters with giant molecular clouds in dense regions, which disrupt open clusters.

In summary, with the advent of Gaia’s accurate astrometric data, stellar clusters can be identified, intensively studied in terms of their internal properties, and put into the context of the present-day structure of the Galactic disk. Gaia’s photometric data furthermore enable us to plot color-magnitude diagrams of stars, which can be used to determine the ages of the coeval stellar populations. An introduction on how to estimate ages using color-magnitude diagrams is provided in the following Section 1.6.

1.6 AGE DATING OF CLUSTERS

To fully understand the formation, structure, and dynamics of the Milky Way disk, we need to know, among other properties, the ages of its stars. Unfortunately, stellar ages are hard to obtain in practice. Unlike other parameters such as the mass or the composition of a star which can be directly measured or determined from basic physics, stellar ages can only be estimated. Soderblom, 2010 reviews stellar age estimation methods, grouping them into three main categories, which will be briefly introduced below: fundamental and semifundamental ages, model-dependent ages, and empirical ages.

The only fundamental age that we know is that of the Sun. Its exact age is 4.567 Myr, which can be determined by measuring Solar System material in the laboratory. However, this is not possible for any other star. Semifundamental methods involve only making a few assumptions. First, *nucleocosmochronometry* measures the decay of U and Th for individual thick-disk or halo stars. Secondly, for young groups of stars *kinematic ages* can be estimated by tracing their stars back in time, making the assumptions of a gravitational potential and that when stars formed they were in closest proximity to one another. Due to the large uncertainties in orbit integration, this method can only be applied to groups younger than ~ 20 Myr.

Most age-dating methods used have built-in model dependencies and are therefore categorized as model-dependent ages. Basically, there are three model-dependent methods: First, *isochrone fitting* is the best known method to estimate the ages of stellar groups and is described in more detail in Section 1.6.1. Secondly, *asteroseismology* is an accurate yet resource-intensive method to estimate ages of individual stars

by detection of stellar oscillation modes. Third, the *lithium depletion boundary (LDB)*, which is based on the presence or absence of lithium in low-mass stars, can be used to determine the ages of young clusters and stellar associations.

Empirical ages are based on observed relations between a measured property and age. The most direct empirical method is called *gyrochronology* and was introduced by [Barnes, 2007](#). This is mostly applied to main-sequence stars and uses their rotation periods to derive ages. A less direct method to derive stellar ages is studying the *decay of stellar activity*, which is dependent on the rotation (e.g. Calcium II chromospheric emission). In addition, the *decrease in lithium abundances*, which can be observed at 6 708 Å, in F, G, and K stars, can be used as an age tracer for ensembles of stars.

In addition, [Soderblom, 2010](#) mentions two statistical trends that could (weakly) relate stars to their ages: the age-metallicity relation (AMR) and the increase in Galactic space motions with time (disk heating). For this thesis, the age determination with isochrone fitting is the method of choice, as the Gaia space mission delivers photometry in three passbands, as well as precise stellar parallaxes for stars in stellar ensembles in the solar vicinity. In the next Section 1.6.1 this method will be introduced in more detail.

1.6.1 CMD ISOCHRONE FITTING

The relationship between the total luminosity L , the temperature T , and the radius R of a star is given by the following relation:

$$L = 4\pi R^2 \sigma T^4,$$

where $4\pi R^2$ represents the surface area of the star, and σ is the Stefan-Boltzmann constant. A powerful tool to visualize this relationship is the Hertzsprung-Russel diagram (HRD) ([Hertzsprung, 1911](#); [Russell, 1914](#)), which shows the luminosity of stars as a function of their temperature or spectral type. However, in practice these quantities are not easy to obtain, which is why the HRD is often substituted by the color-magnitude diagram (CMD), its empirical analogue. This instead shows the absolute magnitude of stars as a function of their color index. The absolute magnitude represents a measure of the brightness of a star, and the color index is the difference in magnitude between two filters, and is a proxy for the temperature of a star. The advantage of these quantities is that they are measured by the Gaia mission, which provides photometric measurements in three passbands, as well as parallax measurements that can be used as distance estimates to obtain the absolute magnitude of stars (see also Section 1.4).

The left panel of Figure 1.8 shows an observational color-magnitude diagram of one million stars within 200 pc from the Sun, measured by the Gaia satellite. It is shown as a 2D-histogram, where the color represents the density of stars in a small 2D grid. The majority of stars are distributed along a narrow stripe that extends from the bottom right to the top left, known as the *main sequence*. Stars spend $\sim 90\%$

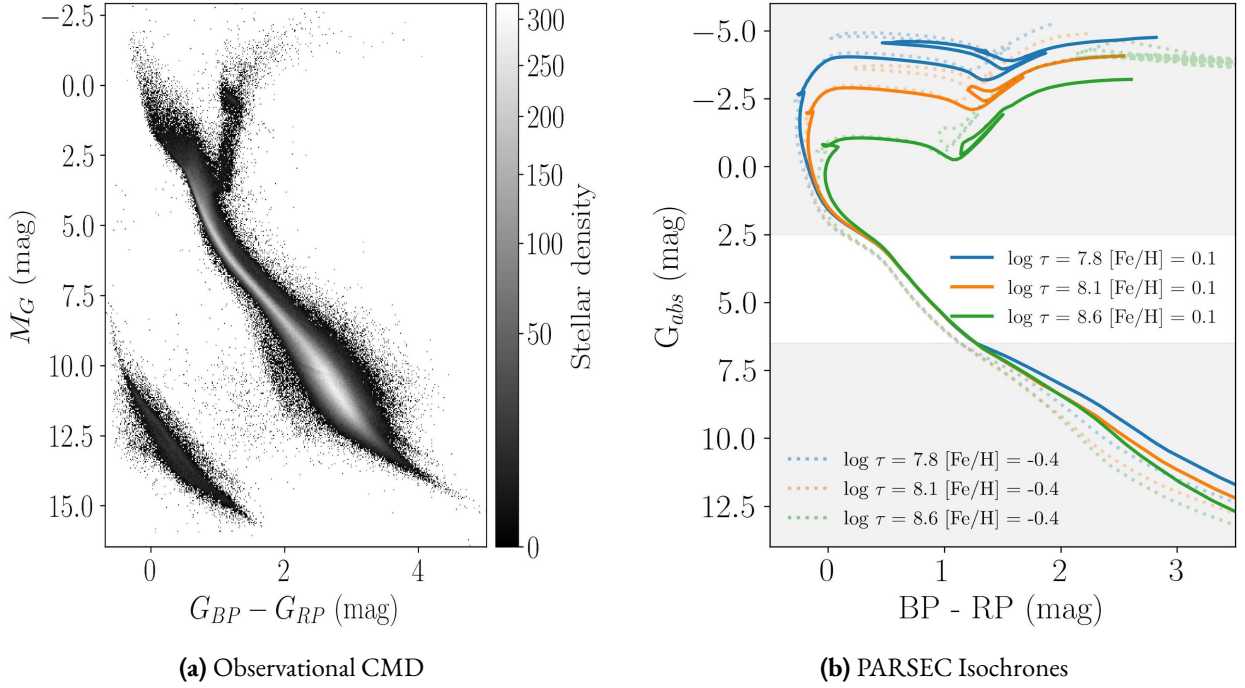


Figure 1.8. *Left:* Observational colour-magnitude diagram (CMD) of one million stars within 200 pc from the Sun as measured by Gaia, color-coded in stellar density. Most stars populate the main sequence, where they spend about 90% of their lifetimes. *Right:* PARSEC Isochrones for a set of three different ages $\log \tau$ and two different metallicities $[\text{Fe}/\text{H}]$. The gray shaded areas indicate the parts of the CMD where most of the age information can be obtained from: the lower main sequence, and the main sequence turn-off.

of their lifetimes on this sequence, while they fuse hydrogen to helium in their cores. They typically have luminosities of 10^{-2} - $10^6 L_{\odot}$, temperatures of 3000-50000 K, and radii between 0.1-10 R_{\odot} . The stars are in hydrostatic equilibrium, and their position on the main sequence depends on their mass, e.g. more massive stars appear towards the upper left corner of the diagram, whereas less massive stars, which are cooler and less luminous, appear towards the lower right corner.

Another populated field on the CMD is the white dwarf region, which is comprised of the remnants of low- to intermediate-mass stars ($M < 8 M_{\odot}$), who occupy the lower left corner of the diagram; e.g. these are stars which are hot but have luminosities lower than those of the main-sequence stars at the same temperatures. Therefore, their radii are much smaller than those of the main sequence stars, with $R \sim 0.01 R_{\odot}$. These stars cool down in their white dwarf phase after they have ejected their outer layers and no longer undergo nuclear fusion.

The *main sequence turn-off* occurs when stars evolve off the main sequence because they exhaust hydrogen in their cores. This leads to a contraction of the core under gravity and hydrogen fusion in the shell around the core, causing the envelope to expand and cool and stars to become redder and more luminous, shifting the stars to the red-giant phase. For star clusters, the location of the turnoff is a key feature in determining their ages, as more massive stars burn their fuel faster and, therefore, evolve faster than low-mass stars, reaching the main-sequence turnoff earlier and indicating the ages of stellar clusters.

1 Introduction

Another indicator to determine the ages of star clusters is the *pre-main sequence*, which is comprised of young stars which have not started fusing hydrogen into helium in their cores yet. These pre-main sequence stars are located offset to the main sequence, appearing cooler and less luminous compared to main sequence stars of the same mass. The evolution of the pre-main-sequence stars follows the so-called Hayashi track (Hayashi, 1961), e.g. a nearly vertical path downward on the CMD as the stars contract and become hotter. The presence of a pre-main sequence is an indicator that a cluster is very young (<100 Myr), and the location where a stars first start to fuse hydrogen to helium in their cores and reach the main sequence is called the zero-age main sequence.

As described in Section 1.5.3, the bottom right panel of Figure 1.6 illustrates that stellar clusters form narrow coeval sequences in a color-magnitude diagram, indicating that they are comprised of stars with the same age spanning a wide range of stellar masses. Theoretical evolutionary tracks of stars can be computed from stellar evolution models and are known as *isochrones*. They are loci in the color-magnitude diagrams representing stars of the same age in the range of different masses. Two popular sets of these stellar evolutionary models used to create isochrones are the ‘PAdova and TRieste Stellar Evolution Code’ (PARSEC) (Bressan et al., 2012) and the ‘MESA Isochrones and Stellar Tracks’ (MIST) (Choi et al., 2016; Dotter, 2016). They differ slightly in their physical ingredients, e.g. whether they include rotational effects such as does MIST, or how well they track the pre-main sequence evolution, where PARSEC isochrones might be the better choice. Obviously, the estimate of ages becomes slightly ambiguous, as it might depend on the isochrone models used.

The right panel of Figure 1.8 shows PARSEC isochrones for a set of three different ages of $\log \tau = [7.8, 8.1, 8.6]$ and two different metallicities of $[\text{Fe}/\text{H}] = [-0.4, 0.1]$. It reveals two main areas in the CMD that incorporate most information of the age: at the hot bright end it is the part of the main sequence turn-off, and at the cool faint end it is the lower zero-age main sequence (pre-main sequence). This is indicated with gray shades in Figure 1.8. From the main-sequence - e.g. between $G_{abs} \sim 2.5-7.0$ mag - almost no information can be obtained about the age, as all isochrones are superimposed. However, different metallicities shift isochrones also in this part of the color-magnitude-diagram: higher metallicities shift the isochrone towards a redder and more luminous location. This indicates that metal-rich populations are expected to be at a different location in the color-magnitude-diagram than metal-poor populations, showing that a correct estimate of a cluster’s metallicity is important to fit its correct age. The metallicity can either be fitted as a variable parameter or estimated before the fitting, e.g. by available spectroscopic measurements of stars in a cluster.

In practice, fitting ages with isochrones is far from trivial. One challenge in terms of this thesis is the availability of 6D orbit and orbital phase space data only in a limited temperature range of $T_{eff} \in [3100, 14500]$ K for bright sources ($G \leq 12$ mag) and $[3100, 6750]$ K for fainter sources (see also Section 1.4), e.g. most of the stars are located in the area of the main sequence with no age information. This can be bypassed by searching for stars in the more complete 5D position-parallax-proper motion space. Still,

also in this data set there frequently is a lack of stars at the hot bright end of the CMD, e.g. at the location of the main-sequence turn-off for young stellar groups. This means that for young groups, the lower main sequence serves as the main age determinant. However, for faint sources located in the lower main sequence area of the diagram, the uncertainties in the measurements become larger, making it necessary to account for these uncertainties when fitting isochrones.

Furthermore, isochrone fitting is highly sensitive to interstellar extinction, which is the effect when stellar light is attenuated by interstellar gas and dust. It depends on the wavelength λ as well as on the composition and sizes of the dust grains, and causes a star to appear redder than it is, which is known as reddening. The amount of reddening is denoted by $E(B-V)$ in the following equation:

$$E(B - V) = (B - V) - (B - V)_0,$$

where $(B - V)$ is the apparent color of an object and $(B - V)_0$ is its intrinsic color. The larger the reddening of a star, the larger is also its extinction. In principle, the amount of extinction depends on the distance d of stars, e.g. the light from more distant stars is more affected by extinction; however, some regions are more gas and dust rich than others (e.g. due to the presence of dense molecular clouds), making the amount of interstellar extinction strongly dependent on the line of sight. In result, member stars of stellar groups that are very extended on the sky might experience different levels of extinction. The extinction A_V (measured in the V band) is correlated with the reddening by the following equation:

$$A_V = R_V \cdot E(B - V),$$

where R_V is the extinction ratio, with an average value of 3.1 for the Milky Way (Schultz & Wiemer, 1975). The extinction can either be optimized in the isochrone fitting (assuming an ensemble value for all member stars of a cluster), or can be accounted for on a star-by-star basis, e.g. by using reddening maps by Fouesneau et al., 2023; Green et al., 2019; Schlegel et al., 1998.

There are several groups of stars that should be excluded from fitting isochrones to stellar clusters. Firstly, interlopers, e.g. contaminant stars that coincidentally share the same position and velocity coordinates, should be removed carefully, and an age estimate of a stellar ensemble should ideally not depend on the position of one single star in the color-magnitude diagram (e.g., this led to an incorrect age determination in Meingast et al., 2019 and was later corrected by Curtis et al., 2019 using gyrochronology). The same applies to stars with large photometric uncertainties or spurious locations in the color-magnitude-diagram, which should also be excluded before isochrone fitting. Furthermore, evolved stars such as white dwarfs should be excluded as they are not part of evolutionary tracks of isochrones. Also, unresolved binaries form a secondary parallel sequence above the main sequence because the presence of a binary companion makes a stellar system appear brighter while not redder than a single star. This binary sequence, which is about 0.7 mag brighter than the single star sequence, should be separated out, so that it does not affect the age determination.

Based on this framework, we develop and apply an isochrone fitting method to estimate the ages of stellar action angle groups, which will be presented in Chapter 3. But first, in Section 1.7 we describe the overall motivation and goals of this thesis and briefly outline the contents of all remaining chapters.

1.7 GOALS AND OUTLINE OF THE THESIS

We know that the distribution of newly born stars is manifestly clustered, some in long-lived (compared to τ_{dyn}) open clusters, others in ephemeral birth clusterings or looser associations. Subsequently, most stars disperse from their birth siblings, spreading in orbit and orbital phase to become field stars. We have learned that the Milky Way galaxy can serve as a benchmark galaxy to study this transition, as we have precise position and velocity measurements of individual stars. The revolutionary data provided by Gaia have proven powerful in studying such stellar groups. This goal of this thesis is to address the following questions:

- Is anything interesting about orbits where stellar clusters are located?
- How can we estimate ages for stellar groups with (limited) 6D phase-space information?
- What can we learn from statistically exploring orbit-age relations of large sets of stellar aggregates?

Subsequently, we want to understand whether we should expect stars to be born on ‘random orbits’ in the Galactic disk, over what scales we expect near-coeval stellar associations to be on very similar orbits, how rapidly these systems disperse, how their structure evolves as a function of time, and to which extent the orbit distribution reflects a possible birth from extended molecular gas filaments.

For a better overview, the structure of the remaining thesis will be as follows⁷.

- Chapter 2: Pearls on a String: Numerous Stellar Clusters Strung Along the Same Orbit

In the first scientific study of this thesis, we identified 55 stellar clusters and associations in orbit and orbital-phase space, within 800 pc from the Sun. We investigated the orbital-phase distribution for all stars located in the same orbit patch as one of the groups and discovered that other distinct orbital-phase overdensities are frequently found on similar orbits, aligned at distinct orbital phases, like *pearls on a string*. This is in contrast to mock and nearby offset orbit patches, which show significantly lower occurrences of orbital-phase overdensities. These findings imply that recent star formation might be clustered towards particular orbits in the Galactic disk.

- Chapter 3: The Age Distribution of Stellar Orbit Space Clumps

⁷In this thesis, apart from a few exceptions the pronoun ‘we’ is used instead of ‘I’ in accordance with the common academic writing style in the field.

In the second scientific work of this thesis, we developed a method to derive ages of stellar orbit and orbital-phase overdensities, by projecting their 6D action-angle distribution into 5D position-parallax-proper motion space and drawing color-magnitude diagrams from the entire Gaia catalog, where the lower (pre-)main sequence is a precious age determinant. We then performed a likelihood isochrone fitting, accounting for varying distances and reddenings, outliers, and binaries, and the possible presence of an intrinsic age spread. The resulting age distribution of conatal groups of stars can constrain on which orbits they had formed, and how rapidly these systems disperse into the field.

- Chapter 4: Ages for large sets of stellar aggregates

In the third scientific chapter of this thesis, we applied the age-dating method to large sets of stellar aggregates. First, we modified the action-angle clustering to identify a set of 695 stellar aggregates, and extended their memberships similarly to as outlined in the previous chapter. Secondly, we selected a set of 836 stellar clusters from a state-of-the-art cluster catalog published by [Hunt and Reffert, 2023](#). As a prior constraint for the isochrone fitting, we derived spectroscopic metallicities for each group from Gaia XP spectra as published by [Andrae et al., 2023](#). The resulting age distributions of both datasets reveal a strong bimodality. This age ambiguity is likely caused by groups where neither the lower main-sequence nor the main-sequence turn-off offer age information.

- Chapter 5: Summary and Outlook

The last chapter will present a summary of the work presented in this thesis. It will also show first steps into the exploration of the orbit-age space of young clusters in the Milky Way, presented as a basis to study their dispersal in the Galactic disk. In addition, it will briefly discuss the implications and future prospects leading from this thesis, in particular in regard of the future Gaia data releases DR4 and DR5, and synergies with other (future) surveys, such as GaiaNIR, the Nancy Grace Roman Space Telescope, 4MOST, and SDSS-V.

2 PEARLS ON A STRING: NUMEROUS STELLAR CLUSTERS STRUNG ALONG THE SAME ORBIT

2.1 DETAILS OF PUBLICATION AND AUTHORSHIP

The content of this chapter is based on the following peer-reviewed publication.

- **Title:** Pearls on a String: Numerous Stellar Clusters Strung Along the Same Orbit
- **Authors:** Johanna Coronado, Verena Fürnkranz, Hans-Walter Rix
- **Journal:** The Astrophysical Journal, Volume 928, Issue 1, id.70, 21 pp. (March 2022)
- **DOI:** [10.3847/1538-4357/ac545c](https://doi.org/10.3847/1538-4357/ac545c)
- **Online data:** <https://cdsarc.cds.unistra.fr/viz-bin/cat/J/ApJ/928/70>

The formatting of the figures and tables has been adjusted to better fit the layout of this thesis.

Contributions:

This paper was produced in a transition phase between Johanna Coronado and me, both supervised by Hans-Walter Rix. The project was started by Johanna Coronado, who left academia in March 2021, and continued by me as part of my PhD starting in November 2020.

All coding, analysis, and figures of the paper were done by Johanna Coronado and myself, under the regular guidance of Hans-Walter Rix. The majority of the work was done collaboratively, but for clarity, here is an overview of the approximate allocation of tasks: Johanna Coronado performed the FoF approach to link stars in 6D action-angle space, similar to [Coronado et al., 2020](#). I created the action patches systematically enclosing the groups and extracting stars inside them. Johanna Coronado algorithmically identified *pearls* by linking stars in 3D angle space and performed the three case studies. I suggested comparing the orbital phase distribution with an ‘offset’ orbit patch in addition to the mock orbit patch. In addition, I suggested performing a statistical analysis of the number of pearls in each action patch and illustrating this in a plot (see Figure 2.9). Johanna Coronado did large parts of the paper writing with

contributions from Hans-Walter Rix and me. I worked on the extensive referee report which comprised 7 major comments, 10 minor comments, and 13 other comments, including e.g. the overlap between pearls and the contamination estimate. Also, I did large parts of paper rewriting after the referee report, with contributions from Johanna Coronado and Hans-Walter Rix.

2.2 ABSTRACT

Stars originate from the dense interstellar medium, which exhibits filamentary structure to scales of ~ 1 kpc in galaxies like our Milky Way. We explore quantitatively how much resulting large-scale correlation there is among different stellar clusters and associations in orbit phase space, characterized here by actions and angles. As a starting point, we identified 55 prominent stellar overdensities in the 6D space of orbit (actions) and orbital phase (angles), among the ~ 2.8 million stars with radial velocities from Gaia EDR3 and with $d \leq 800$ pc. We then explored the orbit-phase distribution of all sample stars in the same orbit patch as any one of these 55 overdensities. We find that very commonly numerous other distinct orbital phase overdensities exist along these same orbits, like pearls on a string. These "pearls" range from known stellar clusters to loose, unrecognized associations. Among orbit patches defined by one initial orbit-phase overdensity 50% contain at least 8 additional orbital-phase pearls of 10 cataloged members; 20% of them contain 20 additional pearls. This is in contrast to matching orbit patches sampled from a smooth mock catalog, or offset nearby orbit patches, where there are only 2 (or 5, respectively) comparable pearls. Our findings quantify for the first time how common it is for star clusters and associations to form at distinct orbital phases of nearly the same orbit. This may eventually offer a new way to probe the 6D orbit structure of the filamentary interstellar medium.

2.3 INTRODUCTION

Clusters form in hierarchically structured, accreting giant molecular clouds (GMCs), which are part of the overall filamentary structure of the cold interstellar medium. Within these GMCs there are density concentrations known as clumps (Krumholz et al., 2019), where individual small regions collapse independently (fragment) and eventually produce stars until the gas is dispersed by feedback.

The densest parts of the hierarchy resist gas removal (until they reach a high star-formation efficiency) and they become dynamically relaxed and well mixed, where they remain bound after gas removal. In the first ~ 100 Myr after the latter, clusters disperse moderately fast (Krumholz et al., 2019). In this scenario, young star clusters are expected to preserve some memory of the physical conditions that are present in their birthplace (Bonatto & Bica, 2010).

Star clusters in the disk of the Milky Way are commonly classified as open clusters (OCs) or associations. And it has not yet been well quantified or understood to which extent distinct OCs and associations are born isolated or in correlated ensembles. Although, gravitating matter tends to cluster and form objects on different scales (Kovaleva et al., 2020). Thus it could be possible that, similar to stars, clusters may form groups and physical pairs (Bonatto & Bica, 2010; Elmegreen & Efremov, 1996; Fujimoto & Kumai, 1997; Gusev & Efremov, 2013).

In nearby external galaxies, such as the Large Magellanic Cloud (LMC) and Small Magellanic Cloud (SMC), where the viewing geometry is simpler, binary OCs or groups of OCs are observed. Some studies have shown that ~ 12 per cent of clusters are in pairs or binary clusters (Pietrzynski & Udalski, 2000). In our own Galaxy, the fraction of binary clusters has been found to be approximately the same (de La Fuente Marcos & de La Fuente Marcos, 2009).

Binary clusters appear to be systematically younger than single clusters (Dieball et al., 2002; Palma et al., 2016), where nearly half of them are < 25 Myr old (de La Fuente Marcos & de La Fuente Marcos, 2009). And clusters that form a binary are often coeval (Kontizas et al., 1993; Mucciarelli et al., 2012). Such cluster multiplicity could be a natural consequence of the cold ISM structure (Elmegreen & Falgarone, 1996).

It is been known for ~ 50 years that some widely separated clusters lie on essentially the same orbit. For example, the Hyades and Praesepe have similar kinematic properties (Eggen, 1959; Eggen, 1960), and are part of the Hyades supercluster (Brandt & Huang, 2015). It has also long been thought that these clusters are coeval, having formed from a single molecular cloud, or cloud complex (Boesgaard et al., 2013). Both clusters seem to have similar (literature) ages, as shown by isochrone fitting (Perryman et al., 1998; Salaris et al., 2004) and gyrochronology (Douglas et al., 2014; Kovács et al., 2014). Moreover, their metallicities are very similar at around $[\text{Fe}/\text{H}] \sim +0.13$ (Boesgaard et al., 2013).

Gaia data now allow us to address more systematically what the correlation or connection among distinct clusters and associations is in *orbit space*. This could help us to understand the both formation of stars, the large-scale dynamics of GMC cores, and the structure and dynamics of our Galaxy. Conrad et al., 2017 used a sample of known open clusters with 6D (pre-Gaia) phase-space information to group them via a (x, v) -space friends-of-friends algorithm (FoF). They found 14 clusters pairs and a handful of larger groups of clusters. And they showed that those were more FoF groupings than expected at random. Here, we build on this initial result by carrying out a more far-reaching analysis of orbit correlations among star clusters and associations, using action-angle space coordinates and drawing on Gaia EDR3 data (Lindegren et al., 2021).

When going beyond the immediate neighbourhood (say, 50 pc) action–angles (J, θ) coordinates stand out as the canonical choice to describe orbits¹; this is because orbital motions take on a particularly simple function form: actions are conserved, and angles (or, orbital phases) grow linearly with time (J. Binney & Tremaine, 2008). Moreover, actions are adiabatic invariants under slow changes of the gravitational potential, gradual orbit evolution may be described as a diffusion in action space (Sanders & Binney, 2015). Actions and angles are also a powerful coordinate system to find more general substructure in the orbit distribution of our Galaxy, where they have been used to identify systematically groups of stars on similar orbits (e.g., Coronado et al., 2020; Trick et al., 2019), even if they are spatially dispersed.

In this paper, we now set out to address the following question: on orbits in the Galactic disk, selected to contain at least one cluster or association, how much more likely is it to find other clusters and associations, compared to offset adjacent orbits?

Conceptually, we do this as follows: We take the sample of Gaia EDR3 stars within 800 pc of the Sun that have 6D phase-space and hence action-angle coordinates, those that have radial velocities. From those we identify 55 prominent overdensities, distinct groups of stars whose members are exceptionally close to one another in orbit *and* orbital phase, following closely the action-angle approach of Coronado et al., 2020. Among them are of course a number of known clusters (e.g. M67, Praesepe and the Pleiades, but also stream-like groups that are very extended across the sky, such as the Pisces Eridanus or Meingast 1 stream; Meingast et al., 2019). For each of these 55 orbit – phase overdensities, we then consider *all* sample stars in the same orbit patch (i.e. at nearly the same action), irrespective of their phase along the orbit. We then look at their distribution in orbital phase. By construction there must be at least one orbit-phase overdensity, namely that which defined the orbit patch. However, our results reveal that commonly there are multiple other orbit-phase overdensities (clusters or associations) on the same orbit. They line up at different orbit phase along the same orbit, like “pearls on a string”. To put this into context, we perform an analogous analysis for a mock-catalog without clusters (Rybizki et al., 2020) and for an orbit patch that is offset from the actions where the initial action-angle density was detected. The goal is then to quantify statistically any differences between the incidence of such orbit-phase overdensities (pearls) on orbits that are centered on one known pearl, compared to orbits that are not. Those differences turn out to be quite dramatic.

The paper is organised as follows. Section 2.4 presents the data used in this study, from Gaia EDR3 and the Gaia EDR3 mock catalog. Section 2.5 reviews our method for finding groups in action-angle space, and then describes how we quantify overdensities in orbital-phase space at a given orbit patch. In Section 2.6 we first show three case studies in some detail, and then present the statistics of pearls on

¹Orbits may be fully described by actions and angles in axisymmetric potentials. In the presence of non-axisymmetric perturbations, such as spiral arms, actions can still serve as approximate orbit labels (Trick et al., 2017). For volumes around the solar neighbourhood that are larger than ~ 100 pc, actions are preferable over commonly used alternatives such as space motions UVW, which are already only approximate orbit labels in axisymmetric potentials.

orbits known to contain at least one pearl to offset similar disk-like orbits. Finally, we summarize the results in Section 2.7. Additional information and plots can be found in the Appendix.

2.4 DATA

2.4.1 THE GAIA EDR3-RVS SAMPLE

For the analysis of this paper we make use of the full 6D information $(\alpha, \delta, \varpi, \mu_{\alpha*}, \mu_{\delta}, v_r)$ from the Gaia Early third Data Release (EDR3, [Lindegren et al., 2021](#)), with $\mu_{\alpha*} = \mu_{\alpha} \cos \delta$. We denote the EDR3 subsample with useable RVS radial velocity measurements as EDR3-RVS.

Compared to Gaia DR2, EDR3 affords a $\sim 30\%$ and $\sim 100\%$ improvement in parallax precision and proper motions, respectively. For this paper, we use of the photogeometric distances derived by [Bailer-Jones et al., 2021](#). We impose the following quality cuts to this dataset: $ruwe < 1.4$ and formally $\varpi/\sigma_{\varpi} > 3$ ([Fabricius et al., 2021](#)); in practice, $> 99.99\%$ of all stars have $\varpi/\sigma_{\varpi} > 20$, making $\varpi/\sigma_{\varpi} > 20$ the effective sample cut.

We restrict ourselves to stars within $d_{photo-geo} \leq 800$ pc, leaving 2.4 million stars. This distance limit still leaves us with a volume that should contain much sub-structure, while limiting the impact of imprecise distances when calculating actions ([Coronado et al., 2018](#)).

In using the full EDR3-RVS we must forego the use of chemical abundances in stellar clustering analyses, as in [Coronado et al., 2020](#). We do this, because *a)* this sample offers an independent confirmation of the action-angle groups found in [Coronado et al., 2020](#); *b)* it is a vastly larger sample ($\times 10$) than the latter and *c)* with this sample we will also have an all-sky coverage, as we are not limited to a spectroscopic survey. The absence of stellar abundances matters little, as young groups ($< 1 - 2$ Gyrs) in the solar neighborhood have almost exclusively metallicities similar to solar metallicity ([Spina et al., 2017](#)).

2.4.2 A MOCK CATALOG WITH A SMOOTH AND PHASE-MIXED ORBIT DISTRIBUTION

As a null hypothesis for our analysis clustering in orbital phase, we want an analogous data set, but with smooth and fully phase-mixed orbit distribution. We do this by creating a ‘mock sample’ that matches our Gaia EDR3 selection in volume and depth, based on the Gaia early DR3 mock stellar catalog by [Rybizki et al., 2020](#). We query stars with $4 < phot_mean_mag < 13$ and $3500 < t_{eff} < 6900$, as this is the temperature and photometry range for stars in the radial velocity sample ([Katz et al., 2019](#)). We invert the parallaxes that gives us exact model distances in this mock catalog ([Rybizki et al., 2018](#)) and we select stars

within $d \leq 800$ pc. To add realism, the mock catalog [Rybizki et al., 2020](#) includes moving groups and clusters, which we remove for this application by including `WHERE popid! = 11` in the query. We calculate actions and angles from the exact values without adding uncertainties.

2.5 QUANTIFYING CLUMPING IN ACTION-ANGLE SPACE: PEARLS

For the analysis approach sketched in the introduction we need to quantify clumping in both 6D action-angle space, and in 3D angle space, to identify compact stellar overdensities. First in orbit and phase space, then in orbital phase for all stars at a given orbit space patch. To do so, we follow closely the method described in Sec. 3 from [Coronado et al., 2020](#), based on the friends-of-friends approach.

2.5.1 ACTION-ANGLE COMPUTATION

The calculation of actions J and angles θ require both (x, v) phase-space coordinates, and a gravitational potential. By assuming that the Galaxy’s potential is close to an axisymmetric Stäckel potential, one can easily calculate actions and angles for the stars in our sample. We make use of the python package `galpy`, with its implementation of the action estimation algorithm *Stäckel fudge* ([J. Binney, 2012](#)) along with the `MWPotential2014` model. The latter considers a simple axisymmetric Milky Way potential model with a circular velocity of 220 km/s at the solar radius of 8 kpc ([Bovy, 2015](#)). Note that the absolute values of the actions never enter the subsequent analysis, just their differences. So, the choice of an updated circular velocity (e.g., [Eilers et al., 2019](#)) would not significantly alter the results.

For the location and velocity of the Sun within the Galaxy we assume $(X, Y, Z) = (8, 0, 0.025)$ kpc and $(U, V, W)_{\odot} = (11.1, 12.24, 7.25)$ km/s ([Schönrich et al., 2010](#)) to first calculate Galactocentric coordinates and then actions from the observed $(\alpha, \delta, d, v_r, \mu_{\alpha^*}, \mu_{\delta})$ of each star. For our sample, which has been restricted to $d \leq 800$ pc and $\varpi/\sigma_{\varpi} > 20$, the largest contribution to the action uncertainties arise from the radial velocity uncertainties.

2.5.2 FINDING ACTION-ANGLE GROUPS IN GEDR3

Any friends-of-friends approach requires a scalar distance measure between any two stars, which is then compared to the linking length to see whether they are “friends”; this in turn requires a 6D or 3D distance metric. To define such a metric, we follow [Coronado et al., 2020](#) where it is defined via a diagonal metric tensor whose elements are determined by the inverse variance of stars’ positions in each of the coordinates (see Section 3.3. and Eqs. 1–5 from [Coronado et al., 2020](#)). This yields a linking length, $l = \log_{10} \Delta(J, \theta)$ in action-angle space, expressed as the (logarithm of the) fraction of the median 6D separation, $\Delta(J, \theta)$

between sample stars. For any choice of l , we consecutively join all distinct pairs closer than l that have a star in common. This results in a number of associations of ≥ 3 members for any linking length; remaining isolated pairs are discarded from further consideration. This FoF approach is strictly algorithmic for a given l , and in Coronado et al., 2020 we showed that we can identify known clusters, as well as known and new associations, even if they are spread across the entire sky. However, one must choose a linking length l . We explored a range of values for it ($\log_{10} \Delta(J, \theta)$: $l_i = [-1.8, -1.7, -1.6]$), and adopted $\log_{10} \Delta(J, \theta) = -1.7$; for more details on the role of the linking length in choosing such groups, see also Coronado et al., 2020.

For the analysis presented in this paper we selected the richest groups identified for this l , as defined by their minimal number of members required: 55 groups with ≥ 20 members each². These are prominent overdensities in action-angle space, stars on nearly the same orbit at nearly the same orbital phase. It should be noted that the number of these FoF groups here (55) is of course much smaller than the number of known clusters or associations in the extended Solar neighbourhood. This is because we require at least 20 members with Gaia RVS velocities. The bright magnitude limit of RVS in EDR3 and the incompleteness for RVS velocities in crowded fields cause many well-known clusters not to be included. This incompleteness of the EDR3-RVS catalog does not affect the subsequent analysis.

Table 2.1: Subsample of the Identified Member Stars of the 55 FoF Groups

Group ID Number (1)	Gaia EDR3 Source ID Number (2)	J_R (kpc km s ⁻¹) (3)	J_z (kpc km s ⁻¹) (4)	J_ϕ (kpc km s ⁻¹) (5)	θ_R (deg) (6)	θ_z (deg) (7)	θ_ϕ (deg) (8)
1	5339073605139436800	0.3411	0.6026	1702.3392	-150.0429	17.4076	-2.5263
1	5338656477916975104	0.2858	0.5262	1706.7127	-161.5242	17.9502	-2.8299
1	5338656310466146176	0.6125	0.6068	1694.0561	-176.3901	15.9946	-3.0948
1	5338707472109552896	1.4188	0.5311	1675.8665	-171.6802	17.8884	-2.7933
1	5338655722002740352	0.5046	0.4669	1698.2721	-166.5107	18.8533	-2.8405
1	5338706544396496768	0.8148	0.4176	1688.9609	-176.2026	19.2856	-3.1229
1	5338705719763247232	0.6474	0.7042	1693.7971	-167.0601	15.3254	-2.7961
1	5338705509263621632	0.3022	0.6473	1705.4578	-170.3867	15.4545	-2.9893
1	5338653454260022784	0.2951	0.6623	1704.5258	177.8306	14.4023	-3.3224
1	5338653282461326336	0.2057	0.5596	1709.5126	-166.5654	16.6565	-2.9947

(This table is available in machine-readable form.)

Their basic properties ($N_{members}$ along with their mean actions and angles) are listed in Table 2.2, and we illustrate their distribution in Figure 2.1: the top and middle row display the groups in action and angle space. By construction, each group forms a compact clump in both orbit and orbital phase space. The bottom row in Fig. 2.1 illustrates a top-down view of the groups in heliocentric Galactic coordinates

²Full Table 2.1 is available in a machine-readable format in the online Journal.

(left), and the spatial distribution of the groups in right ascension and declination (right). Albeit the groups are compact in action angle space, they are spatially more dispersed and extend over several 10s to 100s degrees on the sky.

Table 2.2: Properties of the 55 Initial Groups

Group ID	$N_{members}$	\overline{J}_R	\overline{J}_z	\overline{J}_ϕ	$\overline{\theta}_R$	$\overline{\theta}_z$	$\overline{\theta}_\phi$
Number	Number	(kpc km s ⁻¹)	(kpc km s ⁻¹)	(kpc km s ⁻¹)	(deg)	(deg)	(deg)
(1)	(2)	(3)	(4)	(5)	(6)	(7)	(8)
1	83	0.58	0.61	1697.71	-158.65	17.09	-2.87
2	50	0.82	0.48	1693.89	55.29	96.38	2.1
3	43	0.87	0.24	1814.44	-17.63	-163.69	-1.55
4	70	0.89	0.19	1819.63	-3.71	-152.27	-1.65
5	48	1.08	0.63	1789.01	-44.87	57.7	2.11
6	21	1.27	0.09	1736.38	117.31	57.45	-3.34
7	42	1.47	0.13	1723.99	140.43	146.58	-4.74
8	47	1.82	0.23	1755.3	99.52	164.6	-4.47
9	60	1.84	1.55	1796.04	38.55	-105.69	-2.12
10	23	2.19	0.63	1795.45	16.54	-118.78	-1.4
11	38	2.22	0.06	1697.96	137.12	59.28	-0.11
12	122	2.22	0.64	1671.73	-138.32	-10.57	1.14
13	51	2.36	0.11	1804.01	38.1	54.67	0.05
14	306	2.38	0.97	1831.74	-7.58	-152.6	0.91
15	23	2.42	0.64	1667.65	-163.39	98.79	2.21
16	638	2.47	0.17	1677.98	-146.81	69.97	1.53
17	39	2.54	0.25	1853.75	-7.8	-133.9	0.31
18	69	2.68	0.77	1814.86	-37.65	53.75	2.51
19	231	2.72	0.23	1681.33	-149.47	5.06	0.43
20	22	2.83	0.34	1792.87	52.49	112.42	-4.19
21	40	3.05	1.2	1793.02	33.97	-88.5	-1.95
22	45	3.11	0.18	1867.79	-26.78	92.58	2.4
23	26	3.13	0.78	1675.05	171.99	61.99	1.55
24	28	3.23	0.12	1719.90	160.13	16.99	-1.78
25	22	3.25	0.342	1659.88	130.46	-34.06	-2.99
26	41	3.33	0.21	1847.26	37.92	71.0	-2.07
27	90	3.49	0.14	1693.18	165.17	70.88	-0.54
28	24	3.61	0.13	1691.95	166.78	-89.21	-0.98
29	91	3.62	0.07	1696.48	162.15	30.3	-0.82
30	86	3.71	1.76	1760.63	122.23	-149.5	-1.99
31	52	3.87	0.41	1645.84	120.84	-61.01	-0.76
32	40	4.02	0.16	1807.60	-12.23	-169.8	0.67
33	32	4.26	0.18	1743.87	137.28	124.42	-5.76
34	23	4.32	0.22	1608.60	140.45	108.67	-1.15
35	81	4.52	0.69	1709.20	136.01	49.35	-3.44

Continued on next page

Table 2.2 – continued from previous page

Group ID	$N_{members}$	$\overline{J_R}$	$\overline{J_z}$	$\overline{J_\phi}$	$\overline{\theta_R}$	$\overline{\theta_z}$	$\overline{\theta_\phi}$
Number	Number	(kpc km/s)	(kpc km/s)	(kpc km/s)	(deg)	(deg)	(deg)
(1)	(2)	(3)	(4)	(5)	(6)	(7)	(8)
36	205	5.01	0.33	1651.03	119.79	-66.5	-2.94
37	24	5.12	0.76	1626.60	166.35	25.84	-0.13
38	34	5.22	0.35	1714.87	103.35	-12.59	-6.81
39	94	6.5	0.27	1635.65	169.57	2.75	-1.44
40	24	6.58	0.31	1635.33	172.72	15.01	-1.0
41	622	6.93	0.35	1651.24	-158.07	-114.25	1.21
42	23	7.13	0.37	1719.75	131.52	16.02	-8.61
43	22	7.8	0.24	1746.80	80.48	-63.0	-7.61
44	52	7.99	0.59	1738.90	103.75	-0.54	-6.97
45	39	10.34	0.11	1914.97	0.69	-62.73	-1.8
46	172	10.62	0.37	1773.90	94.65	152.77	-6.055
47	52	13.54	0.72	1757.58	79.15	-3.51	-5.07
48	226	13.76	0.58	1725.25	99.45	84.57	-9.3
49	260	14.1	0.24	1713.48	96.62	-15.29	-9.13
50	31	14.82	0.22	1831.94	-56.86	-171.03	10.55
51	48	16.29	0.9	1566.01	116.47	-156.84	-9.668
52	30	16.6	0.14	1882.98	-39.53	116.69	6.84
53	84	17.79	1.52	1910.88	-35.13	90.18	7.31
54	20	18.36	0.39	1924.46	-42.01	78.04	6.46
55	118	40.95	2.08	1649.94	-81.42	-137.06	16.55

(This table is available in its entirety in machine-readable form.)

We will now turn to the question whether in the same orbit patch (at the nearly the same action) there are other distinct overdensities in orbital phase.

2.5.3 DEFINING ORBIT PATCHES AROUND AN ACTION-ANGLE OVERDENSITY

For any action-angle group of stars we consider, we want to identify all the stars in the entire sample that are on similar orbits J , irrespective of their phases θ . To this end, we first need to define an “orbit patch” in 3D action space around the mean J of the group we had originally found.

We do this by fitting a 3D ellipsoid to the distribution of actions ($J = J_R, J_z, J_\phi$) of each identified group. These ellipsoids are defined by the centroid and covariance matrix of the members’ J , and describe the extent and orientation of the orbit patch in action space. To include all members, we chose to enlarge this ellipsoid to 3σ when defining the orbit patch. This extent also allows the inclusion of most group members if the distribution in action space is not exactly Gaussian.

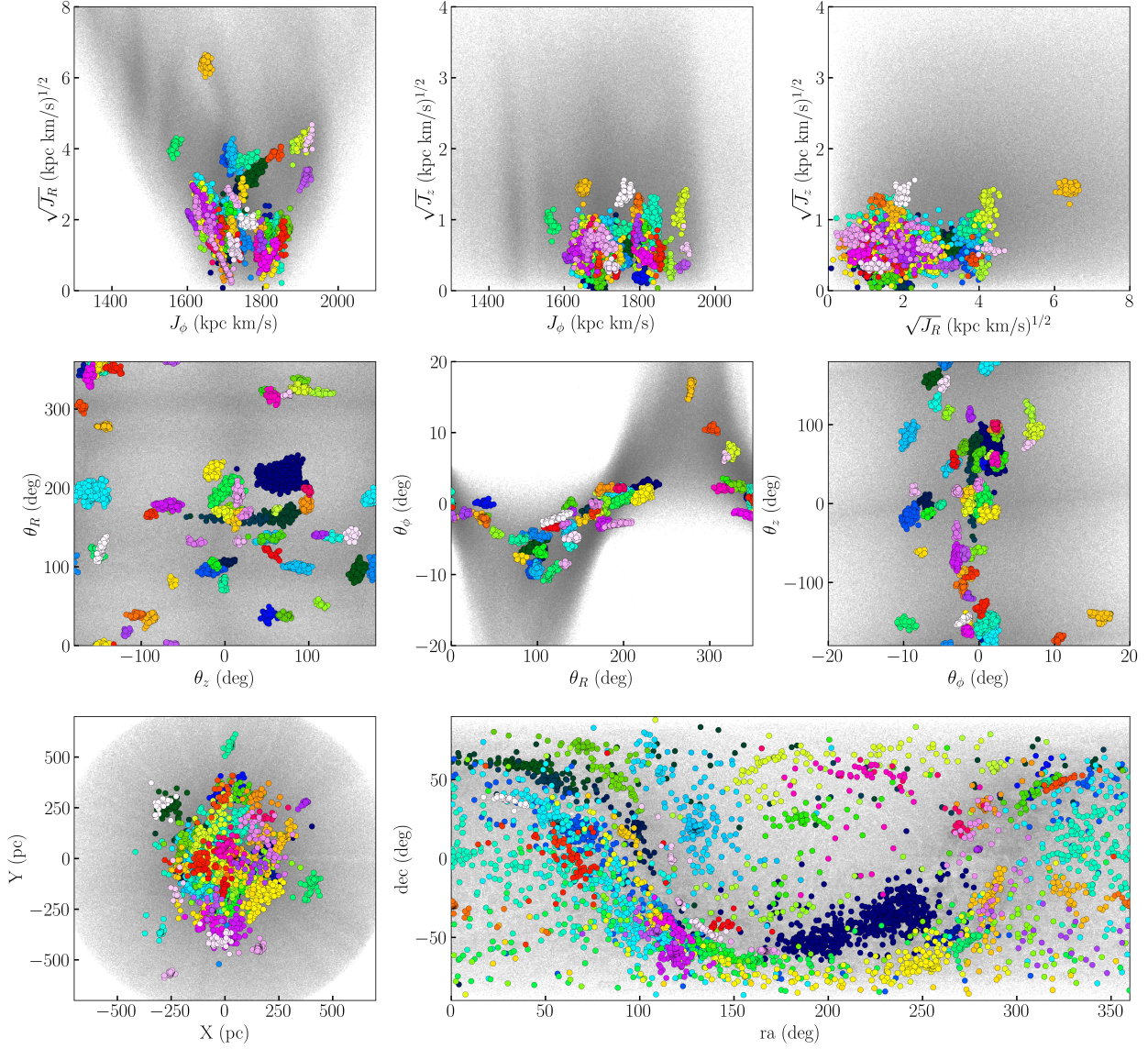


Figure 2.1. The 55 groups in action-angle space with at least 20 members, identified by the FoF algorithm applied to the Gaia 6D data. The different panels show all the members of the (color-coded) 55 groups in different coordinates. Top and middle row: The distribution of the groups in the three projections of action and of angle space; by construction, all groups are tightly clustered in these coordinates. Bottom row: Top-down view of these 55 groups in heliocentric Galactic (X,Y) coordinates (left), and the groups’ on-sky distribution right ascension and declination (right), showing how extended many of them appear in these coordinates.

Throughout the next Sections, we illustrate the various analysis steps using three FoF groups, namely groups 12, 19 and 40 in Table 2.2. These three groups were chosen because they turned out to be typical for the entire sample with respect to the subsequent analysis.

Fig. 2.2 illustrates this approach for one example FoF group with 231 member stars (hereafter *FoF G19*). After having determined J , the covariance matrix and σ we select every star from the Gaia EDR3-RVS whose actions J lie within this patch, as shown by the yellow dots in Fig. 2.2. For *FoF G19* this selection comprises $\sim 12\,700$ stars, whose distribution of J indeed reflect the J of the original action-angle group that we show with grey dots.

2.5.4 THE ANGLE DISTRIBUTION OF STARS WITHIN AN ORBIT PATCH

We now explore the angle (orbital phase) distribution of all stars within an orbit patch. We start by looking at orbit patches centered on various FoF groups, then compare them to "offset" orbit patches.

For the orbit patch centered on *FoF G19* these stars are the yellow dots in the top panel of Fig. 2.2. The three projections of their 3D angle density distribution are illustrated in the lower panels of that same figure, represented by a Gaussian kernel density estimate. By construction, we expect to see at least one clump in angle space, the angles distribution of *FoF G19* with its 231 members, which defined the orbit patch. However, the angle distribution unveils quite a number of distinct compact orbital phase overdensities in the survey volume of 800 pc around us. These overdensities may include star clusters, associations or disk streams, so we need an encompassing terminology for them. And since they are strung along the same orbit at different angles, like pearls on a string, we use the term 'pearls' for all these multiple angle overdensities in the same orbital patch. This generalizes the known notion that several clusters or associations can be found along (nearly) the same orbit.

The lower panels of Fig. 2.2 show the angle distribution of the same orbit patch, but for data drawn from the smooth and phase-mixed Gaia mock catalog described in Section 2.4.2. It reproduces the general features of the real angle distribution: the angle distribution is not uniform, as the finite sample volume – the 800 pc around us – selects particular angles for a given orbit. But the angle distribution drawn from the mock catalog shows no localised clustering, as expected for a smooth phased-mixed distribution. Hence, for a smooth orbital phase distribution (except *FoF G19*) in the top panel we would have expected to see just one distinct orbital-phase overdensity.

We then examine the analogous orbital phase distributions for the orbit patches centered on the remaining 54 FoF groups. Two more examples are shown Figures 2.3 and 2.4 (hereafter *FoF G40* and *FoF G12*, respectively), along with their corresponding orbit patch selections in Figs. 2.10 and 2.11 in the Appendix. These two figures show once again that when selecting all stars in an orbit patch selected for the existence of one action-angle group, the distribution in angle space is highly structured showing: we see many more

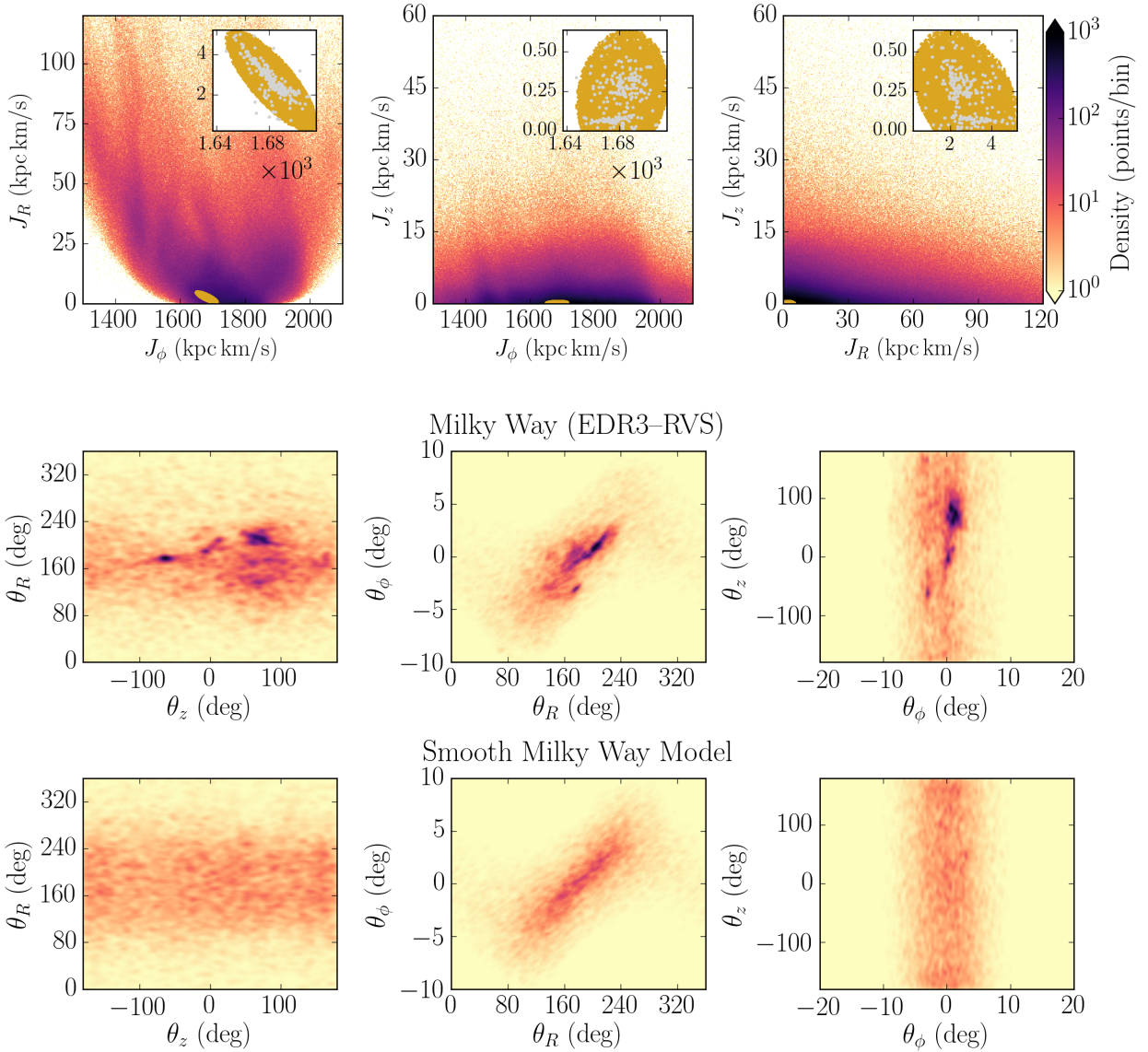


Figure 2.2. Manifestations of “pearls on a string”: the case of the *FoF G19* group. The top row shows three projections of the orbital action distribution of the entire Gaia EDR3-RVS, $p(J) = p(J_R, J_z, J_\phi)$, with the orbit patch of one prominent action-angle overdensity, *FoF G1*, highlighted, which had been defined via a 6D friends-of-friend (FoF) algorithm in orbital phase-space. The actions of the FoF-identified stars are shown as grey points in the inset; the orbit patch as a golden ellipse. In the middle row the color represents the 2D projection of the 3D kernel density estimate of the star-by-star distribution in orbital phase (or angle) $p(\theta_R, \theta_z, \theta_\phi)$ for all stars in the *FoF G19* orbit patch, $J \approx J_{G19}$. The bottom row shows the analogous distribution in the same orbit patch, but with points drawn from a smooth mock catalog. Both angle-distributions contain $\sim 12\,700$ stars, and are based on the same kernel bandwidth. The angle distribution for the observed stars in this *FoF G19* orbit patch is highly structured, with the presence of multiple, distinct orbital-phase overdensities. These are distinct orbit-phase overdensities strung along the nearly the same orbit, like “pearls on a string”. The angles defining the initial *FoF G19* are located at $(\theta_R, \theta_z, \theta_\phi) = (200, 0, 0)$ deg. In stark contrast, the angle distribution drawn from the mock catalog is no-uniform (reflecting spatial selection effects), but smooth.

orbital-phase overdensities than just the one belonging to the selected group. Again, the lower panel in both figures shows the comparison for the same orbit patch to a smooth phased-mixed distribution, highlighting the general features of the data when there is no clustering.

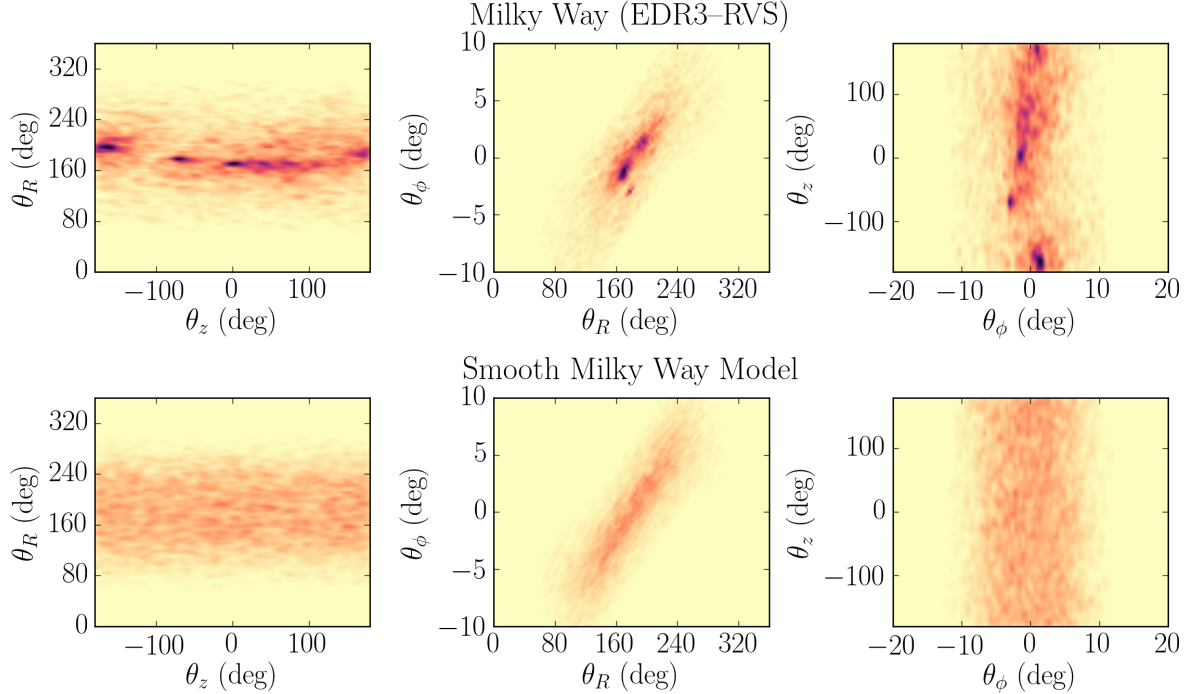


Figure 2.3. Manifestations of "pearls on a string": the case of the *FoF G40* group. This figure panel is analogous to the two bottom rows of Figure 2.2, but here for the *FoF G40* overdensity as a second case study. The top row here shows the projections of the orbital phase (or angle) distribution $p(\theta_R, \theta_z, \theta_\phi)$ (using a kernel density map) for all stars in the *FoF G40* orbit patch, $J \approx J_{G40}$. The bottom row shows the analogous distribution in the same orbit patch, but with points drawn from a smooth mock catalog. Both angle-distributions contain ~ 5700 stars, and are based on the same kernel bandwidth. The angle distribution for the observed stars in this *FoF G40* orbit patch is highly structured, with the presence of multiple, distinct orbital-phase overdensities, which we dub "pearls". The angles defining the initial *FoF G40* is approximately located at $(\theta_R, \theta_z, \theta_\phi) = (170, 5, -1)$ deg, its exact position is shown in the middle panel of Fig. 2.6. Again in contrast, the angle distribution drawn from the mock catalog is no-uniform (reflecting spatial selection effects), but smooth.

THE ORBITAL PHASE DISTRIBUTION IN 'OFFSET' ORBIT PATCHES

There is much structure present in the angle distribution in orbit patches centered on FoF groups. Obviously far more than in the analogous distributions drawn from a smooth mock catalog. We investigate if such rich angle structure is also present in other orbit patches in the real data of the Gaia EDR3-RVS. We do this by choosing offset orbit patches as follows: we start with the orbit patch of one of our 55 FoF group and then shift the patches' center three times the standard deviation σ (in J_R, J_z, J_ϕ). Through

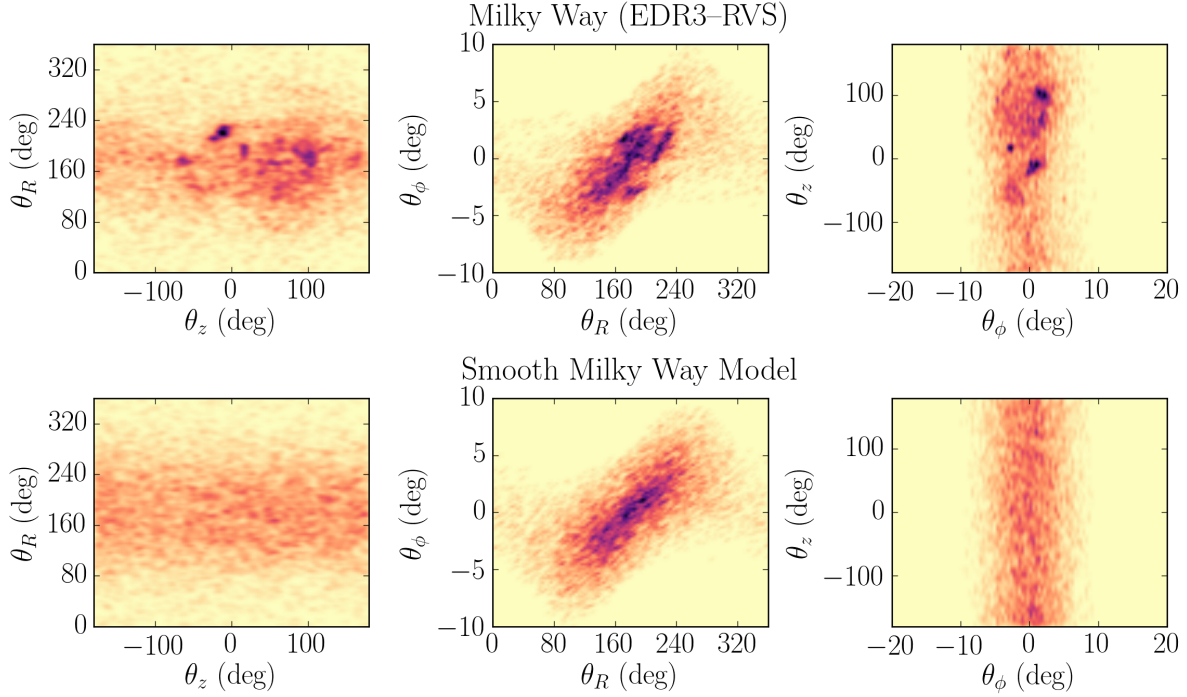


Figure 2.4. Manifestations of ‘pearls on a string’: the case of the *FoF G12* group. This figure panel is analogous to Figure 2.3, but here for the *FoF G12* overdensity as a final case study. The top row here shows a the projected kernel density map of the orbital phase (or angle) distribution $p(\theta_R, \theta_z, \theta_\phi)$ for all stars in the *FoF G12* orbit patch, $J \approx J_{G12}$. The bottom row shows the analogous distribution in the same orbit patch, but with points drawn from a smooth mock catalog. Both angle-distributions contain ~ 7900 stars, and are based on the same kernel bandwidth. The angle distribution for the observed stars in this *FoF G12* orbit patch is highly structured, with the presence of multiple, distinct orbital-phase overdensities, which we dub ‘pearls’. The angles defining the initial *FoF G12* is approximately located at $(\theta_R, \theta_z, \theta_\phi) = (230, -5, 1)$ deg and its exact position is shown in Fig. 2.6. Again in contrast, the angle distribution drawn from the mock catalog is no-uniform (reflecting spatial selection effects), but smooth.

this we pick “offset” orbit patches that are in a comparably dense part of action space, but *not* centered on an FoF group. As two of the actions (J_R and J_z) are positive definite quantities, we take the offsets in the positive action direction. An example of the resulting angle distribution and orbit patch is presented in Fig. 2.5. This orbit patch selection illustrates why we are considering a region well outside the original FoF group (in $J_\phi - J_R$) and even though we are shifting the center 3σ , there is still a small amount of overlap in $J_\phi - J_z$.

In this offset orbit patch of the real data the orbital phase distribution looks noticeably different: it does show substructure, but there are fewer compact overdensities that could be pearls, compared to Figure 2.2. On the other hand, this angle density distribution also differs clearly from that of the mock catalog: we do see one large but very broad overdensity located at approximately $-10 < \theta_z$ (deg) < 150 and $80 < \theta_R$ (deg) < 160 . We should not expect to see a completely smooth distribution as by shifting

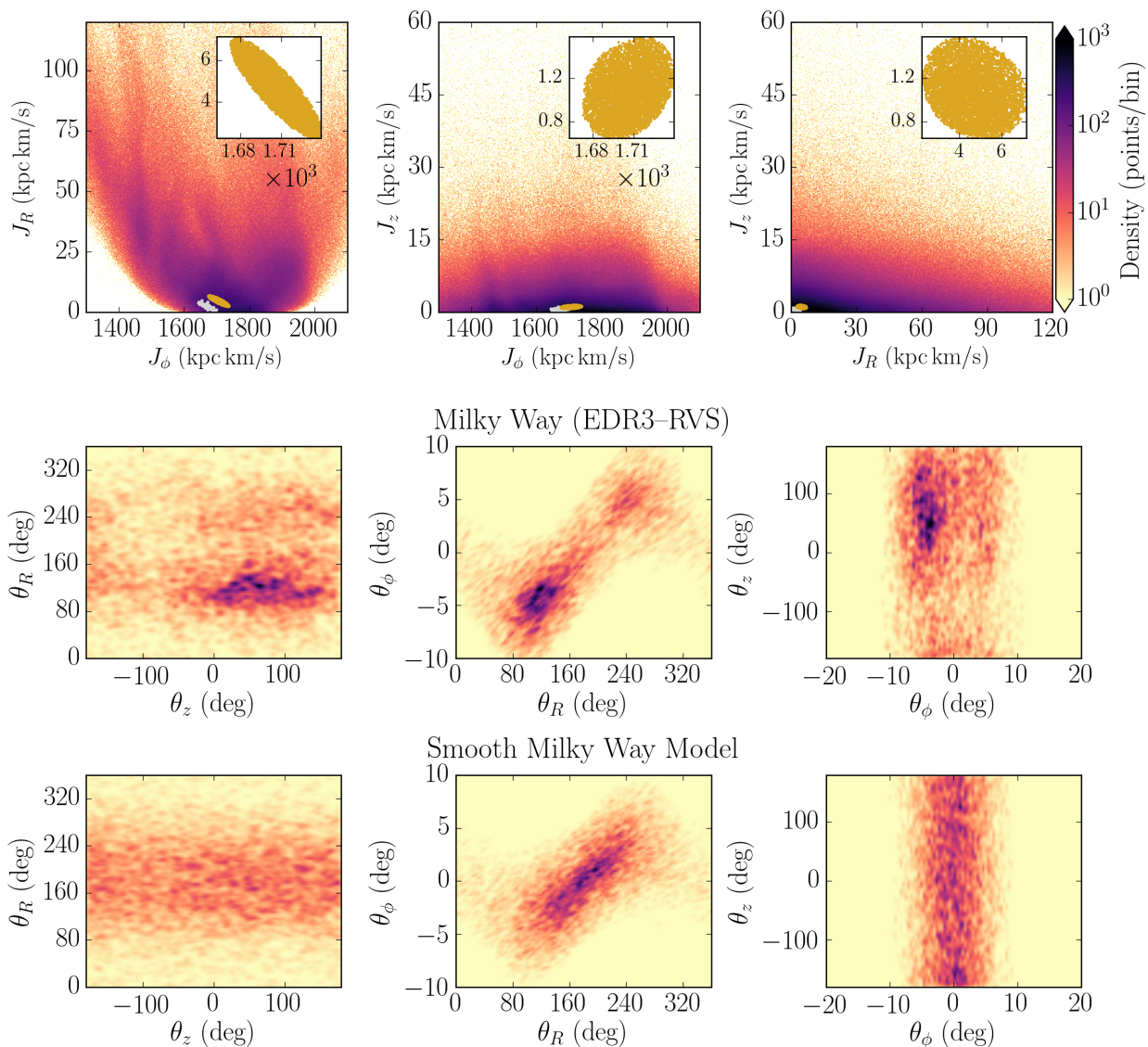


Figure 2.5. The orbital phase (angle) distribution in an “offset” orbit patch. The top row shows three projections of the orbital action distribution of the entire Gaia EDR3-RVS, $p(J) = p(J_R, J_z, J_\phi)$. The orbit patch (golden ellipse) whose angle distribution we illustrate here was chosen to be offset by 3σ from that of *FoFG12* (grey points). The middle row shows the 2D projected kernel density maps of the orbital phase (or angle) distribution $p(\theta_R, \theta_z, \theta_\phi)$ for all stars in an “offset” orbit patch, $J \approx J_{G12}$. The bottom row shows the analogous distribution in the same orbit patch, but with points drawn from a smooth mock catalog. The angle distribution of the Gaia EDR3-RVS data in this offset orbit patch is clearly not as smooth as that of the analogous distribution drawn from the smooth mock catalog. There is some large structure present, e.g. located at $-10 < \theta_z$ (deg) < 150 , $80 < \theta_R$ (deg) < 160 and $-10 < \theta_\phi$ (deg) < 0 . But we do not see multiple compact angle-space overdensities (“pearls”), as seen in the orbit patches centered on the FoF groups (see Figures 2.2, 2.3 and 2.4).

the location of the group we are nevertheless moving the orbit patch into a high density area of the action plot. In contrast to Figs. 2.2, 2.3 and 2.4 the angle distribution of stars within the offset orbit patch does not show any distinct orbital-phase overdensity.

We proceed to apply this method on the remaining 54 groups and show two more example cases for *FoF G19* and *FoF G40* in the Appendix.

2.6 POPULATION PROPERTIES OF PEARLS

2.6.1 PEARLS ON A STRING: THREE CASE STUDIES

We are now in a position to analyze in more detail the angle distribution of stars within a FoF-selected orbital patch, drawing on the three examples shown above. We do this foremost by cross-matching the pearls with a catalog of known clusters and structures by [Cantat-Gaudin and Anders, 2020](#) (hereafter CGA20), which has a list of members for 1481 clusters. We choose this particular catalog because it has a large collection of clusters and it is an updated version of the Gaia DR2 cluster census. It also provides membership determinations for known clusters that had been missed by previous studies and additionally for recently discovered clusters. We further quantify the number of pearls in these orbit patches, and how far apart from one another they are. Finally, we compare all this to simple expectations (the mock catalog and offset orbit patch selection).

FoF G19 AND ITS PROMINENT PEARLS PLATAIS 8 AND IC 2602

We start by taking a closer look at *FoF G19*, shown in Fig. 2.2. Cross-matching the 231 stars that are in *FoF G19* and its orbit patch, we find 46 to also be cluster members in CGA20, mostly members of IC 2602 and Platais 8, as shown in the top panel of Fig. 2.6. These clusters have been identified in the past as OC pairs by [Conrad et al., 2017](#).

It is important to mention that we had already noticed in Fig. 2.2 that (*FoF G19*) appeared bimodal in the vertical action J_z . In fact this reflects these clusters, at $J_z \sim 0$ we find Platais and above that value we identify IC 2602, which got linked by the FoF approach.

Platais 8 is a cluster located at ~ 135 pc similar to the Pleiades ([Soubiran et al., 2018](#)) and IC 2602 is at $d = 150\text{--}170$ pc ([Kharchenko et al., 2005](#)). Both clusters are not only on very similar orbits, but also have very similar ages of ~ 60 Myr and 35 Myr, ($\log(\text{age}) = 7.78$ and 7.545, [Dias et al., 2002](#); [Meingast et al., 2021](#)), respectively.

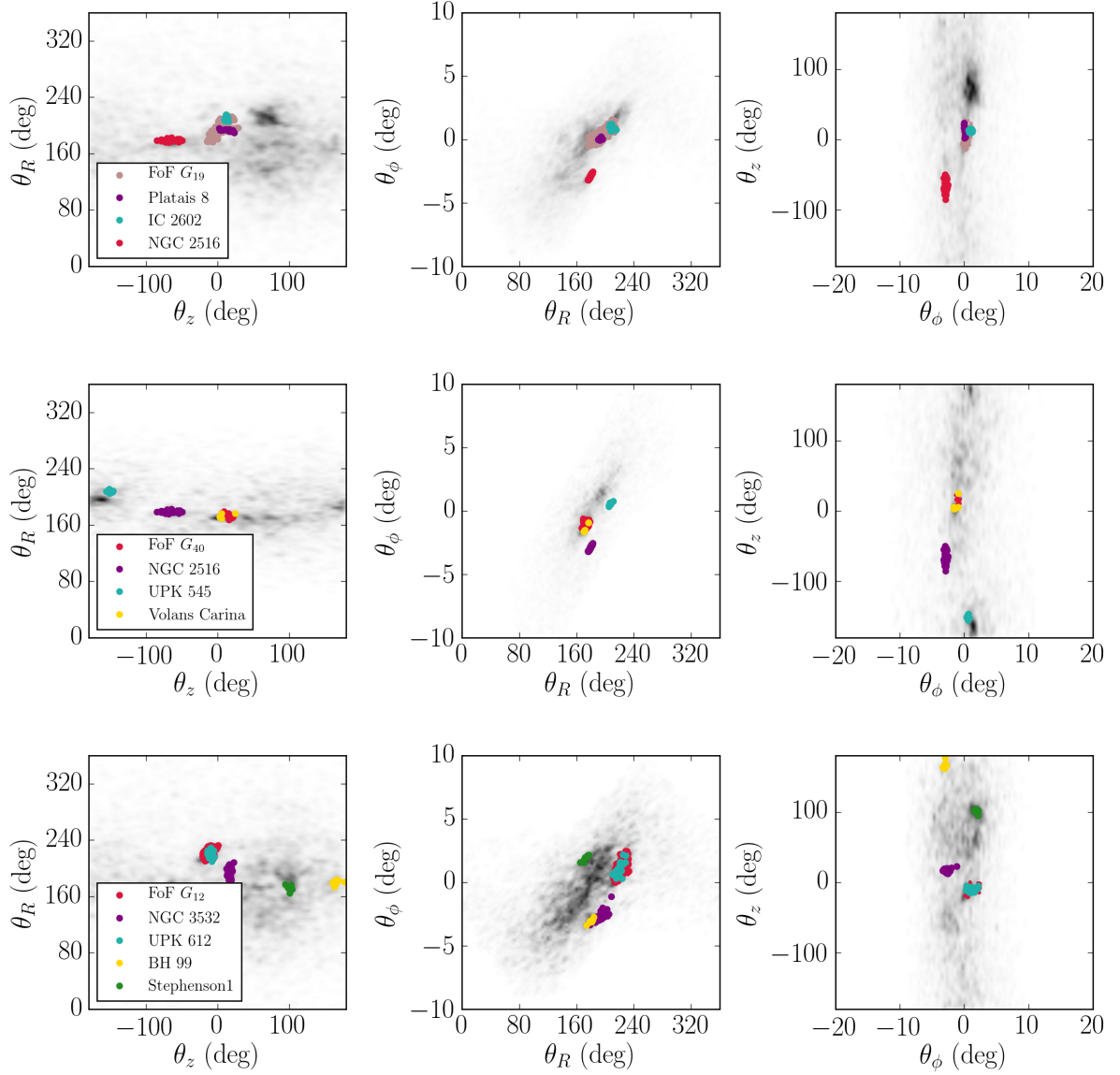


Figure 2.6. Angle distribution of the stars in the *FoF G19*, *FoF G40* and *FoF G12* orbit patches. We cross-match all stars in these FoF orbit patches with members from a catalog of known clusters (CGA20). We highlight these known cluster members with color, along with the members of the orbit-patch defining FoF groups. This Figure illustrates that some pearls are known clusters or associations, others are not. Top panel: *FoF G19* orbit patch. We find that *FoF G19* is comprised of two known clusters: Platais 8 and IC 2602, shown in purple and blue dots, respectively. The figure shows that *FoF G19* has more members, but none of them are part of a known cluster. We also see two prominent orbital phase overdensities or pearls located at $\theta_z - \theta_R (deg) \sim (-60, 160)$ and $(60, 200)$. These are NGC 2516 and UPK 640, respectively. Middle panel: *FoF G40* orbit patch. We find that some of the most prominent pearls are known clusters: NGC 216 and UPK 545. The group that we identify as *FoF G40* is at the same location than the Volans Carina association. Additionally, we find that some of the stars located just below UPK 545, in the pearl located at $\theta_R (deg) \sim 200$ and $\theta_z (deg) < -100$ belongs to the Pleiades. It is remarkable that all of these pearls seem to be aligned along θ_z and all of them have similar ages, between 90–160 Myr. Lower panel: *FoF G12* orbit patch. Once more we find that some of the most prominent pearls are known clusters: NGC 3532, UPK 612, BH 99 and Stephenson 1. The group that we identify as *FoF G12* is at the same location as the UPK 612 cluster.

These two clusters are both members of the patch-defining pearl; but there are two more very prominent pearls in this orbit patch, as Fig. 2.2 shows, and many smaller ones. If we now cross-match the entire sample within this orbit patch to the CGA20 catalog, we find many more known clusters. In particular, NGC 2516 and UPK 640 constitute the two most prominent pearls visible in the angle projection of Fig. 2.2: at $\theta_z - \theta_R$ (deg) $\sim (-60, 160)$ and $(60, 200)$, respectively. NGC 2516 is an intermediate-age open cluster of ~ 251 Myr ($\log(\text{age}) = 8.4$), located at $d \sim 413.8$ pc (Meingast et al., 2021) whereas UPK 640 is among the 207 open star clusters within 1 kpc discovered by Sim et al., 2019 and with an age of 31 Myr ($\log(\text{age}) = 7.5$), located at $d \sim 177$ pc. All of these clusters seem to have very similar young ages, except for NGC 2516 which is slightly older.

FoF G40 AND ITS PROMINENT PEARLS UPK 545 AND NGC 2516

FoF G40 is an orbit patch with particularly many pearls, as seen in Fig. 2.3. Again, we check which of them correspond to known clusters by cross-matching all stars in this orbit patch to the CGA20 catalog. Also in this case, we find a number of known clusters among the pearls of *FoF G40*; among them are UPK 545 and NGC 2516, which are highlighted in the middle panel of Fig. 2.6. For UPK 545 the age estimate is ~ 100 Myr (Sim et al., 2019). Furthermore, we cross-match this orbit patch with the catalog of nearby young associations from Gagné and Faherty, 2018, and we find that the action-angle overdensity that defined the *FoF G40* orbit patch is Volans Carina, a 90 Myr old association (Gagné et al., 2018) (see Fig. 2.6). It is striking that all of these associations are spread widely in θ_z , though they have similar ages. Even though there are many more prominent orbital phase overdensities, we were not able to identify the remaining ones located at $\theta_z > 20$ deg. However, just below UPK 545, at $\theta_R - \theta_z$ (deg) $\sim (200, -150)$, we find some stars that have been attributed to the Pleiades, which is ~ 100 Myr old (Gossage et al., 2018). Except for NGC 2516, the known clusters that we could identify within the *FoF G40* orbit patch all here have similar ages. It is interesting to note that Meingast et al., 2021 provides an age range for many clusters as found in the literature, including NGC 2516. For this particular cluster Meingast et al., 2021 state a most likely age of 251 Myr, with age limits ranging from 63-299 Myr.

FoF G12 AND ITS PROMINENT PEARLS UPK 612 AND NGC 3532

A final example, *FoF G12*, is shown in Fig. 2.4, with its orbit patch presented in Appendix Fig. 2.11. The angle distribution in Fig. 2.4 is very clumpy, with many pearls. As before, we cross-match all sample members in the orbit patch with CGA20 and find numerous matches to known clusters, as shown in the lower panel of Fig. 2.6. The most prominent ones are UPK 612, NGC 3532, BH 99 and Stephenson 1. The UPK 612 cluster stars coincides with the pearl that initially defined *FoF G12*; it is 100 Myr old ($\log(\text{age}) = 8$, Sim et al., 2019). NGC 3532 is 300 Myr old (Fritzewski et al., 2019), Stephenson 1 or δ Lyrae cluster has an age between 30–100 Myr (Bastian, 2019) and cluster BH 99 is 100 Myr old (Carraro & Patat,

2001). Recently, [Kounkel and Covey, 2019](#) suggested that Stephenson 1 is part of a larger and coeval complex with two more clusters (Gaia 8 and ASCC 100). Additionally, [Bastian, 2019](#) discovered a star cluster of 100 members (named β Lyrae) with indications that it belongs to a larger old (extinct) star formation complex, including these two known star clusters. Gaia 8 and ASCC 100 are not part of the CGA20 catalog, therefore from the cross-match we only recover Stephenson 1.

These three case studies that we have shown are typical, with pearls only slightly more abundant than the median case. In most of the cases for our sample of 55 groups we observe very clumpy distributions in angle space, with only a small fraction ($\sim 20\%$) of FoF-defined orbit patches showing only one distinct pearl. It is also striking that in the three examples we present, the pearls (coinciding also with known clusters) tend to be mostly young, where the oldest one is NGC 3532 (300 Myr).

WELL-KNOWN CLUSTERS AS PEARLS

With the framework we just laid out, we can now put the “historical” result into context that the Hyades and Praesepe are two prominent clusters on nearly the same orbit. Indeed both clusters, are among the 55 defining FoF groups (# 48 Praesepe and # 49 Hyades, see Table 2.2). Their respective 3σ orbit patches overlap, but only modestly. Therefore, the Hyades appear as a pearl of Praesepe (though with fewer than 20 pearl members); the converse is not true, but only because fewer than 10 Praesepe members (with Gaia RVS) fall into the Hyades orbital patch.

But analogous situations are true for pairs of other well-known features. As we detail in Appendix 2.8.2, the prominent Coma Berenices cluster (itself FoF group # 18 in Table 2.2) is a pearl of the extensive Pisces-Eridanus or Meingast 1 stream (which is FoF group # 14 in Table 2.2). Again, the converse is not true, owing to the fact that Coma Berenice’s orbit patch is exceptionally compact.

2.6.2 ALGORITHMICALLY IDENTIFYING PEARLS

After this qualitative exposition of the stellar pearls within an orbit patch, we now turn to quantifying this phenomenon. This requires an algorithmic definition of these pearls, and it requires a statistical comparison of the incidence of pearls within an FoF-selected, compared to “offset” orbit patches.

To quantify objectively the number of pearls in an orbit patch, we apply an analogous FoF algorithm to all stars (i.e. stars at all angles) within each of the 55 orbit patches. But of course this FoF analysis is then restricted to the three angle coordinates $p(\theta_R, \theta_z, \theta_\phi | J)$, as laid out in Eqs. 3 and 4 from [Coronado et al., 2020](#). For each orbit patch, we define the linking length as a percentile of the group’s pair-to-pair distance distribution in angle space. After some experimentation with different percentiles, we found that a linking length l_{8th} , which is the 8th percentile of all pairwise angle distances, works best across all groups in picking out “visually” distinct, compact pearls. As before, a pearl must have at least three

member stars by construction. In each orbit patch the statistics of pearls can then be quantified by the number of pearls N_{pearls} with at least K members.

The result of this quantitative pearl definition can be seen in Figs. 2.7 and 2.8, where we illustrate the results of the FoF algorithm to identify the largest orbital-phase overdensities for two examples: the *FoF G40* and *FoF G12* orbit patches, respectively. For *FoF G40*, shown in Fig. 2.7, we find nine rich pearls with ≥ 20 members. For *FoF G12*, shown in Fig. 2.8, we find 13 pearls with ≥ 10 members, where we have chosen a lower member-threshold (as there are only 3 pearls with ≥ 20 members).

These plots illustrate our basic statistic used for all 55 groups: the number of pearls with ≥ 20 and ≥ 10 members. for a given linking length. Subsequently, we calculate the analogous statistic for the 55 corresponding orbit patches in the mock catalog and for the 55 offset orbit patches in the real data. In those latter cases, we use the same linking length l_{gth} as in the FoF-defined orbit patch.

We investigate the “field star” contamination of the pearls by identifying the number of sources in the mock catalog that lie within the angle-space region defined by each pearl. We do this by drawing around each member star of a pearl a sphere in angle-space with the radius given by the corresponding linking length. For each pearl we then count the number of stars in the mock catalog that are located inside any of these spheres. For our total set of 238 pearls, we find that half of them have an estimated contamination $< 25\%$. In other words, pearls typically have a density contrast of 4 over the background in angle-space. About 80% of the pearls have an estimated contamination $< 50\%$.

If group and pearl identification is as powerful as argued here, this significant level of contamination may cause some consternation, as stellar associations have been picked out with lower contamination in the, arguably more intuitive, space of common space velocities. In this context it is important to appreciate that here we are probing a new regime of sparse and dispersed associations (extended over several 100 pc) among stellar associations with relatively few members. Finding them in position or (better) space-velocity space would be all but hopeless for most low-contrast pearls. Here, we show that we can identify them in orbit-space, though with some contamination. Pearls that are clear (low-contamination) stand-outs in velocity space, are also clean in orbit space.

2.6.3 ON-SKY DISTRIBUTION OF PEARLS ON THE SAME STRING

Now that we have properly identified the orbital-phase overdensities we want to explore to which extent they should be characterized as clusters, associations, or streams. And we want to explore how widely they are distributed across the accessible angle-space. We do this by looking at distribution of pearls and pearl members on the sky. The middle left panel of Fig. 2.7 shows the the algorithmically found pearls, the members of each in a distinct color. By construction, they are compact in angle-space, with only the most prominent and largest pearl seemingly split in θ_z , due to the periodicity of the angles. The

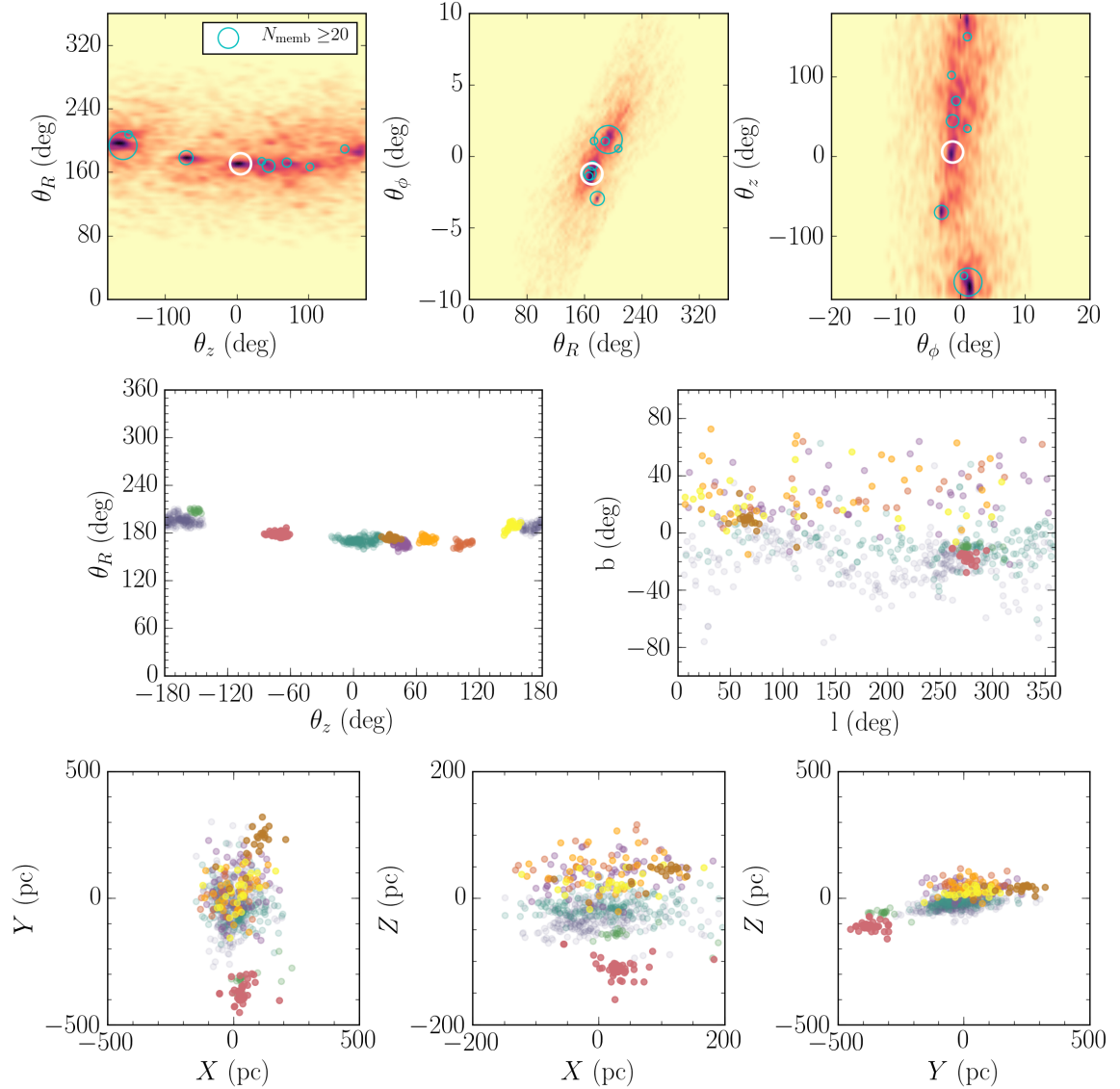


Figure 2.7. Algorithmic identification of the orbital-phase overdensities, i.e. pearls, for the *FoF G40* orbit patch, using a FoF algorithm restricted to 3D angle space, with a linking length that is 8% of the median pair separation. Top panel: We encircle each identified pearl and the size of the circle scales with the size (number of members) of the pearls. Here we show the 9 largest pearls that the FoF finds with a minimum number of members of 20, illustrating the most prominent ones. The location of the original group (*FoF G40*) is illustrated with a white circle. There is a pearl located at $\theta_z - \theta_R (\text{deg}) \sim (150, 180)$ that because of the periodicity of the angles is split in θ_z and it is actually part of the same pearl located at $\theta_z - \theta_R (\text{deg}) \sim (-150, 180)$. This can be seen more clearly in the middle panel, left side. Middle panel left: Angle distribution of these same pearls but now color coded to distinguish them individually. The most prominent and largest pearl (in pale blue dots) is split in θ_z (because of the periodicity of the angles). Middle panel right: Distribution of these pearls in l, b , where we see that some of them (pink and brown for example) are clumped in Galactic longitude and latitude. However, the largest pearls (blue and green) are spread all over the sky. The blue pearl especially extends all over l and seems to oscillate in b . Lower panel: Position in rectangular Galactic coordinates X, Y, Z of these pearls. The Z coordinate is positive pointing towards the North Galactic pole, X increases in the direction of the Galactic center, the Sun is located at $(0, 0, 0)$ and Y is pointing in the direction of rotation of the Galaxy. We notice that some pearls (pink and green) are several hundred parsec away from the rest.

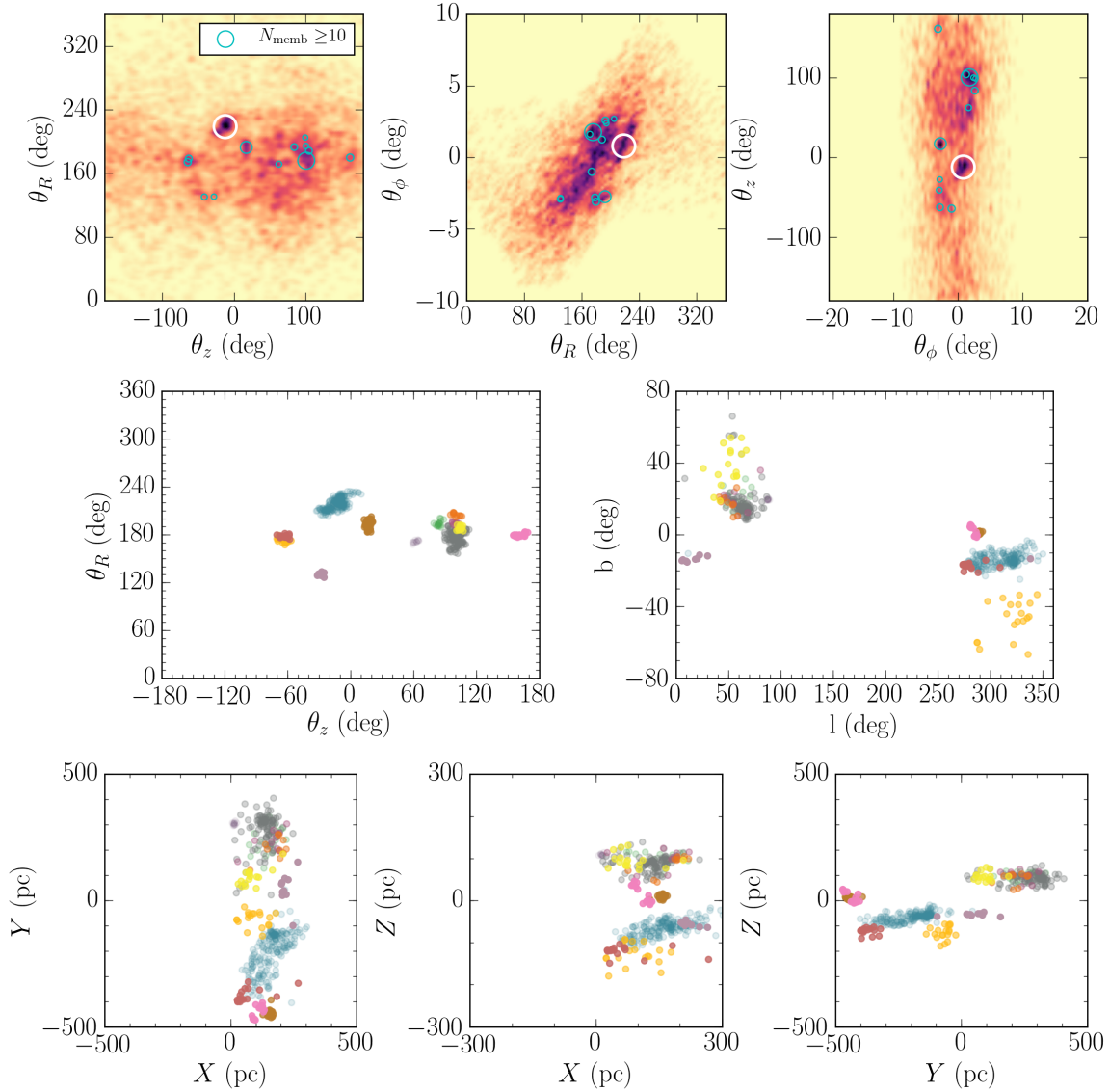


Figure 2.8. Algorithmic identification of the orbital-phase overdensities, i.e. pearls, for the *FoF G12* orbit patch, using a FoF algorithm restricted to 3D angle space, with a linking length that is 8% of the median pair separation. Top panel: We encircle each identified pearl and the size of the circle scales with the size (number of members) of the FoF group. In this case we chose a minimum number of 10 FoF members, yielding 13 pearls. With a minimum of 20 members the FoF still finds 3 pearls. The location of the original group (*FoF G12*) is illustrated with a white circle. Middle panel left: Angle distribution of the same pearls now color coding each one to distinguish them individually. Middle panel right: Distribution of these pearls in l, b , where we see that while some of them (pink and brown) are confined in Galactic longitude and latitude (l, b) there are some that are spread in the sky (for example the yellow and orange pearls). Lower panel: Position in rectangular Galactic coordinates X, Y, Z of the same pearls. The Z coordinate is positive pointing towards the North Galactic pole, X increases in the direction of the Galactic center, the Sun is located at $(0, 0, 0)$ and Y is pointing in the direction of rotation of the Galaxy. We notice that these pearls are separated by several hundred parsec.

distribution of the pearl members on the sky is shown in the middle right panel of Fig. 2.7, in Galactic longitude and latitude (l, b) . Some pearls are tightly clustered in (l, b) , whereas other pearls show very extended distributions: they are spread all across the sky. Interestingly, the largest pearl (in pale blue) does not only extend across all l , but also oscillates up and down in b . This range of on-sky appearances is explained through the lower panel of Fig. 2.7, which shows the position of the pearls in Galactic Cartesian coordinates (X, Y, Z) centered on the Sun. It shows that many pearls span several hundred parsec, an extent comparable to their mutual separation (in X,Y,Z). And of course, pearls that are nearly centered on the Sun’s location, will appear all around us. In Fig. 2.8 we illustrate the sky distribution for *FoF G12*. While some of the pearls in *FoF G12* are spread in (l, b) , but not to the same extent as in Fig. 2.7. This is presumably because the orbit generating *FoF G12* does not cross the Solar locus. Clearly, most pearls are more extended than clusters, or even associations. To which extent we are witnessing associations in the process of dissolution is beyond the scope of the present paper, but will be analyzed in forthcoming work.

2.6.4 THE STATISTICS OF PEARLS

We now have an algorithmic way to quantify the statistics of pearls in each of the 55 orbit patches, $N_{\text{pearls}}(\geq K_{\text{member}})$, using the FoF algorithm in angle space. On this basis we can investigate how common it is to find more than one pearl within an orbit patch. We do this for the 55 FoF-selected orbit patches, and compare this to the statistics of the the mock and the offset orbit patches. We consider two cases, pearls with a minimum of 10 and 20 members. These statistics are illustrated in Fig. 2.9, where we show the fraction of orbit patches among our 55 FoF groups that show at least $N_{\text{pearls}}(\geq 10)$ and $N_{\text{pearls}}(\geq 20)$. In this figure we subtract the ‘patch-defining pearl’ in the FoF-selected orbit patches so we can make an unbiased comparison to the mock and offset orbit patches. We find that 50% of FoF-selected orbit patches have 7 additional pearls of ≥ 10 members, and 20% of these groups show even 25 additional pearls of ≥ 10 members. When considering “rich” pearls of at least 20 members, we find that 50% of the FoF-selected orbit patches show two additional rich pearls, while 20% show eight additional rich pearls. These frequencies of pearls are markedly different from the analogous statistics derived for the orbit patches in the mock catalog and the offset orbit patches: there, we find that $\geq 50\%$ contain no pearls of 20, or even 10 members. For the mock catalog, barely 20% show at least one pearl of ≥ 10 members; while only 7% show one (but not more) pearl of ≥ 20 members. For the offset orbit patches in the real data, the analogous numbers are: 20% show 4 pearls of ≥ 10 members, and two pearls of ≥ 20 members (see Fig. 2.9).

Put differently, the majority of other orbit patches shows no pearls of ≥ 10 members, the vast majority of other orbit patches shows no pearls of ≥ 20 members. By contrast, most orbit patches centered on one known pearl, are rich in other pearls (beyond the one that defined the orbit patch). An interesting subset are the 8 (15%) of FoF orbit patches that only show the defining pearl: orbits with an isolated pearl. We

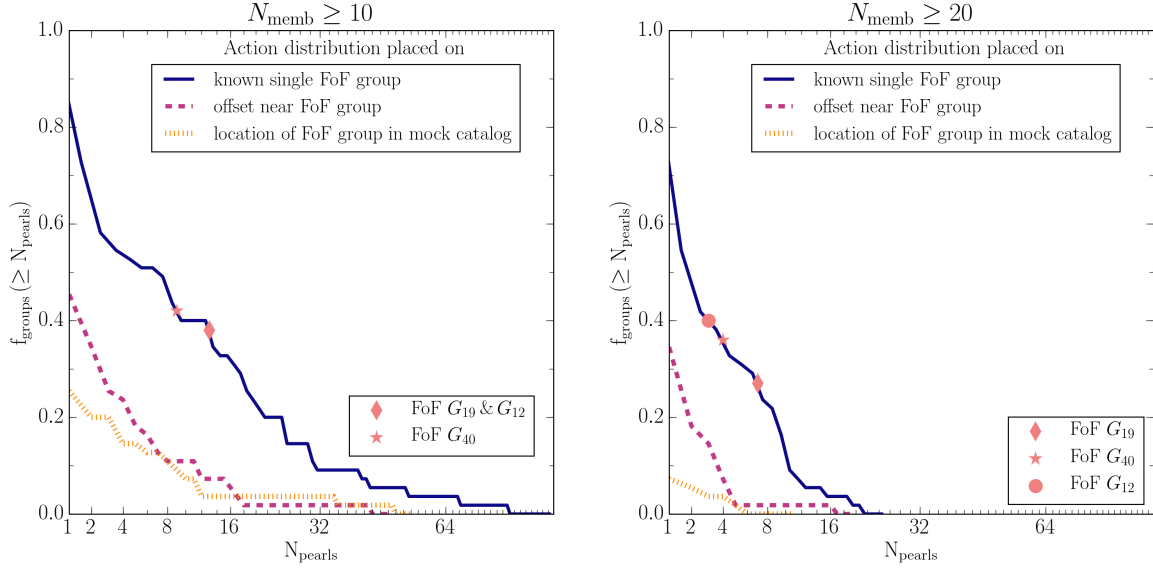


Figure 2.9. Fraction of groups as a function of the number of pearls for the orbit patches in the 55 groups that we find with the FoF algorithm in angle space. We consider two cases: pearls with a minimum number of 10 (left) and 20 members (right). Our orbit patch selection for the FoF groups is shown with a blue solid line, the mock orbit patch with a purple dashed line and the offset orbit patch with an orange dotted line. The ‘patch-defining pearl’ in the known single FoF group (blue solid line) is subtracted in this figure. Left: With the orbit patch selection for the FoF groups, all of them have at least one pearl and 0.7 have 3 pearls. For the offset orbit patch this fraction is ~ 0.4 and for the mock case it drops to ~ 0.2 of the groups having one pearl. Less than 0.1 of the groups in both the offset and mock orbit patch have 5 pearls, whereas for the known FoF groups this fraction is almost 0.6. Right: In this case we find almost one pearl (~ 0.95) in all of the known FoF groups orbit-patch patches. For the offset orbit patches this fraction is ~ 0.38 and for the mock case this drops to almost 0. For the known FoF groups orbit-patch patches ~ 0.6 of them have 2 pearls. Most of the groups that we find have others on similar orbits.

show an example in Appendix 2.8.4). There the only pearl is Platais 3, a known cluster with a (literature) age of nearly 1 Gyr ($\log(\text{age})=8.92$, Yen et al., 2018). Similarly, a number of the other isolated pearls are known clusters of ages well above $t_{\text{dyn}} \sim 200$ Myrs. Qualitatively it is unsurprising that clusters that are “old” and bound are more likely found without discernable birth cousins in pearls on the same orbit. Furthermore, older FoF groups must be particularly compact in action space, if they are to remain also compact in angle space. And of course more compact orbit patches will contain far fewer other stars, boosting their chances to appear as isolated pearls. We will pursue the question of consistent age-dating of pearls, and of its implication in a forthcoming paper.

Fig. 2.9 also puts our three case studies into context: in both the cumulative statistic for pearls of 10 and of 20 members they lie around the 40th percentile: they are typical, with pearls only a little bit more abundant than the median case.

We now address the question of whether the set of all pearls in all orbit patches are actually disjoint sets of stars. Per construction, a star member of a pearl in one orbit patch can also be part of a pearl in another orbit patch. This is because the orbit patches in this context are three times larger than the standard deviation in orbital actions in the FoF group that spawned this orbit patch. To explore this, we have

asked of all stars that are members of at least one pearl, whether they are also members in one or more additional pearls in other patches. We find that for pearl members stars the large majority of them ($\sim 75\%$) are members of only one pearl. However, about 20% are members of 2 or 3 pearls, and about 5% are members of 4 or more pearls. This is true both when considering pearls with at least 10 and at least 20 members.

This 25% overlap among pearls stars belonging to different groups appears to be another manifestation of how clustered orbit-space is. Technically, our 55 FoF groups are – by construction – indeed fully distinct and disjoint. Yet, their surrounding $3\text{-}\sigma$ action-angle space ellipsoids, which we use to search for pearls, do indeed start to overlap among groups in about 25% of cases. As the total fraction of the pertinent action-angle space that is filled by the initial 55 FoF groups is small, this shows how clustered orbit space appears to be. This clustering, presumably a reflection of the structured ISM, deserves further quantification in future work.

2.7 SUMMARY AND DISCUSSION

In this paper we provide the first quantification of the correlation of recent Galactic disk star formation in orbit and orbital phase space. The goal was to provide an empirical basis for understanding how the large-scale filamentary structure of the cold ISM (Alves et al., 2020) might be reflected in the orbit distribution of the stars that have formed from it (within $t_{age} \leq t_{dyn}(R_{\odot}) \approx 200$ Myrs). We were particularly interested in the large-scale ($\gtrsim 100$ pc) correlations among distinct clusters, associations or other aggregates of presumably young stars.

The work presented here builds on earlier quantifications of large-scale correlations among such clusters in configuration-space (x, v) , e.g. by Conrad et al., 2017 and Kounkel and Covey, 2019. And it builds on the longstanding anecdotal evidence that different clusters, widely separated in the sky, can be on very similar orbits (e.g. Eggen, 1959).

There are three new elements we could bring to the issue here: First, the use of action-angle coordinates (J, θ) , which are the canonical coordinates for orbit space. In particular, they offer a neat separation of the 6D coordinates in orbit (action), and orbital phase (angle); and it turns out that $p(\theta | J)$, the distribution of angles in a given orbit-patch is a fruitful way to look at the problem at hand. Second, we do not rely on traditional catalogs of distinct clusters, associations, etc, but find overdensities of stars in actions-angle space algorithmically using a friend-of-friends algorithm (FoF) in (J, θ) -space applied to all stars with radial velocities within Gaia EDR3 and distances < 800 pc, as laid out in our preceding work (Coronado et al., 2020). Third, the Gaia EDR3 data with radial velocities (EDR3-RVS) is a superb data set to explore the 6D stellar phase-space distribution in the 1 kpc around the Sun.

Following [Coronado et al., 2020](#) we start by finding the 55 most prominent clusterings of EDR3-RVS member stars in action angle space $(J, \theta)_{i=1,55}$ using a 6D FoF algorithm. Each of these defines an “orbit patch”, and ellipsoid in action space around J_i . We then consider *all* stars within this orbit patch, i.e. with actions $\approx J_i$, and look at their angle distribution, $p(\theta | J_i)$. By construction (via a 6D overdensity), the distribution $p(\theta | J_i)$ must have at least one compact overdensity in angle space. However, within most of these orbit patches we find many more compact angle (or orbital-phase) overdensities; and we quantify these angle-space overdensities by a 3D FoF algorithm (with a linking length of 8% of the sample median separation). We find that these 55 orbit patches typically contain 8 more overdensities with ≥ 10 EDR3-RVS members; they have 20 more angle-space overdensities in 20% of the cases, strung along the same orbit but at different orbital phases. For nomenclature convenience, we dub these angle-space overdensities ‘pearls’. Detailed investigation of these pearls among three of these orbit patches reveals that these pearls often are well-known clusters or associations; but often, they are previously unrecognized associations, spread out in configuration-space, yet compact in action-angle space.

In the three sample FoF groups where a few pearls coincide with clusters of robust (literature) ages, these tend to be young $t_{age} < 200 \sim \text{Myrs}$. Clearly, a systematic approach to determining ages of pearls, and checking whether they are mono-age populations, is crucial to put these findings into a broader context. For instance, it could clarify whether really most of them are young ($< \text{few } 100 \text{ Myrs}$) and dispersing but not yet phase-mixed. In at least one case (see Appendix B) we could show with literature data that not all pearls on the same string will be approximately co-eval; this means that being pearls on the same string does not necessarily or always imply any form of ‘common birth origin’. Unfortunately, our 6D sample only contains stars over the very limited range on T_{eff} for which RVS information is available ([Rybizki et al., 2021](#)); color magnitude diagrams for those stars exclude the turn-off region of young populations and do not permit meaningful age constraints. We therefore defer a comprehensive age estimate of all pearls to a forth-coming paper.

We then compare the incidence of such pearls found in the 55 orbit patches centered on one prominent pearl with their incidence in two alternate control sets of orbit patches. One set of orbit patches centered on the same $J_{i=1,55}$, but with the member stars drawn from a smooth mock catalog ([Rybizki et al., 2018](#)). Another one, with orbit patches that are offset from the actual $J_{i=1,55}$, and with the members drawn from the actual EDR3-RVS. In both cases, we find a dramatically lower incidence of pearls.

This implies that recent star-formation in the Galactic disk is strongly clustered towards a modest subset of particular orbits, presumably the orbits on which the cold ISM was moving when giving birth to these stars. This opens up new avenues of studying the dynamics of the ISM, as it is generally impossible to get 6D phase-space coordinates for it, except for the relatively sparse set of masers ([Reid et al., 2014](#)). To understand the orbits and positions on which stars are actually born, it would also be good to calculate their orbits back towards their birth position. This requires testing whether pearls are mono-age populations, and determining their ages systematically. In this paper, we have only shown that pearls that are

well-studied clusters tend to be young ($\lesssim 100$ Myrs). A more systematic exposition of this issue will be part of a forthcoming paper. Then we should be in a position to see whether the orbits on which stars are preferentially born are a stochastic sub-sample of disk-like orbits, or are discernible “special” in the overall disk dynamics relating, for example, to orbit resonances.

But for now, we could quantify the extent to which young stars are clustered in orbit space: there is a subset on which distinct aggregates of young stars are common, albeit at widely separate phases. Indeed, stars in the Galactic disk seem to form like pearls on a set of strings.

ACKNOWLEDGEMENTS

We thank the anonymous referee for their exceptionally thorough and constructive report that greatly improved the paper. We thank the MPIA MW group and Greg Green for providing very useful comments. J.C. acknowledges support from the International Max Planck Research School for Astronomy and Cosmic Physics at Heidelberg University (IMPRS-HD). H.W.R. received support from the European Research Council under the European Union’s Seventh Framework Programme (FP 7) ERC Grant Agreement n. [321035]. This work has made use of data from the European Space Agency (ESA) mission Gaia³, processed by the Gaia Data Processing and Analysis Consortium (DPAC)⁴. Funding for the DPAC has been provided by national institutions, in particular the institutions participating in the Gaia Multilateral Agreement.

2.8 APPENDIX

2.8.1 3D ACTION ELLIPSOID CONTINUED

Here we show the orbit patches for the remaining two example groups: *FoFG40* and *FoFG12*. We find 24 members for *FoFG40* and 122 for *FoFG12*. The corresponding orbit patches are presented in Figs. 2.10 and 2.11.

2.8.2 CASE STUDY: COMA BERENICES AS PEARL OF PISCES ERIDANUS

Another interesting case study is the Pisces Eridanus or Meingast 1 stream. We identify one of our FoF groups as the stream by inspecting its location in position (α, δ) and then cross-matching its stars with the candidates and members of this stream presented in Curtis et al., 2019. Pisces Eridanus is a recently

³<http://www.cosmos.esa.int/gaia>

⁴<http://www.cosmos.esa.int/web/gaia/dpac/consortium>

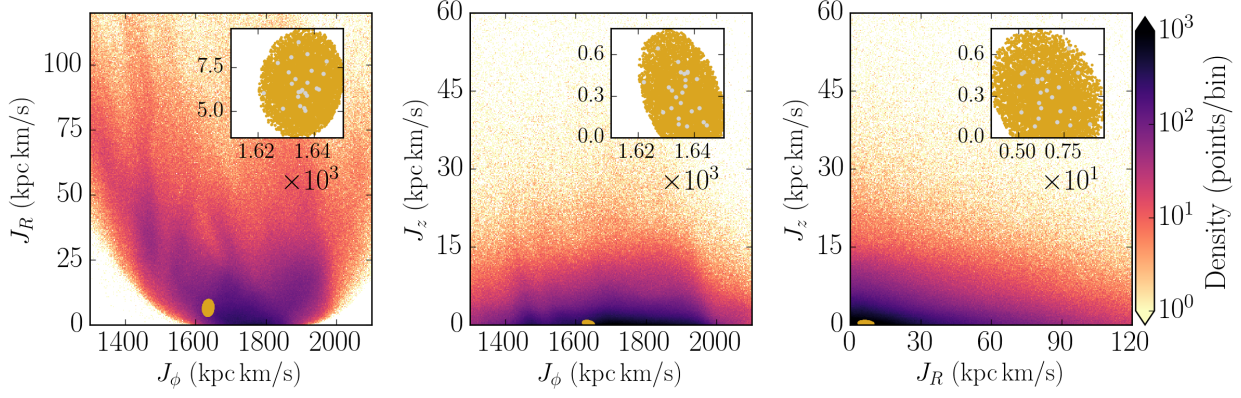


Figure 2.10. Action distribution (J_R , J_z , J_ϕ) for the entire GEDR3-RVS selection and the *FoF G40* orbit patch. With yellow dots we show the orbit patch selection and in grey dots we show the group members. The upper right inset in each panel shows a zoom-in into the orbit patch to highlight clearly its size and also how well this method encloses the group.

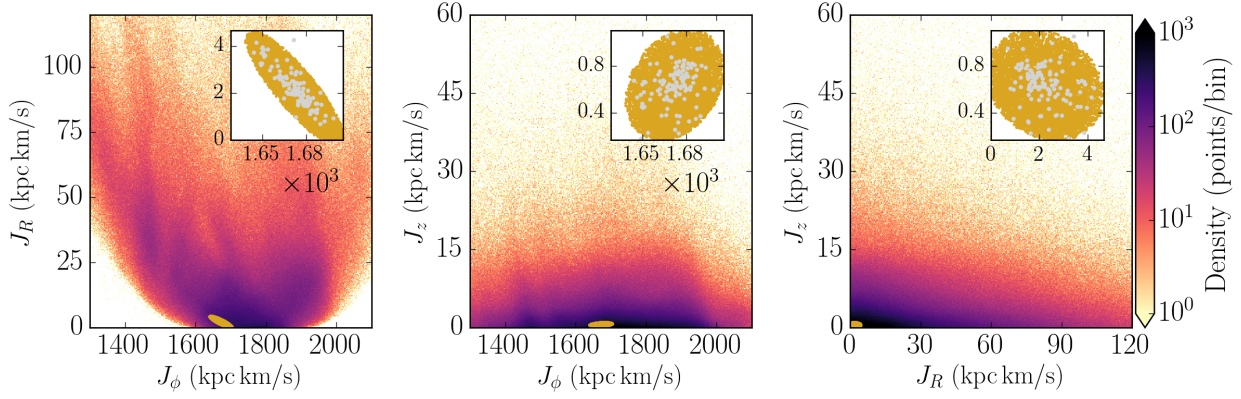


Figure 2.11. Action distribution (J_R , J_z , J_ϕ) for the entire GEDR3-RVS selection and the *FoF G12* orbit patch. With yellow dots we show the orbit patch selection and in grey dots we show the group members. The upper right inset in each panel shows a zoom-in into the orbit patch to highlight clearly its size and also how well this method encloses the group.

discovered stream, and it has been investigated only by a few studies, for example: [Meingast et al., 2019](#), [Curtis et al., 2019](#) and more recently by [Hawkins et al., 2020](#); [Ratzenböck et al., 2020](#). [Meingast et al., 2019](#) first discovered the stream, and besides a detailed kinematic study, they also estimated an age of ~ 1 Gyr through isochrone fitting, using the PARSEC isochrone library ([Bressan et al., 2012](#)). However, later studies ([Curtis et al., 2019](#); [Ratzenböck et al., 2020](#)) concluded that the stream has a similar age as the Pleiades, ≈ 120 Myr.

In the top panel of Fig. 2.12 we show the corresponding orbit patch for this stream and also its angle distribution in the middle and lower panels. This stream appears accompanied by a second pearl, which we identify as Coma Berenices or Melotte 111 that is in the vicinity of the Sun with an estimated age of ~ 700 Myr ([Fürnkranz et al., 2019](#); [Tang et al., 2019](#)). The location of these pearls is clearly visible in the θ_z - θ_R angle projection, with Pisces Eridanus located at θ_ϕ (deg) ~ 0 and θ_z (deg) ~ -150 . Coma Berenices

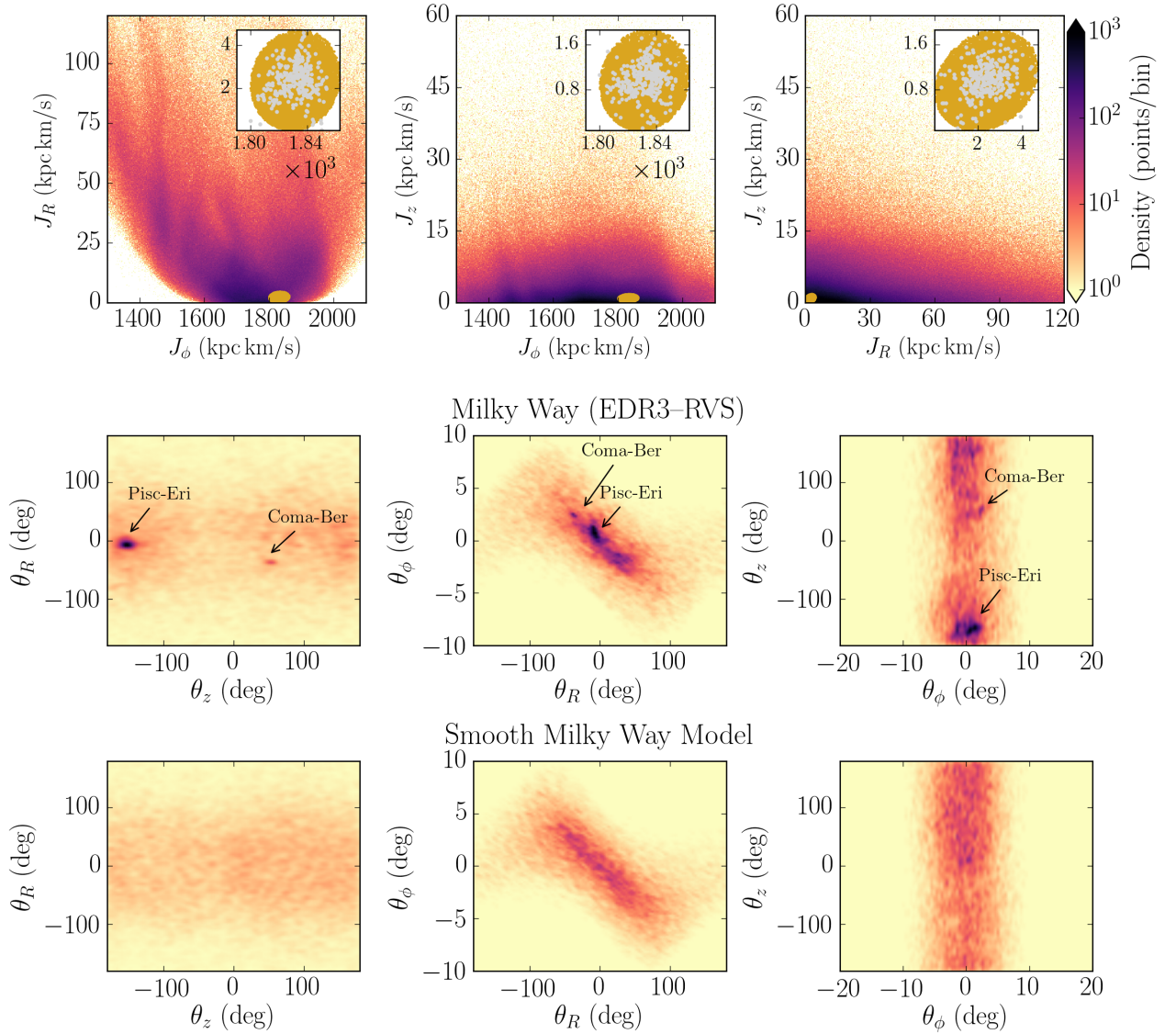


Figure 2.12. Orbit patch and angle distribution for the Pisces Eridanus or Meingast 1 stream. The orbit patch contains $\sim 17\,000$ stars whereas our FoF selection of the Pisces Eridanus stream has 300 stars. The group member's are shown with grey dots. **Middle and lower panels:** The angle distribution is less clumpy than the previous example cases we have discussed throughout this paper. However, at a first glance we can already identify two clusters: the most prominent one (Pisces Eridanus) located at $(\theta_R, \theta_\phi, \theta_z) = (0, 0, -150)$ deg, and the second one is more diffuse but still clearly visible at $(\theta_R, \theta_\phi, \theta_z) = (-30, 2, 50)$ deg, which is Coma Berenices. In the θ_ϕ - θ_z angle projection we notice another pearl next to Pisces Eridanus, located at $\theta_\phi \sim -1$ deg. Stars in this pearl belong to the Collinder 135 and also UBC 7 cluster. Distribution in angle space for the same orbit patch as shown above, but for a smooth-phase mixed distribution. This mock catalog shows the general features of the dataset, but with no clumping.

is located at θ_ϕ (deg) ~ 2 and θ_z (deg) ~ 50 . On a closer inspection to the θ_ϕ - θ_z angle projection we notice another pearl next to Pisces Eridanus. The two appear split in θ_ϕ (deg) ~ 0 , with the secondary pearl located at θ_ϕ (deg) ~ -1 . We find that stars in this third pearl belong to the cluster Collinder 135 and also UBC 7. The latter have been identified as a physical pair of clusters by [Kovaleva et al., 2020](#) with an age between 40–50 Myr.

This case study illustrates an important point that will deserve follow-up: not all pearls on the same string will be approximately co-eval, as evidenced by the large age differences of the pearls here. This means that being pearls on the same string does not necessarily imply any form of "common birth origin".

2.8.3 OFFSET ORBIT PATCH CONTINUED

Here we show two more examples of the offset orbit patch method already described in Section 2.5.4, for *FoF G19* and *FoF G40* in Figs. 2.13 and 2.14, respectively. Similar to the example for the *FoF G12* orbit patch, we observe some orbital-phase overdensities present in both cases (mostly in Fig. 2.13), but nothing as structured as what we see in the original groups. Also we still expect to see some overdensities as we are selecting our offset orbit patch in very dense areas.

2.8.4 ISOLATED GROUPS

In this work we have shown three example cases where the distribution in angle-space is highly structured, with many orbital phase overdensities or pearls. We observe that this is typical for many of the 55 groups where most of them have two or more cluster companions in the angle distribution. However we do have some cases that are isolated ($\sim 15\%$). In Fig. 2.15 we show one example of the distribution in angle space for one of our isolated cases. And this isolated pearl is a known cluster: Platais 3. It has a presumed age of ~ 830 Myr ($\log(\text{age})=8.92$, [Yen et al., 2018](#)), considerably older than many of the pearls discussed so far. A systematic determination of ages for the groups will be presented in a forthcoming paper. The fact that older pearls are more likely to be isolated could be the result of a low survival rate (dispersal) of most clusters and associations within a few 100 Myrs, but it could also show that groups considerably move away from their birth orbits within a few 100 Myrs, as expected from radial migration ([Frankel et al., 2018](#)).

2.8.5 PROPERTIES AND MEMBERSHIP OF THE INITIAL 55 GROUPS

In this section we present a subsample of the identified member stars of the 55 groups in Table 2.1 (the machine-readable format is available in the online Journal) and the properties and membership of the initial 55 groups in Table 2.2.

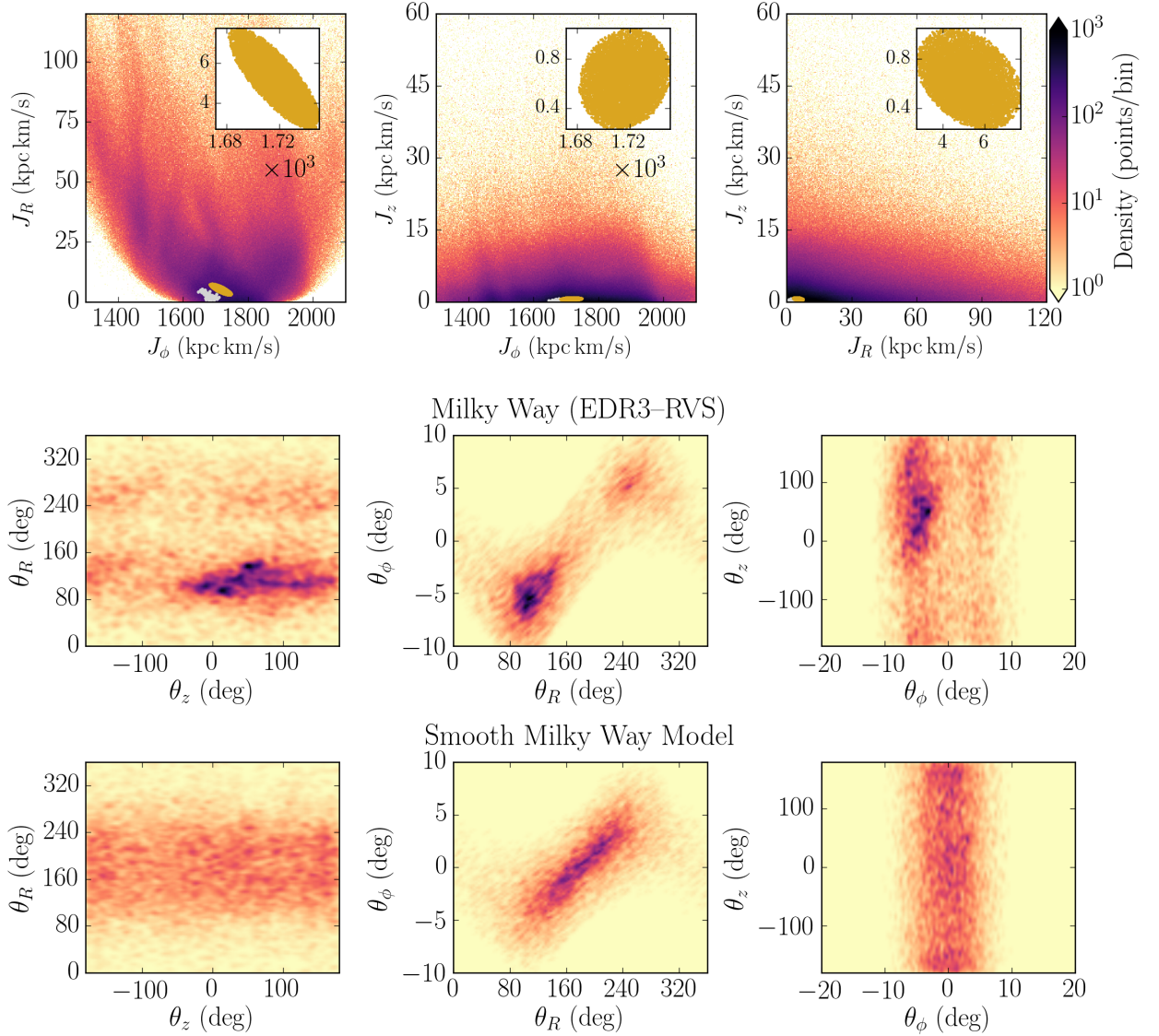


Figure 2.13. Offset orbit patch selection. Here we show the *FoF G19* orbit patch, but we shift its center 3σ (in J_R, J_z, J_ϕ). Additionally we show the 2D projected (Gaussian) kernel density maps of the angle distribution ($\theta_R, \theta_z, \theta_\phi$) of the stars enclosed by the offset orbit patch. For the kernel width we selected the same size bandwidth for both the data and the mock catalog. Top panel: With yellow dots we show the new orbit patch location and in grey dots we show the original FoF group. The upper right inset in each panel shows a zoom-in into the orbit patch. Middle panel: We do see some overdensities and some sort of structure, however it does not resemble what we have shown in Figs. 2.2, 2.3 and 2.4. We see that the distribution is not completely smooth. There is some large structure present approximately at $0 < \theta_z$ (deg) < 100 and $80 < \theta_R$ (deg) < 160 , which is expected as this offset orbit patch selection still falls in a high density region in action space. Lower panel: Distribution in angle space for the same orbit patch as shown above, but for a smooth-phase mixed distribution. This mock catalog shows the general features of the dataset, but with no clumping.

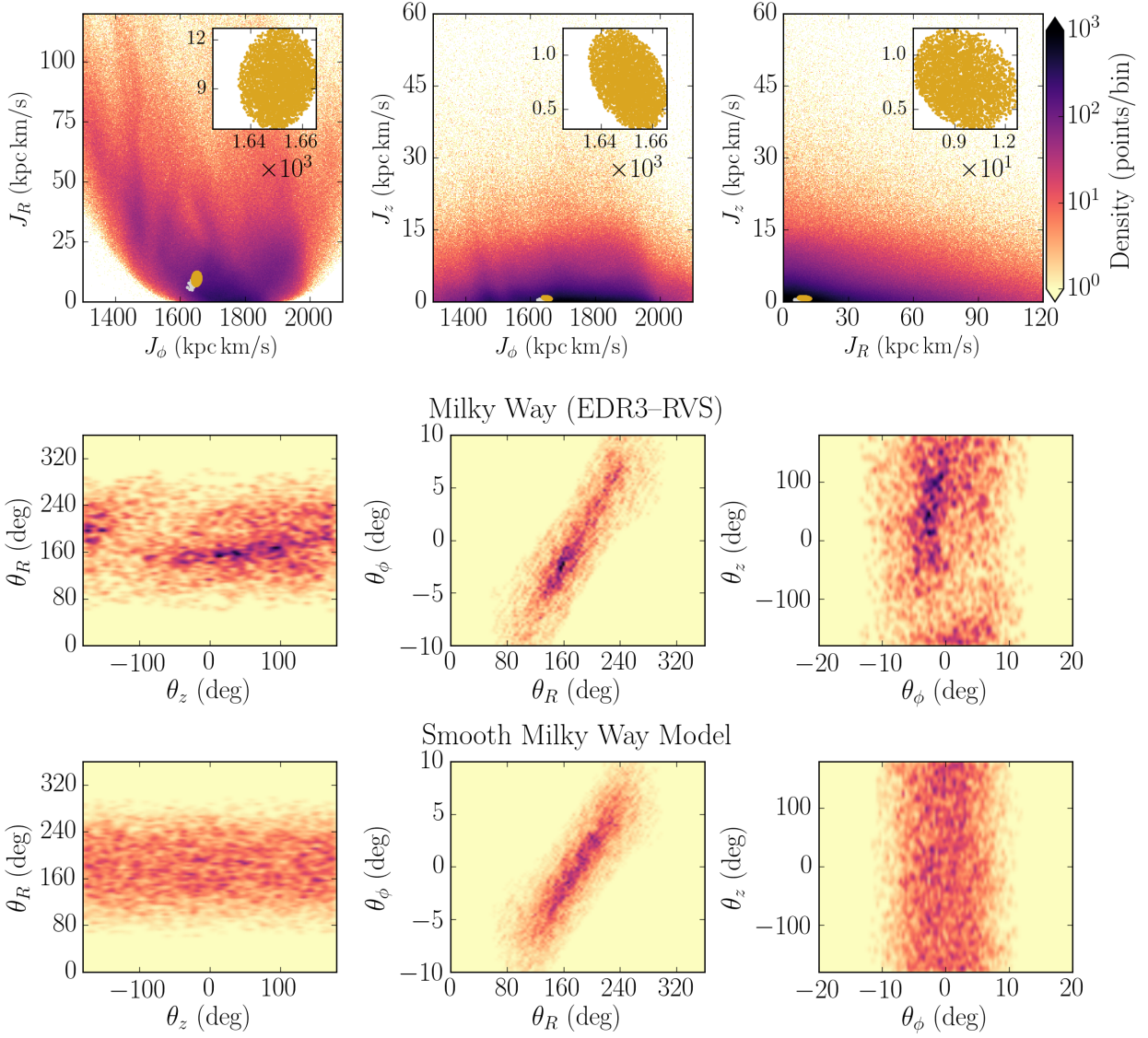


Figure 2.14. Offset orbit patch selection. Here we show the *FoF G40* orbit patch, but we shift its center 3σ (in J_R, J_z, J_ϕ). Additionally we show the 2D projected kernel density maps of the angle distribution ($\theta_R, \theta_z, \theta_\phi$) of the stars enclosed by the offset orbit patch. For the kernel we selected the same size bandwidth for both the data and the mock catalog. Top panel: With yellow dots we show the new orbit patch location and in grey dots we show the original FoF group. The upper right inset in each panel shows a zoom-in into the orbit patch. Middle panel: We do see some overdensities and some sort of structure, however it does not resemble what we have shown in Figs. 2.2, 2.3 and 2.4. We see that the distribution is not completely smooth. There is some large structure present approximately at $0 < \theta_z$ (deg) < 100 and $-10 < \theta_\phi$ (deg) < 0 , which is expected as this offset orbit patch selection still falls in a high density region in action space. Lower panel: Distribution in angle space for the same orbit patch as shown above, but for a smooth-phase mixed distribution. This mock catalog shows the general features of the dataset, but with no clumping.

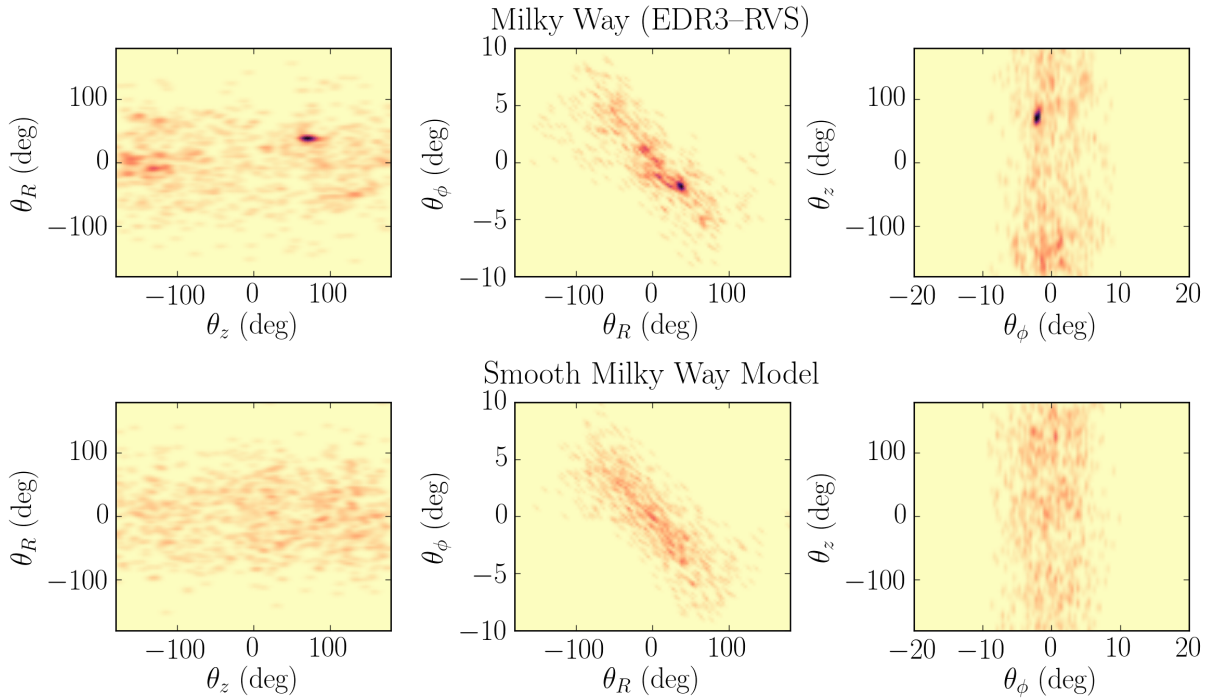


Figure 2.15. 2D projected kernel density maps of the angle distribution $(\theta_R, \theta_z, \theta_\phi)$ of the stars enclosed by the orbit patch of one isolated cluster example. This pearl located at $(\theta_R, \theta_z, \theta_\phi)$ (deg) $\sim (60, 80, -3)$ actually corresponds to a known cluster: Platais 3. The lower panel shows the smooth-phase mixed distribution that reproduces the main trends of the dataset where we don't see the cluster.

ORCID IDs

Johanna Coronado <https://orcid.org/0000-0001-6629-0731>

Verena Fürnkranz <https://orcid.org/0000-0002-9460-0212>

Hans-Walter Rix <https://orcid.org/0000-0003-4996-9069>

3 THE AGE DISTRIBUTION OF STELLAR ORBIT SPACE CLUMPS

3.1 DETAILS OF PUBLICATION AND AUTHORSHIP

The content of this chapter is based on the following peer-reviewed publication.

- **Title:** The Age Distribution of Stellar Orbit Space Clumps
- **Authors:** Verena Fürnkranz, Hans-Walter Rix, Johanna Coronado, Rhys Seeburger
- **Journal:** The Astrophysical Journal, Volume 961, Issue 1, id.113, 14 pp. (January 2024)
- **DOI:** [10.3847/1538-4357/ad0f99](https://doi.org/10.3847/1538-4357/ad0f99)
- **Online data:**
https://content.cld.iop.org/journals/0004-637X/961/1/113/revision1/apjad0f99t1_mrt.txt
https://content.cld.iop.org/journals/0004-637X/961/1/113/revision1/apjad0f99t2_mrt.txt

The formatting of the figures and tables has been adjusted to better fit the layout of this thesis.

Contributions:

I did all scientific work: coding, analysis, figures, text, and referee report reply of the publication. Hans-Walter Rix regularly guided me and helped with the science, method development, and paper writing. Johanna Coronado initiated this follow-up project to the *‘pearls on a string’* paper presented in Chapter 2. Rhys Seeburger provided coding advise.

3.2 ABSTRACT

The orbit distribution of young stars in the Galactic disk is highly structured, from well-defined clusters to streams of stars that may be widely dispersed across the sky, but are compact in orbital action-angle space. The age distribution of such groups can constrain the timescales over which co-natal groups of stars disperse into the ‘field’. Gaia data have proven powerful to identify such groups in action-angle space, but the resulting member samples are often too small and have too narrow a CMD coverage to allow

robust age determinations. Here, we develop and illustrate a new approach that can estimate robust stellar population ages for such groups of stars. This first entails projecting the predetermined action-angle distribution into the 5D space of positions, parallaxes and proper motions, where much larger samples of likely members can be identified over a much wider range of the CMD. It then entails isochrone fitting that accounts for a) widely varying distances and reddenings; b) outliers and binaries; c) sparsely populated main sequence turn-offs, by incorporating the age information of the low-mass main sequence; and d) the possible presence of an intrinsic age spread in the stellar population. When we apply this approach to 92 nearby stellar groups identified in 6D orbit space, we find that they are predominately young ($\lesssim 1$ Gyr), mono-age populations. Many groups are established (known) localized clusters with possible tidal tails, others tend to be widely dispersed and manifestly unbound. This new age-dating tool offers a stringent approach to understanding on which orbits stars form in the solar neighborhood and how quickly they disperse into the field.

3.3 INTRODUCTION

Stars are born in a highly clustered fashion, in position, velocity, and orbit space (e.g. [Kounkel & Covey, 2019](#); [Lada & Lada, 2003](#); [Lamb et al., 2010](#)). It appears that the vast majority of them do not remain in bound clusters after the gas expulsion phase (e.g. [Chandar et al., 2017](#)). And even those that first remain in “open” clusters beyond this phase tend to eventually become unbound from these clusters, by internal two- or three-body interactions, or by external tides. Consequently, most stars with ages > 5 Gyrs have become “field stars”. However, how clustered (bound or unbound) the full population of stars was in their first, say, 10 Myrs, and how, or how rapidly, the transition from star clusters and associations to the Galactic field takes place has yet to be fully understood. Studying this transition process will open a new window on constraining whether all stars are born in clusters, give insights into how hierarchical star formation is, and allow one to tackle how rapidly the dissolution of clusters takes place.

The Gaia mission has provided data that are revolutionary for our understanding of the formation and structure of the stellar component of the Milky Way disk ([Gaia Collaboration et al., 2016](#)). The third Gaia data release (Gaia DR3) on June 13, 2022 has provided precise 6D position measurements (α, δ, ϖ), proper motion (μ_α, μ_δ), and radial velocity measurements (v_r) for millions of stars in the extended solar neighborhood ([Gaia Collaboration et al., 2023](#)). Recent work, e.g. by [Trick et al., 2019](#) and [Coronado et al., 2020](#), had shown that this 6D parameter space – or equivalently *orbit space* – is highly clustered over a wide range of scales. Large-scale structures might be caused by resonances of the Galactic bar and spiral arms, or by satellite infall into the Milky Way Galaxy ([Gaia Collaboration et al., 2018](#)). Small-scale clustering represents the concepts of open clusters, associations, and stellar (disk) streams.

In the immediate neighborhood, the space velocities can serve as orbit proxies. On larger scales, action-angle coordinates (J, Θ) stand out as a powerful coordinate system to search for substructure in the Galac-

tic orbit and orbital phase space: the three actions denote the “orbit”; the three angles the “orbital phase“. Recent work by Coronado et al., 2022 has shown that we can find numerous stellar groups by linking stars in this 6D parameter space: some are simply clusters, others extend over 100’s of parsecs. In Coronado et al., 2022 we discovered that the same orbits that host one of these groups very frequently host numerous other distinct orbit-phase overdensities along these same orbits, which we call *pearls*¹. This might open up a new way to probe the filamentary structure of the ISM.

The central overall goal of our present work is to associate *ages* to stellar action-angle groups in the Galactic disk. These are crucial data for understanding for how long ensembles of stars remember their initially near-identical orbits and orbital phases. Once sets of stars (clusters or associations) are no longer gravitationally bound but still tightly clustered in orbit space (J, Θ), they will continue to disperse into the field by simple phase-mixing and by further relative orbit diffusion, driven e.g. by the Galactic tidal field. To make predictions about the rate of this dispersal, age information about the ensembles of stars is needed.

For coeval ensembles of stars, fitting isochrones to their CMD positions is a long-established approach to age estimates. This suggests that one should simply fit the CMDs of the stellar ensembles identified (see Coronado et al., 2022) in 6D phase space. However, radial velocities from Gaia exist only for stars over a limited range of effective temperatures (3.100 to 14.500 K) and for stars brighter than $G_{RVS} \approx 14$ mag. Furthermore, the radial velocities for hot and cool very young stars are not very precise ($\delta v_r \approx 5 \text{ km s}^{-1}$), which is a serious impediment in orbit clustering studies. At any rate, this means that the CMDs of these 6D sample are incomplete or missing for the uppermost main sequence (including potentially the turn-off for ages $\tau < 200$ Myrs) and for the lowest-mass stars, which are also good age diagnostics as stars may take $> 10^8$ years to settle on the zero-age main sequence.

The practical goal of this paper is to overcome this limitation by projecting the tight 6D action-angle distribution of these stellar ensembles to 5D position-proper motion space, where we can then establish much larger membership samples with higher completeness at the extreme mass and temperature ranges that are so precious for age estimates. This is possible since Gaia is highly complete to $G \approx 19$ mag across a very broad range of colors, if only positions, parallaxes, and proper motions are required. We aim to end up with CMD’s that are much better populated in both total sample size and color range. This requires that the groups, high-density peaks in 6D (J, Θ), still have a distinct density contrast in their 5D projection ($\alpha, \delta, \varpi, \mu_\alpha, \mu_\delta$, but without v_r).

Conceptually, our approach to extending group membership is as follows: we start with a set of stellar groups identified in 6D space. Specifically, we get these by identifying 6D action-angle groups within 800 pc from the Sun in a similar fashion to Coronado et al., 2022. We use the DBSCAN clustering algorithm and choose a search setting that identifies 102 action-angle groups of stars, which is about twice the sample size as the 55 action-angle groups identified in Coronado et al., 2022. For our analysis, we pick all groups with at least 20 member stars. This reduced set of 94 groups largely overlaps with the open

¹These pearls are strung along one orbit, like pearls on a string.

cluster catalog published in [Cantat-Gaudin et al., 2020](#), as well as with the stellar groups detected in [Hunt and Reffert, 2023](#). Additionally, almost all of our stellar groups can be found in the catalog of [Kounkel and Covey, 2019](#), which is known to be complete but highly contaminated (see [Zucker et al., 2022](#)). We project these groups into the 5D position-proper motion space, where we have a factor ~ 8 more stars in the Gaia catalog. For each action-angle group, we assign additional candidate members that are located in the same 5D region. Specifically, we run a kernel density estimate on the 5D distribution of each group and pick all stars in the Gaia catalog that show an excess at high densities, compared to stars in the Gaia mock catalog ([Rybizki et al., 2020](#)).

We then take 92 of these groups with their extended membership to develop, test and apply our new approach to age dating these groups of potentially co-natal stars, accounting for their potentially sparse and widely dispersed nature. This approach entails likelihood isochrone fitting that takes into account a) differential reddening, b) the widely ranging member distances, c) the individual photometry and distance errors, as well as d) binaries and outliers. We also test whether groups can be described as *effectively mono-age*, rather than have evidence for a large age dispersion in their CMD. Accounting for all these aspects in age-dating is crucial in this regime, and has not been implemented before.

With this new approach, we determine the ages and possible intrinsic age spreads of the identified stellar action-angle groups, and find them to be predominately young ($\tau \lesssim 2 \tau_{orbit}$) and mono-age. The analysis of the dispersal of these groups in orbit and orbital phase-space will be subject of upcoming work, as will be the age distribution of any “pearls” along the same orbit, as well as the smallest and most diffuse groups we can identify that still show mono-age CMD sequences.

The paper is organized as follows. In Section 3.4 we describe the data used in this study. Section 3.5 outlines our method for finding groups in 6D action-angle space and associating member stars by extending our search to the 5D position proper motion space. In Section 3.6 we present our likelihood isochrone fitting method which determines ages of the groups. Our results are discussed in Section 3.7. Finally, we summarize our findings and conclude in Section 3.8.

3.4 DATA

3.4.1 EXCERPTS OF THE GAIA DR3 CATALOG

We base our analysis exclusively on Gaia DR3 ([Gaia Collaboration et al., 2023](#)). As our intention is to study the extended solar neighborhood, we limit the analysis to stars with parallax ≥ 1 mas, corresponding to a maximum distance of 1 kpc from the Sun. We clean this sample from sources with spurious astrometry, following [Rybizki et al., 2022](#), and exclude sources with $\text{fidelity_v2} < 0.9$. We also limit the analysis to stars with $\text{parallax_over_error} \geq 10$, to eliminate distance uncertainties as the main source of orbit uncertainty.

This results in a database containing 41.138.028 sources, and we will refer to this catalog as the Gaia sample throughout.

As we start our analysis by identifying groups in the 6D action-angle space, we also introduce a slightly more confined sample with $\varpi \geq 1.25$ (within 800 pc from the Sun), comprising only the stars that also have a radial velocity (v_r) measurement. We adopt the same fidelity cut, but relax it to $\text{parallax_over_error} \geq 3$ to get a larger 6D sample. This 6D database contains 9.080.884 sources, and we will refer to it as Gaia RVS sample.

As we need to fit isochrones to dereddened colors and magnitudes, we query extinction values (A_G, A_{BP}, A_{RP}) from the astrophysical parameter catalog produced by the Apsis processing chain developed by the Gaia DPAC (Fouesneau et al., 2023). Specifically, we query all stars with an extinction entry available, and within 1 kpc from the Sun. Additionally, we limit the catalog to zero-age main sequence stars and apply a $2 \text{ mag} < M_G < 8 \text{ mag}$ cut (see Section 3.6.1), which reduces the catalog to 23.543.432 sources and hereafter we will refer to it as *Gaia extinction sample*. For the most part, it encompasses the Gaia sample.

3.4.2 GAIA EDR3 MOCK CATALOG

Since we will identify overdensities in 5D position-proper motion space, we will need to know what densities we should expect from a smooth distribution. To this end, we make use of the Gaia EDR3 mock catalog by Rybizki et al., 2020, which presents an analogous dataset to the Gaia DR3 catalog, but with a smooth and fully phase-mixed orbit distribution. We apply the same distance cut by only selecting stars with $\varpi \geq 1$, and add `WHERE popid != 11` into the ADQL query, which removes clusters and moving groups. These are otherwise included in the catalog by default. The resulting dataset comprises 46.830.045 stars, and will be named Gaia mock sample throughout the manuscript. The size of the catalog is comparable to the size of the Gaia sample catalog, and therefore it is well suited for comparison.

3.4.3 PARSEC ISOCHRONES

For age determinations via isochrone fitting, we need to choose one (or more) isochrone models. After considerable experimentation, we settled on PARSEC isochrones (Bressan et al., 2012) for our analysis, as they provide the most consistent age estimates between the turn-off and the low-mass main sequence. MIST isochrones (Choi et al., 2016; Dotter, 2016) provide less consistent age estimates for our set of action-angle groups, as they are not optimized for the lower main sequence.

Specifically, we download the default isochrone tables for a set of 6 metallicities in the range of $[\text{Fe}/\text{H}] = -0.4$ to $+0.1$, and 107 ages from $\log \tau = 5$ to 10.3, resulting in an isochrone table comprising 224.951 entries.

Our analysis requires that each individual isochrone can return finely spaced magnitude and color values, which we ensure by linear interpolation. Specifically, for each individual isochrone we loop through all mass points and interpolate Mass , G_{mag} , BP_{mag} , and RP_{mag} whenever $\Delta G_{\text{mag}} > 0.03$ mag between two mass points. After applying this method, we doubled the isochrone entries to a total of 458.181. We will refer to this setup as *isochrone table* in the text.

3.5 STELLAR GROUPS IN ACTION-ANGLE SPACE

We now describe membership identification of the stellar groups whose ages are at the heart of our analysis: their initial identification as prominent overdensities in the 6D action-angle space and the subsequent extended membership identification after projection of each action-angle distribution ("patch") into the 5D position-proper motion space.

3.5.1 ACTION-ANGLE COMPUTATION

The calculation of actions (J) and angles (Θ) requires both the full 6D position-velocity information in Gaia's original coordinates $(\alpha, \delta, \varpi, \mu_\alpha, \mu_\delta, v_r)$ and an assumed gravitational potential. For the potential, we adopt Galpy's axisymmetric MWPotential2014 (Bovy, 2015), which has adopted a circular velocity of 220 km s^{-1} at the Solar radius of 8 kpc, and which comprises a bulge, a disk, and a dark-matter component (Bovy, 2015). We then use the Stäckel Fudge algorithm by J. Binney, 2012 to estimate the actions and angles for all stars in our Gaia RVS sample.

3.5.2 IDENTIFYING STELLAR OVERDENSITIES IN 6D ACTION-ANGLE SPACE

In Coronado et al., 2022 we showed that stellar overdensities – from clusters, to associations, to disk streams – can be identified as groups that are overdense in action-angle space. Here, we follow the same approach applied to our Gaia RVS sample, with modifications that we summarize here. First, we describe all orbital angles via their *sine* and *cosine* functions bypass complexities that arise from the periodicity of these variables. To reach a consistent metric across all six coordinates that serves our purpose, we first normalize each of the action-angle coordinates $(J_R, J_\phi, J_Z, \sin(\Theta_{R,\phi,Z}), \cos(\Theta_{R,\phi,Z}))$ by removing the mean and scaling to unit variance. Additionally, we explore changes in the relative weight of "orbits" vs "orbital angles", and reduce the variance in the six angle coordinates (now sines and cosines of the angles) by multiplying the scaled data with 0.4.

To identify clusters of objects in this 6D space, Coronado et al., 2022 had used a version of the Friends-of-Friends algorithm to link objects. Here, we apply the density-based algorithm DBSCAN (Ester et al.,

1996) to extract clustered ensembles of objects from the $(J_R, J_\phi, J_Z, \sin(\Theta_{R,\phi,Z}), \cos(\Theta_{R,\phi,Z}))$. We choose this clustering algorithm instead of the Friends-of-Friends algorithm because it is much faster in handling large datasets. Running DBSCAN requires two choices: a minimum number of members (minPts), and a maximum distance scale ϵ . We have explored a wide range of ϵ and minPts parameters, and decided on a final setup of $\epsilon = 0.035$ and $\text{minPts} = 20$. In combination with our orbital angle weighting, this parameter choice yields to 0.1% of the stars in the *Gaia RVS sample* to be clustered in about twice as many groups as we had identified in Coronado et al., 2022. With these choices we now identify 102 action-angle groups, and keep the 94 most prominent groups that have at least 20 member stars. This sample is large enough to develop, test, and apply our age estimates; and it is large enough to get a first census which fraction of groups are “young” and approximately “mono-age”.

Fig. 3.1 illustrates these 94 action-angle groups: the top row shows their distribution (color-coded by group) in the three action plane projections, and the middle row shows their distribution in the three angle plane projections. By construction, all groups are very compact in this parameter space. The bottom row shows a top-down view on the 94 groups in Galactic Cartesian Coordinates (left), and their distribution on the sky in Galactic longitude and latitude (right). Although the groups are tightly clustered in action-angle space, most of them extend many degrees on the sky, and a substantive fraction over several 100 parsecs in physical extent.

For six representative action-angle groups Fig. 3.2 displays the CMDs for their members identified in 6D space. In all cases, these members form a narrow sequence in CMD space, as expected for simple stellar populations. However, the overlaid isochrones in Fig. 3.2 also illustrate that these stars only cover a portion of the expected isochrone locus. This is for two reasons: the limited magnitude range and the limited temperature range of the *Gaia RVS sample*, where only stars with $G < 14$ mag and effective temperatures in the range of 3.100 to 14.500 K are included. For the age determinations of these groups this is a serious limitation, as the (upper) main-sequence turn-off (for ages $> 10^8$ yrs) and the lower main sequence (for ages $< 10^8$ yrs) provide the best age constraints for stellar ensembles.

This is apparent from the set of three isochrones overplotted in Fig. 3.2, spanning an age range of $\tau = 60 - 630$ Myrs, specifically $\log \tau = 7.8, 8.4, 8.8$. E.g. for Group 58 in the top row, the group members identified in 6D are located exclusively on the part of the main sequence where all these isochrones coincide.

Hence, determining ages by isochrone fitting requires identifying member stars at temperatures (or stellar masses) that are not included in the *Gaia RVS sample*. Such hotter and cooler stars that are missing here should, however, be in the overall *Gaia* sample, with valid 5D position – proper motion entries.

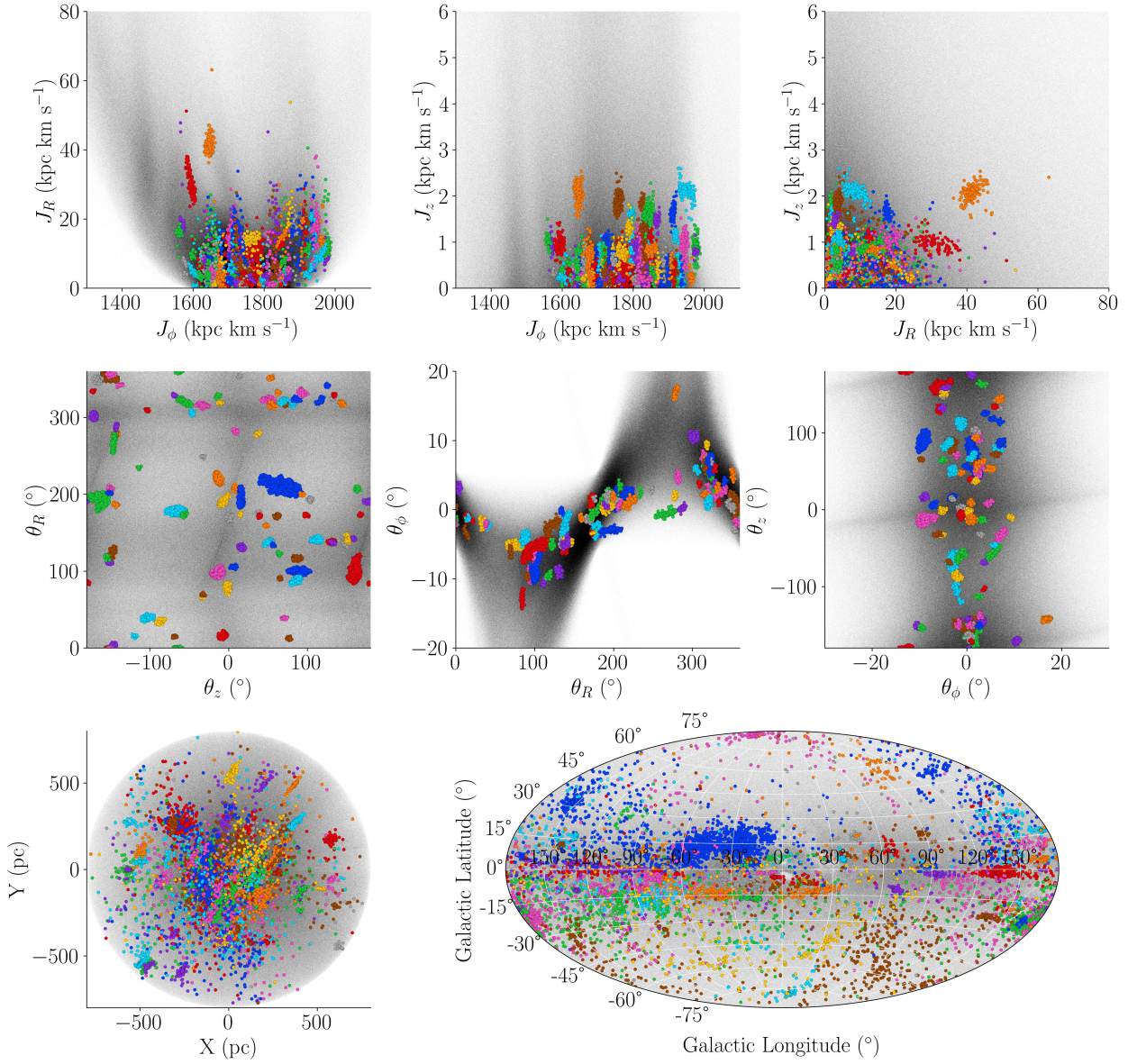


Figure 3.1. The member stars of the 94 most prominent action-angle groups identified with DBSCAN. The various colors represent the different groups. The black background corresponds to all sources in the *Gaia RVS sample*. Top/Middle row: The distribution of the groups in the three projections of the action/angle space. By construction, all groups are tightly clustered in this parameter space. Bottom left: Top-down view on the 94 groups in Galactic Cartesian coordinates, where the Sun is located at $(X,Y) = (0,0)$ pc. Bottom right: The sky distribution of the action-angle groups in Galactic longitude and latitude, illustrated in a Hammer projection. Although all groups are very tightly clustered in action-angle space, most of them are extended across several hundred degrees on the sky.

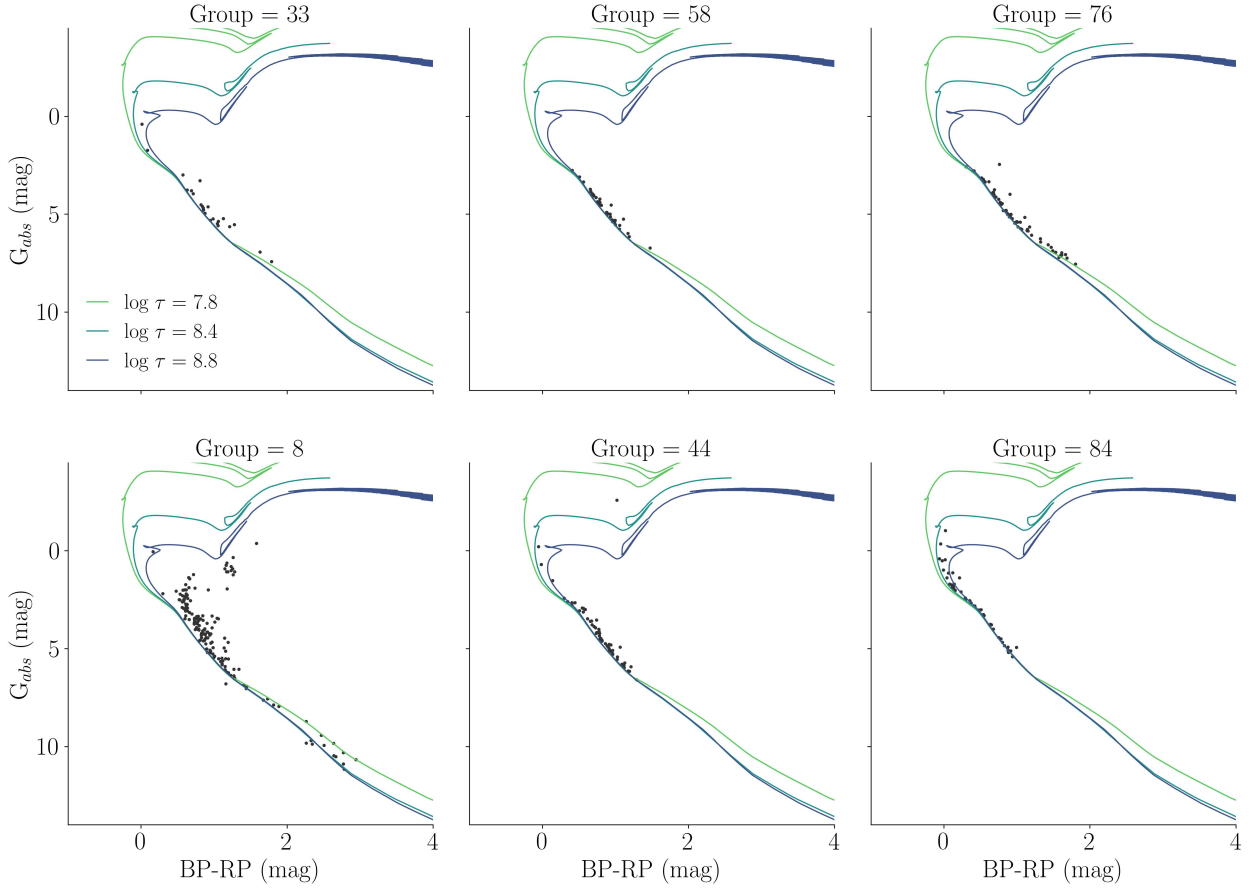


Figure 3.2. Observational CMDs for six representative action-angle groups. The member stars of each group are arranged in narrow, but short, sequences, where stars are clearly missing in the upper and lower main-sequence parts. This is caused by the limited magnitude and temperature range of the Gaia RVS sample, where only stars with $G < 14$ mag and with effective temperatures in the range of 3,100 to 14,500 K are included. In color, we show a set of three isochrones ($\log \tau = 7.8, 8.4, 8.8$), illustrating that stars located on the main sequence only have a small age-diagnosing value.

3.5.3 ASSOCIATING ADDITIONAL MEMBER STARS IN THE 5D SPACE OF POSITIONS AND PROPER MOTIONS

In this section we describe how to extend the stellar membership of the action-angle groups across a wider color or stellar-mass range, in order to overcome the just-described limitations in age dating these groups. We do this by mapping their distribution from 6D (rescaled) action-angle space to 5D position-proper motion space ($X, Y, Z, \mu_\alpha, \mu_\delta$), to search for the most likely members in this projected space, where we do not have the color limitations of the Gaia RVS sample.

We start by constructing an approximate Probability Density Function (PDF) for each group in 6D space. We do this with the help of a kernel density estimate for each group in the rescaled 6D space of $J_R, J_\phi, J_Z, \sin(\Theta_{R,\phi,Z}), \cos(\Theta_{R,\phi,Z})$, using a Gaussian kernel with a unit bandwidth that we can then sample finely. Before doing that, we remove members in each action-angle group that are beyond 2σ from the median in any coordinate, to mitigate the impact of outliers; this leaves about 95% of the stars. We then

3 The Age Distribution of Stellar Orbit Space Clumps

sample this PDF estimate with 5000 random points that we can then map from action-angle space $(J_R, J_\phi, J_Z, \Theta_R, \Theta_\phi, \Theta_Z)$ to position-proper motion space $(\alpha, \delta, \varpi, \mu_\alpha, \mu_\delta, v_r)$. For this mapping we use the MWPotential2014 in the TORUSMAPPER package (J. Binney & McMillan, 2016), which is part of the AGAMA library (Vasiliev, 2019), a software framework offering several tools applicable to galaxy modeling and stellar dynamics. We then remove some "nonphysical" sampled datapoints, e.g. datapoints with negative radial and vertical actions.

Finally, we take the sampled datapoints that have been mapped into 5D space and perform a kernel density estimate, where we choose $(X, Y, Z, \mu_\alpha, \mu_\delta)$ as coordinates, to have an intuitive metric for the spatial part. In each dimension, we use a Gaussian kernel with a unit bandwidth to obtain a density estimate. This smooth 5D density now allows us to assign a local density value ρ to each star in the actual Gaia sample that is within the groups individual boundaries, e.g. minimum and maximum coordinates in $(X, Y, Z, \mu_\alpha, \mu_\delta)$.

Of course the 5D space just described can and will also contain unrelated field stars. We can only identify new members of this group with any confidence, where the 5D density of the actual Gaia sample is higher than the expectation from a smooth mock catalog. Therefore we apply the same procedure to the smooth Gaia mock sample described in Section 3.4.2, leaving us with a local density value assigned to each star in the mock sample.

Now we can identify the domain of this 5D space where each group's 5D density is far higher than the density in the smooth *Gaia mock sample*. To this end, we create a histogram of the number of Gaia (n_{gaia}) and Gaia mock (n_{mock}) stars as a function of their assigned Kernel density ρ . We set a density threshold for each group with the following approach: The first density threshold T_1 is the lowest density bin where the local density of the Gaia sample is 25 times higher than expected from the Gaia mock sample. Given that the *Gaia mock sample* is an imperfect representation of the real data, we decide on the ratio number 25 after some experimentation. This selects all stars in a group as likely 5D members, if their local density is 25 times higher than expected from the Gaia mock sample. Second, we calculate the ratio between n_{gaia} and n_{mock} in each bin and set the second density threshold T_2 at the density with the highest contrast, with the additional condition to contain at least 100 stars. We pick a final density threshold $T_{final} = \min(T_1, T_2)$ for each group by picking the threshold at the lower density (minimum), e.g. to assign as many 5D candidate members as possible to each group.

We find that about half of the groups (41) get the density threshold T_1 assigned, whereas the remaining groups (53) get the density threshold T_2 assigned. From the groups with T_2 , 16 groups get the density threshold at 100 stars, and 37 groups get a density threshold at lower densities with a higher ratio.

For each group we then merge our original group member selection drawn from the Gaia RVS sample with the new group member selection obtained from the full Gaia sample. From this final group member selection, we manually remove two groups that show overpopulated CMD's and end up with a final set of

92 groups with extended memberships to test and apply the age dating method described in Section 3.6. The full "group member selection" is available in a machine-readable format (Table 3.1), including the Gaia DR3 Source ID, the Group membership, and the coordinates α , δ .

Table 3.1: Group Membership Selection

Gaia DR3	RAdeg (deg)	DEdeg (deg)	Group
5239299835545363328	160.0637242181275	-65.48469054214712	1
5255777627880765312	148.9077870953364	-62.8031703550916	1
5252653266828976640	152.00691487601495	-63.502318897070815	1

(This table is available in machine-readable form.)

The above described procedure is illustrated in Fig. 3.3. It shows the density histograms for all Gaia stars (turquoise) and Gaia mock stars (violet) for six representative action-angle groups, selected within the individual group's volume and proper motion range. Most Gaia and Gaia mock stars have small density values, with a tail extending to higher densities. As expected, the actual Gaia stars – in this 6D group selected patch – far exceed the number of Gaia mock stars in the high density regime. This illustrates immediately that we find these groups also as prominent overdensities in the 5D *Gaia sample*. The dotted blue line marks the location of the density cut T_{final} , which varies considerably between the groups, depending on the distribution of the Gaia mock stars. Some groups exhibit a more pronounced excess of Gaia stars in the high density regime than other groups. This could be for two reasons: either some groups might be more compact, or some groups may occur far away from the disk plane, which both provides naturally a higher density contrast.

3.6 AGE DETERMINATION

We now want to determine stellar ages of the 92 action-angle groups. In the end this estimate comes from a forward model of the photometry data, of the group members, $p(\tau|\{data\})$, where *data* incorporates the magnitudes and parallaxes of the stars, as well as their errors. The magnitude errors are not provided in the Gaia catalog, therefore we obtain them from the G, BP and RB band fluxes and flux errors. In this modelling, we want to account for the following effects: The stars are widely spread across the sky (see Fig. 3.1), they may have widely ranging member distances (we obtain distances by inverting the parallax), and they have varying photometric and distance uncertainties. In addition, we need to allow for (unresolved) binaries, possible outliers, and we need to take into account differential reddening.

3 The Age Distribution of Stellar Orbit Space Clumps

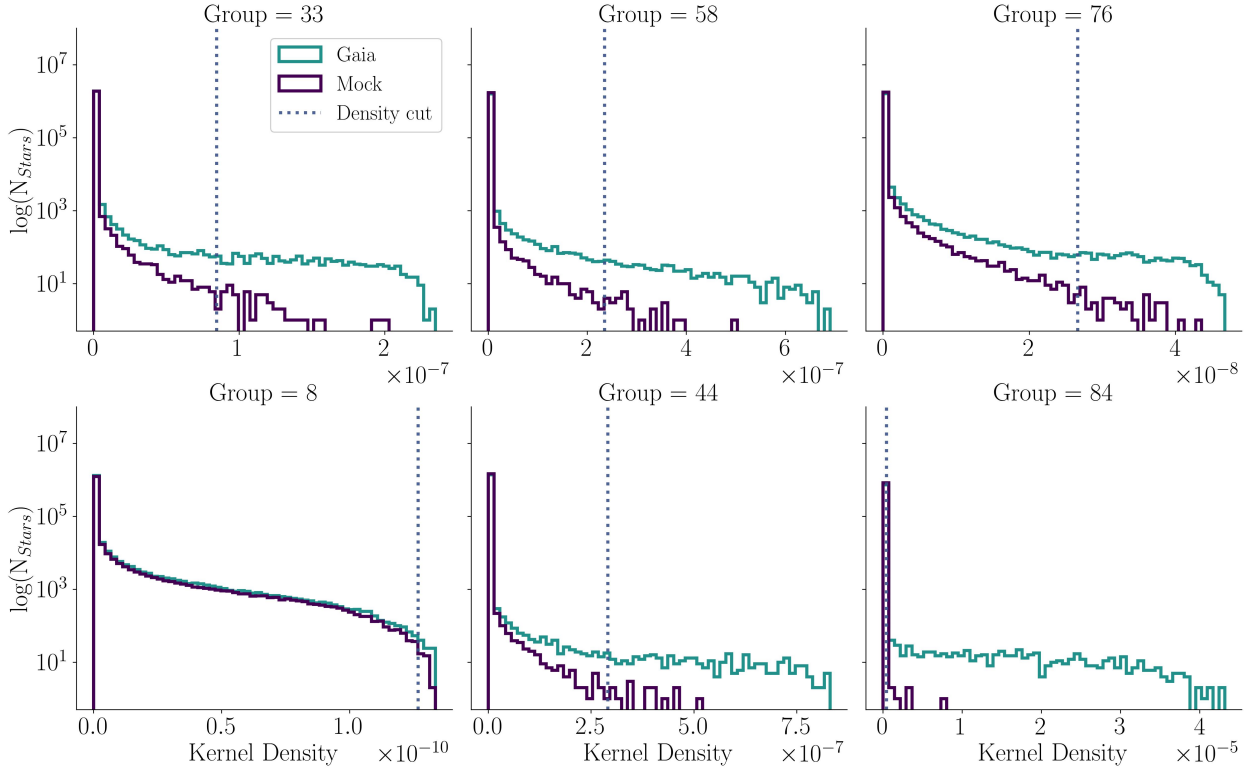


Figure 3.3. Histograms of the allocated density values for all Gaia (turquoise) and Gaia mock stars (violet) within the individual $(X, Y, Z, \mu_\alpha, \mu_\delta)$ ranges for six representative action-angle groups. The dotted blue line marks the location of the final density cut T_{final} as described in Subsection 3.5.3. Most Gaia and Gaia mock stars have a density value close to zero, with a tail extending to higher densities, where typically the amount of Gaia stars exceeds the amount of Gaia mock stars. This is an indication that we find stars clumped in position-proper motion space in the *Gaia* sample.

3.6.1 REDDENING CORRECTION

We start with the reddening correction for each individual star. It is tempting to simply take each group member’s reddening estimate directly from the *Gaia* extinction sample. These estimates are based on the idea to deredden each star until it gets to its most plausible place in the CMD. However, for stars that lie above the solar-metallicity, zero-age main sequence – whether they are young stars or binaries – this often leads to overestimates of their reddening. Instead, we adopt the ensemble median of other stars in the same direction and at the same distance. To obtain robust estimates, we limit these reddening estimates to stars in the *Gaia* extinction sample where we can assume that they are firmly on the zero-age main sequence, requiring $2 \text{ mag} < M_G < 8 \text{ mag}$. We select all stars that are located within a sphere of radius 25 pc around each group member star under consideration for dereddening, and pick the 50th percentiles in A_G , A_{BP} , and A_{RP} to subtract from the member star’s uncorrected Gaia magnitudes G , BP , and RP . Depending on the location of each group and the location of each stars within the group, the spheres contain between 266 and 2059 stars, typically around 800 stars. The effect of this extinction correction is illustrated for Group 68 in the left panel of Fig. 3.4. The colored data points represent the CMD before applying the reddening correction, and the black data points show the reddening corrected sequence.

E.g. for Group 68, the average shift in color is 0.1 mag. Fig. 3.4 illustrates that reddening correction is important for precise isochrone fitting, even for stars located within the extended solar neighborhood of 800 pc from the Sun.

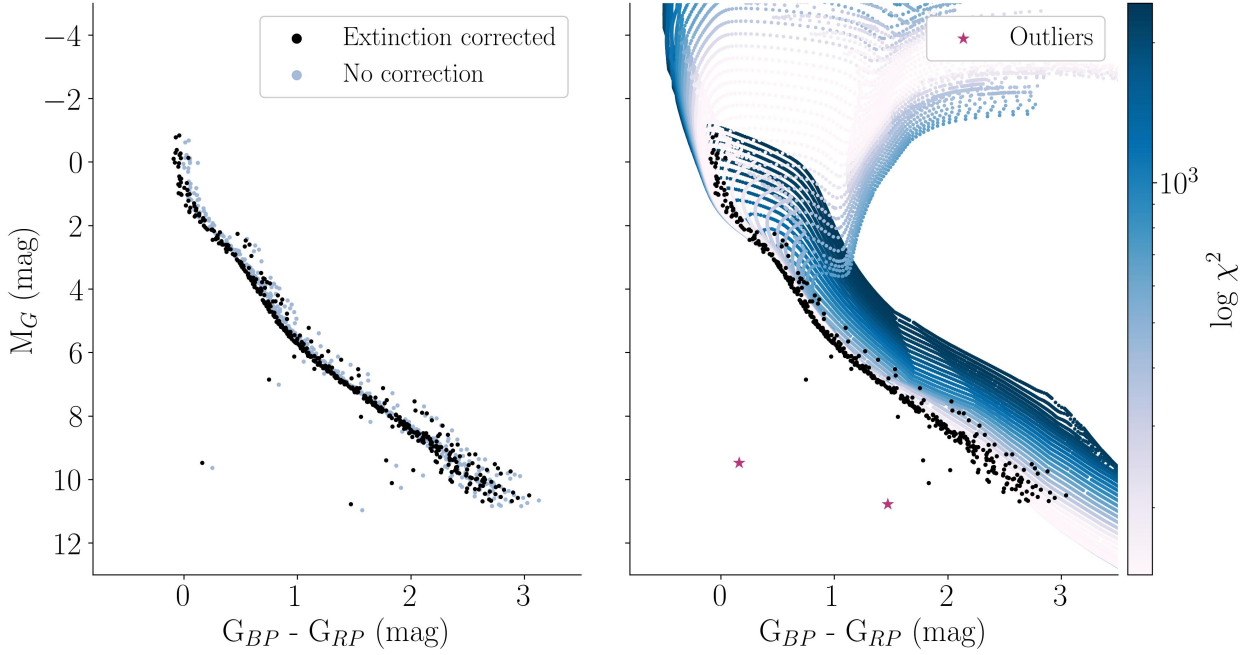


Figure 3.4. Left: The effect of the extinction correction method for stars in Group 68. The correction reveals a significant shift of the uncorrected (colored) stars to the reddening corrected (black) stars, emphasizing the importance of extinction correction for precise age dating via isochrone fitting of CMD’s, even for stars located in the solar neighborhood. The average shift in color for Group 68 is 0.1 mag. Right: Illustration of the likelihood isochrone fitting for Group 68. All isochrones are colored by age (107 different logarithmic τ) for a fixed metallicity of $[\text{Fe}/\text{H}] = 0.1$. The color coding represents the χ^2 value obtained for the different age setups. The plot illustrates that very young as well as very old ages are not likely to fit the group’s distribution, as they lead to a high χ^2 value. The best fit isochrone for this group is the one with the lowest χ^2 value. The stars in magenta mark group members that are labelled as $4\text{-}\sigma$ outliers by our code setup, and are not considered in the likelihood isochrone fitting. We show the isochrones not as solid lines, but as datapoints to illustrate our finely spaced magnitude and color setup, which we obtain by linear interpolation (see Sec. 3.4.3).

3.6.2 BASIC FITTING METHODOLOGY

We now perform isochrone fitting by calculating the likelihood (here χ^2) of the reddening-corrected photometric data and parallax for each group, $\{data\}_{i=1, N_\star}$. Here, N_\star is the number of likely 5D members in the group and each star’s data is given by its apparent magnitudes and parallaxes, as well as their errors: $data \equiv (m_G, m_{BP}, m_{RP}, \varpi; \sigma_{m_G}, \sigma_{m_{BP}}, \sigma_{m_{RP}}, \sigma_\varpi)$. Each isochrone, specified by the two parameters $\log \tau$, $[\text{Fe}/\text{H}]$, provides model predictions $M_{band} = f(\mathcal{M} | \log \tau, [\text{Fe}/\text{H}])$, where $band$ stands for G, BP and RP, and \mathcal{M} is the initial stellar mass.

A priori, we neither know any star’s mass nor its exact distance, and we should treat these quantities as parameters, even if for the current context they are “nuisance parameters”. This means we have to optimize

3 The Age Distribution of Stellar Orbit Space Clumps

both the global parameters $\log\tau$, $[\text{Fe}/\text{H}]$ and the individual masses \mathcal{M} and distance moduli (DM), which are mainly constrained by the parallaxes, ϖ . We perform this optimization by a multi-dimensional grid search. To speed up the computation we only consider a very limited range of DM– \mathcal{M} combinations for each star, constrained by their apparent magnitude and parallax.

We only consider distance moduli that are 2σ consistent with the parallax measurement:

$$\begin{aligned} DM_{min} &= 10 - 5 \cdot \log_{10}(\varpi + 2 \cdot \sigma_{\varpi}) \\ DM_{max} &= 10 - 5 \cdot \log_{10}(\varpi - 2 \cdot \sigma_{\varpi}), \end{aligned} \quad (3.1)$$

and we only consider (pre-computed) $M_G(\mathcal{M})$ in the range

$$\begin{aligned} M_{G_{min}} &= (m_G - 2 \cdot \sigma_{m_G}) + 5 \cdot \log_{10}(\varpi - 2 \cdot \sigma_{\varpi}) \\ M_{G_{max}} &= (m_G + 2 \cdot \sigma_{m_G}) + 5 \cdot \log_{10}(\varpi + 2 \cdot \sigma_{\varpi}). \end{aligned} \quad (3.2)$$

Finally, to treat the parallax measurements as data we need to have a parallax prediction, which is simply

$$\varpi_{pred} = 10^{-\frac{(DM-10)}{5}}. \quad (3.3)$$

On this bases, we can calculate for each assumed parameter set and each star $\chi^2(\text{DM}, \mathcal{M}; \log\tau, [\text{Fe}/\text{H}])$:

$$\chi^2 = \frac{(m_G - DM - M_G)^2}{\sigma_{m_G}^2} + \frac{(m_{BP} - DM - M_{BP})^2}{\sigma_{m_{BP}}^2} + \frac{(m_{RP} - DM - M_{RP})^2}{\sigma_{m_{RP}}^2} + \frac{(\varpi - \varpi_{pred})^2}{\sigma_{\varpi}^2} \quad (3.4)$$

For any set of $\log\tau$, $[\text{Fe}/\text{H}]$ (the outer loop in the optimization) we optimize DM, \mathcal{M} for each star, and then sum all stars' χ^2 to obtain $\chi_{tot}^2(\log\tau, [\text{Fe}/\text{H}])$. This procedure then results in a mapping of the whole data set for any given group as a function of $\log\tau$, $[\text{Fe}/\text{H}]$, including their best fit values.

The right panel in Fig. 3.4 illustrates the outcome of this process for Group 68. In color are shown isochrones for 107 different $\log\tau$, at a fixed metallicity of $[\text{Fe}/\text{H}] = 0.1$. The color coding represents the χ^2 value obtained for the different age setups. The plot illustrates that the ages are well constrained both the upper and lower main sequence, as both regimes lead to a high χ^2 value.

This procedure is straightforward and accounts for the varying distances, reddenings and data uncertainties (including the parallax). We now turn to the generalization of this procedure to incorporate outliers and to consider the possibility of an intrinsic age spread in the stellar groups.

3.6.3 ACCOUNTING FOR BINARIES AND OUTLIERS

Isochrones reflect the color-magnitude locus of single stars, while observed CMDs have “outliers” for a number of reasons. Such outliers may be spurious data or stellar systems whose physics is not captured by the isochrone: (unresolved) binary stars, evolved stars such as white dwarfs, or actual interlopers of different ages and metallicities. In addition, the color prediction of the lowest mass stars may be less robust for isochrone models, which may explain some of the deviations.

In our code, we implement two different approaches to deal with binaries on the one hand, and different outliers on the other. For binaries, we follow [Coronado et al., 2018](#), where we generalize the isochrone prediction of a star’s absolute magnitude M_{iso} to be either that of a single star within a magnitude width σ_M , or – with probability ϵ – to be that of a near-equal mass binary that is 0.7 mag brighter, or to be a binary of any kind between M_{iso} and $M_{iso} + 0.7$ mag. Note that some groups illustrated in [Fig. 3.5](#) exhibit well populated binary sequences, illustrating the need for this methodological extension.

This results in a probability

$$\begin{aligned}
 p(M_\lambda | \mathcal{M}; \log\tau, [\text{Fe}/\text{H}], \epsilon) = & \\
 (1 - \epsilon) \mathcal{G}(M_\lambda - M_{\lambda,iso}, \sigma_M) + & \quad (3.5) \\
 \frac{\epsilon}{2} \left(\mathcal{G}(M_\lambda - (M_{\lambda,iso} - 0.7), \sigma_M) + I(M_\lambda) \right). &
 \end{aligned}$$

where \mathcal{G} is a Gaussian and I is the “in-between” term defined as $1/0.7$ between M_{iso} and $M_{iso} + 0.7$.

The logarithm of $p(M)$ in [Eq. 3.5](#) then simply gets added for each object to the χ^2 in [Eq. 3.4](#).

We deal with the other outliers by limiting all of them to be “ n - σ outliers” at worst: any individual χ^2 -term cannot be larger than $2 \times n^2$. We adopt $n = 4$, or $\chi_{max}^2 = 32$. This is illustrated in [Fig. 3.4](#) for example Group 68, where stars in magenta mark group members that are labeled as 4 - σ outliers by our code setup, and are not considered in the likelihood isochrone fitting.

3.6.4 INCORPORATING AGE DISPERSION

The approach described so far determines ages, assuming a priori that we have mono-age populations. However, we also want to consider the case that groups may have some finite age dispersion: $p(\log\tau | \overline{\log\tau}, \sigma_{\log\tau}) \equiv \mathcal{G}(\log\tau - \overline{\log\tau}, \sigma_{\log\tau})$, where the mean (log) age is $\overline{\log\tau}$ and its dispersion is $\sigma_{\log\tau}$. We im-

plement this by an extension of Eq. 3.4: We consider the “linearized” version of $\chi^2(\log\tau, [\text{Fe}/\text{H}])$, i.e. $\exp \chi^2(\log\tau, [\text{Fe}/\text{H}])$, and then integrate over all $\log\tau$ within $\pm 3\sigma_{\log\tau}$:

$$e^{\chi_{tot}^2} \equiv \int e^{\chi^2(\log\tau|[\text{Fe}/\text{H}])} p(\log\tau | \overline{\log\tau}, \sigma_{\log\tau}) d\log\tau. \quad (3.6)$$

In this case we optimize globally over three parameters, the mean age $\log\tau$, the metallicity $[\text{Fe}/\text{H}]$, and the intrinsic age spread $\sigma_{\log\tau}$.

We then estimate the uncertainty $\delta_{\log\tau}$ of the isochrone fit for each group and compare it to the individual intrinsic age dispersions $\sigma_{\log\tau}$, in order to determine what value of $\sigma_{\log\tau}$ is significant (“effectively mono-age”). We use the χ^2 values to determine the data probabilities and then look at the marginalised distributions to get the uncertainties in the individual parameters. Rather than quoting them individually, we find that the fit uncertainty $\delta_{\log\tau}$ is in 90% (83) of the cases smaller than 0.1, which is less than our $\log\tau$ grid size of 0.1. In 9 cases the fit uncertainties are larger than 0.1, whereas in only 1 case $\delta_{\log\tau}$ is larger than 0.15. Therefore, we choose a value of $\sigma_{\log\tau} = 0.2$ to declare “effectively mono-age” as significant.

3.7 RESULTS

With these isochrone fitting tools in hand, we can now proceed to presenting the results from the CMD’s for 92 groups described in Sect. 3.5.

3.7.1 ILLUSTRATING THE AGE CONSTRAINTS FROM ISOCHRONE FITS

We start by illustrating the results derived from the above procedure for the same six groups from Fig. 3.2, now shown in Fig. 3.5, with the full set of 5D proper motion members: the isochrones are now populated over a wider age range, providing better age constraints. All stars have been individually reddening corrected.

On top of each group the best fitting single-age isochrones are shown in turquoise ($\log\tau, [\text{Fe}/\text{H}]$), derived following Section 3.6. Across all groups, the isochrones fit both the upper and lower main sequences very well. In particular, this Figure illustrates that neither the binary sequence nor any outliers (e.g. below the main sequence) have noticeably biased the fit. The magenta isochrone at the lower main-sequence represents the mean age of the Galactic disk ($\log\tau_{Disk} = 9.7$).

The three groups in the top row are very young (< 25 Myrs), and low-mass stars have clearly not yet reached the true zero age main sequence. This illustrates well the power of low-mass stars for constraining very young population ages, for which the main sequence turn-off is sparsely sampled. The three

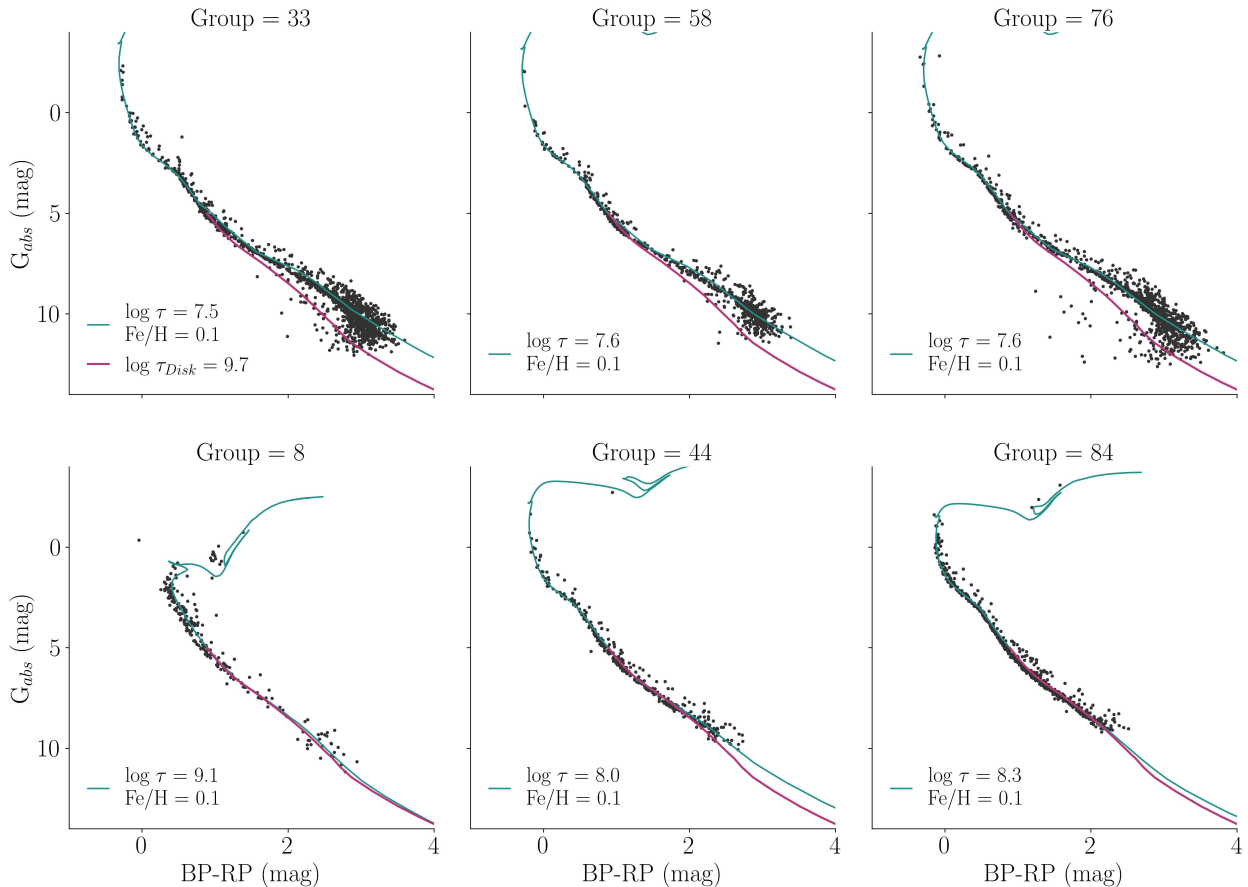


Figure 3.5. Observational CMD’s for six representative groups, with additional member stars associated from the 5D position-proper motion space. All stars are individually extinction corrected. The turquoise curve on top of each sequence shows the best-fitting isochrone ($\log \tau$, $[\text{Fe}/\text{H}]$). Across all groups, the isochrones fit both the upper and lower main sequences very well. The magenta isochrone at the lower main-sequence represents the age of the Galactic disk. The three groups in the top row are very young (< 25 Myrs), and their lower main sequences are clearly offset from the age of the Galactic disk. This again illustrates the power of the lower main sequence to determine the ages of very young populations. The three groups in the bottom row are older, and for them the main-sequence turn-off is the main age determinant.

groups in the bottom row are older. For them low-mass stars provide no two-sided age constraint. But for them the main-sequence turn-off is at lower masses, hence well-population and providing the main age constraint.

While these fits are pleasing, they need to be validated against external results, which we do by comparing them to the ages from [Cantat-Gaudin et al., 2020](#). We crossmatch our groups with known clusters in the [Cantat-Gaudin et al., 2020](#) catalog. We keep all groups for which we obtain at least 20 crossmatches with one literature cluster. Additionally, for groups that have matching sources with more than one literature cluster, we keep the literature cluster with the highest number of – but at least 20 – crossmatches. This applies to 62 of our groups. Figure 3.6 compares our age determinations to those of [Cantat-Gaudin et al., 2020](#), showing overall very good agreement, with no systematic bias and very little scatter. The $\log \tau$ uncertainties for individual clusters in the [Cantat-Gaudin et al., 2020](#) catalog range from 0.1 - 0.25, depending on the age itself and the number of stars ([Cantat-Gaudin et al., 2020](#)). As described in more detail in Sec-

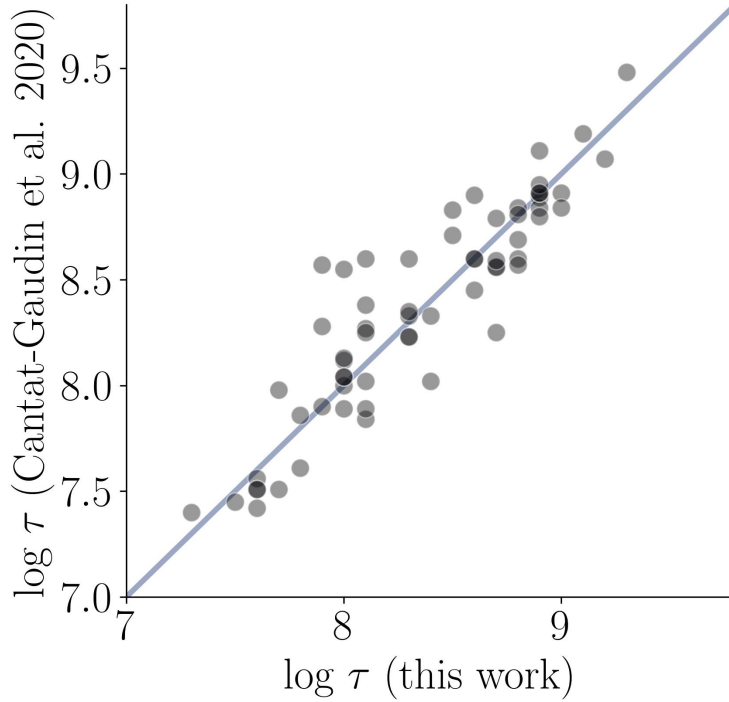


Figure 3.6. Comparison between the age determination of this work with the age determination of Cantat-Gaudin et al., 2020 for 62 established clusters that we could identify in the cluster catalog by Cantat-Gaudin et al., 2020. The plot shows that the age estimates from this work are in very good agreement with the literature values, with only very little scatter. The $\log \tau$ uncertainties of the age fit range from 0.1 - 0.25 for Cantat-Gaudin et al., 2020, and are typically smaller than 0.1 for the method presented in this work.

tion 3.6.4, the $\log \tau$ uncertainties of our isochrone fitting approach are typically smaller than 0.1, which is less than our $\log \tau$ grid of 0.1.

3.7.2 AGES, AGE DISPERSIONS, [M/H] AND SPATIAL STRUCTURE OF THE ACTION-ANGLE GROUPS

These fits, listed in Table 3.2 for the 92 action-angle groups, now put us in a position to address the basic questions we have about the properties of these action-angle groups. Table 3.2 includes the group number of each group, the number of member stars N_* , the median action and angle coordinates, the best age estimate $\log \tau$, the intrinsic age spread estimate $\sigma_{\log \tau}$, and the metallicity [Fe/H] of the likelihood isochrone fitting. Additionally, for the 62 groups we identified in the cluster catalog by Cantat-Gaudin et al., 2020 as described in Section 3.7.1, we list the name of the identified literature cluster. Among the listed groups we find established clusters such as the Pleiades (Melotte 22), the Hyades (Melotte 25), Praesepe (NGC 2632), and Coma Berenices (Melotte 111). We also identify the Meingast 1 (Pisces-Eridanus) stellar stream by crossmatching our sources with Meingast et al., 2019. However, a direct comparison and assignment of our groups to literature cluster is difficult, because each literature work uses a different approach to identify and select member stars of clusters, which leads to a lot of variation in the member

selections (e.g. some of our action-angle groups are overlapping with the same literature cluster identified in [Cantat-Gaudin et al., 2020](#)). A more detailed look at these different member selections additionally shows that our method selects more extended and loose structures (associations, tidal tails, other mechanisms of dispersal) as compared to [Cantat-Gaudin et al., 2020](#) and [Hunt and Reffert, 2023](#), whose member selections focus on cluster cores mainly.

Table 3.2: An Overview of the Main Parameters of the 92 Action-angle Groups

Group	N_*	J_R (kpc km s ⁻²)	J_ϕ (kpc km s ⁻²)	J_Z (kpc km s ⁻²)	Θ_R (rad)	Θ_ϕ (rad)	Θ_Z (rad)	$\log \tau$	$\sigma_{\log \tau}$	[Fe/H]	Cluster
1	207	3.08	1675.39	0.28	3.62	0.02	0.16	7.60	0.10	0.10	IC 2602
2	128	9.33	1599.05	0.34	3.61	0.05	2.85	8.20	0.20	0.10	...
3	1072	10.4	1765.7	0.37	1.71	6.18	2.79	8.80	0.10	0.10	Stock 2
4	136	17.92	1569.64	0.92	1.94	6.1	3.63	8.80	0.05	0.10	Mamajek 4
5	232	3.12	1675.5	0.77	2.99	0.03	1.07	8.10	0.20	0.10	UBC 1
6	1059	14.01	1713.86	0.25	1.7	6.13	6.05	8.60	0.45	0.10	Melotte 25
7	1621	2.47	1677.09	0.13	3.66	0.02	1.22	7.30	0.10	0.10	UPK 640
8	231	13.64	1758.37	0.71	1.37	6.19	6.24	9.10	0.05	0.10	NGC 6991
9	3527	4.14	1660.97	0.37	3.1	6.23	5.14	8.10	0.15	0.10	NGC 2516
10	165	8.2	1744.32	0.6	1.84	6.16	0.11	8.10	0.25	0.10	...
11	147	7.46	1659.19	0.2	3.25	0.02	3.8	8.50	0.35	0.10	...
12	899	7.23	1653.34	0.37	3.35	0.02	3.49	8.00	0.05	0.10	Melotte 22
13	568	0.98	1862.0	0.48	5.39	0.07	4.48	8.00	0.05	0.10	NGC 1039
14	205	14.93	1827.63	0.22	5.26	0.18	3.31	8.60	0.05	0.10	NGC 7092
15	663	2.5	1832.2	1.05	6.15	0.02	3.64	8.30	0.30	0.10	Meingast 1
16	397	17.09	1945.29	1.0	5.51	0.13	5.71	8.90	0.05	0.10	NGC 1662
17	119	4.67	1677.42	0.4	3.57	0.02	3.66	8.10	0.05	0.10	...
18	262	2.26	1688.44	0.27	3.33	0.01	6.16	7.90	0.35	0.10	...
19	283	18.65	1933.09	0.32	5.55	0.12	1.38	8.30	0.20	0.10	ASCC 41
20	1017	13.38	1725.27	0.56	1.74	6.12	1.58	8.50	0.45	0.10	NGC 2632
21	280	41.22	1645.85	2.08	4.85	0.29	3.8	9.30	0.05	0.10	Ruprecht 147
22	785	1.75	1845.02	1.62	4.69	6.27	3.74	8.30	0.05	0.10	NGC 2287
23	204	30.61	1594.95	0.96	1.47	6.06	3.14	9.00	0.05	0.10	Ruprecht 145
24	222	7.73	1718.35	0.35	2.28	6.13	0.29	8.90	0.05	0.10	NGC 2527
25	325	4.72	1643.77	0.24	2.04	6.23	1.52	8.80	0.05	0.10	NGC 6633
26	142	7.48	1637.95	0.27	3.62	0.01	3.66	7.90	0.05	0.10	UPK 545
27	177	4.07	1809.3	0.15	6.09	0.01	3.38	8.60	0.35	0.10	Alessi 9
28	110	6.58	1736.49	0.13	1.15	6.19	5.71	8.00	0.15	0.10	ASCC 99
29	797	1.92	1795.07	1.61	0.69	6.25	4.5	8.10	0.15	0.10	Blanco 1
30	2790	0.31	1705.56	0.58	3.37	6.23	0.27	8.30	0.25	0.10	NGC 3532
31	266	2.02	1672.29	0.69	3.84	0.02	6.06	8.00	0.10	0.10	UPK 612
32	724	11.58	1976.23	0.88	5.59	0.1	5.3	8.70	0.10	0.10	NGC 1647
33	1399	0.93	1688.94	0.48	3.02	0.03	1.71	7.50	0.10	0.10	Stephenson 1
34	107	12.35	1849.22	1.11	5.83	0.02	3.28	8.80	0.05	0.10	Ruprecht 98
35	359	3.87	1757.89	1.82	2.18	6.25	3.71	9.20	0.05	0.10	NGC 752
36	232	2.59	1814.2	0.74	5.62	0.04	0.91	8.80	0.05	0.10	Melotte 111
37	171	4.63	1634.79	0.43	3.06	0.02	0.66	8.10	0.20	0.10	...
38	241	3.29	1790.91	1.3	0.6	6.25	4.77	8.00	0.05	0.10	...
39	294	4.92	1708.36	0.62	2.4	6.23	0.89	8.50	0.35	0.10	...
40	161	17.43	1912.98	1.65	5.64	0.13	1.51	8.80	0.05	0.10	...
41	152	0.95	1790.31	0.61	5.51	0.04	0.97	8.60	0.30	0.10	...
42	229	10.87	1917.12	0.13	6.25	6.25	5.16	8.90	0.05	0.10	Alessi 3
43	871	0.87	1696.0	0.24	3.02	6.22	2.93	7.70	0.15	0.10	BH 99

Continued on next page

3 The Age Distribution of Stellar Orbit Space Clumps

Table 3.2 – continued from previous page

Group	N*	J_R (kpc km s ⁻²)	J_ϕ (kpc km s ⁻²)	J_Z (kpc km s ⁻²)	Θ_R (rad)	Θ_ϕ (rad)	Θ_Z (rad)	log τ	$\sigma_{\log \tau}$	[Fe/H]	Cluster
44	381	3.38	1803.64	0.86	0.06	0.06	3.75	8.00	0.05	0.10	Alessi 12
45	1077	5.67	1740.7	0.31	0.22	6.23	1.33	7.90	0.45	0.10	NGC 6124
46	155	3.02	1867.78	0.16	5.79	0.04	1.63	8.80	0.05	0.10	...
47	127	2.09	1657.79	0.54	3.37	0.04	1.79	7.90	0.30	0.10	...
48	128	2.08	1712.15	0.14	2.56	6.2	2.62	7.60	0.05	0.10	Trumpler 10
49	387	3.32	1851.33	0.99	1.52	6.21	1.49	8.70	0.05	0.10	NGC 2281
50	640	9.01	1646.3	0.2	3.52	0.05	3.63	8.10	0.20	0.10	Melotte 22
51	226	13.22	1963.6	0.25	5.56	0.12	2.5	8.10	0.05	0.10	COIN-Gaia 13
52	297	7.88	1855.43	0.28	5.72	0.06	6.04	8.80	0.05	0.10	...
53	327	2.47	1772.2	0.02	0.29	6.26	6.16	8.30	0.20	0.10	NGC 6475
54	462	7.97	1974.53	0.78	5.74	0.07	5.08	8.70	0.15	0.10	NGC 1647
55	163	17.34	1917.93	0.35	5.53	0.11	1.26	8.40	0.30	0.10	ASCC 41
56	122	3.26	1845.88	0.19	0.68	6.25	1.23	8.70	0.35	0.10	Platais 3
57	171	1.28	1733.91	0.13	2.35	6.2	2.6	7.70	0.05	0.10	Trumpler 10
58	717	1.5	1723.34	0.12	2.44	6.2	2.65	7.60	0.05	0.10	Trumpler 10
59	475	4.44	1605.23	0.21	2.45	6.26	1.96	8.90	0.05	0.00	IC 4756
60	793	12.78	1937.18	0.38	5.95	0.07	2.18	9.00	0.20	0.10	...
61	243	14.54	1851.62	0.83	6.13	0.09	0.93	9.00	0.05	0.10	Alessi 62
62	220	16.2	1561.3	1.04	2.05	6.12	3.59	7.90	0.05	0.10	Mamajek 4
63	428	4.07	1744.38	0.17	2.41	6.18	2.29	8.00	0.05	0.10	NGC 2422
64	653	2.47	1765.78	0.17	2.39	6.19	2.31	8.00	0.05	0.10	NGC 2422
65	121	7.48	1731.42	0.15	1.22	6.17	5.72	8.10	0.20	0.10	...
66	114	4.62	1653.71	0.26	4.92	0.08	0.15	8.90	0.05	0.10	ASCC 90
67	208	16.46	1886.53	0.52	5.65	0.11	2.3	8.90	0.15	0.10	...
68	509	0.1	1715.53	0.55	3.04	6.22	0.26	8.60	0.05	0.10	NGC 3532
69	107	2.17	1794.33	0.78	0.27	6.26	4.21	8.40	0.25	0.10	...
70	875	7.83	1899.92	0.37	5.65	0.09	2.06	8.90	0.10	0.10	...
71	179	4.24	1673.15	0.54	3.49	0.03	1.62	9.30	0.20	0.10	...
72	207	3.45	1717.36	0.78	2.14	6.19	1.11	8.60	0.40	0.10	...
73	2677	16.3	1914.66	0.35	5.74	0.1	2.34	9.00	0.20	0.10	...
74	159	1.65	1719.6	0.14	2.49	6.2	2.76	7.70	0.20	0.10	...
75	477	13.93	1720.57	0.37	1.59	6.11	1.14	9.10	0.20	0.10	...
76	1176	0.84	1822.89	0.19	6.2	6.25	3.67	7.60	0.10	0.10	Collinder 135
77	287	7.68	1575.09	0.3	4.34	0.05	5.72	8.40	0.05	0.10	NGC 6025
78	162	21.5	1872.02	0.38	5.56	0.16	6.1	8.90	0.15	0.10	...
79	536	8.05	1950.77	2.1	5.61	0.02	1.2	8.70	0.05	0.10	NGC 2548
80	624	16.45	1879.6	0.06	5.57	0.12	2.0	9.10	0.25	0.10	...
81	5236	2.7	1684.49	0.22	2.78	6.26	0.83	8.10	0.45	0.10	Platais 3
82	208	4.17	1642.18	0.44	3.03	6.27	5.3	8.70	0.40	0.10	...
83	137	6.28	1618.91	0.39	3.0	0.01	0.69	8.10	0.15	0.10	...
84	704	2.87	1868.11	1.5	5.02	0.01	3.8	8.30	0.05	0.10	NGC 2287
85	213	3.02	1824.24	1.85	0.26	6.22	5.08	8.90	0.05	0.10	NGC 1901
86	161	17.58	1940.0	0.97	5.97	0.05	3.87	8.90	0.05	0.10	...
87	575	0.1	1744.3	0.6	6.17	6.23	0.25	8.10	0.05	0.10	NGC 3532
88	470	1.22	1661.24	0.21	4.86	0.03	0.64	8.50	0.10	0.10	NGC 6281
89	488	3.88	1919.99	1.14	5.34	0.1	5.47	8.90	0.25	0.10	NGC 1342
90	254	2.63	1704.19	0.03	2.34	6.28	1.0	7.80	0.05	0.10	NGC 7058
91	122	18.47	1906.46	0.45	5.8	0.06	1.1	8.70	0.05	0.10	...
92	111	4.04	1619.59	0.55	4.1	0.04	4.3	7.80	0.05	0.10	Alessi 24

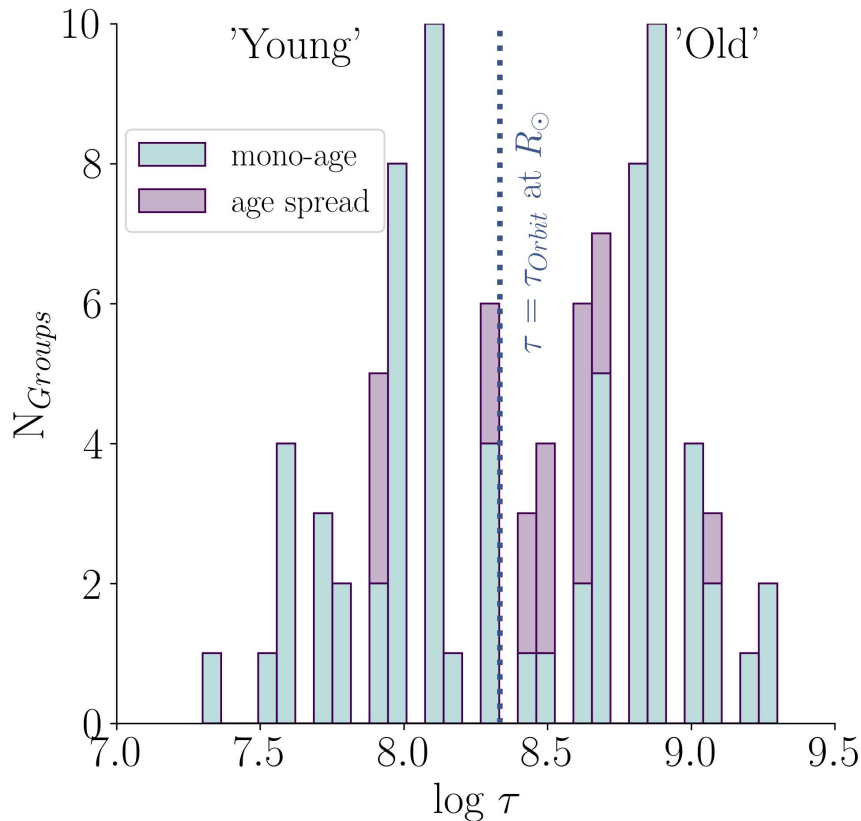


Figure 3.7. Histograms of the distribution of age ($\log \tau$) across the set of 92 groups. About half of them (43) are younger than an orbital period, and 49 of them are older. The central timescale, the orbital period at the Solar radius is indicated by the blue dotted vertical line, for which we adopt $\log \tau = 8.33$. The intrinsic age spread is indicated in the colorcoding of the bars, where groups with an intrinsic age spread are shown in magenta, and mono-age groups are illustrated in turquoise.

Note. We provide the group number, the number of member stars N_* , and the median action and angle coordinates of all groups. Additionally, we state the age $\log \tau$, the intrinsic age spread $\sigma_{\log \tau}$, and the metallicity $[Fe/H]$ as determined by our likelihood isochrone fitting for each group. For the subset of 62 groups which we identified in the cluster catalog by [Cantat-Gaudin et al., 2020](#), we list the literature name in the last column, as well as for the Meingast 1 (Pisces-Eridanus) stellar stream that we identified from [Meingast et al., 2019](#).

(This table is available in machine-readable form.)

HOW OLD ARE THE GROUPS? ARE THEY MONO-AGE?

Figure 3.7 shows the distribution of ages ($\log \tau$) among the 92 groups, which range from 20 Myrs to 2 Gyrs: all are much younger than the mean age of Galactic disk stars ($\sim 3-5$ Gyrs). For our purpose, the definitions of “young” *vs.* “old” revolve around dynamical time-scales: one central timescale, the orbital period at the Solar radius is indicated by the blue dotted vertical line, for which we adopt $\log \tau = 8.33$. We find that half (43) of the groups are young in this sense, younger than one dynamical period. The 49 older groups have ages $\tau = 1 - 7 t_{orbit} \ll t_{Hubble}$.

3 The Age Distribution of Stellar Orbit Space Clumps

Our fitting also shows that almost 80% (72) of the groups seem to be "effectively mono-age", with $\sigma_{\log \tau} \leq 0.2$; only 20 groups show a modest age dispersion of $\sigma_{\log \tau} > 0.2$. The value of 0.2 to distinguish these two regimes was chosen by comparing $\sigma_{\log \tau}$ to the uncertainty $\delta_{\log \tau}$ of the isochrone fit, which is typically around 0.1 (see Section 3.6.4). The intrinsic age spread is indicated in the color coding of the bars in Figure 3.7, where groups with significant intrinsic age spread are shown in magenta, and mono-age groups are shown in turquoise.

This result immediately shows that none of these groups are just stars herded together by orbital resonances, as a wide intrinsic age spread would be expected in this case.

The best fitting metallicities fall almost exclusively on $[Fe/H] = 0.1$, with only one group showing a metallicity of $[Fe/H] = 0.0$. They are essentially all Solar $[Fe/H]$, as expected for young stars near the Solar radius. Whether the slightly super-Solar values, surprising in light of the $[Fe/H]$ of the present-day ISM at the Solar radius, reflect slight $[M/H]$ -systematics in the isochrone fitting, remains open. Our metallicities are purely photometric, and draw in many cases heavily on the colors of lower main-sequence objects, whose isochrone-predicted colors are known to be uncertain. Therefore, our metallicities may well be subject to systematic errors at the 0.2 dex level. We consider this to be not relevant for our analysis, as the covariance between ages and metallicities are not a source of serious systematics in the age determinations.

SPATIAL STRUCTURE OF THE GROUPS

The spatial extent of the 92 groups (color-coded) is shown in Figure 3.8 in a top-down view onto the Milky Way. For a better overview, the left panel shows the 43 groups younger than one Galactic revolution ($\tau < 250$ Myrs), and the right panel shows the 49 old groups with ages > 250 Myrs. This figure reveals a variety of spatial distributions and the internal spatial extents of the groups: some heterogeneous morphologies with little center-to-edge structure, and often an extent of $\gtrsim 100$ pc; some show a tight clustered "core" with or without tidal (or uncertainty-driven) tails. For the most part, these tails extend along the direction of the Galactic rotation as extended for tidal tails, as found and discussed previously in various papers (Fürnkranz et al., 2019; Meingast & Alves, 2019; Meingast et al., 2021; Röser & Schilbach, 2019; Röser et al., 2019; Tang et al., 2019). Overall, most groups extend across several hundred parsecs on the sky.

OVERLAP WITH EXISTING CLUSTER CATALOGS

As was already apparent from the age comparison with Cantat-Gaudin et al., 2020, many of our groups are in published catalogs. Specifically, 33% of stars that are in one of our groups have a crossmatch with the Cantat-Gaudin et al., 2020 cluster catalog, 52% with the Hunt and Reffert, 2023 catalog, and 49% with the catalog of Kounkel and Covey, 2019, known to be complete by also contaminated (Zucker et al., 2022).

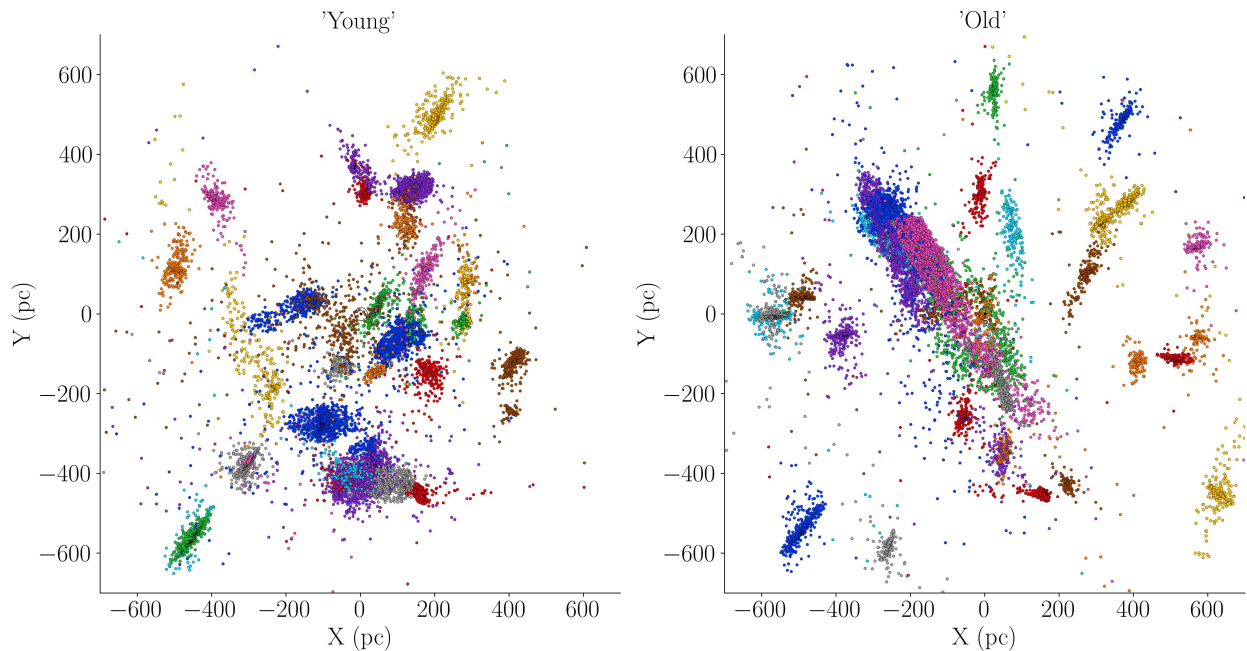


Figure 3.8. Top-down views on the 92 action-angle groups in Galactic Cartesian coordinates, where the Sun is located at $(X,Y) = (0,0)$. Left: 43 young groups with ages < 250 Myrs. Right: 49 old groups with ages > 250 Myrs. Their morphologies are either heterogeneous, or show a tight clustered “core” with or without tidal (or uncertainty-driven) tails.

Among our 92 groups, 22 have no stars in common with any clusters in [Cantat-Gaudin et al., 2020](#); the majority of our groups (51) have stars that overlap with exactly one cluster in [Cantat-Gaudin et al., 2020](#). Remarkably, for 19 of our groups the stars within one group overlap with several (up to ten) clusters in the [Cantat-Gaudin et al., 2020](#) catalog. This shows that our algorithm – designed to also identify loose orbit-space groups – can and does encompass several clusters if they are on near-identical orbits at very similar orbital phases. This is very much in line with the extended structure of our groups, already discussed in [Section 3.7.2](#).

3.8 SUMMARY AND DISCUSSION

We have set out to devise and implement a new stringent two-step method to determine isochrone ages of action-angle groups in the nearby Galactic disk, even if they are sparse and widely dispersed. First, we overcome the limitation that the initial sets of stars, found to be clustered in 6D action-angle space, have a limited T_{eff} -range that hinders age dating with isochrones. We do this by projecting the 6D action-angle patch into the 5D space of position and proper motion, where the Gaia catalog is far more extensive. We can identify typically an order of magnitude more likely members. The second step is the actual isochrone fitting, as a function of both age and metallicity. This fitting accounts for a number of factors important here: the group members may be widely distributed in sky position, distance and reddening; they may have sizeable parallax uncertainties; and we must account for binaries and other “outliers“, such

as stars that are not group members. We do not only determine the mean age of each group, but we also test whether any group’s CMD provides evidence for a significant intrinsic age spread. We find that our approach provides well-constrained ages, age dispersions and metallicities.

We have found that all of the identified 92 action-angle groups are “young“ in a global Galaxy formation sense: $\tau \ll \tau_{disk} \approx 8 - 11$ Gyrs, as they all have $\tau \leq 2$ Gyrs. About half of them are even younger than a dynamical period ($< t_{orbit} \approx 250$ Myrs). The large majority of them is consistent with a mono-age population, $\sigma_{\log \tau} \leq 0.2$ mag.

Not accounting for differential selection effects, we find that the distribution $p(\log \tau)$ is broadly constant between $\log \tau = 7$ and 9, which would naively imply that $p(\tau) \propto \tau^{-1}$.

We also find that some groups are spatially extended and most likely entirely unbound, while others are spatially compact.

These findings fit together in a picture in which these action-angle groups indeed reflect ensembles of stars born at nearly the same time in nearly the same place, and are now dispersing to become field stars. How rapidly these groups of stars disperse, and how compact they once were, would require quantitative modelling of their actions and angles, which we will carry out in a forthcoming paper.

We have also found that we are not severely limited in the age determination by the group member sample size with our approach, as our algorithm provides almost the exact same age estimates for all groups if we randomly sample only half of their stars. This bodes well for applying the same approach in a forthcoming paper to the smallest and most diffuse groups we can identify, such as the *pearls on a string* found by Coronado et al., 2022 for a set of action angle groups: these are – often numerous – further clumps in angle (or orbital phase) space on nearly the same orbit as the initially identified action-angle group.

ACKNOWLEDGEMENTS

We wish to thank the anonymous referee for the useful comments, which improved both the clarity and quality of this study. We also thank the MPIA Milky Way group and Andy Gould for providing useful comments. V.F. acknowledges support from the International Max Planck Research School for Astronomy and Cosmic Physics at Heidelberg University (IMPRS-HD). This work has made use of data from the European Space Agency (ESA) mission Gaia (<https://www.cosmos.esa.int/gaia>), processed by the Gaia Data Processing and Analysis Consortium (DPAC, <https://www.cosmos.esa.int/web/gaia/dpac/consortium>). Funding for the DPAC has been provided by national institutions, in particular the institutions participating in the Gaia Multilateral Agreement. *Software*: we acknowledge various Python packages that were used in the data analysis of this work, including astropy (Astropy Collaboration et al., 2013; 2018), NumPy (Harris et al., 2020), SciPy (Virtanen et al., 2020), Matplotlib (Hunter, 2007), and scikit-

learn (Pedregosa et al., 2011). This research also made use of the TORUSMAPPER package (J. Binney & McMillan, 2016), which is part of the AGAMA library (Vasiliev, 2019).

ORCID IDs

Verena Fürnkranz <https://orcid.org/0000-0002-9460-0212>

Hans-Walter Rix <https://orcid.org/0000-0003-4996-9069>

Johanna Coronado <https://orcid.org/0000-0001-6629-0731>

Rhys Seeburger <https://orcid.org/0000-0001-8898-9463>

4 AGES FOR LARGE SETS OF STELLAR AGGREGATES

4.1 PRE-ABSTRACT

In this scientific chapter, we apply an updated version of the age-dating technique we developed and presented in Chapter 3 to two large sets of stellar aggregates, with the goals a) to obtain their age distributions, b) to map orbit-age correlations of stellar ensembles with sufficient number statistics, c) to understand the nature of sparse stellar groups, e.g. *pearls*¹, and d) to use the results as a basis to further investigate the dispersal of stellar aggregates in the Milky Way disk. When investigating the results of the isochrone fitting, we find the existence of an age ambiguity for groups where neither the lower main sequence nor the main sequence turn-off offers enough age information. This results in a pronounced bimodality in the age distribution of both cluster datasets, with almost no stellar ensembles in the age range around $\log \tau \sim 8-8.5$. This finding forces us to restrict our further analysis; however, first steps in exploration of the orbit age space will be shown in Section 5.1.

4.2 LARGE SETS OF STELLAR CLUSTERS

In order to explore the orbit and age space of stellar aggregates, it is of advantage to use as large as possible stellar ensemble datasets for better statistics. Here, we demonstrate two straight ways of getting large sets of stellar aggregates: first, we identify sparse groups by adapting the DBSCAN clustering parameter settings of the action-angle space clustering as shown in Furnkranz et al., 2024 (also, see Section 4.2.1). Secondly, we take an existing state-of-the-art stellar cluster catalog, with the largest up-to-date one published by Hunt and Reffert, 2023 (see Section 4.2.2). Although this catalog is not designed to find spatially sparse groups (as stars are clustered in a 5D position-proper motion space rather than action angles), it has the

¹Here, we move away from our restriction that *pearls* are only groups that are on orbits similar to the most prominent stellar clusters. We want to find *pearls* (e.g. sparse stellar aggregates) in the whole orbit and orbital phase space, and not only on pre-selected orbits as shown in Coronado et al., 2022. Therefore, we search for sparse groups in the whole orbit and orbital-phase space within 800 pc from the Sun, with the aim of getting a coherent overview of the overall distribution of such groups.

advantage of providing literature age estimates, which we can use to compare to the ages derived with our method.

4.2.1 IDENTIFYING GROUPS WITH ACTION-ANGLE SPACE CLUSTERING

We base our group identification exclusively on Gaia DR3 (Gaia Collaboration et al., 2023). We clean the data set from sources with spurious astrometry by excluding sources with $\text{fidelity_v2} < 0.9$, and apply a $\text{parallax_over_error} \geq 3$ cut to reduce distance uncertainties. We further limit the sample to stars within the extended solar neighborhood with a $\varpi \geq 1.25$ cut, keeping only stars within 800 pc from the Sun. Also, we limit the catalog to stars that have radial velocity (v_r) measurements, resulting in a database of 9,080,884 sources.

For this data sample, we calculate actions (J) and angles (Θ) with the full 6D position–velocity information and an assumed gravitational potential, for which we use Galpy’s axisymmetric MWPotential2014 (Bovy, 2015). We then make use of the Stäckel Fudge algorithm by J. Binney, 2012 to estimate the action angle coordinates.

Based on the method described in Fürnkranz et al., 2024, we identify stellar aggregates in 6D (J, Θ)-space. We describe all orbital angles via their sine and cosine functions to avoid problems with their periodicity. We then normalize the action angle coordinates ($J_R, J_\phi, J_Z, \sin(\Theta_{R,\phi,Z}), \cos(\Theta_{R,\phi,Z})$) by removing the mean and scaling to the unit variance. We also reduce the variance in the angle coordinates by multiplying the scaled data by 0.2. We apply the density-based clustering algorithm DBSCAN (Ester et al., 1996) to this final dataset. In contrast to Fürnkranz et al., 2024, we relax the parameter setup of the clustering to $\epsilon=0.0275$ while keeping $\text{MinPts}=20$. With this setup, we identify 909 clusters, from which we keep a final set of 695 clusters with at least 20 member stars.

4.2.2 STATE-OF-THE-ART CLUSTER CATALOG BY HUNT ET AL. 2023

Another way to obtain a large set of stellar clusters is to extract groups from an established cluster catalog, as is the one published by Hunt and Reffert, 2023, who cluster stars in 5D position-proper motion space using the density-based clustering algorithm HDBSCAN. We download the catalog, which comprises 7167 groups, of which 6818 groups are labeled as open clusters, 228 groups are labeled as moving groups, and 121 groups are globular clusters. We then select all clusters that have a median cluster center within 800 pc to the Sun, which excludes the whole globular cluster sample and leaves a set of 1191 clusters. We further restrict this sample to groups that have at least 10 stars with radial velocity (v_r) measurements to be able to properly explore their orbit space. We decide on a v_r -member star ≥ 10 cut instead of the v_r -member star ≥ 20 cut applied to the action-angle clustering, because this leaves a larger final set of 836 clusters, instead of 558 clusters.

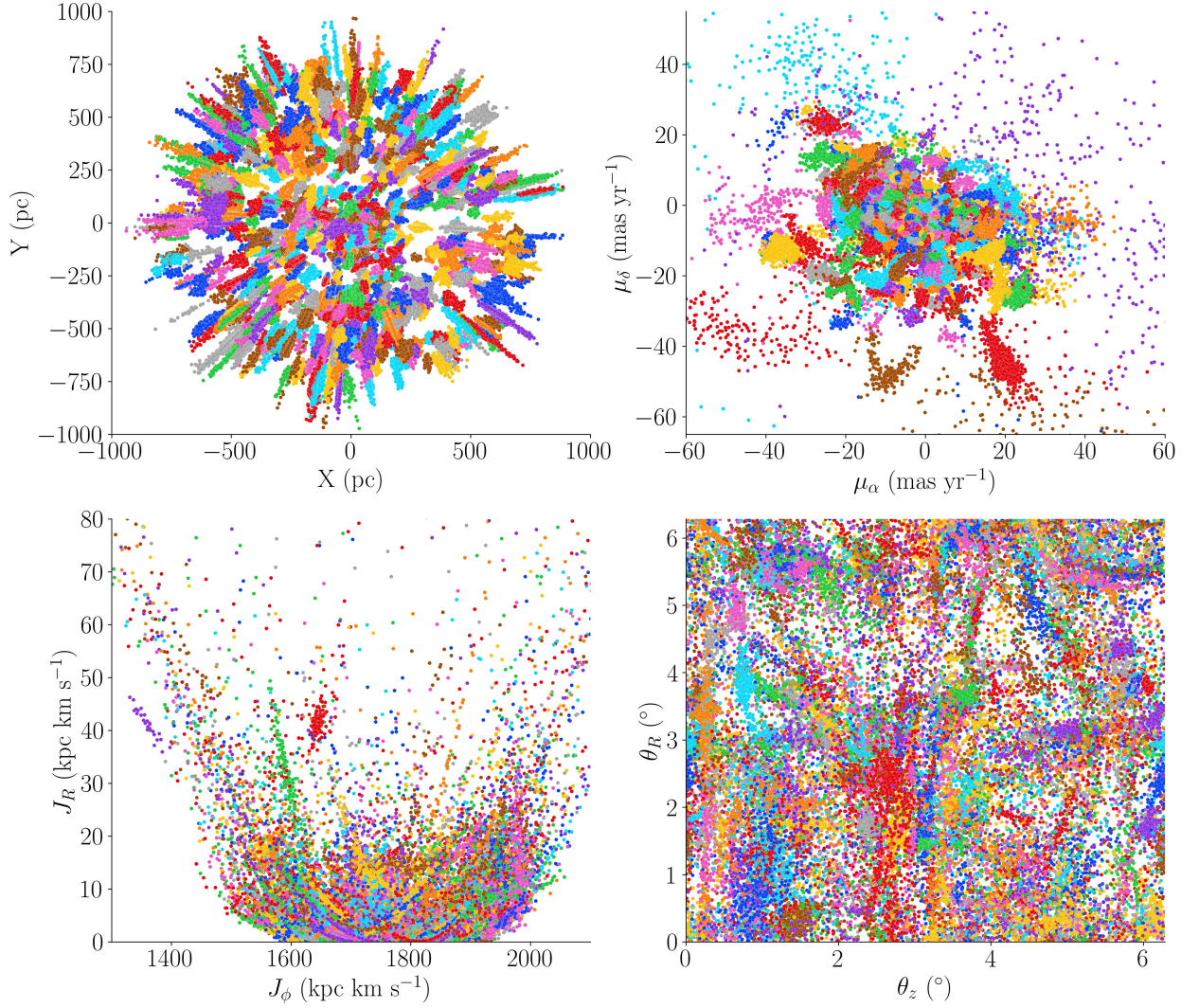


Figure 4.1. The member stars of the 836 stellar clusters within 800 pc from the Sun, extracted from the catalog published by [Hunt and Reffert, 2023](#). The various colors represent the different groups. Top left: top-down view on the 836 groups in Galactic Cartesian coordinates. Top right: proper motion distribution of the 836 groups. Bottom left: (J_Φ, J_R) -action plane showing the distribution of the v_r -subset of the 836 groups. Bottom right: (Θ_Z, Θ_R) -angle distribution of the v_r -subset of the 836 groups. Per construction the groups are tight blobs in position-proper motion space, but appear dispersed in action-angle coordinates.

Figure 4.1 shows the resulting cluster distribution, color-coded by group. The top row shows their distribution in a top-down view on the 836 groups in Galactic Cartesian coordinates (left), and their distribution in proper motion space (right). This group sample comprises 139300 stars with 5D position-parallax-proper motion information. The bottom row illustrates the distribution of the radial velocity subset of all groups, including a limited number of 43836 stars. The left panel illustrates their distribution in the (J_Φ, J_R) -action plane, and the right panel shows the (Θ_Z, Θ_R) -angle plane. [Hunt and Reffert, 2023](#) selected their groups based on the 5D position-proper motion space, which is why, by construction, all groups are tightly clustered in the top row of Figure 4.1, and appear quite dispersed in the action-angle space as can be seen in the bottom row.

4.3 ASSOCIATING ADDITIONAL MEMBER STARS IN 5D POSITION-PROPER MOTION SPACE

Unlike the cluster data set we extract from the [Hunt and Reffert, 2023](#) catalog, the data set in action angle space is derived from the temperature-limited Gaia radial velocity sample. Therefore we apply the method described in [Fürnkranz et al., 2024](#) to associate additional member stars in 5D position-proper motion space, as we need well-populated stellar sequences in the color-magnitude diagrams to estimate robust ages of these groups by fitting isochrones. As described in more detail in [Fürnkranz et al., 2024](#), we first construct an approximate Probability Density Function (PDF) for each group in action-angle space. We then sample 5000 random points from this distribution and map them to position-proper motion space using the TORUSMAPPER package ([J. Binney & McMillan, 2016](#)), which is part of the AGAMA library ([Vasiliev, 2019](#)). We then perform a kernel density estimate (KDE) on the coordinates $(X, Y, Z, \mu_\alpha, \mu_\delta)$. In contrast to [Fürnkranz et al., 2024](#), we do not choose the minimum and maximum coordinates in $(X, Y, Z, \mu_\alpha, \mu_\delta)$ as the KDE box boundaries for each group, but instead define the minimum and maximum KDE box boundaries for each group as three standard deviations of its mean $(X, Y, Z, \mu_\alpha, \mu_\delta)$ -coordinate. We do this because some groups show very large extents in this 5D parameter space, which subsequently would significantly slow down our computation. However, this restriction results in non-physical spatial boundaries of the groups, which can be seen in the top left panel of [Fig. 4.2](#). Since our primary goal is to determine the ages of the groups and not to investigate their spatial structure, these boundaries can be tolerated for now. With this 5D density distribution we then assign a density value ρ to each star in the full Gaia catalog, for which we apply a relaxed distance cut of $\varpi \geq 1$ but a more confined parallax_over_error ≥ 10 cut. This includes 41,138,028 sources.

We then assign density values following the same procedure to a smooth Gaia catalog. We choose the Gaia Early DR3 smooth mock catalog as published by [Rybizki et al., 2020](#), apply the same distance cut of $\varpi \geq 1$ and add WHERE popid !=11 into the ADQL query, which removes clusters and moving groups. The final catalog includes 46,830,045 stars, comparable to the size of the full Gaia catalog. We then set a density threshold where each group's 5D density is significantly higher than the density in the Gaia mock catalog. We slightly change the setup of the density threshold from [Fürnkranz et al., 2024](#): first, we define a density threshold T_1 as the lowest density bin where the density of the Gaia sample is 25 times higher than expected from the Gaia mock sample, with the additional condition of containing ≥ 200 stars. Second, we calculate the ratio between the bins and set the density threshold T_2 to have a ratio ≥ 2 , with the additional condition to contain at least 200 stars. Third, we set the density threshold T_3 to make the cut at the density bin where at least 200 stars are available. We then pick the final density threshold for each group individually by setting the priority of density cuts on the order $T_1 > T_2 > T_3$, to assign as many candidate 5D members as possible to each group. For each group, we then merge the v_r restricted group member selection drawn from the restricted radial velocity data set with the extended selection of members obtained with this method.

The resulting cluster distribution (color coded by group) is presented in Figure 4.2. The top row shows the distribution of the 695 groups in a top-down view in Galactic Cartesian coordinates (left), and their distribution in proper motion space (right). The bottom row illustrates their distribution in the (J_Φ, J_R) -action plane (left) and the (Θ_Z, Θ_R) -angle plane (right). Per construction, the groups are tightly clustered in action-angle space but appear dispersed and extended in position and proper motion space. This is also in clear contrast to the distribution of groups shown in Figure 4.1.

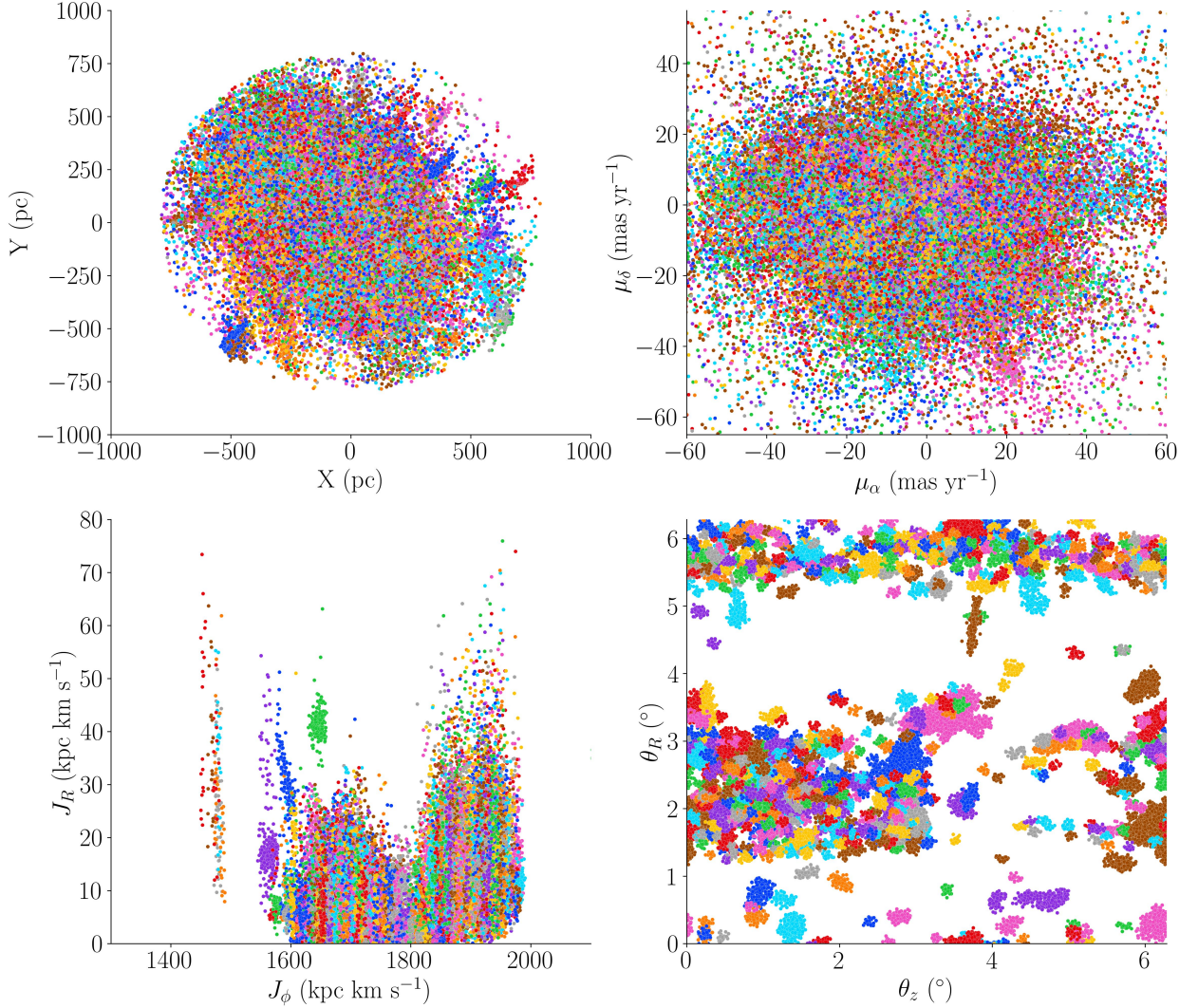


Figure 4.2. The member stars of the 695 stellar groups within 800 pc from the Sun, identified in action-angle space. The various colors represent the different groups. Top left: top-down view on the 695 groups in Galactic Cartesian coordinates. Top right: proper motion distribution of the 695 groups. Bottom left: (J_Φ, J_R) -action plane showing the distribution of the v_r -subset of the 695 groups. Bottom right: (Θ_Z, Θ_R) -angle distribution of the v_r -subset of the 695 groups. Per construction the groups are tight blobs in action-angle space, but appear dispersed and extended in position-proper motion space. The non-physical spatial group boundaries visible in the top left panel are the result of a restricted membership assignment, which we accept for computational speed reasons.

4.4 SPECTROSCOPIC METALLICITIES BY ANDRAE ET AL. 2023

In [Fürnkranz et al., 2024](#) we derive ages for stellar aggregates by optimizing the global parameters $\log \tau$ and $[\text{Fe}/\text{H}]$. Here, we make use of a metallicity prior for each group, which we obtain from spectroscopic metallicities from Gaia low-resolution XP spectra. [Andrae et al., 2023](#) published a catalog of data-driven $[\text{M}/\text{H}]$ estimates for ~ 175 million sources, with a resulting mean precision of 0.1 dex. They show that these metallicity estimates are specifically robust for solar-type stars, e.g. in the regime $0.5 \text{ mag} < G_{BP} - G_{RP} < 1.5 \text{ mag}$ (see Figure 11 (b) in [Andrae et al., 2023](#)).

To make use of these metallicity estimates, we apply this color cut to all stars in the action-angle cluster data set. From 71382 solar-type stars in this dataset, 61748 stars have a spectroscopic metallicity estimate. For each group, we find a minimum of 25 stars with a metallicity estimate, while on average each group has around 57 stars with metallicity estimates. For all groups, we then calculate their median metallicity value from all stars with a metallicity estimate. The resulting distribution $[\text{M}/\text{H}]$ is shown in the left panel in Figure 4.3. The ensemble metallicity for all stars in the action-angle cluster dataset is slightly sub-solar, with a value of -0.052.

We also apply this color cut to all stars in the cluster dataset that we obtain from the [Hunt and Reffert, 2023](#) catalog. This sample comprises 36845 solar type stars, of which 30163 stars have a spectroscopic metallicity. Typically each group has about 23 stars with a metallicity estimate, with a minimum of one star with a metallicity estimate per group. For 61 groups for which we find < 5 stars with an $[\text{M}/\text{H}]$ estimate, we apply the ensemble metallicity for all stars in this cluster dataset, which is -0.102. For the other groups, we calculate their median metallicity value from all stars with metallicity estimates in this group. The resulting distribution of $[\text{M}/\text{H}]$ values is shown in the right panel of Figure 4.3, and is shifted to slightly lower metallicities than the distribution for the action angle cluster sample.

4.5 RESULTS AND DISCUSSION

For our age determination method using a likelihood isochrone approach, we use PARSEC isochrone models ([Bressan et al., 2012](#)). We download the default isochrone tables for a set of six metallicities $[\text{Fe}/\text{H}] = -0.4$ to $+0.1$ and 107 ages from $\log \tau = 5$ to 10.3, resulting in an isochrone table comprising 224.951 entries. For each individual isochrone we then interpolate Mass , G_{mag} , BP_{mag} and RP_{mag} whenever $\Delta G_{mag} > 0.03 \text{ mag}$ between two mass points as described in [Fürnkranz et al., 2024](#), to double the isochrone entries to a total of 458.181.

For the subsequent isochrone fitting, we group the obtained spectroscopic metallicity estimate for each stellar aggregate into the best-fit metallicity value in the predefined isochrone metallicity grid $[\text{Fe}/\text{H}] = -0.4$ to $+0.1$ with a step size of 0.05 dex. We then apply the same isochrone fitting methodology to the

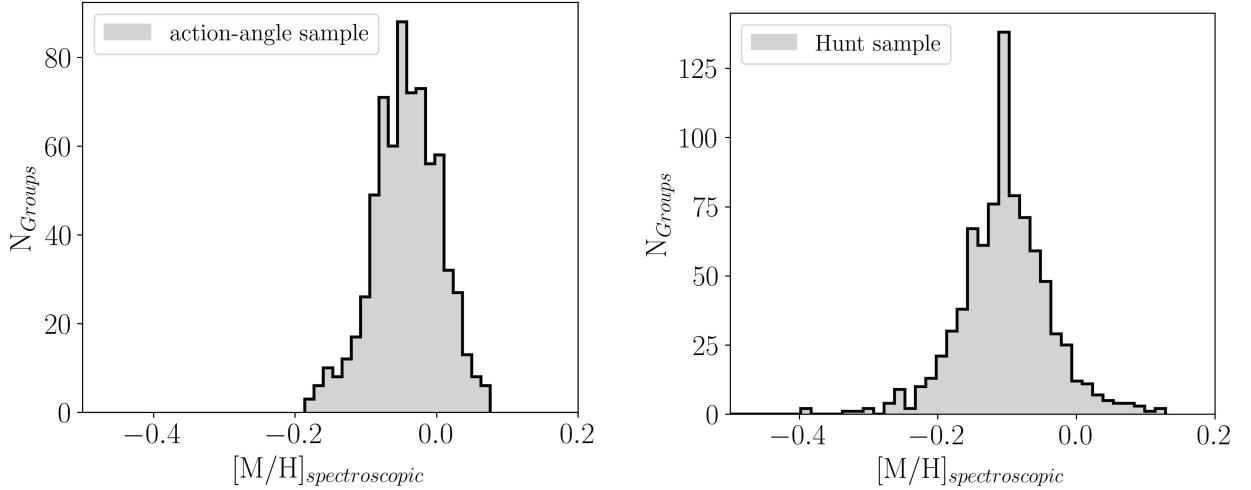


Figure 4.3. Spectroscopic metallicity distributions of stellar aggregates as derived from Gaia XP spectra (Andrae et al., 2023). Left: action angle sample, with a median $[M/H]$ value for all stars in this dataset of -0.052 . Right: cluster sample from Hunt and Reffert, 2023, with a slightly lower median $[M/H]$ value for all stars in this dataset of -0.102 .

groups in both datasets as described in Fürnkranz et al., 2024, with the only difference of using the fixed pre-estimated metallicity for each group, which also speeds up the isochrone fitting code.

4.5.1 AGE DISTRIBUTIONS

The result of the isochrone fitting for all groups is illustrated in Figure 4.4: the left panel shows the age distribution ($\log \tau$) among the 695 stellar groups identified in action-angle space, and the right panel in Figure 4.4 shows the age ($\log \tau$) distribution among the 836 stellar aggregates extracted from the Hunt and Reffert, 2023 catalog. The light gray distribution in the right panel illustrates the literature age distribution as derived by Hunt and Reffert, 2023, who estimate the ages of the stellar groups using a convolutional neural network.

In both cases (both panels), the ages derived with our likelihood isochrone fitting approach show a strong bimodality in the distributions, with most of the clusters having an age estimate of either $\log \tau < 8$ or $\log \tau > 8.5$, and a significant age gap between $8 < \log \tau < 8.5$, corresponding to an age gap between ~ 100 - 300 Myr. This contrasts to the distribution of the ages of the literature, as derived and published by Hunt and Reffert, 2023, whose age estimates form a Gaussian-shaped distribution that peaks at ages around $\log \tau \sim 8$, and a well-populated tail extending to younger ages. In addition, their distribution completely lacks the second bimodality peak at $\log \tau \sim 9$.

Surprisingly, this clear bimodality in the age distribution derived with our isochrone fitting method appears in both kinds of ‘group setups’: for groups clustered in action-angle space and for clusters from the state-of-the-art cluster catalog by Hunt and Reffert, 2023. In order to understand the unexpected lack of groups with ages between $\log \tau > 8$ and $\log \tau < 8.5$ we investigate the likelihood functions of a few

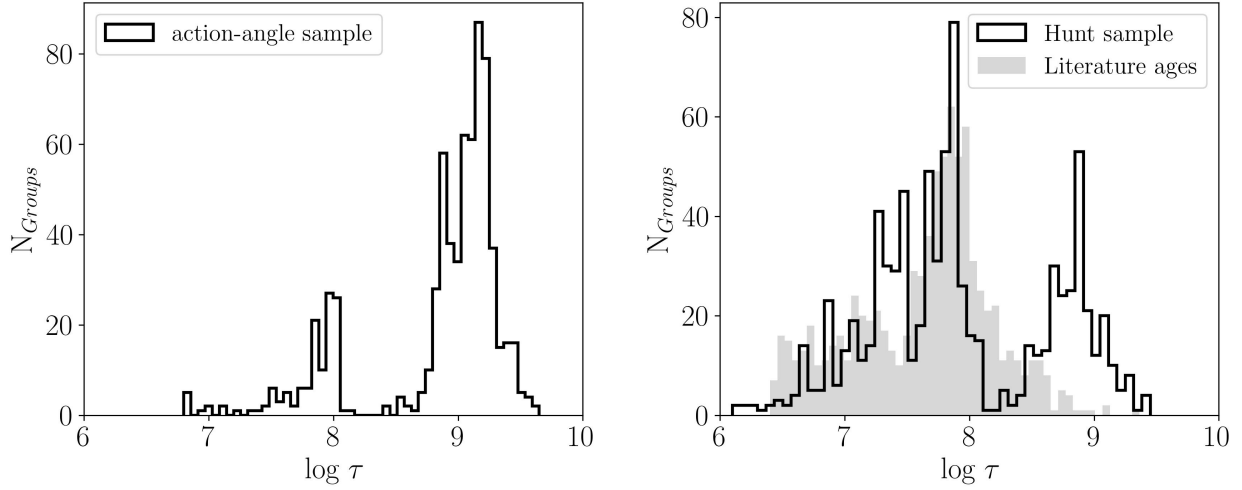


Figure 4.4. Age distributions of stellar aggregates. Left: action angle sample. Right: cluster sample from [Hunt and Reffert, 2023](#), with their literature age estimates in light gray. Both ‘group set-ups’ show a bimodality in their age distributions as derived with our isochrone fitting method.

example groups in more detail, and discuss probable reasons for this unexpected (and probably unreal) distribution of ages.

Figure 4.5 shows two example groups from the action-angle sample: Group 112 and Group 274. The left panel illustrates the calculated value χ^2 as a function of $\log \tau$. The subplot in the top right corner presents a zoom-in version of the region around the lowest χ^2 value. The right panel shows the observational color-magnitude diagram of the group’s member stars as black data points, with the best-fit isochrone as a blue line on top. The value of $[\text{Fe}/\text{H}]$ is pre-estimated from Gaia XP spectra as described in Section 4.4, and the $\log \tau$ value corresponds to the location of the minimum value χ^2 . Both groups represent ‘textbook-examples’ or ‘ideal cases’ for our isochrone fitting methodology, as they show a clear peak towards a specific minimum χ^2 value, indicating that this is the only - and presumably correct - age of the group. The sequences of the groups show narrow distributions, suggesting coeval stellar populations, and the best-fit isochrones match these distributions well. The main age-defining feature for the presumably old Group 112 is the turn-off region, as it is well sampled with a couple of stars beyond the main sequence turn-off. For the presumably young Group 274, the main age-defining feature is the well-populated lower main sequence. For groups younger than ~ 100 Myr ($< \log \tau \sim 8$) the lower main sequence provides the best age constraint, because stars have not settled on the main sequence yet.

Figure 4.6 shows the same likelihood plot and color-magnitude diagram for two other example groups from the action angle sample: Group 384 and Group 217. They represent ‘ambiguous cases’, which frequently occur in the action-angle group dataset. The left panels of Figure 4.6 reveal that both groups do not have a minimum χ^2 peak, but an extended minimum χ^2 region. For Group 384 this region extends between $\log \tau \sim 8 - 10$, where the differences in the χ^2 are minimal. For Group 217 this region extends between $\log \tau \sim 8 - 9$. Within these regions, any age is about equally likely. The right panels reveal that both groups show narrow, coeval sequences on the color-magnitude diagram. However, for

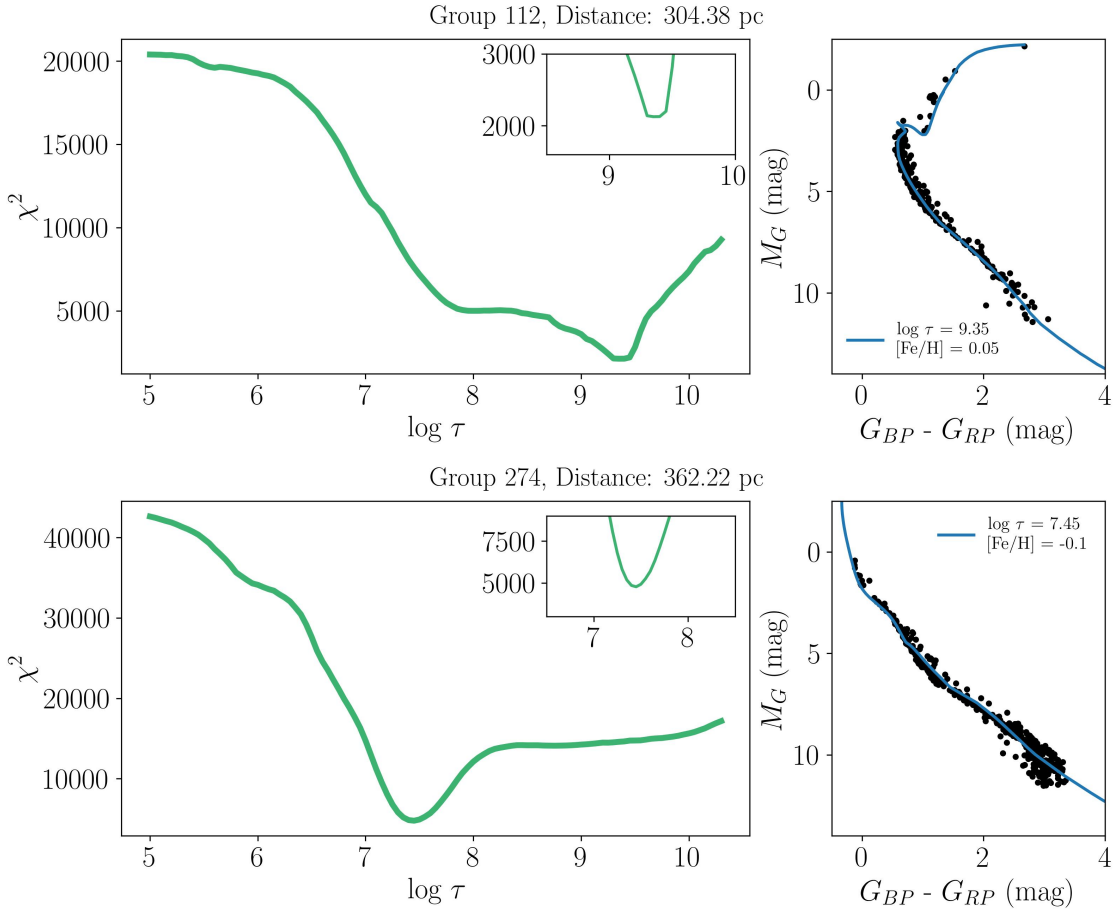


Figure 4.5. Example Groups 112 and 274 as ‘ideal cases’. Left: value χ^2 as a function of $\log \tau$, with a zoom-in subplot in the top right corner. Right: color-magnitude diagram of the groups, with the best-fit isochrone on top in blue.

groups older than ~ 100 Myr ($> \log \tau \sim 8$), the lower main sequence is no longer an age indicator, as all stars have settled on the zero-age main sequence. Therefore, most of the age information is extracted from the turn-off region. As illustrated for Groups 384 and 217, the upper main sequences seem to be too sparsely populated with stars, even after extending the memberships in 5D position-parallax-proper motion space. This is problematic for fitting isochrones to groups older than $\log \tau \sim 8$, where the lower main sequence does not serve as an age indicator, and to groups younger than $> \log \tau \sim 8.5$, where the turn-off region is often too sparsely populated. This is the region where groups cannot be properly aged via our likelihood isochrone fitting, and where our likelihood code assigns them to an age either $\log \tau < 8$ or $\log \tau > 8.5$.

Furthermore, we investigate the dependence of the bimodal age distribution on the extinction estimate and on the distance of the groups. For this, we calculate the median extinction A_G and group all stellar aggregates from the action angle sample into a low extinction sample ($A_G < 0.4$ mag) of 132 groups, a medium extinction sample ($0.4 \text{ mag} \leq A_G \leq 0.5$ mag) of 319 groups, and a high extinction sample ($A_G > 0.5$ mag) of 244 groups. Similarly to this, we also calculate the median distance of all stellar aggregates and group them into a close distance sample ($d < 200$ pc) of 244 groups, a medium distance

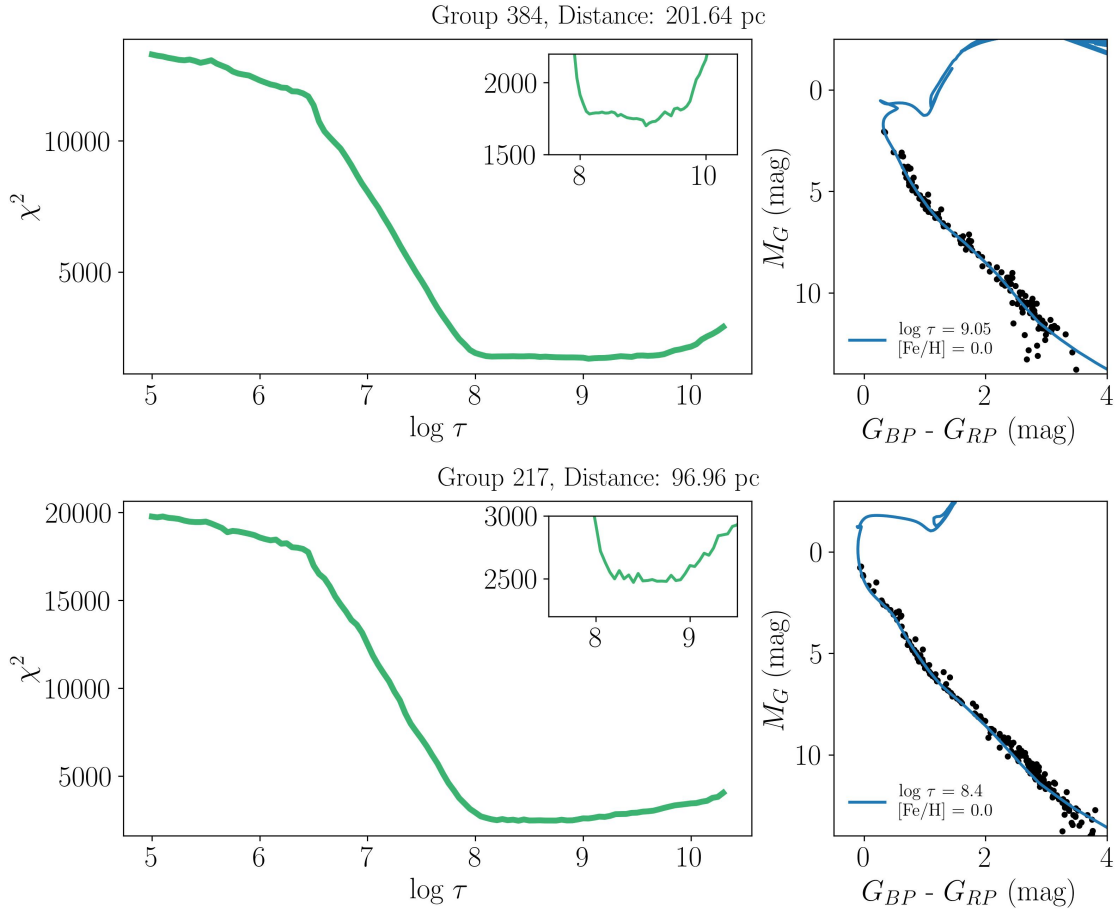


Figure 4.6. Example Groups 384 and 217 as ‘ambiguous cases’. Left: value χ^2 as a function of $\log \tau$, with a zoom-in subplot in the top right corner. Right: color-magnitude diagram of the groups, with the best-fit isochrone on top in blue.

sample ($200 \text{ pc} \leq d \leq 350 \text{ pc}$) of 322 groups, and a far distance sample ($d > 350 \text{ pc}$) of 129 groups. We then investigate the $\log \tau$ distributions of all subsets and find that the age bimodality occurs in all the selected extinction and distance subsets, indicating that neither the distance nor the extinction play a significant role in the bimodal shape of the age distribution.

4.5.2 COMPARISON WITH LITERATURE AGES

To investigate the nature of the second bimodal peak at around $\log \tau \sim 9$, we select all groups with age estimates from our isochrone fitting method between $8.5 < \log \tau < 9.5$, that have a significantly younger age estimate between $7.5 < \log \tau < 8$ from the literature age determination as published by [Hunt and Reffert, 2023](#). This results in a sample of 89 groups, and we illustrate the likelihood function of four example groups in Figure 4.7. This plot shows the likelihood functions of Groups 4059, 5565, 5602, and 5623 in the left panel, and the distribution of the member stars in a color-magnitude diagram as selected by [Hunt and Reffert, 2023](#) in the right panel. On top of each group, the blue isochrone indicates

our age estimate, and the orange isochrone indicates the age estimate of the literature by [Hunt and Reffert, 2023](#).

In contrast to the action angle dataset, some groups comprise only a few member stars due to the different member selection in [Hunt and Reffert, 2023](#). This is of disadvantage for age dating with isochrone fitting, as their sequences also reveal a lack of stars at the turn-off region and the lower main sequence, where most age information comes from. We do not extend the sequences with our method for two reasons: first, we want to compare our age estimates to the age estimates of [Hunt and Reffert, 2023](#) applied to the same member selection and because their member selection was already based on a 5D space. Second, the groups are, per definition, not necessarily tight clumps in action-angle space, which makes our method to extend the membership not directly applicable.

Similarly to what has been seen already in Figure 4.6, all groups reveal an extended minimum region χ^2 rather than a prominent peak χ^2 . For Group 4059, all ages between $\log \tau \sim 7-9$ appear to have a low χ^2 , however, a couple of stars at the bright hot end of the sequence suggest a rather older age of $\log \tau = 8.85$, and not 7.9 as estimated by [Hunt and Reffert, 2023](#). Groups 5565 and 5602 are clearly ambiguous cases: both have very extended χ^2 regions, and the isochrone fits of both our method and the method by [Hunt and Reffert, 2023](#) can be argued well when visually inspecting the group sequences. For Group 5623, ages between $\log \tau \sim 7.8-8.9$ seem plausible, with a few stars at the turn-off region suggesting a rather older age of $\log \tau = 8.8$ rather than $\log \tau = 8.8$ as estimated by [Hunt and Reffert, 2023](#).

In general, we notice that our isochrone fitting method tends to estimate older ages than the isochrone fitting method by [Hunt and Reffert, 2023](#), which can already be seen in Figure 4.4. We note that the member selections as illustrated in the right panels of Figure 4.7 show the stars corrected for extinction as derived with our method. However, comparing the extinction estimates of [Hunt and Reffert, 2023](#) with the extinction estimates derived with our method, we find that for the extinction estimates between 0-1 mag we typically obtain higher extinction values than [Hunt and Reffert, 2023](#). For the few higher extinction cases (>1 mag) the extinction estimates of [Hunt and Reffert, 2023](#) are on average higher than those estimated by us. For each group in our group dataset from [Hunt and Reffert, 2023](#) we also compare our age estimate with the age estimates published in the catalog by [Hunt and Reffert, 2023](#). We find good agreement between the age range of $\log \tau \sim 6-8.2$, but clear age offsets for older ages, which we estimate to be in the age region between $8.5 < \log \tau < 9.5$ in contrast to [Hunt and Reffert, 2023](#) who estimate them to be in the age region between $7.5 < \log \tau < 8.5$.

4.5.3 FINAL REMARKS

We have shown that when we apply our isochrone fitting method to two large cluster datasets obtained by action angle clustering and from a state-of-the-art cluster catalog by [Hunt and Reffert, 2023](#), we find a significant bimodality in the resulting age distributions of both samples, with a lack of groups with

4 Ages for large sets of stellar aggregates

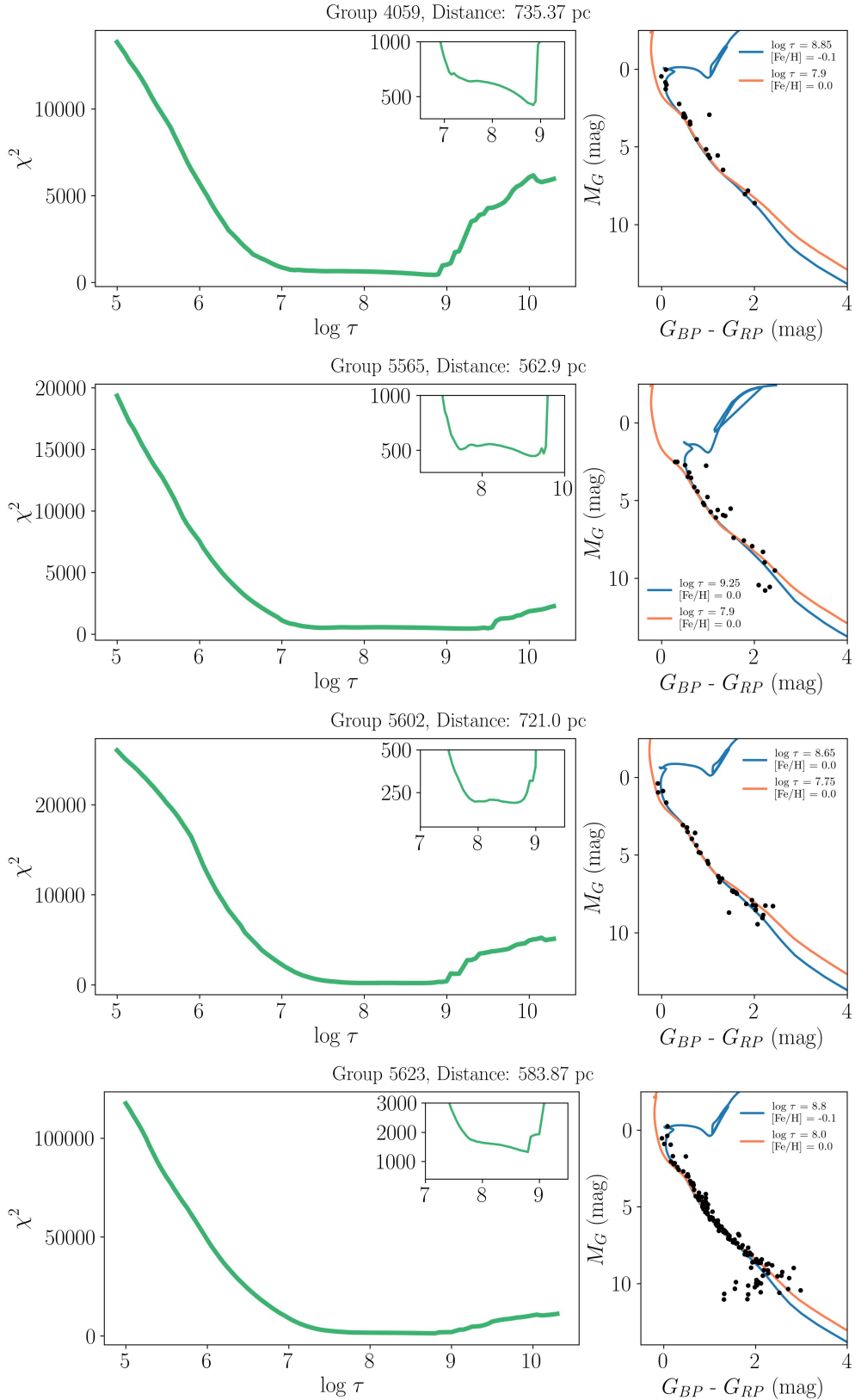


Figure 4.7. Example Groups 4059, 5565, 5602 and 5623 as ‘ambiguous cases’. Left: value χ^2 as a function of $\log \tau$, with a zoom-in in the top right corner. Right: color-magnitude diagram of both groups, with the best-fit isochrone from the isochrone fitting in blue, and the literature isochrone from [Hunt and Reffert, 2023](#) in orange.

ages between $8 < \log \tau < 8.5$. We suspect that this lack of groups in this age region is driven by two main factors. First, in this age range the lower main sequence no longer serves as an age indicator, or more accurately, only serves a lower age limit, since for the group younger than $\log \tau = 8$ the lower main sequence would be clearly offset. Second, these groups have their main sequence turn-off's still at the very hot and bright end, where sequences on the color-magnitude diagram are often too sparsely sampled in the Gaia dataset.

In summary, this implies that up to this point we feel confident only in age-dating very young groups of stars (e.g. with ages $\log \tau < 8$), and old groups with more populated main-sequence turn-offs. Many of the groups in-between are very difficult to age-date with isochrone models, as the information we can obtain from their sequences in the color-magnitude diagram is very ambiguous. Therefore, for most groups, we can only confidently provide clear upper and lower age limits. However, for groups that are young or that comprise stars at the main sequence turn-off, our outlines method works beautifully.

It should be noted here that in addition to having not well-populated enough stellar sequences, even more factors can make isochrone fitting a rather challenging age-estimation tool. Correcting for extinction of stars is essential, but the results can vary significantly depending on the data and method setups used, and can lead to stellar sequences being shifted in the color-magnitude-diagram, resulting in different isochrone age fits. Also, different isochrone models (e.g. PARSEC versus MIST) isochrones also slightly vary in their shapes, influencing the resulting age estimates of stellar ensembles.

One part in which our age estimation method conceptually differs from the age determination method by [Hunt and Reffert, 2023](#) is the luminosity function, which we have not taken into account (yet). For now, we are only taking into account the proximity of a star to an isochrone, but not how many stars we would assume. This would be the most obvious next step to implement in our approach. In this regard, the next and last Chapter 5 will summarize the main results of this thesis, and will discuss more future prospects that will follow from it.

5 SUMMARY AND OUTLOOK

In this thesis, we used the revolutionary data by Gaia to study stellar groups in the Milky Ways disk. In particular, we closely investigated the orbits on which stellar clusters are located, estimated ages for stellar groups with limited 6D phase-space information, and applied this method to large sets of stellar aggregates, where this thesis highlights age-dating ambiguities that exist for groups where neither the lower main sequence nor the main sequence turn-off offer age information (around $\log \tau \sim 8-8.5$). We briefly summarize all the studies conducted below.

In Chapter 2, we linked stars in action-angle space and picked the most prominent 55 groups within 800 pc from the Sun. We then picked stars within an ‘orbit patch’ around each group and looked at their angle distribution, where we commonly found other clusters on the same orbit at different phases, such as ‘pearls on a string’. We found that the incidence of such pearls is much higher than that seen in adjacent orbits.

In Chapter 3, we clustered the most prominent 92 groups in action-angle space within 800 pc of the Sun. We then mapped their 6D action-angle distribution into a 5D position-parallax-proper motion space to increase their CMD coverage. We performed a likelihood isochrone fitting on their extended sequences in the color-magnitude diagrams, accounting for varying distances and reddenings, outliers and binaries, and a possible intrinsic age spread, and found that our age estimates for known clusters are in good agreement with the literature. The age distribution showed that the groups are predominantly young (<1 Gyr) populations. Their morphologies are either heterogeneous or show a tight clustered core with or without tidal (or uncertainty-driven) tails.

In Chapter 4 we picked two large datasets of stellar aggregates within 800 pc from the Sun: we identified 695 groups in 6D action-angle space and extended their sequences by mapping them into 5D position-parallax-proper motion space, and we picked 836 clusters published by [Hunt and Reffert, 2023](#). We obtained a spectroscopic metallicity for each group from Gaia XP spectra ([Andrae et al., 2023](#)) as a prior constraint for the isochrone fitting, which we performed in the following. For both group setups, we got a bimodality in their age distributions. We discussed that isochrone fitting is ambiguous if neither the lower-main sequence serves an age indicator (for groups older than $\log \tau \sim 8$), nor the turn-off region for these groups is sampled well enough. Therefore, for many groups, we can confidently only estimate upper and lower age limits.

5.1 EXPLORATION OF THE ORBIT-AGE SPACE

There are some obvious future avenues for this project which have not been pursued as much as planned due to the ambiguities of the age determination, which were discussed in Chapter 4. One natural next step is the investigation of orbit and age-space relations of large sets of stellar aggregates as a basis to actually map the dispersal of stellar groups in the Milky Way disk.

Figure 5.1 illustrates the distribution of all stars in the action angle sample of the 695 groups identified as described in Section 4.2.1: from left to right, Figure 5.1 shows the distribution of stars in the three action coordinates (J_ϕ , J_R , J_z). The different histograms represent different age bins derived from our age estimates in Section 4.5, where the gray-filled histogram represents all stars within 580 groups older than $\log \tau = 8.0$ and the black histogram illustrates all stars within 115 groups younger than $\log \tau = 8$. Furthermore, we chose to present an even younger subset of all stars within 31 groups with ages of $\log \tau < 7.7$ in a dotted style. As can be seen, our efficiency in selecting clusters seems to be sensitive to specific orbits, in particular in angular momentum (J_ϕ) space (left panel), where the member stars of stellar aggregates are not uniformly distributed, but show a strong bimodality, with almost no stars found around $J_\phi \sim 1750 \text{ kpc km s}^{-1}$. This is the case for all selected age bins, only with the peaks of the distribution slightly varying for the different subsets. This bimodal structure is in clear contrast to the angular momentum distribution of all stars within 800 pc in the Gaia dataset, which does not show such a bimodal pattern. Whether this is a manifestation of local spiral patterns in action space could and should be explored. The middle panel shows that young stars have small radial actions, while older stars are located on average on higher eccentric orbits, probably an effect of orbital disk heating. The vertical action in the right panel does not reveal any clear differences between old and young stars; however, stars in the very young subset with ages of $\log \tau < 7.7$ are strongly concentrated in the Galactic midplane, with very little vertical extent, showing that these stars are probably still located close to their birth orbits in the Galactic midplane.

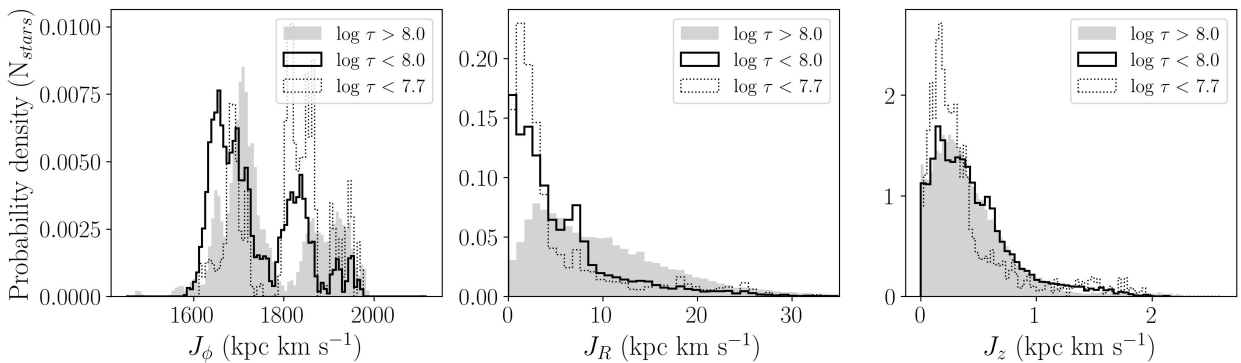


Figure 5.1. The orbit distribution of stars in different age subsets: from left to right the distribution of stars in the azimuthal action J_ϕ , the radial action J_R , and the vertical action J_z are presented for three different age bins: for all stars within 580 groups older than $\log \tau = 8$ (filled gray), for all stars within 115 groups younger than $\log \tau = 8$ (black), and for an even younger subset of all stars within 31 groups younger than $\log \tau = 7.7$ (dotted).

Another way to look at orbit-age space correlations of stellar aggregates is to compare the differences in orbit ($\Delta J_{\phi,R,Z}$) with the differences in age ($\Delta \log \tau$) for all possible pairs of groups. If we assume a molecular gas filament being prone to multiple star formation events, we can test the hypothesis that groups of similar age are located preferentially on similar orbits. We expect this to be true only for very young groups that did not disperse much from their birth orbit and did not experience any large perturbations or orbit migration effects yet; therefore, we perform the analysis illustrated in Figure 5.2 for the action angle sample identified as described in Section 4.2.1, but only for a subset of groups younger than $\log \tau = 8$. The three panels represent the three action differences (ΔJ_{ϕ} , ΔJ_R , ΔJ_Z) on the x-axis, and the y-axis in each panel represents the age difference $\Delta \log \tau$. The color illustrates the probability of $\Delta J_{\phi,R,Z}$ between all possible pairs of groups given $\Delta \log \tau$ of the group pairs. To obtain a group orbit, for each of the three action coordinates we calculate the median from all member stars with radial velocity measurements of each group. We find that groups with similar ages (small $\Delta \log \tau$) are likely to be close in angular momentum space (small ΔJ_{ϕ}), which is in contrast to groups with larger age differences (left panel). This might be the suggested manifestation of dispersal of groups from their birth orbits, or it might be caused by perturbations from, e.g. local spiral arms. We also observe similar but weaker trends for the other two action coordinates in the middle and right panels, although we find these only for age differences greater than $\log \tau = 1$, while for all other age differences the differences in radial and vertical action are comparably small. This weak trend in radial and vertical actions could be a manifestation of orbital disk heating; however, fully understanding and trusting these results will require further and future investigation.

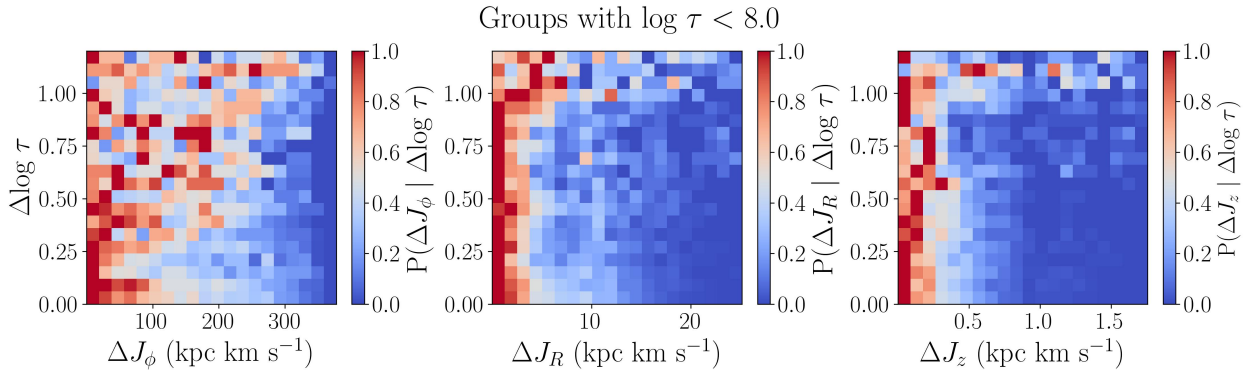


Figure 5.2. The differences in the three actions (from left to right) as a function of the age differences between all pairs of groups younger than $\log \tau = 8$. The histograms are row-normalized, e.g. in color is showing the probability of the orbit difference between two groups given their age difference.

Another idea on how to pursue this project is to properly account for the large uncertainties of the orbit and orbital phase-space coordinates when identifying stellar aggregates in this 6D phase space, which are dominantly caused by the radial velocity measurement errors from Gaia. Due to the complex pattern of the uncertainties (see Fig 1.4) this is not trivial and would need further investigation. In addition and as discussed in Chapter 4, we could improve our isochrone fitting code as follows: for now, we are only taking into account the proximity of a star to an isochrone, but not how many stars we would as-

sume. Therefore, implementing and accounting for the luminosity function would possibly lead to an improvement of our age estimations.

5.2 FUTURE PROSPECTS

Progress in the project will be made with the availability of even better data. First, working with more accurate orbit and orbital-phase space coordinates will improve the identification of ‘real’ clusters in this parameter space. This shows the need for more accurate radial velocity measurements, as illustrated in Figure 1.4. Along with a better measurement accuracy, a larger temperature range for radial velocities measurements will increase the 6D-all-sky Gaia dataset and will probably result in the identification of more clusters in this parameter space. Also, better parallax and proper motion data - which will be available with longer observation baselines - will increase the correct assignment of additional member stars to stellar aggregates, and better parallaxes will also improve the distance estimates and absolute magnitude calculations for the stars.

The science in this thesis was exclusively based on the data of the Gaia mission (see Section 1.4): in Chapter 2 we carry out our analysis based on Gaia EDR3 data, and the analysis in Chapters 3 and Chapter 4 is conducted with Gaia DR3 data. Although the nominal mission of the Gaia satellite ended after a five-year mission phase in 2019 already, the mission was extended and is expected to operate until 2025, when the spacecraft is predicted to run out of micro-propulsion fuel (Brown, 2021). In this context, two further data releases are foreseen: Gaia DR4 and Gaia DR5, which will include data collected from the extended mission phase (Gaia Collaboration et al., 2023).

Gaia DR4 is expected to be published not before the second half of 2026, and will be based on 66 months (5.5 years) of observations, which is about twice as long as the 34 month baseline of Gaia DR3 data. Gaia DR5 will not be released before the end of 2030 and will be based on all mission data, which will result in a ~ 120 months (~ 10 years) baseline. These longer baselines of observations will result in a higher S/N for all data as compared to already published data releases. This improves with \sqrt{t} for all data products (e.g., parallaxes) and results in a precision gain of 1.4 and 1.9 for DR4 and DR5, respectively, as compared to Gaia DR3. For proper motions, the S/N improvement scales with $t^{1.5}$, resulting in more precise data by factors of 2.7 and 6.6 for both future data releases, respectively, with respect to Gaia DR3 (Gaia Collaboration et al., 2023). Furthermore, Gaia DR4 will provide all time series data for each source for astrometry, photometry, radial velocities, and BP, RP and RVS spectra (Brown, 2021). In addition, Gaia DR4 is expected to provide radial velocity measurements for more stars, possibly increasing the magnitude limit from $G \sim 14$ mag in Gaia DR3 to fainter sources until a magnitude limit of $G \sim 16$ mag, along with possible improvements in the accuracy of the radial velocity. Working with these improved Gaia datasets - in particular with the upcoming Gaia DR4 - will improve the identification and membership selection of stellar aggregates in the solar vicinity and represents an obvious next step of this project.

To further improve the data set provided by the Gaia mission, a future all-sky astrometry mission called *GaiaNIR* was first proposed in 2016 (Hobbs et al., 2016), and submitted as a mission proposal white paper in 2019 (Hobbs et al., 2019). Its main goal is to complement the Gaia dataset by delivering high-accuracy astrometry in near-infrared (400-1800 nm) instead of optical wavelengths and to observe parts of the sky that are obscured by interstellar gas and dust. This will immensely improve the number count of stars in star-forming regions, spiral arms, and the bulge region, and provide a dense star sampling over a large volume in the Galactic disk (~ 8 billion sources, Brown, 2021). The mission is designed with a nominal mission lifetime of 5-6 years, with a planned launch in about 20 years from now (2035-2040). In addition to the increased number of measurements, the combination with Gaia data will provide a long baseline of ~ 20 years, and therefore largely improve parallax and proper motion accuracies, e.g. an order of magnitude for proper motion measurements (nanoarcsecond accuracy) as compared to Gaia DR4. The mission would allow the study of low-mass stellar populations in the Milky Way, as well as stars that are obscured by interstellar gas and dust. Therefore, this would not only improve the number of member stars for known stellar clusters but also open up the possibility to detect very young stellar clusters in the vicinity of their dusty birth sites.

Looking into the near rather than the distant future, a NASA space mission named the *Nancy Grace Roman Space Telescope* is scheduled to be launched in the mid-2020s (former mission name: Wide-Field Infrared Survey Telescope, Spergel et al., 2015). It will operate in the infrared (0.48 - 2.3 μm) with a primary mirror of 2.4 meter diameter and a field of view that is 100 times greater than that of Hubble's infrared instrument. A 'Galactic Roman Infrared Plane Survey' (GRIPS) white paper was proposed by Paladini et al., 2023 with the objective of using Roman's wide field of view and infrared coverage to map a significant fraction (> 100 billion) of stars in the Galactic disk, and also in the bulge/bar. The proposed sky coverage is $-60 < l < +60$ deg and $|b| < 3$ deg, e.g. 1000 deg² in total. The Roman space mission will be able to observe in dust-obscured regions which are inaccessible to Gaia, and provide proper motion measurements of stars located in dust-obscured regions. In combination with e.g. 2MASS, it will create a long time baseline, which will lead to an improvement of the precision of proper motion measurements of stars.

Improved radial velocity measurements will have a significant effect on the work presented in this thesis, as their precision has a major impact when working in orbit and orbital phase space (as was shown, e.g. in Fig 1.4). The *4-meter Multi-Object Spectroscopic Telescope* (4MOST) is a spectroscopic facility installed on the ESO VISTA telescope at the Paranal observatory in Chile and will start its observations in the wavelength range 270-950 nm in 2025 (de Jong et al., 2019). It is planned to operate for at least five years, where each night it will simultaneously obtain 2400 spectra of objects in the southern sky. It will provide radial velocity measurements for stars in the Milky Way halo, bulge, and disk to complement the measurements provided by Gaia. It consists of a low-resolution ($R > 4000-7800$) and a high-resolution spectrograph ($R > 18500$), where the latter will obtain radial velocities for stars which are too faint for Gaia to observe, and will provide a better precision for objects observed in both Gaia and 4MOST.

5 Summary and Outlook

In addition, the *Sloan Digital Sky Survey V* (SDSS-V), an all-sky optical and infrared spectroscopic survey, has been collecting observations since 2020 for a planned time of about five years (Kollmeier et al., 2019). It uses the Apache Point Observatory in New Mexico and the Las Campanas Observatory in Chile to map the entire sky in five wavelengths: 355.1, 468.6, 616.6, 748.0 und 893.2 nm. One of its three main programs called the ‘Milky Way Mapper program’ (MWM) targets low resolution spectra ($R \sim 2000$) in the optical and medium resolution spectra ($R \sim 22500$) in the near-infrared of more than 6 million stars during its five-year lifetime. It will provide radial velocity measurements for fainter stars as the Gaia mission and will also provide follow-up spectroscopy for stars with uncertain Gaia measurements, which will improve the overall census and accuracy of the available radial velocity data.

That said, the outlined missions will largely improve the performance of scientific studies on the structure of the Milky Way disk through the orbits and ages of its stars: precise radial velocity measurements will naturally improve the uncertainties of orbit and orbital phase-space coordinates of stars, and better proper motion measurements will lead to a more accurate assignment of stars to stellar clusters or associations. Expanding measurements to fainter sources will improve the completeness of observational color-magnitude diagrams of stellar groups, and obtaining measurements for a larger region in the Galactic disk will improve our picture of larger-scale structures (e.g. spiral arms) in the Milky Way disk. Also, mapping stars in the infrared will lead to measurements of stars in dust-obscured regions and make it possible to detect and study even younger stellar aggregates, which are still embedded in their birth environment. Overall, this thesis has shown that better measurements are needed to successfully perform an analysis of the orbit and age space of stars in the solar vicinity. The prospect of future missions that will improve the currently available data draws an optimistic picture on this and will make it exciting to continue studying the ages and the dispersal of the small-scale orbit and orbital-phase space clusters in the Milky Way disk.

LIST OF FIGURES

1.1	Dark Matter and galaxy formation	4
1.2	Face-on and edge-on view on two spiral galaxies	6
1.3	Gaia image of the components of the Milky Way	8
1.4	Impact of radial velocity uncertainties on the action-angle computation	15
1.5	Star formation site Pillars of Creation and open cluster Pleiades	17
1.6	How to detect stellar clusters	22
1.7	Gaia’s impact on understanding the Galactic structure and open cluster dissolution	24
1.8	Observational CMD and PARSEC isochrones	27
2.1	55 FoF action-angle groups	42
2.2	Pearls on a string: FoF Group 19	44
2.3	Pearls on a string: FoF Group 40	45
2.4	Pearls on a string: FoF Group 12	46
2.5	Offset action patch: FoF Group 12	47
2.6	Pearls in three case studies: FoF Groups 19, 40, 12	49
2.7	Pearls overview of FoF Group 40	53
2.8	Pearls overview of FoF Group 12	54
2.9	Pearl statistics	56
2.10	Orbit patch of FoF Group 40	60
2.11	Orbit patch of FoF Group 12	60
2.12	Pisces-Eridanus and Coma Berenices	61
2.13	Offset orbit patch for FoF Group 19	63
2.14	Offset orbit patch for FoF Group 40	64
2.15	Isolated cluster	65
3.1	94 DBSCAN action-angle groups	74
3.2	Observational CMDs of six groups	75
3.3	Density histograms of six groups	78
3.4	Extinction correction	79
3.5	Complete observational CMDs for six groups	83
3.6	Comparison with literature ages	84

List of Figures

3.7	Age distribution	87
3.8	Spatial distribution	89
4.1	836 Hunt et al. 2023 stellar aggregates	95
4.2	695 DBSCAN action-angle stellar aggregates	97
4.3	Spectroscopic metallicity distributions of stellar aggregates	99
4.4	Age distributions of stellar aggregates	100
4.5	Likelihood plot of Groups 112 and 274	101
4.6	Likelihood plot of Groups 384 and 217	102
4.7	Comparison with literature ages	104
5.1	Action age space of stellar aggregates	108
5.2	Action age differences of stellar aggregates	109

LIST OF TABLES

1.1	Overview of action coordinates	11
2.1	Subsample of identified members of 55 FoF action-angle groups	39
2.2	Properties of 55 FoF action-angle groups	40
3.1	Subsample of identified members of 92 DBSCAN action-angle groups	77
3.2	Parameters of 92 DBSCAN action-angle groups	85

ACKNOWLEDGEMENTS

Firstly, I would like to thank my family for their continuous support over the last few decades and my partner Lukas Belazzi, who has gone through all this with me since we were at school. I also thank his family and my Austrian friends for making me feel home whenever I am in Austria.

I would like to thank my Heidelberg friends who made me have a great time during my PhD, and I can only mention a small number of them here. I would like to thank Sarah Jeffreson, Andrew Winter, Jaeyeon Kim, and Sebastian Trujillo-Gomez for supporting me in particular during my first year in Heidelberg. I also would like to thank Nico Winkel, Eric Rohr, Sebastian Zieba, and Evert Nasedkin for fun ski and ski touring trips in Austria, Italy, and Switzerland, morning bike commutes up the Königstuhl, bike tours in the Odenwald, hikes in the Alps and on the Canary Islands, and lots of dinners together during the last couple of years. Also, I also would like to thank Luzian Seeburger for always helping me with technical problems and together with Sebastian Zieba for their Austrian support in Germany.

I would like to thank Christian Fendt and Johanna Coronado for giving me a smooth and welcoming start at MPIA, as well as the IMPRS-HD program and the MPIA Data Science Department for their continuous support. I am thankful to Evert Nasedin, Luzian Seeburger, Johanna Müller-Horn, and Eric Rohr for commenting and helping with parts of this thesis. I also thank Eva Grebel and Hans-Walter Rix for refereeing this thesis, and Sabine Reffert and Matthias Bartelman for agreeing to be part of my examination committee.

Lastly, I would like to emphasize the support of Lukas Belazzi, Nico Winkel, and Hans-Walter Rix. I would like to thank Lukas Belazzi for being the most positive and Nico Winkel for being the most helpful person during my PhD, in all areas of life. Of course, I especially would like to thank my advisor Hans-Walter Rix for giving me the opportunity to do a PhD at MPIA, which is a wonderful work environment. Also, I would like to thank Hans-Walter Rix for always being incredibly patient when explaining things to me, for making me leave every meeting with a positive feeling, and for showing me how much fun you can have doing your job.

PERSONAL BIBLIOGRAPHY

Bibliography of first and co-author publications used in this thesis:

- **V. Fürnkranz**, H.-W. Rix, J. Coronado, and R. Seeburger. The Age Distribution of Stellar Orbit Space Clumps. *The Astrophysical Journal*, 961:113, January 2024
- J. Coronado, **V. Fürnkranz**, and H.-W. Rix. Pearls on a String: Numerous Stellar Clusters Strung along the Same Orbit. *The Astrophysical Journal*, 928:70, March 2022

Bibliography of first and co-author publications not included in this thesis:

- S. Meingast, et al. (incl. **V. Fürnkranz**). VISIONS: The VISTA Star Formation Atlas I. Survey overview. *Astronomy & Astrophysics*, 673:A58, May 2023
- S. Meingast, H. Bouy, **V. Fürnkranz**, D. Hernandez, A. Rottensteiner, and E. Brändli. VISIONS: The VISTA Star Formation Atlas II. The data processing pipeline. *Astronomy & Astrophysics*, 673:A59, May 2023
- **V. Fürnkranz**, S. Meingast, and J. Alves. Extended stellar systems in the solar neighborhood - III. Like ships in the night: the Coma Berenices neighbor moving group. *Astronomy & Astrophysics*, 624:L11, April 2019
- S. Meingast, J. Alves, and **V. Fürnkranz**. Extended stellar systems in the solar neighborhood - II. Discovery of a nearby 120° stellar stream in Gaia DR2. *Astronomy & Astrophysics*, 622:L13, January 2019
- J. E. Großschedl, J. Alves, S. Meingast, C. Ackerl, J. Ascenso, H. Bouy, A. Burkert, J. Forbrich, **V. Fürnkranz**, A. Goodman, A. Hacar, G. Herbst-Kiss, C. J. Lada, I. Larreina, K. Leschinski, M. Lombardi, A. Moitinho, D. Mortimer, and E. Zari. 3D shape of Orion A from Gaia DR2. *Astronomy & Astrophysics*, 619:A106, August 2018

BIBLIOGRAPHY

- Agertz, O., Renaud, F., Feltzing, S., Read, J. I., Ryde, N., Andersson, E. P., Rey, M. P., Bensby, T., & Feuillet, D. K. (2021). VINTERGATAN - I. The origins of chemically, kinematically, and structurally distinct discs in a simulated Milky Way-mass galaxy. *MNRAS*, *503*(4), 5826–5845. DOI: [10.1093/mnras/stab322](https://doi.org/10.1093/mnras/stab322).
- Alves, J., Zucker, C., Goodman, A. A., Speagle, J. S., Meingast, S., Robitaille, T., Finkbeiner, D. P., Schlafly, E. F., & Green, G. M. (2020). A Galactic-scale gas wave in the solar neighbourhood. *Nature*, *578*(7794), 237–239. DOI: [10.1038/s41586-019-1874-z](https://doi.org/10.1038/s41586-019-1874-z).
- Anders, F., Cantat-Gaudin, T., Quadrino-Lodoso, I., Gieles, M., Jordi, C., Castro-Ginard, A., & Balaguer-Núñez, L. (2021). The star cluster age function in the Galactic disc with Gaia DR2. Fewer old clusters and a low cluster formation efficiency. *A&A*, *645*, Artikel L2, L2. DOI: [10.1051/0004-6361/202038532](https://doi.org/10.1051/0004-6361/202038532).
- Andrae, R., Rix, H.-W., & Chandra, V. (2023). Robust Data-driven Metallicities for 175 Million Stars from Gaia XP Spectra. *ApJS*, *267*(1), Artikel 8, 8. DOI: [10.3847/1538-4365/acd53e](https://doi.org/10.3847/1538-4365/acd53e).
- Astropy Collaboration, Price-Whelan, A. M., Sipőcz, B. M., Günther, H. M., Lim, P. L., Crawford, S. M., Conseil, S., Shupe, D. L., Craig, M. W., Dencheva, N., Ginsburg, A., VanderPlas, J. T., Bradley, L. D., Pérez-Suárez, D., de Val-Borro, M., Aldcroft, T. L., Cruz, K. L., Robitaille, T. P., Tollerud, E. J., ... Astropy Contributors. (2018). The Astropy Project: Building an Open-science Project and Status of the v2.0 Core Package. *AJ*, *156*(3), Artikel 123, 123. DOI: [10.3847/1538-3881/aabc4f](https://doi.org/10.3847/1538-3881/aabc4f).
- Astropy Collaboration, Robitaille, T. P., Tollerud, E. J., Greenfield, P., Droettboom, M., Bray, E., Aldcroft, T., Davis, M., Ginsburg, A., Price-Whelan, A. M., Kerzendorf, W. E., Conley, A., Crighton, N., Barbary, K., Muna, D., Ferguson, H., Grollier, F., Parikh, M. M., Nair, P. H., ... Streicher, O. (2013). Astropy: A community Python package for astronomy. *A&A*, *558*, Artikel A33, A33. DOI: [10.1051/0004-6361/201322068](https://doi.org/10.1051/0004-6361/201322068).
- Bailer-Jones, C. A. L., Rybizki, J., Fouesneau, M., Demleitner, M., & Andrae, R. (2021). Estimating Distances from Parallaxes. V. Geometric and Photogeometric Distances to 1.47 Billion Stars in Gaia Early Data Release 3. *AJ*, *161*(3), Artikel 147, 147. DOI: [10.3847/1538-3881/abd806](https://doi.org/10.3847/1538-3881/abd806).
- Bailer-Jones, C. A. L., Rybizki, J., Fouesneau, M., Mantelet, G., & Andrae, R. (2018). Estimating Distance from Parallaxes. IV. Distances to 1.33 Billion Stars in Gaia Data Release 2. *AJ*, *156*(2), Artikel 58, 58. DOI: [10.3847/1538-3881/aacb21](https://doi.org/10.3847/1538-3881/aacb21).

- Barnes, S. A. (2007). Ages for Illustrative Field Stars Using Gyrochronology: Viability, Limitations, and Errors. *ApJ*, 669(2), 1167–1189. DOI: [10.1086/519295](https://doi.org/10.1086/519295).
- Bastian, U. (2019). Gaia 8: Discovery of a star cluster containing β Lyrae. *A&A*, 630, Artikel L8, L8. DOI: [10.1051/0004-6361/201936595](https://doi.org/10.1051/0004-6361/201936595).
- Beccari, G., Boffin, H. M. J., & Jerabkova, T. (2020). Uncovering a 260 pc wide, 35-Myr-old filamentary relic of star formation. *MNRAS*, 491(2), 2205–2216. DOI: [10.1093/mnras/stz3195](https://doi.org/10.1093/mnras/stz3195).
- Binney, J., & Tremaine, S. (2008). *Galactic Dynamics: Second Edition*. Princeton University Press.
- Binney, J. (2012). Actions for axisymmetric potentials. *MNRAS*, 426(2), 1324–1327. DOI: [10.1111/j.1365-2966.2012.21757.x](https://doi.org/10.1111/j.1365-2966.2012.21757.x).
- Binney, J., & McMillan, P. J. (2016). Torus mapper: a code for dynamical models of galaxies. *MNRAS*, 456(2), 1982–1998. DOI: [10.1093/mnras/stv2734](https://doi.org/10.1093/mnras/stv2734).
- Bird, S., Ni, Y., Di Matteo, T., Croft, R., Feng, Y., & Chen, N. (2022). The ASTRID simulation: galaxy formation and reionization. *MNRAS*, 512(3), 3703–3716. DOI: [10.1093/mnras/stac648](https://doi.org/10.1093/mnras/stac648).
- Bland-Hawthorn, J., & Gerhard, O. (2016). The Galaxy in Context: Structural, Kinematic, and Integrated Properties. *ARA&A*, 54, 529–596. DOI: [10.1146/annurev-astro-081915-023441](https://doi.org/10.1146/annurev-astro-081915-023441).
- Boesgaard, A. M., Roper, B. W., & Lum, M. G. (2013). The Chemical Composition of Praesepe (M44). *ApJ*, 775(1), Artikel 58, 58. DOI: [10.1088/0004-637X/775/1/58](https://doi.org/10.1088/0004-637X/775/1/58).
- Bonatto, C., & Bica, E. (2010). Hierarchical structures in the Large and Small Magellanic Clouds. *MNRAS*, 403(2), 996–1008. DOI: [10.1111/j.1365-2966.2009.16177.x](https://doi.org/10.1111/j.1365-2966.2009.16177.x).
- Bovy, J. (2015). galpy: A python Library for Galactic Dynamics. *ApJS*, 216, Artikel 29, 29. DOI: [10.1088/0067-0049/216/2/29](https://doi.org/10.1088/0067-0049/216/2/29).
- Bovy, J., Allende Prieto, C., Beers, T. C., Bizyaev, D., da Costa, L. N., Cunha, K., Ebelke, G. L., Eisenstein, D. J., Frinchaboy, P. M., García Pérez, A. E., Girardi, L., Hearty, F. R., Hogg, D. W., Holtzman, J., Maia, M. A. G., Majewski, S. R., Malanushenko, E., Malanushenko, V., Mészáros, S., ... Zasowski, G. (2012). The Milky Way's Circular-velocity Curve between 4 and 14 kpc from APOGEE data. *ApJ*, 759(2), Artikel 131, 131. DOI: [10.1088/0004-637X/759/2/131](https://doi.org/10.1088/0004-637X/759/2/131).
- Bovy, J., Leung, H. W., Hunt, J. A. S., Mackereth, J. T., García-Hernández, D. A., & Roman-Lopes, A. (2019). Life in the fast lane: a direct view of the dynamics, formation, and evolution of the Milky Way's bar. *MNRAS*, 490(4), 4740–4747. DOI: [10.1093/mnras/stz2891](https://doi.org/10.1093/mnras/stz2891).
- Brandt, T. D., & Huang, C. X. (2015). The Age and Age Spread of the Praesepe and Hyades Clusters: a Consistent, ~800 Myr Picture from Rotating Stellar Models. *ApJ*, 807(1), Artikel 24, 24. DOI: [10.1088/0004-637X/807/1/24](https://doi.org/10.1088/0004-637X/807/1/24).
- Bressan, A., Marigo, P., Girardi, L., Salasnich, B., Dal Cero, C., Rubele, S., & Nanni, A. (2012). PARSEC: stellar tracks and isochrones with the PAdova and TRieste Stellar Evolution Code. *MNRAS*, 427(1), 127–145. DOI: [10.1111/j.1365-2966.2012.21948.x](https://doi.org/10.1111/j.1365-2966.2012.21948.x).
- Brown, A. G. A. (2021). Microarcsecond Astrometry: Science Highlights from Gaia. *ARA&A*, 59, 59–115. DOI: [10.1146/annurev-astro-112320-035628](https://doi.org/10.1146/annurev-astro-112320-035628).

- Buder, S., Sharma, S., Kos, J., Amarsi, A. M., Nordlander, T., Lind, K., Martell, S. L., Asplund, M., Bland-Hawthorn, J., Casey, A. R., de Silva, G. M., D’Orazi, V., Freeman, K. C., Hayden, M. R., Lewis, G. F., Lin, J., Schlesinger, K. J., Simpson, J. D., Stello, D., ... Galah Collaboration. (2021). The GALAH+ survey: Third data release. *MNRAS*, *506*(1), 150–201. DOI: [10.1093/mnras/stab1242](https://doi.org/10.1093/mnras/stab1242).
- Cantat-Gaudin, T., & Anders, F. (2020). Clusters and mirages: cataloguing stellar aggregates in the Milky Way. *A&A*, *633*, Artikel A99, A99. DOI: [10.1051/0004-6361/201936691](https://doi.org/10.1051/0004-6361/201936691).
- Cantat-Gaudin, T., Anders, F., Castro-Ginard, A., Jordi, C., Romero-Gómez, M., Soubiran, C., Casamiquela, L., Tarricq, Y., Moitinho, A., Vallenari, A., Bragaglia, A., Krone-Martins, A., & Kounkel, M. (2020). Painting a portrait of the Galactic disc with its stellar clusters. *A&A*, *640*, Artikel A1, A1. DOI: [10.1051/0004-6361/202038192](https://doi.org/10.1051/0004-6361/202038192).
- Cantat-Gaudin, T., Jordi, C., Vallenari, A., Bragaglia, A., Balaguer-Núñez, L., Soubiran, C., Bossini, D., Moitinho, A., Castro-Ginard, A., Krone-Martins, A., Casamiquela, L., Sordo, R., & Carrera, R. (2018). A Gaia DR2 view of the open cluster population in the Milky Way. *A&A*, *618*, Artikel A93, A93. DOI: [10.1051/0004-6361/201833476](https://doi.org/10.1051/0004-6361/201833476).
- Cantat-Gaudin, T., Jordi, C., Wright, N. J., Armstrong, J. J., Vallenari, A., Balaguer-Núñez, L., Ramos, P., Bossini, D., Padoan, P., Pelkonen, V. M., Mapelli, M., & Jeffries, R. D. (2019). Expanding associations in the Vela-Puppis region. 3D structure and kinematics of the young population. *A&A*, *626*, Artikel A17, A17. DOI: [10.1051/0004-6361/201834957](https://doi.org/10.1051/0004-6361/201834957).
- Cantat-Gaudin, T., Mapelli, M., Balaguer-Núñez, L., Jordi, C., Sacco, G., & Vallenari, A. (2019). A ring in a shell: the large-scale 6D structure of the Vela OB2 complex. *A&A*, *621*, Artikel A115, A115. DOI: [10.1051/0004-6361/201834003](https://doi.org/10.1051/0004-6361/201834003).
- Cantat-Gaudin, T. (2022a). Milky Way Star Clusters and Gaia: A Review of the Ongoing Revolution. *Universe*, *8*(2), Artikel 111, 111. DOI: [10.3390/universe8020111](https://doi.org/10.3390/universe8020111).
- Cantat-Gaudin, T. (2022b). Milky Way Star Clusters and Gaia: A Review of the Ongoing Revolution. *Universe*, *8*(2), Artikel 111, 111. DOI: [10.3390/universe8020111](https://doi.org/10.3390/universe8020111).
- Carraro, G., & Patat, F. (2001). Star clusters in the Carina complex: UBVR photometry of NGC 3114, Collinder 228 and vdB-Hagen 99. *A&A*, *379*, 136–146. DOI: [10.1051/0004-6361:20011314](https://doi.org/10.1051/0004-6361:20011314).
- Castro-Ginard, A., Jordi, C., Luri, X., Álvarez Cid-Fuentes, J., Casamiquela, L., Anders, F., Cantat-Gaudin, T., Monguió, M., Balaguer-Núñez, L., Solà, S., & Badia, R. M. (2020). Hunting for open clusters in Gaia DR2: 582 new open clusters in the Galactic disc. *A&A*, *635*, Artikel A45, A45. DOI: [10.1051/0004-6361/201937386](https://doi.org/10.1051/0004-6361/201937386).
- Castro-Ginard, A., Jordi, C., Luri, X., Cantat-Gaudin, T., & Balaguer-Núñez, L. (2019). Hunting for open clusters in Gaia DR2: the Galactic anticentre. *A&A*, *627*, Artikel A35, A35. DOI: [10.1051/0004-6361/201935531](https://doi.org/10.1051/0004-6361/201935531).
- Castro-Ginard, A., Jordi, C., Luri, X., Cantat-Gaudin, T., Carrasco, J. M., Casamiquela, L., Anders, F., Balaguer-Núñez, L., & Badia, R. M. (2022). Hunting for open clusters in Gaia EDR3: 628 new

- open clusters found with OCfinder. *A&A*, 661, Artikel A118, A118. DOI: [10.1051/0004-6361/202142568](https://doi.org/10.1051/0004-6361/202142568).
- Castro-Ginard, A., Jordi, C., Luri, X., Julbe, F., Morvan, M., Balaguer-Núñez, L., & Cantat-Gaudin, T. (2018). A new method for unveiling open clusters in Gaia. New nearby open clusters confirmed by DR2. *A&A*, 618, Artikel A59, A59. DOI: [10.1051/0004-6361/201833390](https://doi.org/10.1051/0004-6361/201833390).
- Castro-Ginard, A., McMillan, P. J., Luri, X., Jordi, C., Romero-Gómez, M., Cantat-Gaudin, T., Casamiquela, L., Tarricq, Y., Soubiran, C., & Anders, F. (2021). Milky Way spiral arms from open clusters in Gaia EDR3. *A&A*, 652, Artikel A162, A162. DOI: [10.1051/0004-6361/202039751](https://doi.org/10.1051/0004-6361/202039751).
- Chandar, R., Fall, S. M., Whitmore, B. C., & Mulia, A. J. (2017). The Fraction of Stars That Form in Clusters in Different Galaxies. *ApJ*, 849(2), Artikel 128, 128. DOI: [10.3847/1538-4357/aa92ce](https://doi.org/10.3847/1538-4357/aa92ce).
- Choi, J., Dotter, A., Conroy, C., Cantiello, M., Paxton, B., & Johnson, B. D. (2016). Mesa Isochrones and Stellar Tracks (MIST). I. Solar-scaled Models. *ApJ*, 823(2), Artikel 102, 102. DOI: [10.3847/0004-637X/823/2/102](https://doi.org/10.3847/0004-637X/823/2/102).
- Conrad, C., Scholz, R. .-, Kharchenko, N. V., Piskunov, A. E., Röser, S., Schilbach, E., de Jong, R. S., Schnurr, O., Steinmetz, M., Grebel, E. K., Zwitter, T., Bienaymé, O., Bland-Hawthorn, J., Gibson, B. K., Gilmore, G., Kordopatis, G., Kunder, A., Navarro, J. F., Parker, Q., ... Wyse, R. (2017). A RAVE investigation on Galactic open clusters . II. Open cluster pairs, groups and complexes. *A&A*, 600, Artikel A106, A106. DOI: [10.1051/0004-6361/201630012](https://doi.org/10.1051/0004-6361/201630012).
- Coronado, J., Fürnkranz, V., & Rix, H.-W. (2022). Pearls on a String: Numerous Stellar Clusters Strung Along the Same Orbit. *ApJ*, 928(1), Artikel 70, 70. DOI: [10.3847/1538-4357/ac545c](https://doi.org/10.3847/1538-4357/ac545c).
- Coronado, J., Rix, H.-W., & Trick, W. H. (2018). Unbiased TGAS×LAMOST distances and the role of binarity. *MNRAS*, 481(3), 2970–2980. DOI: [10.1093/mnras/sty2468](https://doi.org/10.1093/mnras/sty2468).
- Coronado, J., Rix, H.-W., Trick, W. H., El-Badry, K., Rybizki, J., & Xiang, M. (2020). From birth associations to field stars: mapping the small-scale orbit distribution in the Galactic disc. *MNRAS*, 495(4), 4098–4112. DOI: [10.1093/mnras/staa1358](https://doi.org/10.1093/mnras/staa1358).
- Curtis, J. L., Agüeros, M. A., Mamajek, E. E., Wright, J. T., & Cummings, J. D. (2019). TESS Reveals that the Nearby Pisces-Eridanus Stellar Stream is only 120 Myr Old. *AJ*, 158(2), Artikel 77, 77. DOI: [10.3847/1538-3881/ab2899](https://doi.org/10.3847/1538-3881/ab2899).
- Davé, R., Anglés-Alcázar, D., Narayanan, D., Li, Q., Rafieferantsoa, M. H., & Appleby, S. (2019). SIMBA: Cosmological simulations with black hole growth and feedback. *MNRAS*, 486(2), 2827–2849. DOI: [10.1093/mnras/stz937](https://doi.org/10.1093/mnras/stz937).
- de Jong, R. S., Agertz, O., Berbel, A. A., Aird, J., Alexander, D. A., Amarsi, A., Anders, F., Andrae, R., Ansarinejad, B., Anson, W., Antilogus, P., Anwand-Heerwart, H., Arentsen, A., Arnadottir, A., Asplund, M., Auger, M., Azais, N., Baade, D., Baker, G., ... Zucker, D. (2019). 4MOST: Project overview and information for the First Call for Proposals. *The Messenger*, 175, 3–11. DOI: [10.18727/0722-6691/5117](https://doi.org/10.18727/0722-6691/5117).
- de La Fuente Marcos, R., & de La Fuente Marcos, C. (2009). Double or binary: on the multiplicity of open star clusters. *A&A*, 500(2), L13–L16. DOI: [10.1051/0004-6361/200912297](https://doi.org/10.1051/0004-6361/200912297).

- de Vaucouleurs, G. (1959). Classification and Morphology of External Galaxies. *Handbuch der Physik*, 53, 275. DOI: [10.1007/978-3-642-45932-0_7](https://doi.org/10.1007/978-3-642-45932-0_7).
- Deason, A. J., Belokurov, V., & Sanders, J. L. (2019). The total stellar halo mass of the Milky Way. *MNRAS*, 490(3), 3426–3439. DOI: [10.1093/mnras/stz2793](https://doi.org/10.1093/mnras/stz2793).
- Dias, W. S., Alessi, B. S., Moitinho, A., & Lépine, J. R. D. (2002). New catalogue of optically visible open clusters and candidates. *A&A*, 389, 871–873. DOI: [10.1051/0004-6361:20020668](https://doi.org/10.1051/0004-6361:20020668).
- Dieball, A., Müller, H., & Grebel, E. K. (2002). A statistical study of binary and multiple clusters in the LMC. *A&A*, 391, 547–564. DOI: [10.1051/0004-6361:20020815](https://doi.org/10.1051/0004-6361:20020815).
- Dotter, A. (2016). MESA Isochrones and Stellar Tracks (MIST) 0: Methods for the Construction of Stellar Isochrones. *ApJS*, 222(1), Artikel 8, 8. DOI: [10.3847/0067-0049/222/1/8](https://doi.org/10.3847/0067-0049/222/1/8).
- Douglas, S. T., Agüeros, M. A., Covey, K. R., Bowsher, E. C., Bochanski, J. J., Cargile, P. A., Kraus, A., Law, N. M., Lemonias, J. J., Arce, H. G., Fierroz, D. F., & Kundert, A. (2014). The Factory and the Beehive. II. Activity and Rotation in Praesepe and the Hyades. *ApJ*, 795(2), Artikel 161, 161. DOI: [10.1088/0004-637X/795/2/161](https://doi.org/10.1088/0004-637X/795/2/161).
- Eggen, O. J. (1959). Further tests of the reality of the Hyades group. *The Observatory*, 79, 143–148.
- Eggen, O. J. (1960). Stellar groups, VII. The structure of the Hyades group. *MNRAS*, 120, 540. DOI: [10.1093/mnras/120.6.540](https://doi.org/10.1093/mnras/120.6.540).
- Eilers, A.-C., Hogg, D. W., Rix, H.-W., & Ness, M. K. (2019). The Circular Velocity Curve of the Milky Way from 5 to 25 kpc. *ApJ*, 871(1), Artikel 120, 120. DOI: [10.3847/1538-4357/aaf648](https://doi.org/10.3847/1538-4357/aaf648).
- Elmegreen, B. G., & Efremov, Y. N. (1996). An Extension of Hierarchical Star Formation to Galactic Scales. *ApJ*, 466, 802. DOI: [10.1086/177554](https://doi.org/10.1086/177554).
- Elmegreen, B. G., & Falgarone, E. (1996). A Fractal Origin for the Mass Spectrum of Interstellar Clouds. *ApJ*, 471, 816. DOI: [10.1086/178009](https://doi.org/10.1086/178009).
- Ester, M., Kriegel, H.-P., Sander, J., & Xu, X. (1996). A density-based algorithm for discovering clusters a density-based algorithm for discovering clusters in large spatial databases with noise. *Proceedings of the Second International Conference on Knowledge Discovery and Data Mining*, 226–231. <http://dl.acm.org/citation.cfm?id=3001460.3001507>
- Fabrizio, C., Luri, X., Arenou, F., Babusiaux, C., Helmi, A., Muraveva, T., Reylé, C., Spoto, F., Vallenari, A., Antoja, T., Balbinot, E., Barache, C., Bauchet, N., Bragaglia, A., Busonero, D., Cantat-Gaudin, T., Carrasco, J. M., Diakité, S., Fabrizio, M., ... Weiler, M. (2021). Gaia Early Data Release 3. Catalogue validation. *A&A*, 649, Artikel A5, A5. DOI: [10.1051/0004-6361/202039834](https://doi.org/10.1051/0004-6361/202039834).
- Fall, S. M., & Efstathiou, G. (1980). Formation and rotation of disc galaxies with haloes. *MNRAS*, 193, 189–206. DOI: [10.1093/mnras/193.2.189](https://doi.org/10.1093/mnras/193.2.189).
- Fouesneau, M., Frémat, Y., Andrae, R., Korn, A. J., Soubiran, C., Kordopatis, G., Vallenari, A., Heiter, U., Creevey, O. L., Sarro, L. M., de Laverny, P., Lanzafame, A. C., Lobel, A., Sordo, R., Rybizki, J., Slezak, I., Álvarez, M. A., Drimmel, R., Garabato, D., ... Zorec, J. (2023). Gaia Data Release 3. Apsis. II. Stellar parameters. *A&A*, 674, Artikel A28, A28. DOI: [10.1051/0004-6361/202243919](https://doi.org/10.1051/0004-6361/202243919).

- Frankel, N., Rix, H.-W., Ting, Y.-S., Ness, M., & Hogg, D. W. (2018). Measuring Radial Orbit Migration in the Galactic Disk. *ApJ*, 865(2), Artikel 96, 96. DOI: [10.3847/1538-4357/aadba5](https://doi.org/10.3847/1538-4357/aadba5).
- Frankel, N., Sanders, J., Rix, H.-W., Ting, Y.-S., & Ness, M. (2019). The Inside-out Growth of the Galactic Disk. *ApJ*, 884(2), Artikel 99, 99. DOI: [10.3847/1538-4357/ab4254](https://doi.org/10.3847/1538-4357/ab4254).
- Freeman, K., & Bland-Hawthorn, J. (2002). The New Galaxy: Signatures of Its Formation. *ARA&A*, 40, 487–537. DOI: [10.1146/annurev.astro.40.060401.093840](https://doi.org/10.1146/annurev.astro.40.060401.093840).
- Friedmann, A. (1922). Über die Krümmung des Raumes. *Zeitschrift für Physik*, 10, 377–386. DOI: [10.1007/BF01332580](https://doi.org/10.1007/BF01332580).
- Friedmann, A. (1924). Über die Möglichkeit einer Welt mit konstanter negativer Krümmung des Raumes. *Zeitschrift für Physik*, 21(1), 326–332. DOI: [10.1007/BF01328280](https://doi.org/10.1007/BF01328280).
- Fritzewski, D. J., Barnes, S. A., James, D. J., Geller, A. M., Meibom, S., & Strassmeier, K. G. (2019). Spectroscopic membership for the populous 300 Myr-old open cluster NGC 3532. *A&A*, 622, Artikel A110, A110. DOI: [10.1051/0004-6361/201833587](https://doi.org/10.1051/0004-6361/201833587).
- Fujimoto, M., & Kumai, Y. (1997). Star Clusters Driven to Form by Strong Collisions Between Gas Clouds in High-Velocity Random Motion. *AJ*, 113, 249. DOI: [10.1086/118249](https://doi.org/10.1086/118249).
- Fürnkranz, V., Meingast, S., & Alves, J. (2019). Extended stellar systems in the solar neighborhood. III. Like ships in the night: the Coma Berenices neighbor moving group. *A&A*, 624, Artikel L11, L11. DOI: [10.1051/0004-6361/201935293](https://doi.org/10.1051/0004-6361/201935293).
- Fürnkranz, V., Rix, H.-W., Coronado, J., & Seeburger, R. (2024). The Age Distribution of Stellar Orbit Space Clumps. *ApJ*, 961(1), Artikel 113, 113. DOI: [10.3847/1538-4357/ad0f99](https://doi.org/10.3847/1538-4357/ad0f99).
- Gagné, J., & Faherty, J. K. (2018). BANYAN. XIII. A First Look at Nearby Young Associations with Gaia Data Release 2. *ApJ*, 862(2), Artikel 138, 138. DOI: [10.3847/1538-4357/aaca2e](https://doi.org/10.3847/1538-4357/aaca2e).
- Gagné, J., Faherty, J. K., & Mamajek, E. E. (2018). Volans-Carina: A New 90 Myr Old Stellar Association at 85 pc. *ApJ*, 865(2), Artikel 136, 136. DOI: [10.3847/1538-4357/aadaed](https://doi.org/10.3847/1538-4357/aadaed).
- Gaia Collaboration, Katz, D., Antoja, T., Romero-Gómez, M., Drimmel, R., Reylé, C., Seabroke, G. M., Soubiran, C., Babusiaux, C., Di Matteo, P., Figueras, F., Poggio, E., Robin, A. C., Evans, D. W., Brown, A. G. A., Vallenari, A., Prusti, T., de Bruijne, J. H. J., Bailer-Jones, C. A. L., ... Zwitter, T. (2018). Gaia Data Release 2. Mapping the Milky Way disc kinematics. *A&A*, 616, Artikel A11, A11. DOI: [10.1051/0004-6361/201832865](https://doi.org/10.1051/0004-6361/201832865).
- Gaia Collaboration, Prusti, T., de Bruijne, J. H. J., Brown, A. G. A., Vallenari, A., Babusiaux, C., Bailer-Jones, C. A. L., Bastian, U., Biermann, M., Evans, D. W., Eyer, L., Jansen, F., Jordi, C., Klioner, S. A., Lammers, U., Lindegren, L., Luri, X., Mignard, F., Milligan, D. J., ... Zschocke, S. (2016). The Gaia mission. *A&A*, 595, Artikel A1, A1. DOI: [10.1051/0004-6361/201629272](https://doi.org/10.1051/0004-6361/201629272).
- Gaia Collaboration, Vallenari, A., Brown, A. G. A., Prusti, T., de Bruijne, J. H. J., Arenou, F., Babusiaux, C., Biermann, M., Creevey, O. L., Ducourant, C., Evans, D. W., Eyer, L., Guerra, R., Hutton, A., Jordi, C., Klioner, S. A., Lammers, U. L., Lindegren, L., Luri, X., ... Zwitter, T. (2023). Gaia Data Release 3. Summary of the content and survey properties. *A&A*, 674, Artikel A1, A1. DOI: [10.1051/0004-6361/202243940](https://doi.org/10.1051/0004-6361/202243940).

- Gillessen, S., Eisenhauer, F., Trippe, S., Alexander, T., Genzel, R., Martins, F., & Ott, T. (2009). Monitoring Stellar Orbits Around the Massive Black Hole in the Galactic Center. *ApJ*, *692*(2), 1075–1109. DOI: [10.1088/0004-637X/692/2/1075](https://doi.org/10.1088/0004-637X/692/2/1075).
- Gossage, S., Conroy, C., Dotter, A., Choi, J., Rosenfield, P., Cargile, P., & Dolphin, A. (2018). Age Determinations of the Hyades, Praesepe, and Pleiades via MESA Models with Rotation. *ApJ*, *863*(1), Artikel 67, 67. DOI: [10.3847/1538-4357/aad0a0](https://doi.org/10.3847/1538-4357/aad0a0).
- Green, G. M., Schlafly, E., Zucker, C., Speagle, J. S., & Finkbeiner, D. (2019). A 3D Dust Map Based on Gaia, Pan-STARRS 1, and 2MASS. *ApJ*, *887*(1), Artikel 93, 93. DOI: [10.3847/1538-4357/ab5362](https://doi.org/10.3847/1538-4357/ab5362).
- Großschedl, J. E., Alves, J., Meingast, S., Ackerl, C., Ascenso, J., Bouy, H., Burkert, A., Forbrich, J., Fürnkranz, V., Goodman, A., Hacar, Á., Herbst-Kiss, G., Lada, C. J., Larreina, I., Leschinski, K., Lombardi, M., Moitinho, A., Mortimer, D., & Zari, E. (2018). 3D shape of Orion A from Gaia DR2. *A&A*, *619*, Artikel A106, A106. DOI: [10.1051/0004-6361/201833901](https://doi.org/10.1051/0004-6361/201833901).
- Großschedl, J. E., Alves, J., Meingast, S., & Herbst-Kiss, G. (2021). 3D dynamics of the Orion cloud complex. Discovery of coherent radial gas motions at the 100-pc scale. *A&A*, *647*, Artikel A91, A91. DOI: [10.1051/0004-6361/202038913](https://doi.org/10.1051/0004-6361/202038913).
- Grudić, M. Y., Guszejnov, D., Hopkins, P. F., Offner, S. S. R., & Faucher-Giguère, C.-A. (2021). STAR-FORGE: Towards a comprehensive numerical model of star cluster formation and feedback. *MNRAS*, *506*(2), 2199–2231. DOI: [10.1093/mnras/stab1347](https://doi.org/10.1093/mnras/stab1347).
- Gusev, A. S., & Efremov, Y. N. (2013). Regular chains of star formation complexes in spiral arms of NGC 628. *MNRAS*, *434*(1), 313–324. DOI: [10.1093/mnras/stt1019](https://doi.org/10.1093/mnras/stt1019).
- Gutcke, T. A., Pakmor, R., Naab, T., & Springel, V. (2021). LYRA - I. Simulating the multiphase ISM of a dwarf galaxy with variable energy supernovae from individual stars. *MNRAS*, *501*(4), 5597–5615. DOI: [10.1093/mnras/staa3875](https://doi.org/10.1093/mnras/staa3875).
- Hao, C. J., Xu, Y., Wu, Z. Y., Lin, Z. H., Liu, D. J., & Li, Y. J. (2022). Newly detected open clusters in the Galactic disk using Gaia EDR3. *A&A*, *660*, Artikel A4, A4. DOI: [10.1051/0004-6361/202243091](https://doi.org/10.1051/0004-6361/202243091).
- Harris, C. R., Millman, K. J., van der Walt, S. J., Gommers, R., Virtanen, P., Cournapeau, D., Wieser, E., Taylor, J., Berg, S., Smith, N. J., Kern, R., Picus, M., Hoyer, S., van Kerkwijk, M. H., Brett, M., Haldane, A., del Río, J. F., Wiebe, M., Peterson, P., ... Oliphant, T. E. (2020). Array programming with NumPy. *Nature*, *585*(7825), 357–362. DOI: [10.1038/s41586-020-2649-2](https://doi.org/10.1038/s41586-020-2649-2).
- Hawkins, K., Lucey, M., & Curtis, J. (2020). The chemical nature of the young 120-Myr-old nearby Pisces-Eridanus stellar stream flowing through the Galactic disc. *MNRAS*, *496*(2), 2422–2435. DOI: [10.1093/mnras/staa1673](https://doi.org/10.1093/mnras/staa1673).
- Hayashi, C. (1961). Stellar evolution in early phases of gravitational contraction. *PASJ*, *13*, 450–452.
- He, Z., Wang, K., Luo, Y., Li, J., Liu, X., & Jiang, Q. (2022). A Blind All-sky Search for Star Clusters in Gaia EDR3: 886 Clusters within 1.2 kpc of the Sun. *ApJS*, *262*(1), Artikel 7, 7. DOI: [10.3847/1538-4365/ac7c17](https://doi.org/10.3847/1538-4365/ac7c17).

- He, Z.-H., Xu, Y., Hao, C.-J., Wu, Z.-Y., & Li, J.-J. (2021). A catalogue of 74 new open clusters found in Gaia Data-Release 2. *Research in Astronomy and Astrophysics*, 21(4), Artikel 093, 093. DOI: [10.1088/1674-4527/21/4/93](https://doi.org/10.1088/1674-4527/21/4/93).
- Helmi, A. (2020). Streams, Substructures, and the Early History of the Milky Way. *ARA&A*, 58, 205–256. DOI: [10.1146/annurev-astro-032620-021917](https://doi.org/10.1146/annurev-astro-032620-021917).
- Helmi, A., Babusiaux, C., Koppelman, H. H., Massari, D., Veljanoski, J., & Brown, A. G. A. (2018). The merger that led to the formation of the Milky Way's inner stellar halo and thick disk. *Nature*, 563(7729), 85–88. DOI: [10.1038/s41586-018-0625-x](https://doi.org/10.1038/s41586-018-0625-x).
- Hertzsprung, E. (1911). Number 63. Zweiundzwanzigsten Bandes Erstes Stuck. Uber die verwendung photographischer effektiver wellenlangen zur bestimmung von farbenaquivalenten. *Publikationen des Astrophysikalischen Observatoriums zu Potsdam*, 22, A1–A40.1.
- Hobbs, D., Høg, E., Mora, A., Crowley, C., McMillan, P., Ranalli, P., Heiter, U., Jordi, C., Hambly, N., Church, R., Anthony, B., Tanga, P., Chemin, L., Portell, J., Jiménez-Esteban, F., Klioner, S., Mignard, F., Fynbo, J., Wyrzykowski, Ł., ... Lindegren, L. (2016). GaiaNIR: Combining optical and Near-Infra-Red (NIR) capabilities with Time-Delay-Integration (TDI) sensors for a future Gaia-like mission. *arXiv e-prints*, Artikel arXiv:1609.07325, arXiv:1609.07325. DOI: [10.48550/arXiv.1609.07325](https://doi.org/10.48550/arXiv.1609.07325).
- Hobbs, D., Leitz, C., Bartlett, J., Hepburn, I., Kawata, D., Cropper, M., Mazin, B., Brown, A., Makarov, V., McArthur, B., Moore, A., Sharp, R., Gilbert, J., & Høg, E. (2019). Astro2020 Activity, Project of State of the Profession Consideration (APC) White Paper: All-Sky Near Infrared Space Astrometry. State of the Profession Considerations: Development of Scanning NIR Detectors for Astronomy. *arXiv e-prints*, Artikel arXiv:1907.05191, arXiv:1907.05191. DOI: [10.48550/arXiv.1907.05191](https://doi.org/10.48550/arXiv.1907.05191).
- Hubble, E. P. (1926). Extragalactic nebulae. *ApJ*, 64, 321–369. DOI: [10.1086/143018](https://doi.org/10.1086/143018).
- Hubble, E. (1929). A Relation between Distance and Radial Velocity among Extra-Galactic Nebulae. *Proceedings of the National Academy of Science*, 15(3), 168–173. DOI: [10.1073/pnas.15.3.168](https://doi.org/10.1073/pnas.15.3.168).
- Hunt, E. L., & Reffert, S. (2021). Improving the open cluster census. I. Comparison of clustering algorithms applied to Gaia DR2 data. *A&A*, 646, Artikel A104, A104. DOI: [10.1051/0004-6361/202039341](https://doi.org/10.1051/0004-6361/202039341).
- Hunt, E. L., & Reffert, S. (2023). Improving the open cluster census. II. An all-sky cluster catalogue with Gaia DR3. *A&A*, 673, Artikel A114, A114. DOI: [10.1051/0004-6361/202346285](https://doi.org/10.1051/0004-6361/202346285).
- Hunter, J. D. (2007). Matplotlib: a 2d graphics environment. *Computing in Science & Engineering*, 9(3), 90–95. DOI: [10.1109/MCSE.2007.55](https://doi.org/10.1109/MCSE.2007.55).
- Jeans, J. H. (1902). The Stability of a Spherical Nebula. *Philosophical Transactions of the Royal Society of London Series A*, 199, 1–53. DOI: [10.1098/rsta.1902.0012](https://doi.org/10.1098/rsta.1902.0012).
- Jerabkova, T., Beccari, G., Boffin, H. M. J., Petr-Gotzens, M. G., Manara, C. F., Prada Moroni, P. G., Tognelli, E., & Degl'Innocenti, S. (2019). When the tale comes true: multiple populations and

- wide binaries in the Orion Nebula Cluster. *A&A*, 627, Artikel A57, A57. DOI: [10.1051/0004-6361/201935016](https://doi.org/10.1051/0004-6361/201935016).
- Jerabkova, T., Boffin, H. M. J., Beccari, G., & Anderson, R. I. (2019). A stellar relic filament in the Orion star-forming region. *MNRAS*, 489(3), 4418–4428. DOI: [10.1093/mnras/stz2315](https://doi.org/10.1093/mnras/stz2315).
- Jönsson, H., Holtzman, J. A., Allende Prieto, C., Cunha, K., García-Hernández, D. A., Hasselquist, S., Masseron, T., Osorio, Y., Shetrone, M., Smith, V., Stringfellow, G. S., Bizyaev, D., Edvardsson, B., Majewski, S. R., Mészáros, S., Souto, D., Zamora, O., Beaton, R. L., Bovy, J., ... Sobeck, J. (2020). APOGEE Data and Spectral Analysis from SDSS Data Release 16: Seven Years of Observations Including First Results from APOGEE-South. *AJ*, 160(3), Artikel 120, 120. DOI: [10.3847/1538-3881/aba592](https://doi.org/10.3847/1538-3881/aba592).
- Katz, D., Sartoretti, P., Cropper, M., Panuzzo, P., Seabroke, G. M., Viala, Y., Benson, K., Blomme, R., Jasiewicz, G., Jean-Antoine, A., Huckle, H., Smith, M., Baker, S., Crifo, F., Damerdjji, Y., David, M., Dolding, C., Frémat, Y., Gosset, E., ... Žerjal, M. (2019). Gaia Data Release 2. Properties and validation of the radial velocities. *A&A*, 622, Artikel A205, A205. DOI: [10.1051/0004-6361/201833273](https://doi.org/10.1051/0004-6361/201833273).
- Katz, D., Sartoretti, P., Guerrier, A., Panuzzo, P., Seabroke, G. M., Thévenin, F., Cropper, M., Benson, K., Blomme, R., Haigron, R., Marchal, O., Smith, M., Baker, S., Chemin, L., Damerdjji, Y., David, M., Dolding, C., Frémat, Y., Gosset, E., ... Viala, Y. (2023). Gaia Data Release 3. Properties and validation of the radial velocities. *A&A*, 674, Artikel A5, A5. DOI: [10.1051/0004-6361/202244220](https://doi.org/10.1051/0004-6361/202244220).
- Kharchenko, N. V., Berczik, P., Petrov, M. I., Piskunov, A. E., Röser, S., Schilbach, E., & Scholz, R. -. (2009). Shape parameters of Galactic open clusters. *A&A*, 495(3), 807–818. DOI: [10.1051/0004-6361/200810407](https://doi.org/10.1051/0004-6361/200810407).
- Kharchenko, N. V., Piskunov, A. E., Röser, S., Schilbach, E., & Scholz, R. -. (2005). Astrophysical parameters of Galactic open clusters. *A&A*, 438(3), 1163–1173. DOI: [10.1051/0004-6361:20042523](https://doi.org/10.1051/0004-6361:20042523).
- Kharchenko, N. V., Piskunov, A. E., Schilbach, E., Röser, S., & Scholz, R. -. (2013). Global survey of star clusters in the Milky Way. II. The catalogue of basic parameters. *A&A*, 558, Artikel A53, A53. DOI: [10.1051/0004-6361/201322302](https://doi.org/10.1051/0004-6361/201322302).
- Kollmeier, J., Anderson, S. F., Blanc, G. A., Blanton, M. R., Covey, K. R., Crane, J., Drory, N., Frinchaboy, P. M., Froning, C. S., Johnson, J. A., Kneib, J. .-, Kreckel, K., Merloni, A., Pellegrini, E. W., Pogge, R. W., Ramirez, S. V., Rix, H. W., Sayres, C., Sánchez-Gallego, J., ... Weinberg, D. H. (2019). SDSS-V Pioneering Panoptic Spectroscopy. *Bulletin of the American Astronomical Society*, 51, Artikel 274, 274.
- Kontizas, E., Kontizas, M., & Michalitsianos, A. (1993). Indications for common origin and gravitational interaction in three binary LMC clusters. *A&A*, 267, 59–65.
- Kos, J., Bland-Hawthorn, J., Asplund, M., Buder, S., Lewis, G. F., Lin, J., Martell, S. L., Ness, M. K., Sharma, S., De Silva, G. M., Simpson, J. D., Zucker, D. B., Zwitter, T., Čotar, K., & Spina, L.

- (2019). Discovery of a 21 Myr old stellar population in the Orion complex*. *A&A*, 631, Artikel A166, A166. DOI: [10.1051/0004-6361/201834710](https://doi.org/10.1051/0004-6361/201834710).
- Kos, J., Bland-Hawthorn, J., Buder, S., Nordlander, T., Spina, L., Beeson, K. L., Lind, K., Asplund, M., Freeman, K., Hayden, M. R., Lewis, G. F., Martell, S. L., Sharma, S., De Silva, G., Simpson, J. D., Zucker, D. B., Zwitter, T., Čotar, K., Horner, J., ... Traven, G. (2021). The GALAH survey: Chemical homogeneity of the Orion complex. *MNRAS*, 506(3), 4232–4250. DOI: [10.1093/mnras/stab1767](https://doi.org/10.1093/mnras/stab1767).
- Kos, J., de Silva, G., Buder, S., Bland-Hawthorn, J., Sharma, S., Asplund, M., D’Orazi, V., Duong, L., Freeman, K., Lewis, G. F., Lin, J., Lind, K., Martell, S. L., Schlesinger, K. J., Simpson, J. D., Zucker, D. B., Zwitter, T., Bedding, T. R., Čotar, K., ... Traven, G. (2018). The GALAH survey and Gaia DR2: (non-)existence of five sparse high-latitude open clusters. *MNRAS*, 480(4), 5242–5259. DOI: [10.1093/mnras/sty2171](https://doi.org/10.1093/mnras/sty2171).
- Kounkel, M., & Covey, K. (2019). Untangling the Galaxy. I. Local Structure and Star Formation History of the Milky Way. *AJ*, 158(3), Artikel 122, 122. DOI: [10.3847/1538-3881/ab339a](https://doi.org/10.3847/1538-3881/ab339a).
- Kounkel, M., Covey, K., & Stassun, K. G. (2020). Untangling the Galaxy. II. Structure within 3 kpc. *AJ*, 160(6), Artikel 279, 279. DOI: [10.3847/1538-3881/abc0e6](https://doi.org/10.3847/1538-3881/abc0e6).
- Kovács, G., Hartman, J. D., Bakos, G. Á., Quinn, S. N., Penev, K., Latham, D. W., Bhatti, W., Csubry, Z., & de Val-Borro, M. (2014). Stellar rotational periods in the planet hosting open cluster Praesepe. *MNRAS*, 442(3), 2081–2093. DOI: [10.1093/mnras/stu946](https://doi.org/10.1093/mnras/stu946).
- Kovaleva, D. A., Ishchenko, M., Postnikova, E., Berczik, P., Piskunov, A. E., Kharchenko, N. V., Polyachenko, E., Reffert, S., Sysoliatina, K., & Just, A. (2020). Collinder 135 and UBC 7: A physical pair of open clusters. *A&A*, 642, Artikel L4, L4. DOI: [10.1051/0004-6361/202039215](https://doi.org/10.1051/0004-6361/202039215).
- Krumholz, M. R., McKee, C. F., & Bland-Hawthorn, J. (2019). Star Clusters Across Cosmic Time. *ARA&A*, 57, 227–303. DOI: [10.1146/annurev-astro-091918-104430](https://doi.org/10.1146/annurev-astro-091918-104430).
- Kuhn, M. A., Hillenbrand, L. A., Sills, A., Feigelson, E. D., & Getman, K. V. (2019). Kinematics in Young Star Clusters and Associations with Gaia DR2. *ApJ*, 870(1), Artikel 32, 32. DOI: [10.3847/1538-4357/aaef8c](https://doi.org/10.3847/1538-4357/aaef8c).
- Lada, C. J., & Lada, E. A. (2003). Embedded Clusters in Molecular Clouds. *ARA&A*, 41, 57–115. DOI: [10.1146/annurev.astro.41.011802.094844](https://doi.org/10.1146/annurev.astro.41.011802.094844).
- Lahén, N., Naab, T., Johansson, P. H., Elmegreen, B., Hu, C.-Y., Walch, S., Steinwandel, U. P., & Moster, B. P. (2020). The GRIFFIN Project—Formation of Star Clusters with Individual Massive Stars in a Simulated Dwarf Galaxy Starburst. *ApJ*, 891(1), Artikel 2, 2. DOI: [10.3847/1538-4357/ab7190](https://doi.org/10.3847/1538-4357/ab7190).
- Lamb, J. B., Oey, M. S., Werk, J. K., & Ingleby, L. D. (2010). The Sparsest Clusters with O Stars. *ApJ*, 725(2), 1886–1902. DOI: [10.1088/0004-637X/725/2/1886](https://doi.org/10.1088/0004-637X/725/2/1886).
- Lamers, H. J. G. L. M., Baumgardt, H., & Gieles, M. (2010). Mass-loss rates and the mass evolution of star clusters. *MNRAS*, 409(1), 305–328. DOI: [10.1111/j.1365-2966.2010.17309.x](https://doi.org/10.1111/j.1365-2966.2010.17309.x).

- Larson, R. B. (1976). Models for the formation of disc galaxies. *MNRAS*, *176*, 31–52. DOI: [10.1093/mnras/176.1.31](https://doi.org/10.1093/mnras/176.1.31).
- Lemaître, G. (1927). Un Univers homogène de masse constante et de rayon croissant rendant compte de la vitesse radiale des nébuleuses extra-galactiques. *Annales de la Société Scientifique de Bruxelles*, *47*, 49–59.
- Licquia, T. C., & Newman, J. A. (2015). Improved Estimates of the Milky Way’s Stellar Mass and Star Formation Rate from Hierarchical Bayesian Meta-Analysis. *ApJ*, *806*(1), Artikel 96, 96. DOI: [10.1088/0004-637X/806/1/96](https://doi.org/10.1088/0004-637X/806/1/96).
- Lin, C. C., & Shu, F. H. (1964). On the Spiral Structure of Disk Galaxies. *ApJ*, *140*, 646. DOI: [10.1086/147955](https://doi.org/10.1086/147955).
- Lindgren, L., Klioner, S. A., Hernández, J., Bombrun, A., Ramos-Lerate, M., Steidelmüller, H., Bastian, U., Biermann, M., de Torres, A., Gerlach, E., Geyer, R., Hilger, T., Hobbs, D., Lammers, U., McMillan, P. J., Stephenson, C. A., Castañeda, J., Davidson, M., Fabricius, C., ... Vecchiato, A. (2021). Gaia Early Data Release 3. The astrometric solution. *A&A*, *649*, Artikel A2, A2. DOI: [10.1051/0004-6361/202039709](https://doi.org/10.1051/0004-6361/202039709).
- Liu, L., & Pang, X. (2019). A Catalog of Newly Identified Star Clusters in Gaia DR2. *ApJS*, *245*(2), Artikel 32, 32. DOI: [10.3847/1538-4365/ab530a](https://doi.org/10.3847/1538-4365/ab530a).
- López-Corredoira, M., Cabrera-Lavers, A., Garzón, F., & Hammersley, P. L. (2002). Old stellar Galactic disc in near-plane regions according to 2MASS: Scales, cut-off, flare and warp. *A&A*, *394*, 883–899. DOI: [10.1051/0004-6361:20021175](https://doi.org/10.1051/0004-6361:20021175).
- Luhman, K. L., & Eskin, T. L. (2020). Refining the Census of the Upper Scorpius Association with Gaia. *AJ*, *160*(1), Artikel 44, 44. DOI: [10.3847/1538-3881/ab9599](https://doi.org/10.3847/1538-3881/ab9599).
- Maoz, D. (2016). *Astrophysics in a Nutshell. Second Edition*.
- Martínez-Barbosa, C. A., Brown, A. G. A., Boekholt, T., Portegies Zwart, S., Antiche, E., & Antoja, T. (2016). The evolution of the Sun’s birth cluster and the search for the solar siblings with Gaia. *MNRAS*, *457*(1), 1062–1075. DOI: [10.1093/mnras/stw006](https://doi.org/10.1093/mnras/stw006).
- Mather, J. C., Cheng, E. S., Eplee, J., R. E., Isaacman, R. B., Meyer, S. S., Shafer, R. A., Weiss, R., Wright, E. L., Bennett, C. L., Boggess, N. W., Dwek, E., Gulkis, S., Hauser, M. G., Janssen, M., Kelsall, T., Lubin, P. M., Moseley, J., S. H., Murdock, T. L., Silverberg, R. F., ... Wilkinson, D. T. (1990). A Preliminary Measurement of the Cosmic Microwave Background Spectrum by the Cosmic Background Explorer (COBE) Satellite. *ApJL*, *354*, L37. DOI: [10.1086/185717](https://doi.org/10.1086/185717).
- McMillan, P. J. (2011). Mass models of the Milky Way. *MNRAS*, *414*(3), 2446–2457. DOI: [10.1111/j.1365-2966.2011.18564.x](https://doi.org/10.1111/j.1365-2966.2011.18564.x).
- Meingast, S., & Alves, J. (2019). Extended stellar systems in the solar neighborhood. I. The tidal tails of the Hyades. *A&A*, *621*, Artikel L3, L3. DOI: [10.1051/0004-6361/201834622](https://doi.org/10.1051/0004-6361/201834622).
- Meingast, S., Alves, J., & Fürnkranz, V. (2019). Extended stellar systems in the solar neighborhood . II. Discovery of a nearby 120° stellar stream in Gaia DR2. *A&A*, *622*, Artikel L13, L13. DOI: [10.1051/0004-6361/201834950](https://doi.org/10.1051/0004-6361/201834950).

- Meingast, S., Alves, J., & Rottensteiner, A. (2021). Extended stellar systems in the solar neighborhood. V. Discovery of coronae of nearby star clusters. *A&A*, 645, Artikel A84, A84. DOI: [10.1051/0004-6361/202038610](https://doi.org/10.1051/0004-6361/202038610).
- Messier, C. (1781, January). Catalogue des Nébuleuses et des Amas d'Étoiles (Catalog of Nebulae and Star Clusters).
- Mo, H., van den Bosch, F. C., & White, S. (2010). *Galaxy Formation and Evolution*.
- Mucciarelli, A., Origlia, L., Ferraro, F. R., Bellazzini, M., & Lanzoni, B. (2012). Blood Ties: The Real Nature of the LMC Binary Globular Clusters NGC 2136 and NGC 2137. *ApJL*, 746(2), Artikel L19, L19. DOI: [10.1088/2041-8205/746/2/L19](https://doi.org/10.1088/2041-8205/746/2/L19).
- Mutch, S. J., Croton, D. J., & Poole, G. B. (2011). The Mid-life Crisis of the Milky Way and M31. *ApJ*, 736(2), Artikel 84, 84. DOI: [10.1088/0004-637X/736/2/84](https://doi.org/10.1088/0004-637X/736/2/84).
- Paladini, R., Zucker, C., Benjamin, R., Nataf, D., Minniti, D., Zasowski, G., Peek, J., Carey, S., Allen, L., Alonso-Garcia, J., Alves, J., Anders, F., Athanassoula, E., Beers, T. C., Bird, J., Bland-Hwathorn, J., Brown, A., Buder, S., Casagrande, L., ... Zakamska, N. (2023). Roman Early-Definition Astrophysics Survey Opportunity: Galactic Roman Infrared Plane Survey (GRIPS). *arXiv e-prints*, Artikel arXiv:2307.07642, arXiv:2307.07642. DOI: [10.48550/arXiv.2307.07642](https://doi.org/10.48550/arXiv.2307.07642).
- Palma, T., Gramajo, L. V., Clariá, J. J., Lares, M., Geisler, D., & Ahumada, A. V. (2016). Catalogue of Large Magellanic Cloud star clusters observed in the Washington photometric system. *A&A*, 586, Artikel A41, A41. DOI: [10.1051/0004-6361/201527305](https://doi.org/10.1051/0004-6361/201527305).
- Pedregosa, F., Varoquaux, G., Gramfort, A., Michel, V., Thirion, B., Grisel, O., Blondel, M., Prettenhofer, P., Weiss, R., Dubourg, V., Vanderplas, J., Passos, A., Cournapeau, D., Brucher, M., Perrot, M., & Duchesnay, E. (2011). Scikit-learn: machine learning in Python. *Journal of Machine Learning Research*, 12, 2825–2830.
- Penzias, A. A., & Wilson, R. W. (1965). A Measurement of Excess Antenna Temperature at 4080 Mc/s. *ApJ*, 142, 419–421. DOI: [10.1086/148307](https://doi.org/10.1086/148307).
- Perlmutter, S., Aldering, G., Goldhaber, G., Knop, R. A., Nugent, P., Castro, P. G., Deustua, S., Fabbro, S., Goobar, A., Groom, D. E., Hook, I. M., Kim, A. G., Kim, M. Y., Lee, J. C., Nunes, N. J., Pain, R., Pennypacker, C. R., Quimby, R., Lidman, C., ... Project, T. S. C. (1999). Measurements of Ω and Λ from 42 High-Redshift Supernovae. *ApJ*, 517(2), 565–586. DOI: [10.1086/307221](https://doi.org/10.1086/307221).
- Perryman, M. A. C., Brown, A. G. A., LEBRETON, Y., Gomez, A., Turon, C., Cayrel de Strobel, G., Merrillioid, J. C., Robichon, N., Kovalevsky, J., & Crifo, F. (1998). The Hyades: distance, structure, dynamics, and age. *A&A*, 331, 81–120.
- Pietrzynski, G., & Udalski, A. (2000). The Optical Gravitational Lensing Experiment. Multiple Cluster Candidates in the Large Magellanic Cloud. *AcA*, 50, 355–367.
- Pillepich, A., Springel, V., Nelson, D., Genel, S., Naiman, J., Pakmor, R., Hernquist, L., Torrey, P., Vogelsberger, M., Weinberger, R., & Marinacci, F. (2018). Simulating galaxy formation with the IllustrisTNG model. *MNRAS*, 473(3), 4077–4106. DOI: [10.1093/mnras/stx2656](https://doi.org/10.1093/mnras/stx2656).

- Planck Collaboration, Aghanim, N., Akrami, Y., Ashdown, M., Aumont, J., Baccigalupi, C., Ballardini, M., Banday, A. J., Barreiro, R. B., Bartolo, N., Basak, S., Battye, R., Benabed, K., Bernard, J. .-, Bersanelli, M., Bielewicz, P., Bock, J. J., Bond, J. R., Borrill, J., ... Zonca, A. (2020). Planck 2018 results. VI. Cosmological parameters. *A&A*, *641*, Artikel A6, A6. DOI: [10.1051/0004-6361/201833910](https://doi.org/10.1051/0004-6361/201833910).
- Portail, M., Wegg, C., Gerhard, O., & Martinez-Valpuesta, I. (2015). Made-to-measure models of the Galactic box/peanut bulge: stellar and total mass in the bulge region. *MNRAS*, *448*(1), 713–731. DOI: [10.1093/mnras/stv058](https://doi.org/10.1093/mnras/stv058).
- Preibisch, T., & Mamajek, E. (2008). The Nearest OB Association: Scorpius-Centaurus (Sco OB2). In B. Reipurth (Ed.), *Handbook of star forming regions, volume ii* (p. 235, Vol. 5). DOI: [10.48550/arXiv.0809.0407](https://doi.org/10.48550/arXiv.0809.0407).
- Price-Jones, N., Bovy, J., Webb, J. J., Allende Prieto, C., Beaton, R., Brownstein, J. R., Cohen, R. E., Cunha, K., Donor, J., Frinchaboy, P. M., García-Hernández, D. A., Lane, R. R., Majewski, S. R., Nidever, D. L., & Roman-Lopes, A. (2020). Strong chemical tagging with APOGEE: 21 candidate star clusters that have dissolved across the Milky Way disc. *MNRAS*, *496*(4), 5101–5115. DOI: [10.1093/mnras/staa1905](https://doi.org/10.1093/mnras/staa1905).
- Price-Whelan, A. M., Hogg, D. W., Johnston, K. V., Ness, M. K., Rix, H.-W., Beaton, R. L., Brownstein, J. R., García-Hernández, D. A., Hasselquist, S., Hayes, C. R., Lane, R. R., Shetrone, M., Sobek, J., & Zasowski, G. (2021). Orbital Torus Imaging: Using Element Abundances to Map Orbits and Mass in the Milky Way. *ApJ*, *910*(1), Artikel 17, 17. DOI: [10.3847/1538-4357/abe1b7](https://doi.org/10.3847/1538-4357/abe1b7).
- Quillen, A. C., Dougherty, J., Bagley, M. B., Minchev, I., & Comparetta, J. (2011). Structure in phase space associated with spiral and bar density waves in an N-body hybrid galactic disc. *MNRAS*, *417*(1), 762–784. DOI: [10.1111/j.1365-2966.2011.19349.x](https://doi.org/10.1111/j.1365-2966.2011.19349.x).
- Ratzenböck, S., Meingast, S., Alves, J., Möller, T., & Bomze, I. (2020). Extended stellar systems in the solar neighborhood. IV. Meingast 1: the most massive stellar stream in the solar neighborhood. *A&A*, *639*, Artikel A64, A64. DOI: [10.1051/0004-6361/202037591](https://doi.org/10.1051/0004-6361/202037591).
- Reid, M. J., Menten, K. M., Brunthaler, A., Zheng, X. W., Dame, T. M., Xu, Y., Wu, Y., Zhang, B., Sanna, A., Sato, M., Hachisuka, K., Choi, Y. K., Immer, K., Moscadelli, L., Rygl, K. L. J., & Bartkiewicz, A. (2014). Trigonometric Parallaxes of High Mass Star Forming Regions: The Structure and Kinematics of the Milky Way. *ApJ*, *783*(2), Artikel 130, 130. DOI: [10.1088/0004-637X/783/2/130](https://doi.org/10.1088/0004-637X/783/2/130).
- Riedel, A. R., Blunt, S. C., Lambrides, E. L., Rice, E. L., Cruz, K. L., & Faherty, J. K. (2017). LACEwING: A New Moving Group Analysis Code. *AJ*, *153*(3), Artikel 95, 95. DOI: [10.3847/1538-3881/153/3/95](https://doi.org/10.3847/1538-3881/153/3/95).
- Riess, A. G., Filippenko, A. V., Challis, P., Clocchiatti, A., Diercks, A., Garnavich, P. M., Gilliland, R. L., Hogan, C. J., Jha, S., Kirshner, R. P., Leibundgut, B., Phillips, M. M., Reiss, D., Schmidt, B. P., Schommer, R. A., Smith, R. C., Spyromilio, J., Stubbs, C., Suntzeff, N. B., & Tonry, J. (1998).

- Observational Evidence from Supernovae for an Accelerating Universe and a Cosmological Constant. *AJ*, 116(3), 1009–1038. DOI: [10.1086/300499](https://doi.org/10.1086/300499).
- Rix, H.-W., & Bovy, J. (2013). The Milky Way's stellar disk. Mapping and modeling the Galactic disk. *A&A Rev*, 21, Artikel 61, 61. DOI: [10.1007/s00159-013-0061-8](https://doi.org/10.1007/s00159-013-0061-8).
- Robertson, B. E., Banerji, M., Brough, S., Davies, R. L., Ferguson, H. C., Hausen, R., Kaviraj, S., Newman, J. A., Schmidt, S. J., Tyson, J. A., & Wechsler, R. H. (2019). Galaxy formation and evolution science in the era of the Large Synoptic Survey Telescope. *Nature Reviews Physics*, 1(7), 450–462. DOI: [10.1038/s42254-019-0067-x](https://doi.org/10.1038/s42254-019-0067-x).
- Robertson, H. P. (1935). Kinematics and World-Structure. *ApJ*, 82, 284. DOI: [10.1086/143681](https://doi.org/10.1086/143681).
- Röser, S., & Schilbach, E. (2019). Praesepe (NGC 2632) and its tidal tails. *A&A*, 627, Artikel A4, A4. DOI: [10.1051/0004-6361/201935502](https://doi.org/10.1051/0004-6361/201935502).
- Röser, S., Schilbach, E., & Goldman, B. (2019). Hyades tidal tails revealed by Gaia DR2. *A&A*, 621, Artikel L2, L2. DOI: [10.1051/0004-6361/201834608](https://doi.org/10.1051/0004-6361/201834608).
- Rubin, V. C., Ford, J., W. K., & Thonnard, N. (1980). Rotational properties of 21 SC galaxies with a large range of luminosities and radii, from NGC 4605 (R=4kpc) to UGC 2885 (R=122kpc). *ApJ*, 238, 471–487. DOI: [10.1086/158003](https://doi.org/10.1086/158003).
- Rubin, V. C., & Ford, J., W. Kent. (1970). Rotation of the Andromeda Nebula from a Spectroscopic Survey of Emission Regions. *ApJ*, 159, 379. DOI: [10.1086/150317](https://doi.org/10.1086/150317).
- Russell, H. N. (1914). Relations Between the Spectra and Other Characteristics of the Stars. *Popular Astronomy*, 22, 275–294.
- Rybizki, J., Demleitner, M., Bailer-Jones, C., Tio, P. D., Cantat-Gaudin, T., Foesneau, M., Chen, Y., Andrae, R., Girardi, L., & Sharma, S. (2020). A Gaia Early DR3 Mock Stellar Catalog: Galactic Prior and Selection Function. *PASP*, 132(1013), Artikel 074501, 074501. DOI: [10.1088/1538-3873/ab8cb0](https://doi.org/10.1088/1538-3873/ab8cb0).
- Rybizki, J., Demleitner, M., Foesneau, M., Bailer-Jones, C., Rix, H.-W., & Andrae, R. (2018). A Gaia DR2 Mock Stellar Catalog. *PASP*, 130(989), 074101. DOI: [10.1088/1538-3873/aabd70](https://doi.org/10.1088/1538-3873/aabd70).
- Rybizki, J., Green, G. M., Rix, H.-W., El-Badry, K., Demleitner, M., Zari, E., Udalski, A., Smart, R. L., & Gould, A. (2022). A classifier for spurious astrometric solutions in Gaia eDR3. *MNRAS*, 510(2), 2597–2616. DOI: [10.1093/mnras/stab3588](https://doi.org/10.1093/mnras/stab3588).
- Rybizki, J., Rix, H.-W., Demleitner, M., Bailer-Jones, C. A. L., & Cooper, W. J. (2021). Characterizing the Gaia radial velocity sample selection function in its native photometry. *MNRAS*, 500(1), 397–409. DOI: [10.1093/mnras/staa3089](https://doi.org/10.1093/mnras/staa3089).
- Salaris, M., Weiss, A., & Percival, S. M. (2004). The age of the oldest Open Clusters. *A&A*, 414, 163–174. DOI: [10.1051/0004-6361:20031578](https://doi.org/10.1051/0004-6361:20031578).
- Sanders, J. L., & Binney, J. (2015). Extended distribution functions for our Galaxy. *MNRAS*, 449(4), 3479–3502. DOI: [10.1093/mnras/stv578](https://doi.org/10.1093/mnras/stv578).
- Sanders, J. L., Smith, L., & Evans, N. W. (2019). The pattern speed of the Milky Way bar from transverse velocities. *MNRAS*, 488(4), 4552–4564. DOI: [10.1093/mnras/stz1827](https://doi.org/10.1093/mnras/stz1827).

- Schaye, J., Crain, R. A., Bower, R. G., Furlong, M., Schaller, M., Theuns, T., Dalla Vecchia, C., Frenk, C. S., McCarthy, I. G., Helly, J. C., Jenkins, A., Rosas-Guevara, Y. M., White, S. D. M., Baes, M., Booth, C. M., Camps, P., Navarro, J. F., Qu, Y., Rahmati, A., ... Trayford, J. (2015). The EAGLE project: simulating the evolution and assembly of galaxies and their environments. *MNRAS*, *446*(1), 521–554. DOI: [10.1093/mnras/stu2058](https://doi.org/10.1093/mnras/stu2058).
- Schlegel, D. J., Finkbeiner, D. P., & Davis, M. (1998). Maps of Dust Infrared Emission for Use in Estimation of Reddening and Cosmic Microwave Background Radiation Foregrounds. *ApJ*, *500*(2), 525–553. DOI: [10.1086/305772](https://doi.org/10.1086/305772).
- Schönrich, R., Binney, J., & Dehnen, W. (2010). Local kinematics and the local standard of rest. *MNRAS*, *403*(4), 1829–1833. DOI: [10.1111/j.1365-2966.2010.16253.x](https://doi.org/10.1111/j.1365-2966.2010.16253.x).
- Schultz, G. V., & Wiemer, W. (1975). Interstellar reddening and IR-excesses of O and B stars. *A&A*, *43*, 133–139.
- Sellwood, J. A., & Binney, J. J. (2002). Radial mixing in galactic discs. *MNRAS*, *336*(3), 785–796. DOI: [10.1046/j.1365-8711.2002.05806.x](https://doi.org/10.1046/j.1365-8711.2002.05806.x).
- Sellwood, J. A., & Carlberg, R. G. (2014). Transient Spirals as Superposed Instabilities. *ApJ*, *785*(2), Artikel 137, 137. DOI: [10.1088/0004-637X/785/2/137](https://doi.org/10.1088/0004-637X/785/2/137).
- Shu, F. H. (2016). Six Decades of Spiral Density Wave Theory. *ARA&A*, *54*, 667–724. DOI: [10.1146/annurev-astro-081915-023426](https://doi.org/10.1146/annurev-astro-081915-023426).
- Sim, G., Lee, S. H., Ann, H. B., & Kim, S. (2019). 207 New Open Star Clusters within 1 kpc from Gaia Data Release 2. *Journal of Korean Astronomical Society*, *52*, 145–158. DOI: [10.5303/JKAS.2019.52.5.145](https://doi.org/10.5303/JKAS.2019.52.5.145).
- Smoot, G. F., Bennett, C. L., Kogut, A., Wright, E. L., Aymon, J., Boggess, N. W., Cheng, E. S., de Amici, G., Gulkis, S., Hauser, M. G., Hinshaw, G., Jackson, P. D., Janssen, M., Kaita, E., Kelsall, T., Keegstra, P., Lineweaver, C., Loewenstein, K., Lubin, P., ... Wilkinson, D. T. (1992). Structure in the COBE Differential Microwave Radiometer First-Year Maps. *ApJL*, *396*, L1. DOI: [10.1086/186504](https://doi.org/10.1086/186504).
- Soderblom, D. R. (2010). The Ages of Stars. *ARA&A*, *48*, 581–629. DOI: [10.1146/annurev-astro-081309-130806](https://doi.org/10.1146/annurev-astro-081309-130806).
- Sohn, S. T., Anderson, J., & van der Marel, R. P. (2012). The M31 Velocity Vector. I. Hubble Space Telescope Proper-motion Measurements. *ApJ*, *753*(1), Artikel 7, 7. DOI: [10.1088/0004-637X/753/1/7](https://doi.org/10.1088/0004-637X/753/1/7).
- Soubiran, C., Cantat-Gaudin, T., Romero-Gómez, M., Casamiquela, L., Jordi, C., Vallenari, A., Antoja, T., Balaguer-Núñez, L., Bossini, D., Bragaglia, A., Carrera, R., Castro-Ginard, A., Figueras, F., Heiter, U., Katz, D., Krone-Martins, A., Le Campion, J. .-, Moitinho, A., & Sordo, R. (2018). Open cluster kinematics with Gaia DR2. *A&A*, *619*, Artikel A155, A155. DOI: [10.1051/0004-6361/201834020](https://doi.org/10.1051/0004-6361/201834020).
- Spergel, D., Gehrels, N., Baltay, C., Bennett, D., Breckinridge, J., Donahue, M., Dressler, A., Gaudi, B. S., Greene, T., Guyon, O., Hirata, C., Kalirai, J., Kasdin, N. J., Macintosh, B., Moos, W., Perlmutter,

- ter, S., Postman, M., Rauscher, B., Rhodes, J., ... Zhao, F. (2015). Wide-Field Infrared Survey Telescope-Astrophysics Focused Telescope Assets WFIRST-AFTA 2015 Report. *arXiv e-prints*, Artikel arXiv:1503.03757, arXiv:1503.03757. DOI: [10.48550/arXiv.1503.03757](https://doi.org/10.48550/arXiv.1503.03757).
- Spina, L., Magrini, L., Sacco, G. G., Casali, G., Vallenari, A., Tautvaišienė, G., Jiménez-Esteban, F., Gilmore, G., Randich, S., Feltzing, S., Jeffries, R. D., Bensby, T., Bragaglia, A., Smiljanic, R., Carraro, G., Morbidelli, L., & Zaggia, S. (2022). The Gaia-ESO Survey: Chemical tagging in the thin disk. Open clusters blindly recovered in the elemental abundance space. *A&A*, 668, Artikel A16, A16. DOI: [10.1051/0004-6361/202243316](https://doi.org/10.1051/0004-6361/202243316).
- Spina, L., Randich, S., Magrini, L., Jeffries, R. D., Friel, E. D., Sacco, G. G., Pancino, E., Bonito, R., Bravi, L., Franciosini, E., Klutsch, A., Montes, D., Gilmore, G., Vallenari, A., Bensby, T., Bragaglia, A., Flaccomio, E., Koposov, S. E., Korn, A. J., ... Zaggia, S. (2017). The Gaia-ESO Survey: the present-day radial metallicity distribution of the Galactic disc probed by pre-main-sequence clusters. *A&A*, 601, Artikel A70, A70. DOI: [10.1051/0004-6361/201630078](https://doi.org/10.1051/0004-6361/201630078).
- Spitzer, J., Lyman. (1942). The Dynamics of the Interstellar Medium. III. Galactic Distribution. *ApJ*, 95, 329. DOI: [10.1086/144407](https://doi.org/10.1086/144407).
- Stewart, K. R., Bullock, J. S., Wechsler, R. H., Maller, A. H., & Zentner, A. R. (2008). Merger Histories of Galaxy Halos and Implications for Disk Survival. *ApJ*, 683(2), 597–610. DOI: [10.1086/588579](https://doi.org/10.1086/588579).
- Swiggum, C., D’Onghia, E., Alves, J., Großschedl, J., Foley, M., Zucker, C., Meingast, S., Chen, B., & Goodman, A. (2021). Evidence for Radial Expansion at the Core of the Orion Complex with Gaia EDR3. *ApJ*, 917(1), Artikel 21, 21. DOI: [10.3847/1538-4357/ac0633](https://doi.org/10.3847/1538-4357/ac0633).
- Tang, S.-Y., Pang, X., Yuan, Z., Chen, W. P., Hong, J., Goldman, B., Just, A., Shukirgaliyev, B., & Lin, C.-C. (2019). Discovery of Tidal Tails in Disrupting Open Clusters: Coma Berenices and a Neighbor Stellar Group. *ApJ*, 877(1), Artikel 12, 12. DOI: [10.3847/1538-4357/ab13b0](https://doi.org/10.3847/1538-4357/ab13b0).
- Tarricq, Y., Soubiran, C., Casamiquela, L., Castro-Ginard, A., Olivares, J., Miret-Roig, N., & Galli, P. A. B. (2022). Structural parameters of 389 local open clusters. *A&A*, 659, Artikel A59, A59. DOI: [10.1051/0004-6361/202142186](https://doi.org/10.1051/0004-6361/202142186).
- Tian, H.-J. (2020). Discovery of a Young Stellar Snake with Two Dissolving Cores in the Solar Neighborhood. *ApJ*, 904(2), Artikel 196, 196. DOI: [10.3847/1538-4357/abbbf4b](https://doi.org/10.3847/1538-4357/abbbf4b).
- Toomre, A. (1964). On the gravitational stability of a disk of stars. *ApJ*, 139, 1217–1238. DOI: [10.1086/147861](https://doi.org/10.1086/147861).
- Trick, W. H., Bovy, J., D’Onghia, E., & Rix, H.-W. (2017). Action-based Dynamical Modeling for the Milky Way Disk: The Influence of Spiral Arms. *ApJ*, 839(1), Artikel 61, 61. DOI: [10.3847/1538-4357/aa67db](https://doi.org/10.3847/1538-4357/aa67db).
- Trick, W. H., Coronado, J., & Rix, H.-W. (2019). The Galactic disc in action space as seen by Gaia DR2. *MNRAS*, 484(3), 3291–3306. DOI: [10.1093/mnras/stz209](https://doi.org/10.1093/mnras/stz209).
- Tully, R. B., & Fisher, J. R. (1977). A new method of determining distances to galaxies. *A&A*, 54, 661–673.

- Tully, R. B., Courtois, H., Hoffman, Y., & Pomarède, D. (2014). The Laniakea supercluster of galaxies. *Nature*, *513*(7516), 71–73. DOI: [10.1038/nature13674](https://doi.org/10.1038/nature13674).
- Vasiliev, E. (2019). AGAMA: action-based galaxy modelling architecture. *MNRAS*, *482*(2), 1525–1544. DOI: [10.1093/mnras/sty2672](https://doi.org/10.1093/mnras/sty2672).
- Virtanen, P., Gommers, R., Oliphant, T. E., Haberland, M., Reddy, T., Cournapeau, D., Burovski, E., Peterson, P., Weckesser, W., Bright, J., van der Walt, S. J., Brett, M., Wilson, J., Millman, K. J., Mayorov, N., Nelson, A. R. J., Jones, E., Kern, R., Larson, E., ... SciPy 1.0 Contributors. (2020). SciPy 1.0: Fundamental Algorithms for Scientific Computing in Python. *Nature Methods*, *17*, 261–272. DOI: [10.1038/s41592-019-0686-2](https://doi.org/10.1038/s41592-019-0686-2).
- Walch, S., Girichidis, P., Naab, T., Gatto, A., Glover, S. C. O., Wünsch, R., Klessen, R. S., Clark, P. C., Peters, T., Derigs, D., & Baczynski, C. (2015). The SILCC (SIMulating the LifeCycle of molecular Clouds) project - I. Chemical evolution of the supernova-driven ISM. *MNRAS*, *454*(1), 238–268. DOI: [10.1093/mnras/stv1975](https://doi.org/10.1093/mnras/stv1975).
- Walker, A. G. (1937). On Milne's Theory of World-Structure. *Proceedings of the London Mathematical Society*, *42*, 90–127. DOI: [10.1112/plms/s2-42.1.90](https://doi.org/10.1112/plms/s2-42.1.90).
- Wang, F., Tian, H., Qiu, D., Xu, Q., Fang, M., Tian, H., Di, L., Bird, S. A., Shi, J., Fu, X., Liu, G., Cui, S., & Zhang, Y. (2022). The stellar 'Snake' - I. Whole structure and properties. *MNRAS*, *513*(1), 503–515. DOI: [10.1093/mnras/stac843](https://doi.org/10.1093/mnras/stac843).
- Ward, J. L., Kruijssen, J. M. D., & Rix, H.-W. (2020). Not all stars form in clusters - Gaia-DR2 uncovers the origin of OB associations. *MNRAS*, *495*(1), 663–685. DOI: [10.1093/mnras/staa1056](https://doi.org/10.1093/mnras/staa1056).
- Wegg, C., Gerhard, O., & Portail, M. (2015). The structure of the Milky Way's bar outside the bulge. *MNRAS*, *450*(4), 4050–4069. DOI: [10.1093/mnras/stv745](https://doi.org/10.1093/mnras/stv745).
- Weigert, A., & Wendker, H. J. (1989). *Astronomie und Astrophysik - ein Grundkurs*.
- White, S. D. M., & Rees, M. J. (1978). Core condensation in heavy halos: a two-stage theory for galaxy formation and clustering. *MNRAS*, *183*, 341–358. DOI: [10.1093/mnras/183.3.341](https://doi.org/10.1093/mnras/183.3.341).
- Wielen, R., Fuchs, B., & Dettbarn, C. (1996). On the birth-place of the Sun and the places of formation of other nearby stars. *A&A*, *314*, 438.
- Wright, N. J., & Mamajek, E. E. (2018). The kinematics of the Scorpius-Centaurus OB association from Gaia DR1. *MNRAS*, *476*(1), 381–398. DOI: [10.1093/mnras/sty207](https://doi.org/10.1093/mnras/sty207).
- Yen, S. X., Reffert, S., Schilbach, E., Röser, S., Kharchenko, N. V., & Piskunov, A. E. (2018). Reanalysis of nearby open clusters using Gaia DR1/TGAS and HSOY. *A&A*, *615*, Artikel A12, A12. DOI: [10.1051/0004-6361/201731905](https://doi.org/10.1051/0004-6361/201731905).
- Zari, E., Brown, A. G. A., & de Zeeuw, P. T. (2019). Structure, kinematics, and ages of the young stellar populations in the Orion region. *A&A*, *628*, Artikel A123, A123. DOI: [10.1051/0004-6361/201935781](https://doi.org/10.1051/0004-6361/201935781).
- Žerjal, M., Ireland, M. J., Crundall, T. D., Krumholz, M. R., & Rains, A. D. (2023). CHRONOSTAR - II. Kinematic age and substructure of the Scorpius-Centaurus OB2 association. *MNRAS*, *519*(3), 3992–4009. DOI: [10.1093/mnras/stac3693](https://doi.org/10.1093/mnras/stac3693).

Bibliography

Zucker, C., Peek, J. E. G., & Loebman, S. (2022). Disconnecting the Dots: Re-examining the Nature of Stellar “Strings” in the Milky Way. *ApJ*, 936(2), Artikel 160, 160. DOI: [10.3847/1538-4357/ac898c](https://doi.org/10.3847/1538-4357/ac898c).